ELECTROCHEMICALLY-MODULATED SEMICONDUCTOR CRYSTAL GROWTH FROM LIQUID METAL ELECTRODES

by

Eli Fahrenkrug

A dissertation submitted in partial fulfillment
of the requirements for the degree of
Doctor of Philosophy
(Chemistry)
in The University of Michigan
2016

Doctoral Committee:

Professor Stephen Maldonado, Chair
Professor Adam J. Matzger
Professor Michael D. Morris
Professor Jamie D. Phillips

DEDICATION

To the notion that *"only the ideas that we really live have any value."* H.H.

ACKNOWLEDGEMENTS

I thank my parents for all of life, my friends and family for giving it color, and my wife Kate, for helping me relish in all of its grandeur.

Beyond that, I'm not much for hierarchies of gratitude. I have had the great fortune to work within a constellation of fantastic people – you know who you are.

TABLE OF CONTENTS

LIST OF FIGURES

LIST OF TABLES

ABSTRACT

This thesis describes a new electrochemical synthetic strategy for direct growth of crystalline covalent group IV and III–V semiconductor materials at or near ambient temperature conditions. This strategy, which we call "electrochemical liquid–liquid–solid" (ec-LLS) crystal growth, marries the semiconductor solvation properties of liquid metal melts with the utility and simplicity of conventional electrodeposition. A low-temperature liquid metal (i.e., Hg, Ga, or alloy thereof) acts simultaneously as the source of electrons for the heterogeneous reduction of oxidized semiconductor precursors dissolved in an electrolyte as well as the solvent for dissolution of the zero-valent semiconductor. Supersaturation of the semiconductor in the liquid metal triggers eventual crystal nucleation and growth. In this way, the liquid electrolyte–liquid metal–solid crystal phase boundary strongly influences crystal growth.

The intent of this thesis is to summarize the key elements of ec-LLS identified to date, first contextualizing this method with respect to other semiconductor crystal growth methods in Chapter 1 and then highlighting some unique capabilities of ec-LLS in subsequent chapters. Specifically, Chapter 2 describes the first demonstration of an epitaxial ec-LLS growth process of single-crystalline germanium (Ge) nanowires at room temperature in a massively parallel fashion. Chapter 3 further extends the concept of heterogeneous nucleation in ec-LLS into the micron-sized scale regime by describing highly ordered crystalline Ge microwire arrays. Chapter 4 addresses the hypothesis as to whether the liquid metal electrode in ec-LLS can also serve as a reactant source for preparation of the compound semiconductor, GaAs. Chapter 5 demonstrates a new electrochemically-induced alloy formation process to directly prepare crystalline InAs films in aqueous electrolytes at room temperature. And Chapter 6 summarizes and contextualizes the cumulative conclusions of this thesis while describing future research directions.

CHAPTER 1

Introduction

1.1. Context and Importance

Semiconductors at Scale

As the quest for a more electronically-integrated society marches forward, research, development, and production of semiconductor materials will continue to burgeon. Crystalline covalent semiconductors are ubiquitous in society as they comprise the active components of most electronics, lighting, energy, and sensing technologies.[1-4] The global semiconductor market contributed over $330 billion in 2015 alone. To frame that within a temporal perspective, the industry's contribution to the U.S. economy has grown by more than any other manufacturing industry over the last 25 years, directly employing over 250,000 people and indirectly over 1 million more.[5]

Further motivation for semiconductor research spawns from the inexorable drive to device miniaturization. As this trajectory begins to converge with the fundamental limits of materials science and physics, microelectronics architectures are transitioning from conventional planar structures to new 3D nanostructured designs (Figure 1.1). Thus new synthetic techniques which simultaneously satisfy the high material quality and nanoscale size demands are warranted.

Many semiconductors exist, but in the combined trillion dollar electronics, photovoltaics and lighting industries,[6] silicon (Si), germanium (Ge), and gallium-based materials are most widely employed.[5] Corresponding global production of Si and Ge in 2015 was 7680 kt, 16.5 t, respectively.[7]

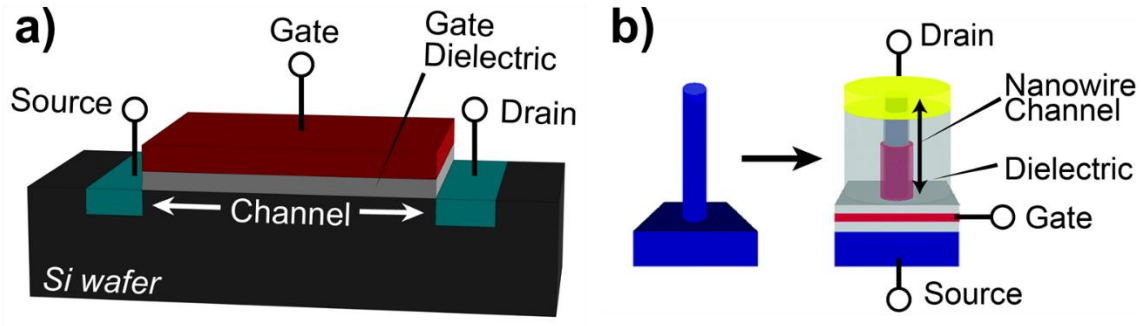

Figure 1.1. Drawings of (a) a conventional planar MOSFET device used commonly in integrated circuitry and (b) a 3D vertically-integrated nanowire transistor design that decreases the component's areal footprint without compromising channel length or performance.

Semiconductor Basics

Semiconductor materials possess three distinct physical characteristics which contribute to their technological pervasiveness. First, as their name implies, the intrinsic electrical resistance of semiconductors lies between that of metals and insulators. Through a process called doping, these conduction properties can be precisely controlled via the deliberate introduction of elemental impurities into the crystal lattice. When a doped semiconductor contains mostly free electrons it is known as 'n-type' and when it contains mostly free holes, it is considered 'p-type'.

The second property of semiconductors is the unique behavior of charge carriers at the interface of p- and n-type regions, called p-n junctions. Such junctions define the underlying action of all diodes, transistors, solar cells, and light emitting diodes (LEDs).

Last, the electronic structure of semiconductor materials possess an inherent energy range where no population of electrons exists. This forbidden 'band gap' energy is similar to the concept of highest occupied and lowest unoccupied molecular orbitals (HOMO/LUMO) in molecules. If photons with energy exceeding the bandgap impinge on the semiconductor, electrons can be promoted across the energy gap, giving rise to the photovoltaic effect. For certain semiconductors, the same process can be reversed to emit specific colors of light. Semiconductors with smaller bandgaps on the order of thermal energies can convert heat into electricity via the thermoelectric effect.

Most inorganic semiconductors can exist in crystalline or amorphous forms. However, the vast majority of commercial applications require materials of high crystalline quality with low defect densities to facilitate the highest optoelectronic character. The key to controlling semiconductor crystal growth is a tacit understanding of the energetic and kinetic bounds which constrain it within the physical and experimental world.

1.2. Technical Background

Crystal Nucleation and Growth

All crystallization phenomena begin with nucleation. Nucleation is crucial as it can determine properties and size distributions of the resulting crystals. In solutions, nucleation is the period of time during which a new distinct thermodynamic phase emerges. If this

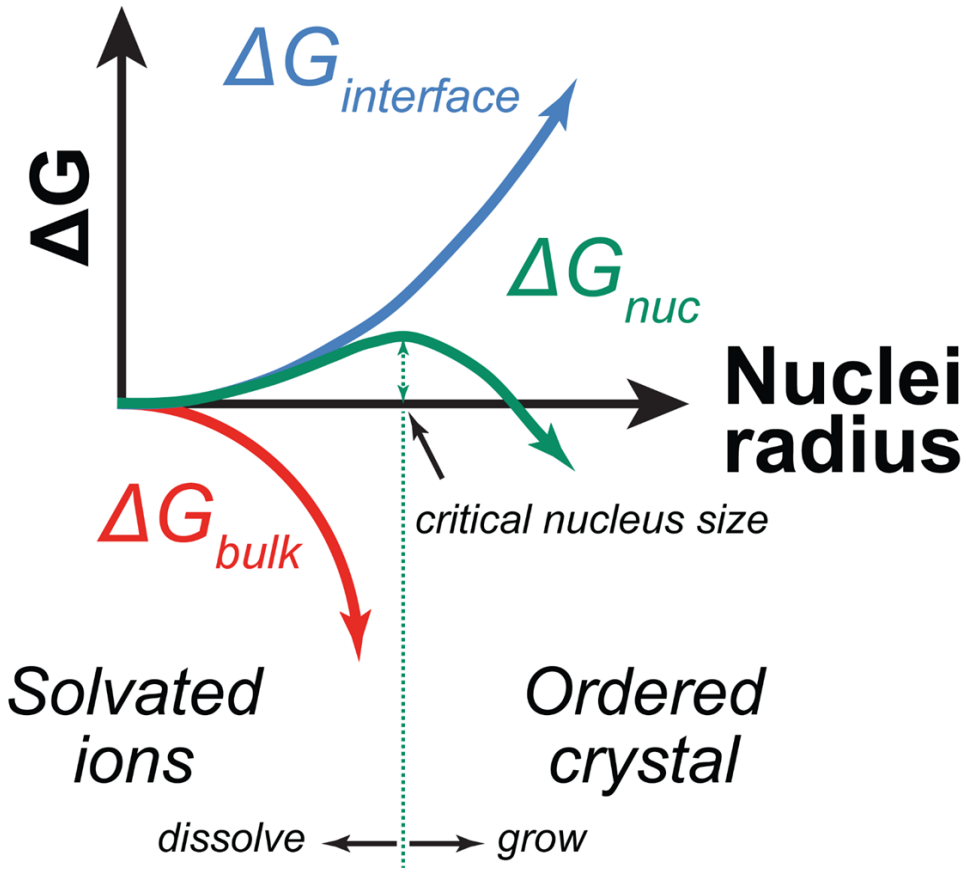

Figure 1.2. Free energy of crystal nucleation shown as a function of nuclei radius. Nuclei with radii smaller than the critical size are driven to dissolve, while larger nuclei represent a new phase more stable than the old phase.

new phase continues to grow in size, this is termed crystal growth. A driving force favoring nucleation arises when the chemical potential of a new emerging phase is lower than the old phase. This condition is described in Equation 1.1:

$$\Delta\mu = \mu_{solute} - \mu_{crystal} > 0 \tag{1.1}$$

In semiconductor crystal growth from solutions, the extent of supersaturation (σ) can be determined by comparing the solubility obtained from the equilibrium phase diagram (C_{eq}) to the time-dependent solubility($C(t)$) through the expression,

$$\sigma = \frac{C(t)}{C_{eq}} - 1 \tag{1.2}$$

This non-equilibrium condition can be achieved through myriad environmental perturbations including temperature change, mechanical agitation, solvent evaporation, and mass transport, among others.

Classical nucleation theory (CNT) divides the energetics of nucleation (ΔG_{nuc}) into bulk (ΔG_{bulk}) and interfacial (ΔG_{int}) components. As the new phase with lower chemical potential emerges, a thermodynamically favorable reduction in the free energy of the bulk solid occurs (ΔG_{bulk}). At the same time, the different bonding environment at this new solid/liquid interface leads to a free energy gain (ΔG_{int}) which scales with the nuclei surface area. As depicted in Figure 1.2, surface effects are strongest in small nuclei where a driving force to re-dissolve exists. But as the surface area to volume ratio reaches a certain point, the free energy reduction from the bulk phase dominates and leads to a stable crystal. The inflection point in the ΔG_{nuc} curve in Figure 1.2 describes both the energetic barrier to nucleation and the critical nucleus size. For a spherical nucleus, the energetic barrier (ΔG_{nuc}) can be described quantitatively by,

$$\Delta G_{nuc} = \left(\frac{16}{3}\pi {\Delta G_{int}}^3\right)\left(\frac{\Omega}{kT\sigma}\right)^2 \tag{1.3}$$

where Ω is the volume per molecule, k is Boltzmann's constant, T is absolute temperature and other variables have been defined. One important implication of this model is that as the supersaturation increases, the critical size drops. One should generally note that CNT is a simple model with many demonstrated exceptions, but in this thesis, it serves only to highlight the interplay and importance of key parameters contributing to semiconductor crystal nucleation and growth.

From Equation 1.3, one strategy to exert control over the nucleation barrier is to reduce the interfacial contribution (ΔG_{int}) by introducing a foreign surface for nucleation. In many cases, the energetics at the nucleus/surface interface are more favorable than the nucleus/solution interface. In other words, the bond enthalpies between the nucleus and the substrate are stronger than those of solvation. Whether a crystal emerges at a solid interface or from the bulk solution, heterogeneous or homogeneous nucleation occurs, respectively. Since many of semiconductor applications are dictated by characteristics at the interface of a semiconductor heterojunction, heterogeneous nucleation is arguably the most important strategy employed in commercial semiconductor crystal growth. It also highlights the importance of crystal growth methods that are amenable to growth on a variety of substrate types.

Although thermodynamics detail the driving force for crystal growth, kinetics describe the rate. As long as the inequality in Equation 1.1 is satisfied, crystallization will always inevitably occur. However, the rate of nucleation (J_{nuc}) is dictated by the barrier (ΔG_{nuc}) to nucleation, both of which are related through an expression of typical Arrhenius form,

$$J_{nuc} = Ae^{-\frac{\Delta G_{nuc}}{kT}} \tag{1.4}$$

where the pre-exponential factor A depends on a variety of factors and the other variables have been defined. In general, Equation 1.4 describes how intrinsic thermodynamic parameters like supersaturation and critical nucleus size are inextricably intertwined with the rate at which crystals nucleate. Understanding the interplay between crystal nucleation energetics and kinetics is the key to demonstrating exquisite control over new phases and is certainly the crux of all semiconductor crystal growth methods.

Conventional Semiconductor Manufacturing

Current industrial manufacturing methods for Groups IV and III-V semiconductors are energy- and resource-intensive,[8-10] since no group IV or III-V semiconductor occurs naturally on this planet. Instead, they must be prepared from heavily oxidized ores and oxides found in nature.

Preparation of covalent semiconductor materials can be broadly classified as bulk or thin film methods. Methods that produce bulk macroscopic semiconductors generally first involve steps to reduce raw oxides to elemental semiconductors. The raw zero-valent materials are then re-crystallized in hot (T>1400 °C for Si) melts of the target semiconductor using Czochralski, Bridgman, or float-zone techniques. These multi-step processes can yield large (> 1 cm^3) high quality single crystals but are unsuitable for thin films.[11] A variation of this concept is liquid phase epitaxy (LPE). In LPE, a previously-prepared raw semiconductor powder is first dissolved into a liquid metal solvent at an elevated temperature. The temperature of the metal melt is then lowered to attain supersaturation and promote crystal nucleation and growth (Figure 1.3a).[12] LPE is naturally suited for the preparation of semiconductor films with few defects, low levels of impurities, and large crystalline domains.[12] However, LPE is not actively used in industrial semiconductor manufacturing because thin films cannot be deposited with sufficient precision and LPE reactor designs are cumbersome (Figure 1.4a).[12,13] Liquid phase electroepitaxy (LPEE) is a variation of LPE where a large, non-Faradaic electrical current is passed through the metal melt during crystal growth. The current is large (10^1 A cm^{-2}) to induce local Joule heating and Peltier cooling at the respective electrodes, enhancing the driving force for nucleation.[14]

For growth of micro- and nanoscale crystals, vapor liquid solid (VLS) and solution liquid solid (SLS) methods are similar to LPE but employ much smaller diameter (10^{-9} – 10^{-6} m) liquid metals (Figure 1.3b). VLS specifically involves the decomposition of gas-phase reactants in a hot reactor (typically) under vacuum to introduce zero-valent semiconductors into the molten liquid metal. SLS separately requires the decomposition of molecular reactants dissolved in a hot liquid solvent free of any water or O_2. VLS and SLS have proven useful for the synthesis and study of micro- and nanocrystalline materials but also share some intrinsic drawbacks as manufacturing strategies.[15-17] First, high

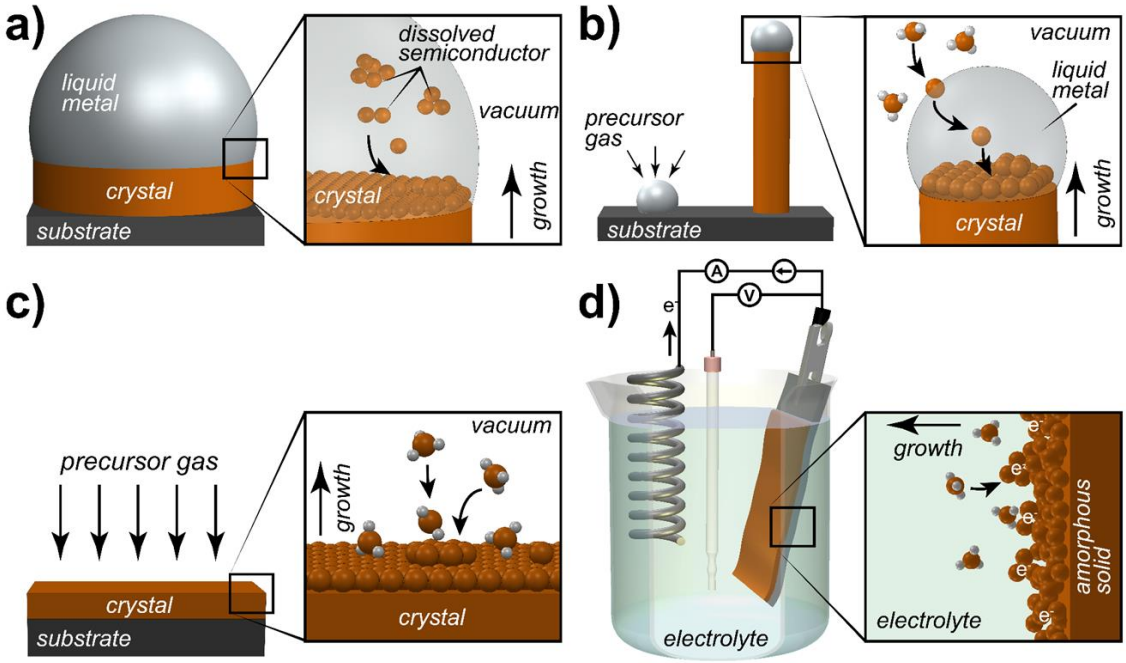

Figure 1.3. Schematic representations of select semiconductor crystal growth strategies including (a) liquid phase epitaxy, (b) vapor-liquid-solid or solution-liquid-solid growth, (c) vapor phase deposition, and (d) conventional electrodeposition. Not drawn to scale.

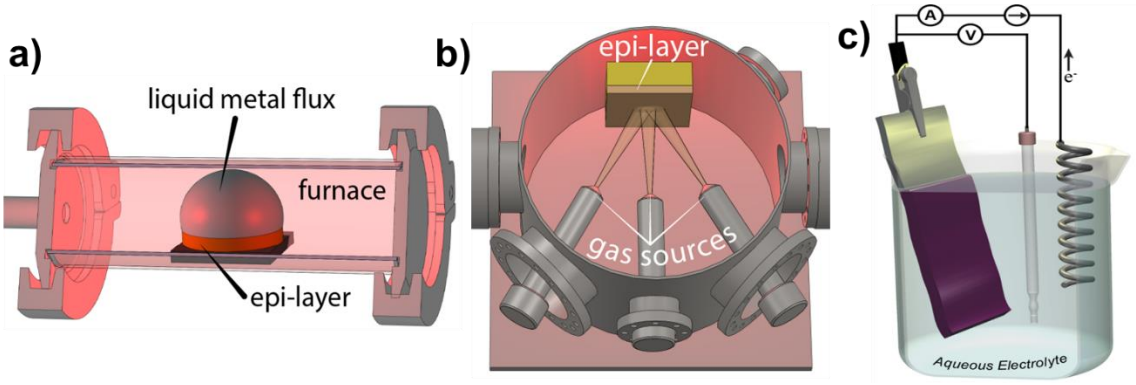

Figure 1.4. Comparing experimental setups for (a) LPE, (b) MBE, (c) electrodeposition.

temperatures and/or low pressures are required to drive the thermal decomposition of precursors to their zero-valent forms.[15,16,18,19] Second, both techniques employ heavily refined and expensive semiconductor precursor compounds that are often toxic and are themselves resource-intensive to synthesize, handle, and store.[19,20] Third, the combination of high temperature, low pressure, and noxious precursors imposes serious constraints on the compatibility of deposition substrates,[21,22] metal catalyst identity,[23] and high-throughput reactor designs that don't introduce substantial material inhomogeneity.[15-17]

The preparation of thin semiconductors films does not usually involve melts. Molecular beam epitaxy (MBE) and metal organic chemical vapor deposition (MOCVD) are gas-phase deposition strategies based on the reaction of atomic or molecular precursors impinging on a hot deposition substrate (Figures 1.3c and 1.4b). Compositionally complex crystalline semiconductor thin films can be produced with excellent electrical properties and thickness control. However, both techniques require elaborate and expensive vacuum-based reactors,[8,11,24] vapor phase precursors that are heavily processed/refined/energy-rich,[8] and high process temperatures (T >600 °C) to promote good crystallinity.[8,24]

Semiconductor Electrodeposition

In contrast, electrodeposition has long been explored as a possible alternative route for semiconductor films. The principal draw is the comparatively simple instrumentation/setup and the possibility of deposition at low temperatures (Figure 1.4c).[25,26] 'Conventional' electrodeposition is defined by solid electrodes immersed in an electrolyte bath with dissolved oxidized precursors. A negative bias applied to the solid cathode drives the heterogeneous electroreduction to the zero-valent state (Figure 1.3d). Despite the simplicity, 'conventional' electrodeposition has three major drawbacks. First, low temperature (T<500 °C) electrodeposition always produces amorphous solids with high impurity content (e.g. solvent and supporting electrolyte). The poor purity/crystallinity of these films necessitates thermal processing, negating any cost-advantage.[27-29] Second, high temperature electrodeposition requires solvents such as the aforementioned melts and the use of sacrificial anodes.[30-32] Third, electrodeposition of compositionally complex (e.g. binary, ternary, quaternary) semiconductors requires simultaneous co-electrodeposition of multiple species. Doing so with sufficient precision

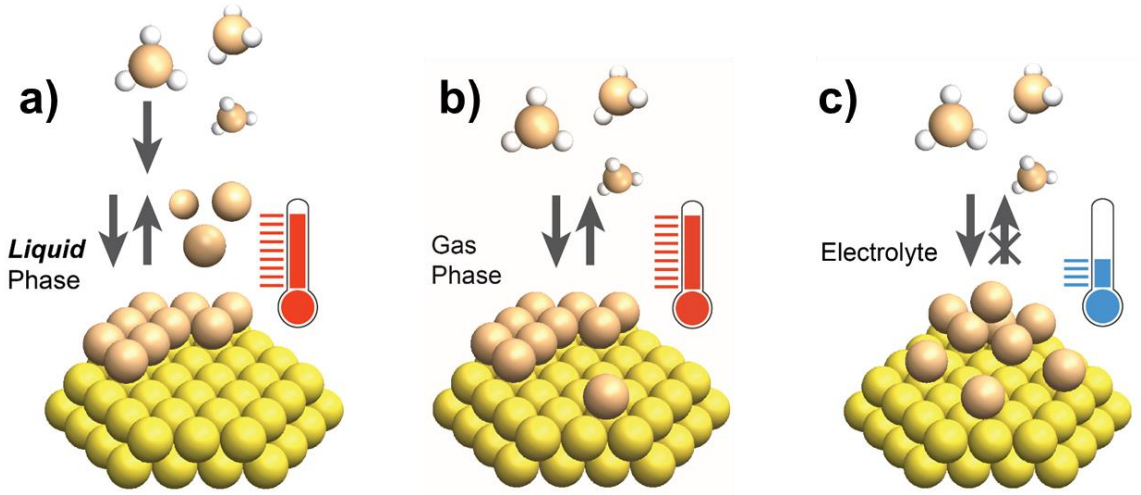

Figure 1.5. General classification of different crystallization pathways. (a) is a high temperature reversible liquid phase crystallization like melt or solution-based growth, (b) is a high temperature reversible path from vapor, and (c) is low temperature irreversible mode like conventional electrodeposition.

to effect a precise stoichiometry throughout the entirety of the film is extremely challenging.[29,33] Electrochemical atomic layer epitaxy (ECALE)[34,35] stands apart in this regard, as stoichiometric and highly ordered II-VI films can be made via ECALE. However, although ECALE methods are apt for ionic semiconductors, ECALE of covalent Groups IV and III-V semiconductor films is extremely challenging.

In summary, two general crystallization classes have been described. First, high temperature strategies that favors a reversible growth pathway and high surface and bulk mobilities often result in higher quality crystals. All of the melt (Czochralski, Bridgman, float zone), solution (LPE, LPEE), and vapor phase epitaxy (MBE, MOCVD) fall generally under this category. Second is the simpler, often lower temperature strategy that doesn't employ a solvating medium. For example, in the case of conventional electrodeposition, an irreversible crystallization pathway is traversed which typically yields crystals with high defect concentrations and poor crystallinity. Figure 1.5 schematically contrasts the two crystallization classifications while framing the motivation for developing a hybrid method that enables a lower temperature reversible pathway.

Electrochemical Liquid Liquid Solid Crystal Growth (ec-LLS)

The hallmark of ec-LLS is a liquid metal acting both as an electron source for the heterogeneous reduction of oxidized precursors and as a separate phase for solvating the deposit. This strategy marries the semiconductor solvation properties of liquid metal melts with the utility and simplicity of conventional electrodeposition. In certain cases, the liquid metal can also act as a reagent. Two specific variations of ec-LLS will be the focus of this thesis and are shown in Figure 1.6. In either type, ec-LLS begins with application of an electrochemical potential to a liquid metal electrode, providing the driving force for reduction of the dissolved precursor to the zero-valent state (Figure 1.6, Step 1). Electrical connection to the liquid metals is made using a small Pt wire in macroscale electrodes[36-38] and directly through a conductive support in the case of micro- and nanoscale liquid metals.[39-41] Continued electrochemical reduction of the precursor establishes a concentration gradient between the surface and interior of the liquid metal, which drives dissolution of the semiconductor into the bulk of the liquid metal solution (Step 2). When concentrations surpass the equilibrium solubility of the semiconductor in the metal solution,

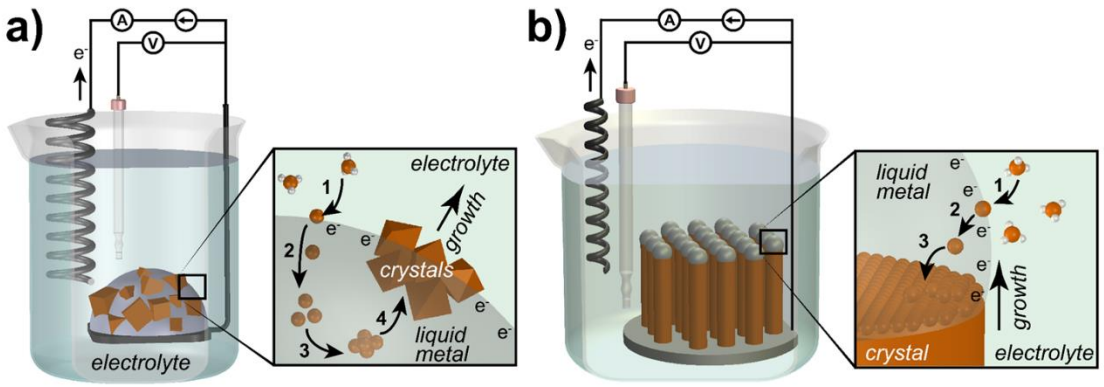

Figure 1.6. Schematic depictions of the experimental setup and steps (insets) of ec-LLS semiconductor crystal growth from (a) bulk and (b) nano/micro scale liquid metal droplet electrodes. Ec-LLS proceeds through (1) electrochemical reduction of a dissolved ionic precursor in the electrolyte solution followed by (2) dissolution of the zero-valent semiconductor into the liquid metal electrode. In (a), steps (3) and (4) highlight homogeneous nucleation and subsequent crystal growth, respectively. In (b), step (3) depicts heterogeneous nucleation at a crystal seed interface and subsequent layer by layer crystal growth. Not drawn to scale.

crystal nucleation (Step 3) and growth (Step 4) ensue. Removal of the electrochemical driving force results in immediate cessation of ec-LLS.

Ec-LLS is a true hybrid, combining the best features of all the methods described in Figure 1. As in conventional electrodeposition, raw, oxidized precursors are used as inputs. In this sense, ec-LLS is a *synthetic* method and thus stands apart from the melt recrystallizations described above that require separate prior steps to form the reduced semiconductor. However, unlike conventional electrodeposition, ec-LLS products are fully crystalline, even at low temperatures. As in melt growths, the liquid metals in ec-LLS solvate fully reduced semiconductors and facilitate crystal growth. Accordingly, our group has demonstrated the direct production of crystalline Ge, Si, Ga-based III-V semiconductors and In-containing III-V semiconductors under purely benchtop conditions.

As a synthetic strategy, ec-LLS has several intrinsic features that are attractive for preparing covalent semiconductor crystals. First, ec-LLS does not require high temperatures, toxic precursors, or high energy density semiconductor reagents. This largely simplifies equipment complexity and expense. In practice, ec-LLS can be performed with only a beaker filled with electrolyte and an electrical circuit capable of supplying a defined current (e.g. a battery in series with a resistor). By this same token, ec-LLS is compatible with thermally and chemically sensitive substrates (e.g. plastics) that cannot be used as deposition substrates in conventional syntheses of covalent semiconductors. Second, ec-LLS affords control over a host of crystal shapes and sizes through simple change of common experimental parameters. As described in detail in the next section, large and small semiconductor crystals can be grown both homogeneously within a liquid metal electrode and heterogeneously at the interface of a liquid metal electrode and a seed substrate, depending on the particular details chosen for ec-LLS. Third, the rate of introduction of zero-valent materials into the liquid metal are precisely gated with a high degree of resolution by the applied potential/current.

The concept of ec-LLS was first demonstrated through the aqueous electrodeposition of Ge nanofilaments on bulk Hg cathodes (Figure 1.7a).[36] Soon after, faceted crystals with dimensions on the micron-scale were prepared simply by exchanging the cathode for Ga(*l*) (Figure 1.7b). Figure 1.7C depicts further extension of the ec-LLS

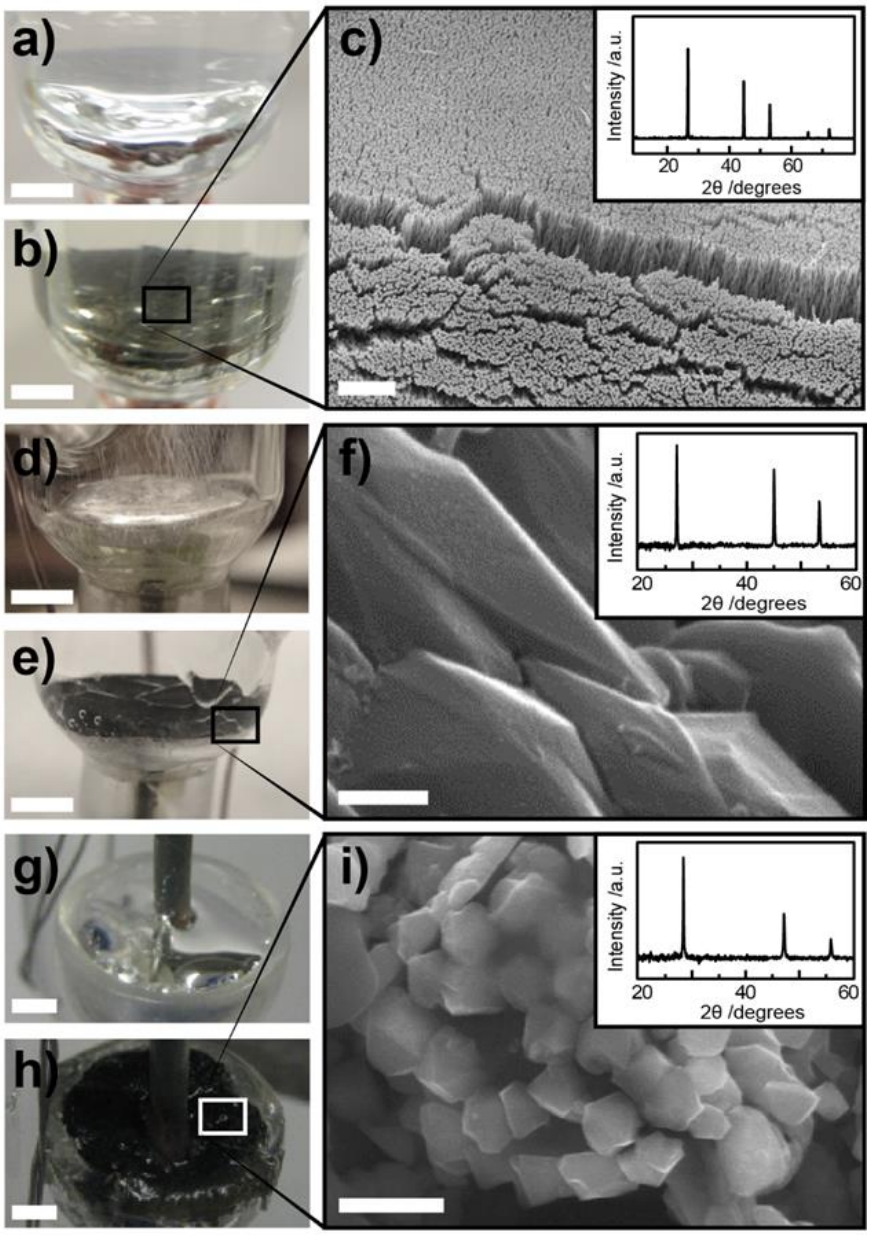

Figure 1.7. Optical photographs of a bulk Hg(*l*) electrode (a) before and (b) after room temperature Ge ec-LLS at -2.7 V vs. Ag/AgCl from an aqueous electrolyte containing 0.05 M GeO_2 and 0.01 M $Na_2B_4O_7$. (c) Corresponding electron micrograph and powder X-ray diffraction pattern collected from the as-deposited material shown in b). Optical photographs of a bulk Ga(*l*) electrode (d) before and (e) after room temperature Ge ec-LLS at -1.6 V vs. Ag/AgCl from the same aqueous electrolyte as that used in (b). (f) Tilted electron micrograph and powder X-ray diffractogram (inset) of crystals produced in (e). Optical photographs of a bulk Ga(*l*) electrode (g) before and (h) after Si ec-LLS at 20 mA cm^{-2} for two hours at 100 °C from a propylene carbonate electrolyte with 0.5 M $SiCl_4$ and 0.2 M TBACl. (i) Scanning electron micrograph and diffraction pattern (inset) of crystals produced in h). Scales are 2 mm for (a,b,d,e,g,h) and 1 μm for (c,f,i).

system toward the low temperature electrodeposition of Si nanocrystals, again from Ga(*l*) cathodes.[38] Although not reported in detail here, these initial reports were instrumental in shaping the hypothesis of this thesis.

The intent of this thesis is to summarize the key elements of ec-LLS identified to date, first contextualizing this method with respect to other semiconductor crystal growth methods and then highlighting some unique capabilities of ec-LLS. Specifically, descriptions of ec-LLS as a platform to prepare Ge and Si crystals from bulk- (~1 cm^3), micro- (~10^{-10} cm^3), and nano- (~10^{-16} cm^3) sized liquid metal electrodes in common solvents at low temperature will be detailed. In addition, preparation of more compositionally complex binary covalent III-V semiconductors will be described.

1.3. Content Description

Chapter 2 describes the first demonstration of an epitaxial ec-LLS growth process of single-crystalline germanium (Ge) nanowires at room temperature in a massively parallel fashion. Electrodeposition was carried out at the wafer scale through the electroreduction of dissolved GeO_2(*aq*) in water at hundreds of thousands of isolated liquid gallium (Ga) nanodroplet electrodes resting on single-crystalline Ge or Si supports. A variety of electron microscopies were employed to validate both the epitaxial and single crystal nature of the as-deposited structures. Atomically-resolved high resolution TEM images of the nanowire/substrate junction revealed a defect free structural interface. Growth on a variety of substrate orientations and identities further confirmed the atomic registry between the electrodeposited Ge crystal and the native substrate. Energy dispersive spectroscopic elemental mapping of single nanowires still attached to the Ge(111) growth substrate indicated the Ga remains affixed to the tip of the growing nanowire through the electrodeposition process. At the same time, the diameter of the nanowire strongly followed the initial diameter of the liquid Ga nanodroplet. Since this is an electrochemical process, the length of the wire could also be controlled precisely by measuring and limiting the total Faradaic charge passed in an experiment. To probe the electrical properties of the nanowire/substrate junction, conductive atomic force microscopy was use to collect solid-state current-voltage responses across many individual nanowire/substrate junctions. The responses were highly reproducible, reaffirming both the structural and electrical fidelity

of the as-prepared junctions. The presented data cumulatively show epitaxial growth of a covalent group IV semiconductor in a highly parallel fashion at the wafer scale using simple electrochemical methods.

Chapter 3 further extends the concept of heterogeneous ec-LLS into the micron-sized scale regime. Highly ordered crystalline Ge microwire arrays with individual diameters between 1-10 μm were prepared by ec-LLS in an aqueous electrolyte. To access this size regime, a new liquid metal patterning strategy was developed. The fabrication process combines the utility of photolithography with the simplicity of doctor blading to produce macroscopic (> $1cm^2$) arrays of liquid metal microelectrodes. The versatility of the patterning and growth was demonstrated on an assortment of different conductive substrates including silicon, fluorine-doped tin oxide (FTO), copper foil, titanium foil, stainless steel, and the conductive polymer PEDOT:PSS. Furthermore, a simple chemical bath lift-off procedure was developed to fully remove the Ge microwire arrays embedded in SU-8 photoresist without perturbing the order or quality of the material, resulting in a free-standing composite membrane. The embedded arrays could then be re-cast onto virtually any receiving substrate regardless of conductivity or thermal sensitivity. Data from energy-dispersive spectroscopy, Auger nanoprobe spectroscopic mapping and four-terminal single microwire electrical measurements indicated that the specific liquid metal used for ec-LLS impacts the morphology and electrical properties of the resultant Ge micowires. Specifically, microwires grown from pure Ga electrodes were tapered and more conductive. Whereas microwires prepared from $Ga_{75}In_{25}$ (wt. %) electrodes achieved high aspect ratios with less incorporation of the liquid metal into the crystal structure. This new platform enables systematic study of the impacts of liquid metal size and composition on the crystallinity, microstructure, and electrical behavior of the resultant structures.

Chapter 4 addresses the hypothesis as to whether the liquid metal electrode in ec-LLS can also serve as a reactant source. The chosen model system was the electroreduction of As_2O_3 dissolved in an alkaline aqueous solution at a liquid gallium (Ga(*l*)) electrode at modest temperatures ($T \geq 80$ °C) to effect crystalline phase GaAs. Ga(*l*) pool electrodes yielded consistent electrochemical behavior, affording repetitive measurements that illustrated the interdependences of applied potential, concentration of dissolved As_2O_3, and

electrodeposition temperature on the quality of the resultant crystalline GaAs(*s*). Raman spectra indicated the composition of the resultant film was strongly dependent on both the electrodeposition temperature and dissolved concentration of As_2O_3 but not to the applied bias. For electrodepositions performed either at room temperature or with high ($\geqslant$0.01 M) concentrations of dissolved As_2O_3, Raman spectra of the electrodeposited films were consistent with amorphous As(*s*). X-ray diffractograms of As(*s*) films collected after thermal annealing indicated metallurgical alloying occurred only at temperatures in excess of 200 °C. Optical images and Raman spectra separately showed the composition of the as-electrodeposited film in dilute ($\leq$ 0.001 M) solutions of dissolved As_2O_3(*aq*) was pure crystalline GaAs(*s*) at much lower temperatures than 200 °C. Diffractograms and transmission electron microscopy performed on as-prepared films confirmed the identity of crystalline GaAs(*s*). The collective results thus provide the first clear demonstration of an electrochemical liquid–liquid–solid (ec-LLS) process involving a liquid metal that serves simultaneously as an electrode, a solvent/medium for crystal growth, and a coreactant for the synthesis of a polycrystalline semiconductor. The presented data serve as impetus for the further development of the ec-LLS process as a controllable, simple, and direct route for technologically important optoelectronic materials such as crystalline GaAs(*s*).

Chapter 5 demonstrates a new electrochemically-induced alloy formation process to directly prepare crystalline InAs films in aqueous electrolytes at room temperature. Electrochemical reduction of dissolved As_2O_3 at In(*s*) foils consistently yielded crystalline InAs films. Steady-state Raman spectra, transmission electron microscopy, and selected area electron diffraction indicated that the as-prepared films crystallize in the zincblende phase with no further thermal treatments. Cyclic voltammetry measurements, optical images, and steady-state Raman spectra confirmed that a clean oxide-free interface is critical for the successful formation of the binary InAs phase. The salient feature of this work is the use of simple aqueous electrochemistry to simultaneously remove passive metal oxides from the In(*s*) metal surface while controllably reducing dissolved arsenic oxide at the interface to drive the In–As alloying reaction. Raman spectral mapping data illustrate that the resulting film coverage and homogeneity are a strong function of the formal As_2O_3 concentration and the duration of the electrodeposition experiment. Potential-dependent in

situ Raman spectroscopy was used to implicate the solid-state reaction as the rate-limiting step in InAs film formation over the first 160 min, after which solid-state diffusion dominated the kinetics. The collective results establish a precedent for an alternative synthetic strategy for crystalline InAs thin films that does not require vacuum or sophisticated furnaces, toxic gaseous precursors like arsine, or exotic solvents.

Chapter 6 summarizes and contextualizes the cumulative conclusions of this thesis while describing future research directions. First, an adaptation of ec-LLS to large area thin film technology is outlined. Practical constraints, cell design, and preliminary results for epitaxial Ge film growth over 1 in^2 is highlighted. Second, merits for investigation of the ec-LLS mechanism with in-situ electrochemical transmission electron microscopy are discussed. Experimental challenges, sample preparation, and preliminary data are shown.

1.4. References

1. Hu, C. *Modern semiconductor devices for integrated circuits*; Prentice Hall: Upper Saddle River, N.J., 2010.
2. Razeghi, M.; Rogalski, A. *J. Appl. Phys.* **1996**, *79*, 7433.
3. Razykov, T. M.; Ferekides, C. S.; Morel, D.; Stefanakos, E.; Ullal, H. S.; Upadhyaya, H. M. *Sol. Energy* **2011**, *85*, 1580.
4. Shah, A.; Torres, P.; Tscharner, R.; Wyrsch, N.; Keppner, H. *Science* **1999**, *285*, 692.
5. *U.S. Dept. Commerce, Top Markets Report, Semiconductors & Semiconductor Manufacturing*, 2015.
6. *Semiconductor Industry Association Factbook*, 2015.
7. Survey, G. *Mineral Commodity Summaries, 2015*; U.S. Government Printing Office, 2015.
8. Cowley, A. H.; Jones, R. A. *Angew. Chem., Int. Ed.* **1989**, *28*, 1208.
9. Tao, C. S.; Jiang, J.; Tao, M. *Sol. Energy Mater.* **2011**, *95*, 3176.
10. Williams, E. D.; Ayres, R. U.; Heller, M. *Environ. Sci. Technol.* **2002**, *36*, 5504.
11. Razeghi, M. In *Fundamentals of Solid State Engineering*; Springer US: New York City, New York, 2002, p 349.
12. Capper, P.; Mauk, M.; Wiley Online, L. *Liquid phase epitaxy of electronic, optical, and optoelectronic materials*; Wiley: Chichester, England ; Hoboken, NJ, 2007.
13. Dost, S.; Lent, B. *Single crystal growth of semiconductors from metallic solutions*; Elsevier: Amsterdam ; Boston, 2007.
14. Bryskiewicz, T. *Prog. Cryst. Growth Ch.* **1986**, *12*, 29.
15. Law, M.; Goldberger, J.; Yang, P. *Ann. Rev. Mater. Res.* **2004**, *34*, 83.
16. Lu, W.; Lieber, C. M. *J. Phys. D-Appl. Phys.* **2006**, *39*, R387.
17. Kolasinski, K. W. *Curr. Opin. Solid State Mater. Sci.* **2006**, *10*, 182.
18. Westwater, J.; Gosain, D. P.; Tomiya, S.; Usui, S.; Ruda, H. *J. Vac. Sci. Technol., B* **1997**, *15*, 554.
19. Wang, F. D.; Dong, A. G.; Sun, J. W.; Tang, R.; Yu, H.; Buhro, W. E. *Inorg. Chem.* **2006**, *45*, 7511.
20. Yang, H.-J.; Yuan, F.-W.; Tuan, H.-Y. *Chem. Commun.* **2010**, *46*, 6105.
21. Kim, B. J.; Wen, C. Y.; Tersoff, J.; Reuter, M. C.; Stach, E. A.; Ross, F. M. *Nano Lett.* **2012**, *12*, 5867.
22. McAlpine, M. C.; Ahmad, H.; Wang, D.; Heath, J. R. *Nat Mater* **2007**, *6*, 379.
23. Renard, V. T.; Jublot, M.; Gergaud, P.; Cherns, P.; Rouchon, D.; Chabli, A.; Jousseaume, V. *Nat Nano* **2009**, *4*, 654.
24. Melloch, M. R.; Woodall, J. M.; Harmon, E. S.; Otsuka, N.; Pollak, F. H.; Nolte, D. D.; Feenstra, R. M.; Lutz, M. A. *Annu. Rev. Mater. Sci.* **1995**, *25*, 547.
25. Zein El Abedin, S.; Endres, F. *ChemPhysChem* **2006**, *7*, 58.
26. Meng, X.; Liu, X.; Zhao, J.; Xin, W.; Li, Y. *Progress in Chemistry* **2010**, *22*, 277.
27. Munisamy, T.; Bard, A. J. *Electrochim. Acta* **2010**, *55*, 3797.
28. Mallet, J.; Molinari, M.; Martineau, F.; Delavoie, F.; Fricoteaux, P.; Troyon, M. *Nano Lett.* **2008**, *8*, 3468.
29. Yang, M. C.; Landau, U.; Angus, J. C. *J. Electrochem. Soc.* **1992**, *139*, 3480.
30. Oishi, T.; Watanabe, M.; Koyama, K.; Tanaka, M.; Saegusa, K. *J. Electrochem. Soc.* **2011**, *158*, E93.

31. Rao, G. M.; Elwell, D.; Feigelson, R. S. *J. Electrochem. Soc.* **1980**, *127*, 1940.
32. De Mattei, R. C.; Elwell, D.; Feigelson, R. S. *J. Cryst. Growth* **1978**, *43*, 643.
33. Dalchiele, E.; Cattarin, S.; Musiani, M.; Casellato, U.; Guerriero, P.; Rossetto, G. *J. Electroanal. Chem.* **1996**, *418*, 83.
34. Gregory, B. W.; Stickney, J. L. *J. Electroanal. Chem.* **1991**, *300*, 543.
35. Gregory, B. W.; Suggs, D. W.; Stickney, J. L. *J. Electrochem. Soc.* **1991**, *138*, 1279.
36. Carim, A. I.; Collins, S. M.; Foley, J. M.; Maldonado, S. *J. Am. Chem. Soc.* **2011**, *133*, 13292.
37. Fahrenkrug, E.; Gu, J.; Maldonado, S. *J. Am. Chem. Soc.* **2013**, *135*, 330.
38. Gu, J.; Fahrenkrug, E.; Maldonado, S. *J. Am. Chem. Soc.* **2013**, *135*, 1684.
39. Fahrenkrug, E.; Biehl, J.; Maldonado, S. *Chem. Mater.* **2015**, *27*, 3389.
40. Fahrenkrug, E.; Gu, J.; Jeon, S.; Veneman, P. A.; Goldman, R. S.; Maldonado, S. *Nano Lett.* **2014**, *14*, 847.
41. Gu, J.; Collins, S. M.; Carim, A. I.; Hao, X.; Bartlett, B. M.; Maldonado, S. *Nano Lett.* **2012**, *12*, 4617.

CHAPTER 2

Electrochemical Liquid Liquid Solid Epitaxial Crystal Growth of Single-Crystalline Germanium Nanowires at Room Temperature in Water

2.1. Introduction

This chapter describes a major evolution in the capacity of benchtop electrochemistry to prepare crystalline covalent semiconductor nanomaterials at room temperature. An electrochemical liquid liquid solid (ec-LLS) strategy was developed for direct epitaxial preparation of single crystalline Ge nanowires at room temperature in aqueous electrolytes. Liquid gallium (Ga(*l*)) nanodroplets decorated over large area (> 1 in^2) conductive wafer supports acted as discrete sites for GeO_2 reduction and subsequent ec-LLS growth of Ge NWs from each droplet. Nanowire morphology and growth orientation were probed by tilted and plan view scanning electron microscopy. High resolution transmission electron microscopy and compositional mapping revealed details of the crystal growth direction, crystallographic defect formation, and aspects of the ec-LLS nanowire growth mechanism. Solid-state current-voltage measurements yielded consistent and reproducible resistance values of multiple nanowires. The cumulative data explicitly detail the capacity of the ec-LLS strategy for epitaxial growth of covalent group IV semiconductor crystals from the electrochemical reduction of a dissolved oxide under purely benchtop conditions.

The ability to synthesize structurally and electrically integrated group IV semiconductor nanowire arrays directly onto device platforms is desirable for continued miniaturization of transistor footprints.[1-6] However, the stringent purity and thermal constraints associated with complementary metal oxide semiconductor (CMOS) technologies are incompatible with the temperatures, growth catalysts, and environments currently used to synthesize covalent inorganic semiconductor nanowires.[7-10] In comparison, electrodeposition is an alternative synthetic method for nanowires that

bypasses these constraints. Still, although heavily used for metallization in the semiconductor industry,[11,12] electrodeposition is not presently used for covalent semiconductor nanowires because exotic solvents are necessary[13] and the resultant material is amorphous,[14] requiring high-temperature refining.

The key distinguishing feature of an ec-LLS process is the use of a liquid metal both as an electron source for the heterogeneous electrochemical reduction of dissolved species (i.e., as a conventional electrode) and as a separate phase for crystal growth (i.e., as a melt solvent). An oxidized semiconductor precursor is initially electrochemically reduced and then dissolves into, or reacts with, the liquid metal electrode. As the liquid metal reaches saturation and then supersaturation conditions, concomitant precipitation of crystalline material follows.[15-18]

This chapter advances three separate hypotheses regarding the development of ec-LLS as a nanomaterials synthetic strategy: (*1*) liquid Ga nanodroplets represent a platform for high yield Ge nanowire ec-LLS at room temperature; (*2*) single-crystalline Ge nanowires can be prepared from an aqueous solution at room temperature with liquid metal nanodroplets; and (*3*) epitaxial crystal growth for a covalent semiconductor is possible electrochemically with liquid metal nanodroplets at room temperature.

2.2. Methods

Materials and Chemicals

Methanol (ACS grade, BDH), acetone (ACS grade, BDH), GeO_2 (99.999%, Acros Organics), $Na_2B_4O_7 \cdot 10H_2O$ (Analytical Reagent Grade, Mallinckrodt), hydrofluoric acid (49%, Transene Inc.), KNO_3 (99+%, Acros Organics), In(*s*) (99.9+%, Aldrich) and Ga(*l*) (99.99%, Aldrich) were used as received. Wafers used as growth substrates included Ge (MTI, <111> Sb-doped n-type, 24.8 – 30.0 ohm cm, 0.5 mm thick), Ge (MTI, <100> Sb-doped n-type, 0.2 – 0.23 ohm cm, 0.5 mm thick), Si (Crysteco, <100> As-doped n-type, < 0.007 ohm cm, 0.625 ± 0.020 mm thick). Water with a resistivity > 18.2 MΩ cm (Barnsted Nanopure) was used throughout.

Electrodeposition and Electrochemical Measurements

A CHI760C workstation was used for electrochemical experiments. All electrochemical data were acquired under open atmosphere in either a custom-made PTFE

cell with 0.101 cm^2 exposed area (small scale) or in 400 mL glass beaker (wafer-scale). A standard three-electrode configuration with a Pt mesh counter electrode and a Ag/AgCl (sat. KCl) reference electrode was employed. All reported electrochemical potentials are with respect to E(Ag/AgCl)(sat. KCl). Electrical contact to either Ge or Si wafer substrates was established by applying a thin layer of InGa eutectic on the back of the wafer and pressing the substrate against a thin stainless steel electrode support. Electrodeposition of Ge nanowires was conducted in a temperature-controlled recirculating bath (Polystat) held at 40 °C. Gallium nanodroplets were electrodeposited on Ge(111) or Si(100) substrates from a solution containing 0.1 M $Ga(NO_3)_3$ and 0.1 M KNO_3 at a potentiostatic bias of -1.6 V for 5 s. Samples were rinsed in DI H_2O for 30 s and dried under $N_2(g)$.

Scanning and Transmission Electron Microscopy

TEM samples for dispersed nanowires were prepared by first removing the nanowires from the growth substrate using a razor blade. The razor blade was then sonicated in a glass vial containing 1 mL of methanol for 30 min to fully disperse the nanowires in the solvent. 100 μL of the nanowire suspension was drop-cast on a 400 mesh copper TEM grid coated with an ultra-thin carbon film (Ted Pella). Cross-sectional TEM samples were prepared by mechanical polishing as described here.[19] Briefly, a 1.5 x 2.5 mm rectangular section was cut from a Ge wafer containing the as-grown wires and glued face-to-face between two clean Si pieces of equivalent dimension. Samples were mounted on a tripod polisher (Precision TEM) (Appendix A.0) and mechanically polished to a thickness of 10 μm. They were transferred onto a slotted Ni TEM grid (Ted Pella) and thinned to electron transparency using cryo-Ar^+ ion milling (-160 °C) at 4.5 keV for 3.5 h. High resolution transmission electron microscopy (HRTEM) were conducted with a JEOL 2010F analytical microscope equipped with a zirconated tungsten (100) thermal field emission source at 200 keV acceleration voltage as well as a JEOL 3011 high resolution electron microscope equipped with a LaB_6 source operated at 300 keV. All HRTEM images were recorded along the $[1\bar{1}0]$ zone axis of the Ge crystal. Scanning transmission electron microscopy (STEM) was conducted using the JEOL 2010F analytical microscope with 1.0 nm probe size and 8 cm camera length. Energy dispersive X-ray maps were generated using 500 μs dwell time per pixel each frame at 512x400 resolution using an

EDAX r-TEM Detector. Scanning electron microscopy was performed with an FEI NOVA Nanolab Dualbeam Workstation with a Schottky field emitter operated at 15 keV beam voltage and 0.14 nA beam current coupled with a through-the-lens detector (TLD). Cross-sectional images were collected with the vertically-mounted substrate tilted 4° towards the substrate surface plane.

Molecular Beam Epitaxy

Gallium (Ga) droplets were prepared on Ge(111) wafers by molecular beam epitaxy. Prior to growth, the substrate was cleaned chemically by dipping in HCl(36 %)/H_2O 1:4 solution for 30 s to remove native GeO_2. Substrates were introduced into the load-lock of the GEN II MBE chamber within 10 min of etching. The load-lock was baked at 150 °C for 8 hours prior to substrate transfer into the MBE growth chamber. Substrates were heated at 800 °C for 30 min in the growth chamber, at which point a streaky RHEED pattern was observed revealing a smooth Ge surface free of GeO_2. The substrate temperature was reduced to 550 °C for growth and Ga droplets were deposited at a constant Ga beam equivalent pressure of 3.7×10^{-7} torr for 10 s, corresponding to 7.5 ML of Ga.

Conducting Probe Atomic Force Microscopy (AFM)

Conducting probe AFM measurements were made with a Veeco Dimension 3100 AFM equipped with the extended TUNA module. Ohmic contacts were made to the Ge substrates by abrasion with a diamond scribe, 60 s etch in 5 % HF(*aq*) and the application of indium-gallium eutectic. Mikromasch NSC15 cantilevers were used for tapping mode images. Platinum wire probes (25Pt300B, Rocky Mountain Nano) were used as top-contacts for CP-AFM experiments. Cantilever displacements of 5 nm were used, resulting in probe-sample forces of ca. 100 nN. Nanowires of interest were centered in scan areas of decreasing size until two successive scans showed acceptably small piezo creep, allowing current-voltage curves to be obtained on the top of the nanowire. During these measurements, the probe is held at virtual ground and the sample bias is ramped. Subsequently, a much larger force (ca. 1 μN) was applied and the probe was allowed to scan until the nanowire was broken off and pushed out of the image area. The same procedure was then followed to obtain current-voltage curves on the nanowire "stump". Before measuring the I-V response for the bare Ge substrate, additional bias cycling from

-10 to 10 V was applied until steady I-V curves were recorded in order to locally vaporize the oxide.

2.3. Results

Ge nanowire films were prepared through ec-LLS with only a digital potentiostat and the setup shown in Figure 2.1. A conductive wafer substrate decorated with Ga(*l*) nanodroplets (Figure 2.1a) was immersed in a solution of 0.05 M GeO_2(*aq*) and 0.01 M $Na_2B_4O_7$(*aq*) and served as the working electrode in a standard three-electrode cell configuration. Application of an electrochemical potential more negative than −1.3 V vs Ag/AgCl triggered electrodeposition of reduced Ge(*s*) selectively at the discrete Ga(*l*) nanodroplets through Equation 2.1.

$$HGeO_3^-(aq) + 4e^- + 2H_2O(l) \rightarrow Ge(s) + 5OH^-(aq) \qquad (2.1)$$

The current–potential responses for a bare n^+-Ge(111) wafer substrate and a wafer substrate coated with liquid metal nanodroplets separately indicated that electrochemical reduction of dissolved GeO_2 only occurred in the presence of liquid Ga (Figure 2.1b). The increase in current density at potentials more negative than -1.3 V vs. Ag/AgCl corresponds to GeO_2(*aq*) reduction on discrete Ga(*l*) nanodroplets. Sustained electrolysis resulted in free-standing Ge nanowires at each Ga nanodroplet electrode (Figure 2.1a). Figure 2.1c illustrates the uniformity of the electrodeposited Ge nanowire film across the immersed portion of a 50 mm wafer substrate. The entire submerged portion of the wafer developed a dull, gray film that visibly changed over the course of the ec-LLS process.

Cross-sectional scanning electron micrographs collected from the substrate in Figure 2.1c before and after electrodeposition indicated the density of initial Ga nanodroplets and the density of as-prepared Ge nanowires were equivalent (3.1 ± 0.1 μm^{-2}). (Figure 2.2a,b). Tilted scanning electron micrographs (SEM) collected after ec-LLS growth of nanowires further confirmed each individual Ga nanodroplet seeded the electrochemical growth of a single Ge nanowire and that the ec-LLS process was spatially uniform over the entire field of view (Figure 2.2c). The histogram of measured Ga

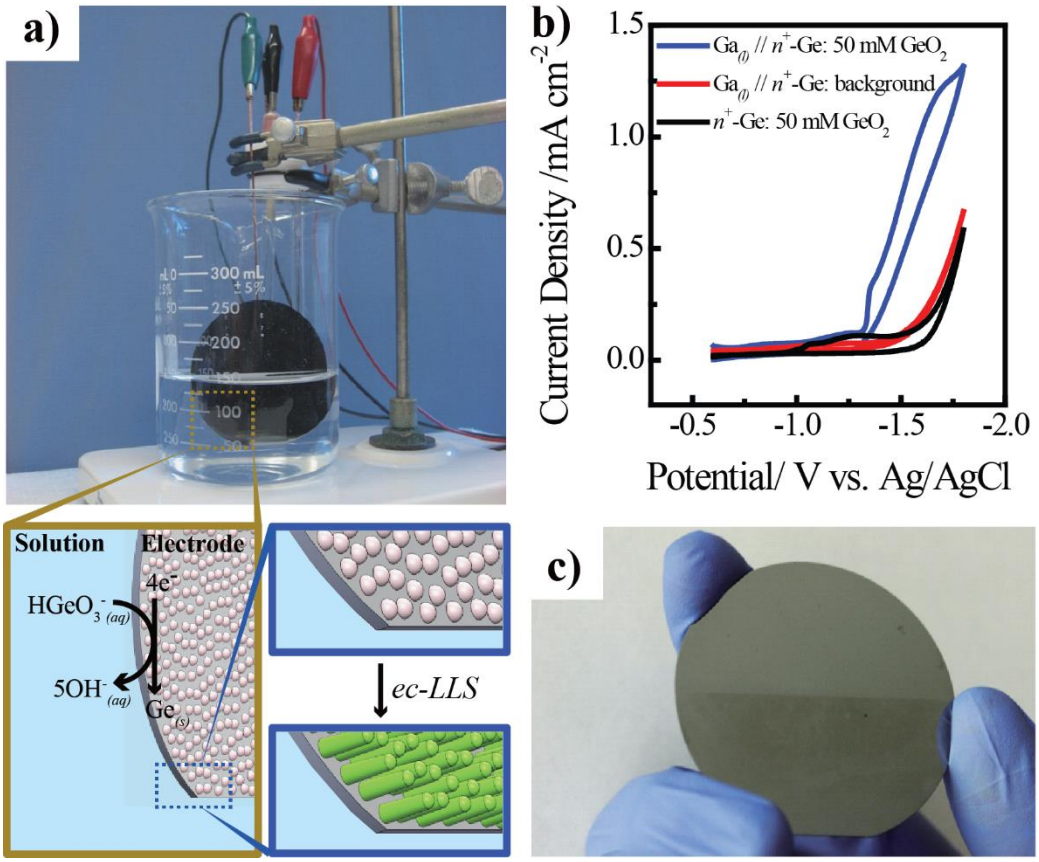

Figure 2.1. (a) Optical image depicting the benchtop experimental setup used for wafer-scale ec-LLS of Ge nanowire films. Insets: Schematic depiction of ec-LLS process. (b) Cyclic voltammetric response of an n-Ge(111) electrode (R = 24.8 – 30 Ω·cm) decorated with (blue) and without (black) Ga(l) nanodroplets in 0.05 M GeO_2 and 0.01 M $Na_2B_4O_7$. The current-potential behavior for the same Ga(l) decorated n-Ge(111) electrode in the absence of dissolved GeO_2 is shown in red. (c) Optical image of a 2 in. wafer coated with Ge nanowires after 300 s ec-LLS nanowire deposition over the bottom half of the wafer.

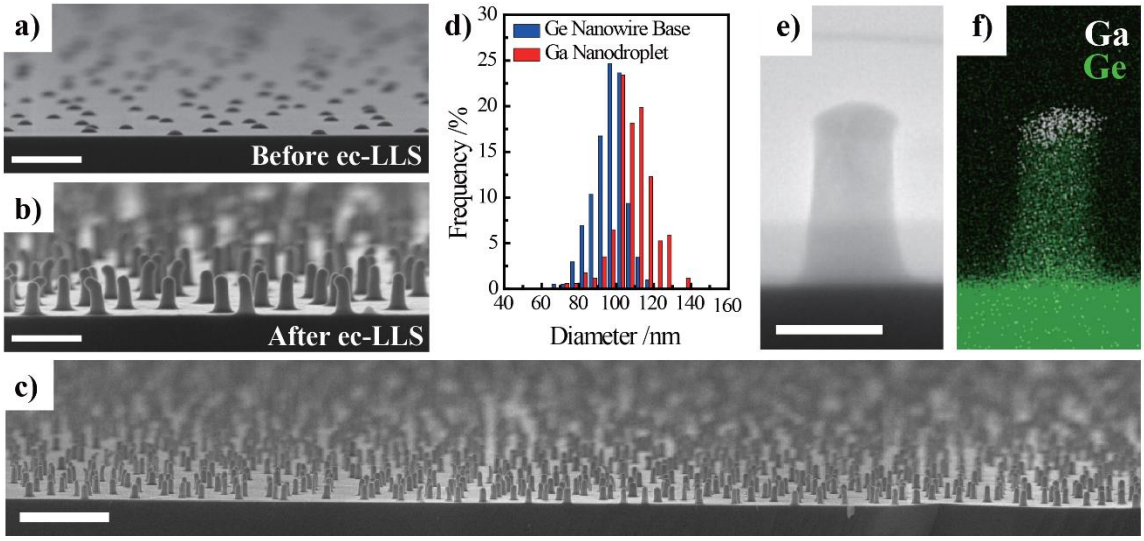

Figure 2.2. (a) A cross-sectional scanning electron micrograph of a Ge(111) substrate decorated with discrete liquid Ga nanodroplets. (b) Same as (a) but after 60 s ec-LLS process. Scale bars are 500 nm.(c) Scanning electron micrograph collected from Ge nanowires grown for 30 s from a Ge(111) substrate. Growth was conducted in a solution of 0.05 M GeO_2 and 0.01 M $Na_2B_4O_7$ at an applied potential of -1.6 V vs. Ag/AgCl. Scale bar: 1 µm. (d) Size distribution of the Ga nanodroplet electrodes and resultant Ge nanowire base widths obtained after a 30 s ec-LLS experiment. (e) Cross-sectional high-resolution transmission electron micrograph of an as-prepared single Ge nanowire on a wafer substrate produced after a 30 s ec-LLS. (f) Energy dispersive X-ray spectroscopic elemental map of the structure in (e). Scale bar: 100 nm. Ga(*l*) nanodroplets were deposited on the wafer support by molecular beam epitaxy at 550 °C with a constant Ga beam equivalent pressure of 3.7×10^{-7} Torr for 10 s. ec-LLS conditions: $E_{app} = -1.6$ V vs Ag/AgCl, T = 40 ± 2 °C, 0.05 M GeO_2 and 0.01 M $Na_2B_4O_7$.

nanodroplet diameters and Ge nanowire base widths in Figure 2.2d describes the correlation between nanodroplet and nanowire size. The resultant Ge nanowires were

slightly smaller (96.6 ± 8.6 nm, N = 203) than the Ga nanodroplets (108.7 ± 10.3 nm, N = 171) with comparable relative standard deviations (8.9 and 9.4%, respectively). The specific location of the original Ga droplet relative to the as-grown Ge nanowire was probed by high-resolution transmission electron microscopy (HRTEM) and X-ray energy dispersive spectroscopic (XEDS) mapping of individual Ge nanowires after a short (t = 30 s) ec-LLS experiment (Figures 2.2e,f). A high concentration of Ga was consistently measured at the tip of the nanowires and spherical droplet was observed in HRTEM images. Accordingly, only elemental Ge was observed at the base of the nanowires which is similar to the metal catalyst position observed in vapor–liquid–solid nanowire growth[20] but in contrast to our prior ec-LLS observations.[15,17]

Analysis of the current-time transient recorded during an ec-LLS experiment at -1.6 V vs. Ag/AgCl (Figure 2.3a) revealed an acute increase in the current density at early deposition times (~1.8 s) which is consistent with transient responses recorded during three-dimensional electrocrystallization.[21] The initial monotonic decay in current density prior to reaching a steady-state condition indicates the nanowire size/shapes ceases to change after 150 s. The specific electrocrystallization modality was probed by first normalizing the current and time axes in Figure 2.3a to maximum current (i_{max}) and the corresponding time (t_{max}) followed by comparing the normalized transient data with two simulated transients based on common instantaneous nucleation and progressive nucleation models (Figure 2.3b).[21] The close agreement with the instantaneous nucleation model supports the notion that all nanowires are nucleated simultaneously. The narrow observed (Figure 2.3c) and measured (Figure 2.3d) height distribution of 125 ± 9 nm (N = 196) for Ge nanowires prepared by an ec-LLS experiment lasting 30 s separately supported the notion of uniform nanowire growth.

Electron microscopy was performed to assess the crystallinity of individual nanowires and to identify any evidence of preferred growth orientation. Representative cross-sectional and plan-view scanning electron micrographs (SEM) collected after a short (t = 30 s) ec-LLS experiment on a Ge(111) wafer substrate are shown in Figures 2.4a and 2.4b, respectively. Short ec-LLS experiments were specifically targeted to avoid

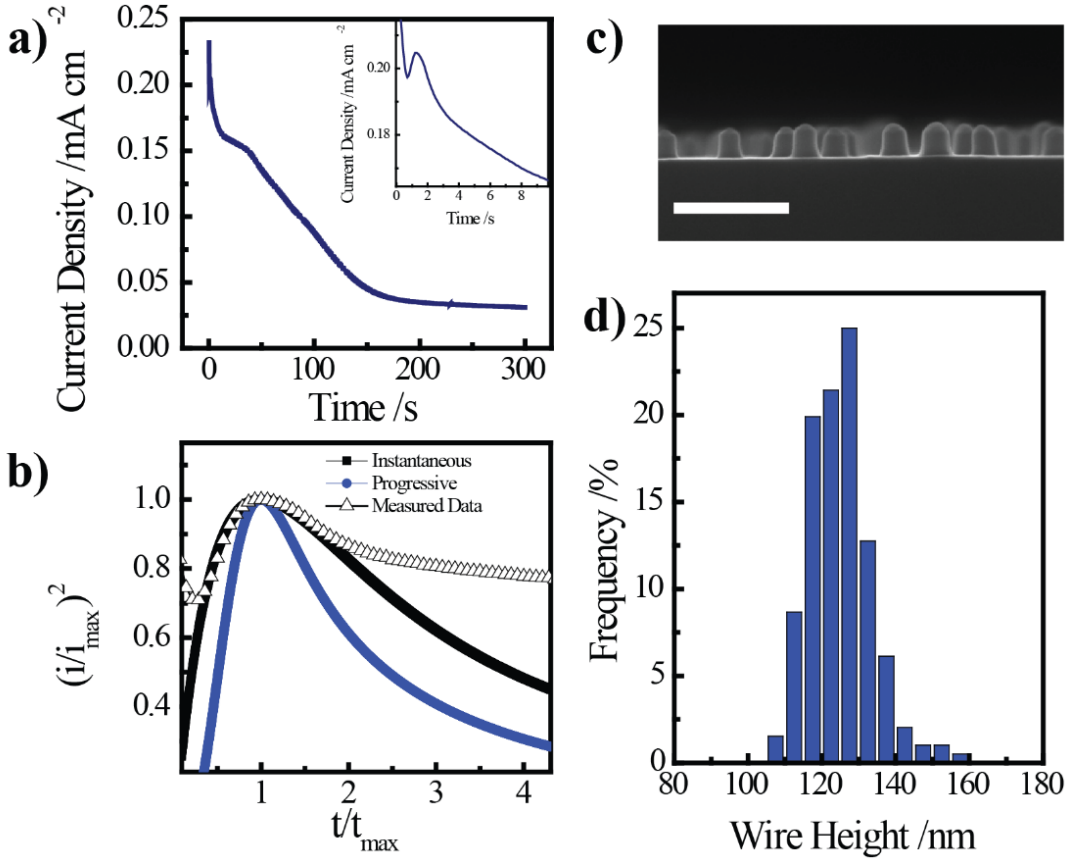

Figure 2.3. (a) Chronoamperometric response for an n-Ge(111) electrode coated with Ga(*l*) nanodroplets in 0.05 M GeO_2 and 0.01 M $Na_2B_4O_7$ biased at -1.6 V vs. Ag/AgCl for 300 s. Inset highlights the first 10 s of the current profile. (b) Same current-transient data with current density normalized to the peak current density and time normalized to the time with maximal current (triangle). Models for progressive (blue line) and instantaneous (black line) nucleation models are also shown. (c) Cross-sectional scanning electron micrograph of Ge nanowires grown for 30 s at -1.6 V vs. Ag/AgCl. Scale bar: 500 nm. (d) Corresponding histogram of Ge nanowire heights (N = 196) after 30 s extracted from SEM images.

mechanical perturbation of nanowire orientation from capillary forces during drying.[22] As depicted in the cross-sectional scanning electron micrographs, every Ge nanowire across

the entire substrate area was oriented normal to the substrate plane, i.e. collinear with the [111] direction of the wafer substrate. The plan-view images reveal nanowires growing in a perfectly vertical orientation, parallel to only one of the possible [111] directions. The regularity in nanowire orientation observed in Figures 2.4a and 2.4b supports the notion of an epitaxial crystal growth process coincident with a single [111] growth direction.[23] To further test the possibility of epitaxy, cross-sectional transmission electron micrographs were collected from the interface between an individual as-grown Ge nanowire and the native n^+-Ge(111) substrate. Figure 2.4c depicts the atomically resolved interface between the Ge nanowire and the substrate. Well-resolved lattice spacings of 3.31 and 2.86 Å continued smoothly from the substrate into the electrodeposited nanowire, consistent with the d_{111} and d_{200} lattice spacings, respectively, of a single Ge crystal.[24] No discontinuities in the lattice planes extending from the substrate into the nanowire base were observed. The inset selected area electron diffraction (SAED) pattern in Figure 2.4c showed a single set of diffraction spots for a Ge single crystal viewed along the $[1\bar{1}0]$ zone axis, further confirming the epitaxial nature of the Ge nanowire/substrate interface. Separately, XEDS mapping showed no detectable diffuse or occluded concentration of Ga at the substrate/nanowire interface. Moiré fringes, additional diffraction spots, rotational asymmetries, or diffuse rings in the collected diffraction patterns suggestive of Ga(Ge) alloys or grain boundaries were not observed. Collectively, these data argue that crystalline Ge nanowires were epitaxially deposited on Ge(111) substrates via ec-LLS.

Evidence supporting homoepitaxial and heteroepitaxial Ge nanowire growth on other substrate orientations was also collected (Figures 2.4d-g). In Figure 2.4d, the use of a Ge(100) substrate resulted in initial collinear nanowire growth in the lowest portion (91.4 ± 14.5 nm) directly above the substrate surface. Above this height, the Ge nanowires showed a systemic change in orientation with respect to the surface plane. As seen in the plan-view micrograph in Figure 2.4e, the nanowire growth continued at four distinct angles with 90° in-plane angle separation, consistent with continued crystal growth along a ⟨111⟩ direction. Heteroepitaxy on lattice-mismatched substrates is also shown (Figures 2.4f,g). In Figure 2.4f, nanowire electrodeposition on Si(100) substrates resulted in wires oriented

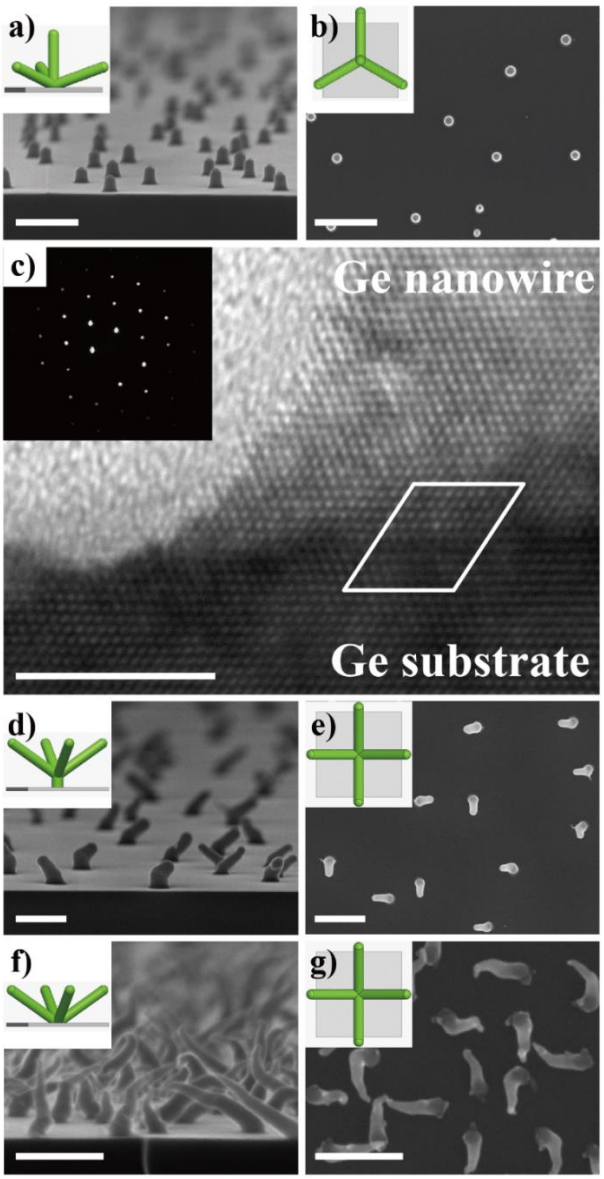

Figure 2.4. Electron micrographs showing Ge nanowire orientations grown from various electrode substrates. (a) Cross-sectional view and (b) top-down (plan) view of Ge nanowire films prepared through a 30 s ec-LLS experiment on an n^+-Ge(111) electrode substrate. Scale bar: 500 nm. Insets: possible orientation for nanowire growth along any ⟨111⟩ direction from a (111) substrate. (c) A high-resolution transmission electron micrograph cross-sectional view of the interface between the base of a Ge nanowire prepared by ec-LLS and the n+-Ge (111) substrate viewed along the [1$\bar{1}$0] zone axis. Scale bar: 5 nm. Inset: selected area electron diffraction pattern collected over the nanowire/substrate interface. (d) Cross-sectional view and (e) plan view of Ge nanowire films prepared through a 30 s ec-LLS experiment on a degenerately doped n^+-Ge(100) electrode substrate. Scale bar: 500 nm. Insets: possible orientation for nanowire growth along any ⟨111⟩ direction from a (100) substrate. (f) Cross-sectional view and (g) plan view of Ge nanowire films prepared through a 30 s ec-LLS experiment on a degenerately doped n^+-Si(100) electrode substrate. Scale bar: 200 nm. Insets: possible orientation for nanowire growth along any ⟨111⟩ direction from a (100) substrate.

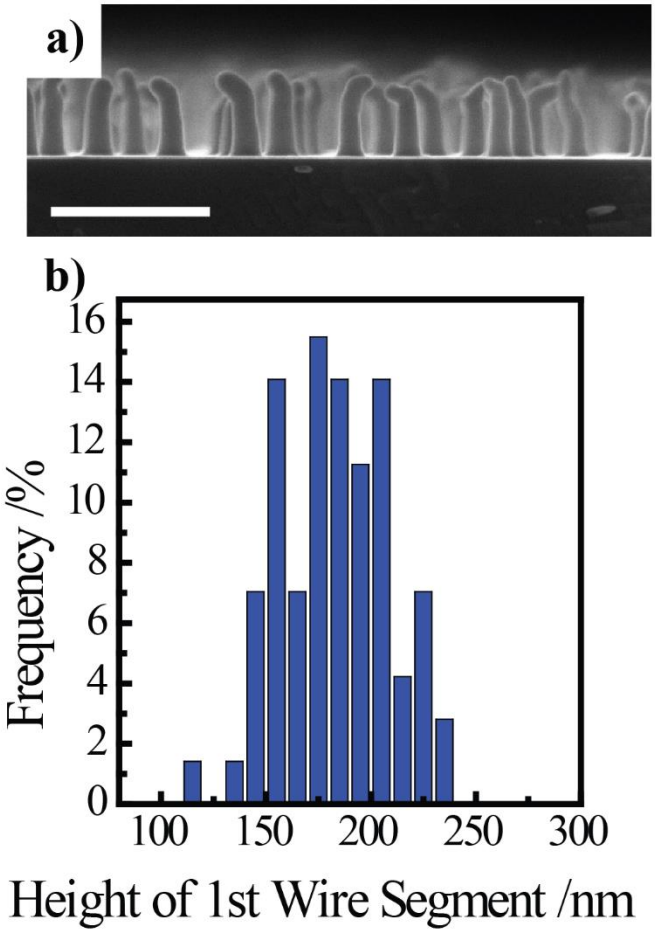

Figure 2.5. (a) Cross-sectional scanning electron micrograph of Ge nanowires grown from n-Ge(111) electrode biased at -1.6 V in a solution of 0.05 M GeO_2 and 0.01 M $Na_2B_4O_7$ for 60 s. Scale bar: 500 nm. (b) Corresponding height histogram of Ge nanowires grown from Ge(111) substrates prior to the first kink (N = 102).

36 ± 3° from the surface plane. The plan view image in Figure 2.4g additionally reveals nanowires oriented along four separate 90° relative in-plane angles. This observation is in accord with epitaxial crystal orientation along the four possible ⟨111⟩ directions on (100)-oriented substrates. In combination, the data implicate the capacity to perform both homoepitaxy and heteroepitaxy through ec-LLS.

Additional analyses were performed to ascertain whether the electrodeposited Ge nanowires remained single-crystalline throughout the course of longer ec-LLS experiments. The cross-sectional scanning electron micrograph in Figure 2.5a indicated that nanowires prepared by ec-LLS on Ge(111) wafers showed at least one kink with a concomitant change in apparent growth orientation after a 60 s growth. Analysis of the micrographs revealed a vertical height distribution of 185.7 ± 25.8 nm over N = 102 measured nanowires (Figure 2.5b) indicating uniform nanowire growth even at longer (t > 30 s) ec-LLS growth durations.

Figure 2.6a shows a bright field transmission electron micrograph of a representative Ge nanowire prepared by ec-LLS for 300 s (the coating apparent in the micrograph is due to in-situ carbon deposition inside the microscope during image acquisition). Two separate changes in the nanowire growth direction were apparent. Figures 2.6b-f show the local crystallinity of selected regions of the nanowire in Figure 2.6a. As evidenced by the lattice-resolved HRTEM images in Figures 2.6b-d, the crystal lattice orientation in the nanowire remained consistent over the entire length, that is, the nanowire comprised a single continuous crystalline domain. Similarly, the SAED patterns collected from each nanowire segment (insets in Figures 2.6b-d) were superimposable on each other indicating no discontinuity in the nanowire crystal orientation across a kink. Figures 2.6e-f explicitly show the continuous lattice arrangement across the two nanowire kink segments. Stacking faults within the {111} lattice planes were observed immediately before each kink, angled at 70° with respect to the initial growth front. The new growth direction was collinear with the stacking fault direction, suggesting the kinks were directed by stacking fault formation. Figure 2.6g summarizes one possible crystal growth sequence that incorporates a stacking fault during ec-LLS growth of Ge nanowires. At the initial stage (t < 30 s), epitaxial growth in a layer-by-layer fashion proceeds vertically along the [111] direction. As crystal growth proceeds, stacking faults nucleate within the $(11\bar{1})$ lattice

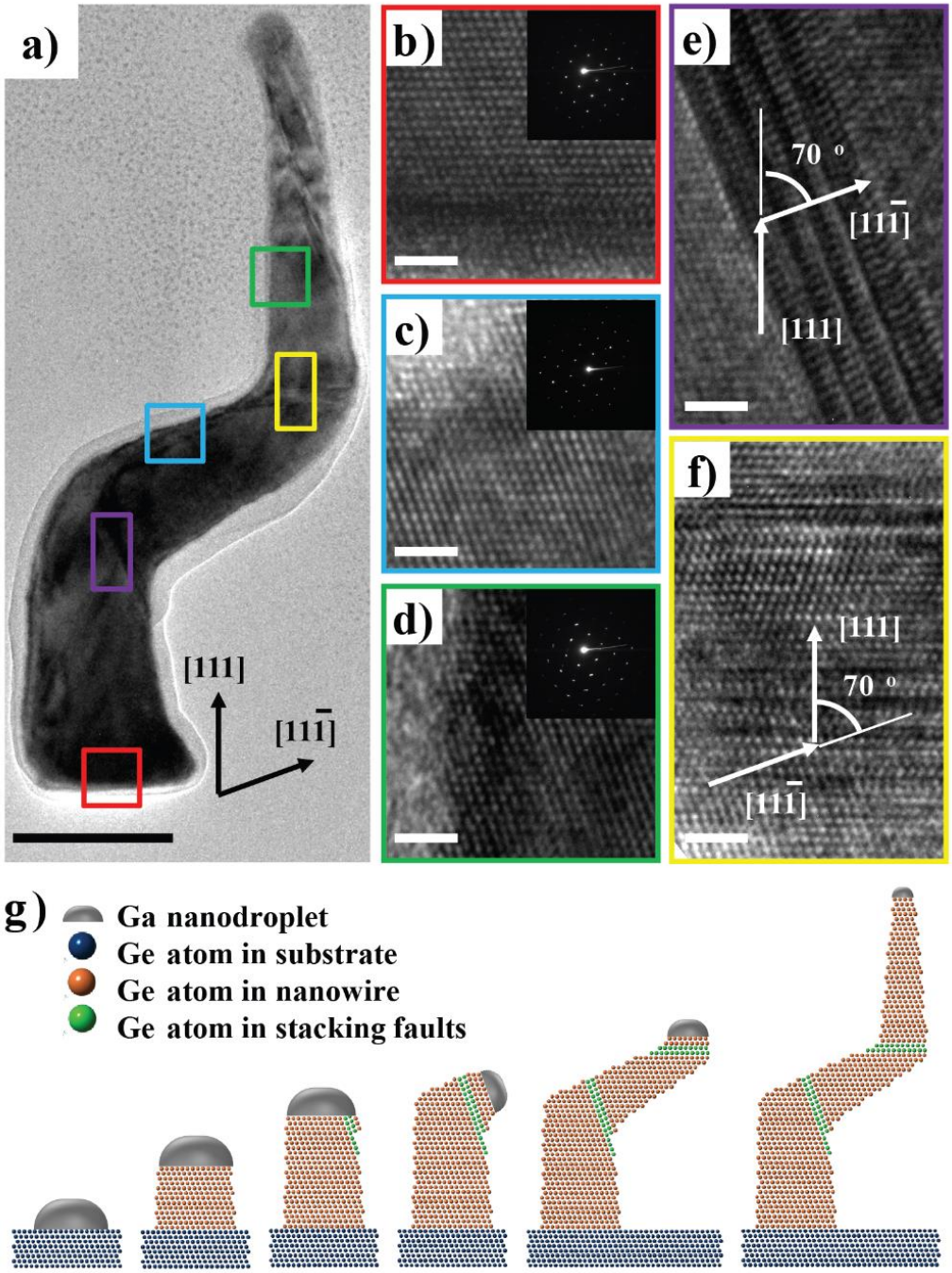

Figure 2.6. (a) Transmission electron micrograph of a Ge nanowire prepared with a 300 s ec-LLS experiment. Scale bar: 100 nm (b–f) High-resolution transmission electron micrographs for the corresponding boxed regions in (a). Scale bar: 2 nm. Insets: selected area electron diffraction patterns of the corresponding region. (g) Schematic depiction of the crystal growth process of the nanowire, highlighting the formation of stacking faults and kinking of the nanowire.

plane because of low stacking fault formation energy (13 meV/bond),[25] shifting the crystal growth direction by 70° from $[11\bar{1}]$, resulting in a kinked yet single crystalline nanowire.

To ascertain whether the model in Figure 2.6g applies systemically across an entire film, plan view scanning electron micrographs were collected to identify the nanowire growth orientations following the first kink (Figure 2.7a). Analyses shown in the histogram in Figure 2.7b reveal nanowire with categorically six discrete growth orientations with measured relative in-plane angle intervals of 60°. These data were consistent with the premise that crystal growth continued along the three possible ⟨111⟩ directions or the three mirrored ⟨111⟩ directions introduced by in-plane inversion of a crystal growth front following stack fault formation.[26] Because stacking faults and twinning in single-crystalline semiconductor nanowires can arise from depletion of precursor at a metal catalyst in high-temperature nanowire growth,[27] attempts were made to augment the twinning density in this ec-LLS process through perturbations in the concentration of dissolved GeO_2 through solution convection. Figures 2.8a-b show a plan-view scanning electron micrograph of Ge nanowires grown for 300 s on a Ge(111) wafer in a stirred solution and the corresponding histogram of the first relative kink angle of each nanowire. Six preferred growth orientations separated by 60 deg in-plane angles were observed, nominally identical to nanowires produced in quiescent solutions with 0.05 M GeO_2(*aq*). Ostensibly identical results were obtained for Ge nanowires grown from a diluted GeO_2(*aq*) solution (0.001 M) under 5 μA galvanostatic conditions for 3600 s (Figures 2.8c,d). Neither method of changing the local concentration of dissolved GeO_2 significantly impacted the occurrence of kinks in the electrodeposited nanowires (Figures 2.8a-d), indicating precursor concentration was not the defining factor in kink (stacking fault) formation. In the case of using electrodeposited Ga nanoparticles as growth seeds, a 300-sec ec-LLS process at -1.6 V vs. Ag/AgCl yielded Ga nanowires with first kinks at only three angles separated by 120° (Figures 2.8e-f), suggesting nanowire epitaxy occurred with no in-plane inversion of the initial crystal growth front. However, no epitaxial growth was not observed if electrodeposited Ga(*l*) nanodroplets were allowed to age in lab ambient for weeks prior to Ge nanowire electrodeposition.

To ascertain the relative electrical resistance at the interfacial contact between the epitaxial Ge nanowire and the underlying n-Ge(111) substrate, current–voltage responses

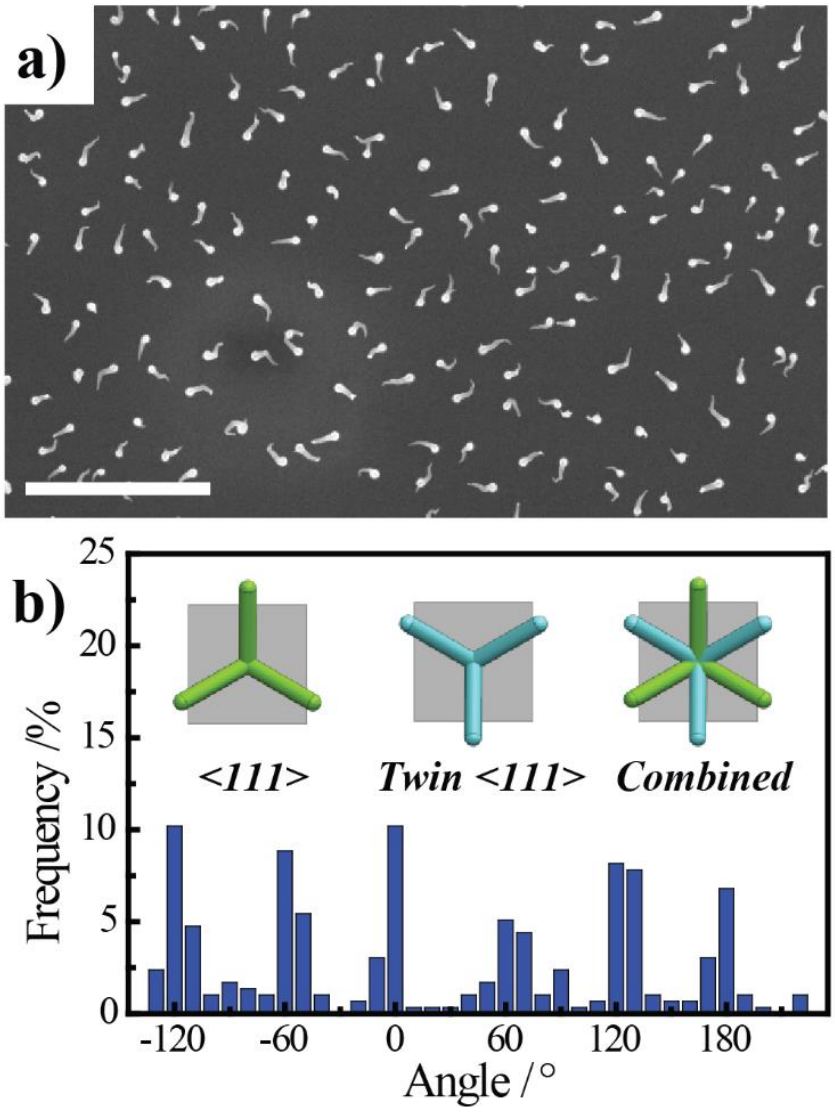

Figure 2.7. (a) Plan-view scanning electron micrograph of a Ge nanowire film prepared with a 300 s ec-LLS experiment. Scale bar: 2 μm. (b) Distribution of the Ge nanowire orientations from plan view images (as in (a)) after the first kink. Insets: Schematic of the expected orientations for nanowire growth along the ⟨111⟩ family. Ga(*l*) nanodroplets were deposited on the wafer support by molecular beam epitaxy at 550 °C with a constant Ga beam equivalent pressure of 3.7×10^{-7} Torr for 10 s. ec-LLS conditions: $E_{app} = -1.6$ V vs Ag/AgCl, T = 40 ± 2 °C, 0.05 M GeO_2, and 0.01 M $Na_2B_4O_7$.

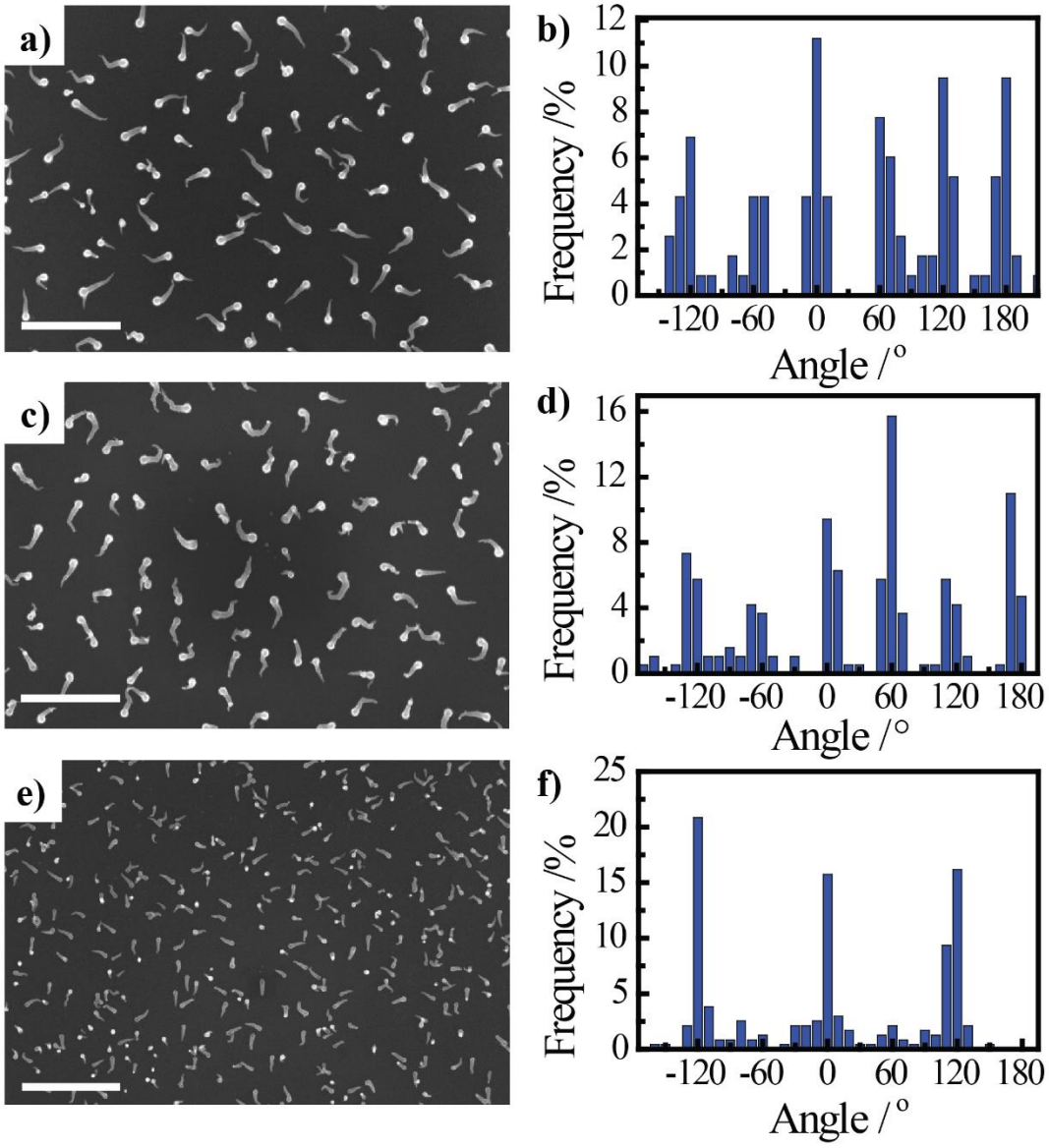

Figure 2.8. (a) Plan-view scanning electron micrograph of Ge nanowires grown on n-Ge(111) coated with Ga(*l*) nanodroplets biased at -1.6 V for 300 s during vigorous solution convection. Scale bar: 1 µm. (b) Corresponding histogram of nanowire growth orientations normalized to 0° (*N* = 116). c) Plan-view scanning electron micrograph of Ge nanowires grown on n-Ge(111) coated with Ga(*l*) nanodroplets electrodeposited galvanostatically at 5 µA for 1 hr from 0.001 M GeO_2 and 0.01 M $Na_2B_4O_7$, 0.1 M KNO_3. Scale bar: 1 µm. d) Corresponding histogram of nanowire growth orientations normalized to 0° (*N* = 191). (c) Plan-view scanning electron micrograph of Ge nanowires grown on n-Ge(111) coated with electrodeposited Ga(*l*) nanodroplets biased at -1.6 V for 300 s. Scale bar: 1 µm. (b) Corresponding histogram of nanowire growth orientations normalized to 0^O (N = 235).

through individual nanowires were measured across a nanowire film. A Pt–Ir AFM probe was used to electrically contact individual Ge nanowires (Figure 2.9a). Following measurement of the electrical response, individual nanowires were laterally fractured with the same AFM probe ~20–30 nm from the base and the electrical characteristics were remeasured. Figure 2.9b shows a representative current–voltage profile for an individual Ge nanowire, a Ge nanowire laterally fractured at the base, and the oxide-free n-Ge substrate. At large applied bias, the current through the Pt/Ge nanowire/n-Ge wafer series had rectifying character in accord with metal/n-Ge contacts[28] (Figure 2.9c-e)The quasi-linear region of the current–voltage characteristic near zero bias was used to estimate relative resistance values through the Ge nanowire/n-Ge substrate junction, the fractured Ge nanowire/substrate junction, and the Pt/n-Ge substrate interface. Average resistance values extracted from full length nanowires and fractured nanowires were ostensibly identical within the error of the measurement (Figure 2.9b), indicating the overall Ohmic contribution through the nanowire was negligible. The contact resistance at the Pt/n-Ge substrate junction contributed 27% to the cumulative measured resistance with the remaining resistance mostly from the contact resistance at the Ge nanowire/n-Ge substrate junction rather than through the nanowire itself (Figure 2.9b). Previous work by our group has shown that conductivity values measured across polycrystalline Ge nanowires obtained with Hg(*l*) were consistent with Hg incorporation at dopant-levels in accord with the solubility of the liquid metal in Ge at ambient temperature.[15] As Ga is a p-type dopant in Ge, the substrate/nanowire contact resistance measured here is nominally consistent with a p-n homojunction formed between the n-type Ge substrate and a p-type nanowire. Further measurements are needed to explore this point comprehensively. Nevertheless, the electrical measurements shown here did reveal uniformity in the apparent resistance values, with a relative standard deviation of 17% (N = 20).

2.4. Discussion

The presented data illustrate that semiconductor electrodeposition via ec-LLS with liquid metal nanodroplets possesses three unique synthetic features. No other known synthetic method combines the possibility of epitaxial and single-crystalline growth with ambient process conditions, aqueous solutions, and simple equipment. The electrochemical process described here uses only an oxidized precursor and requires no exotic solvents or

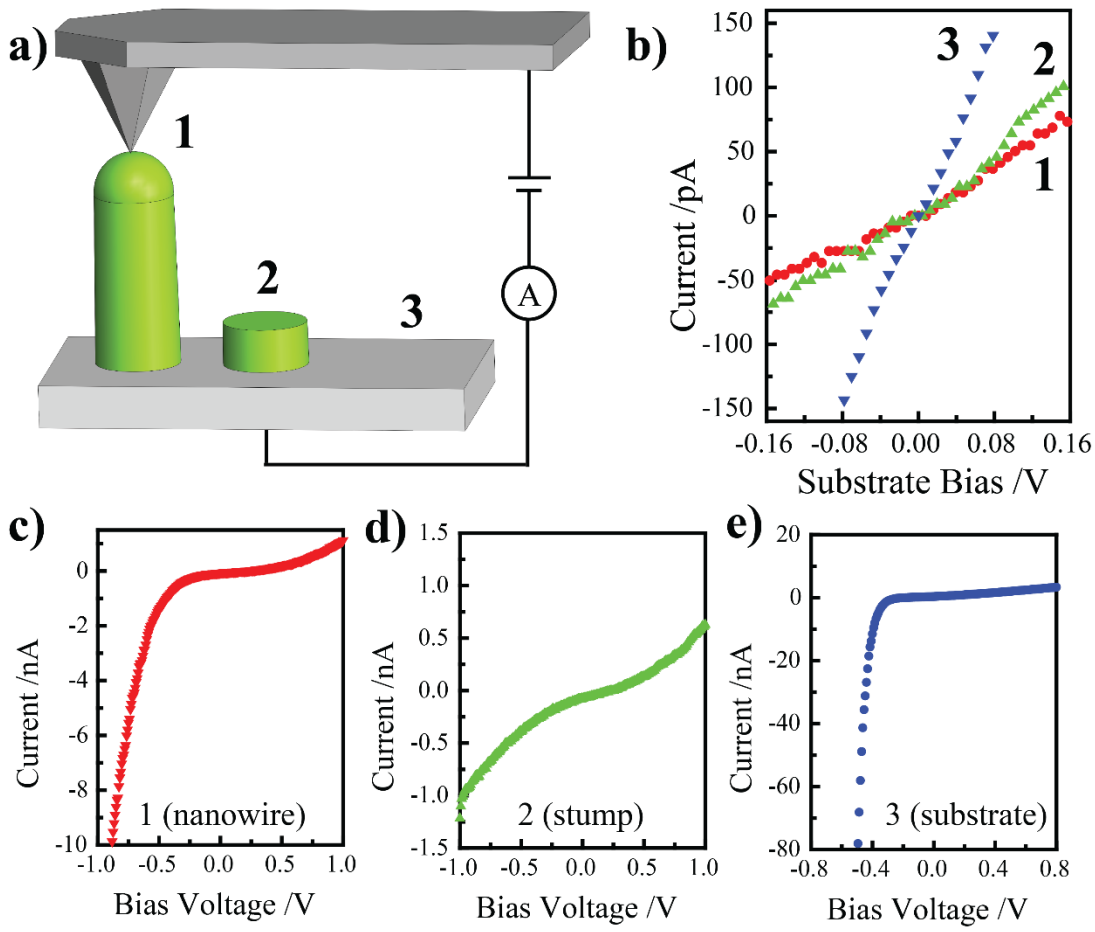

Figure 2.9. (a) Schematic depiction of the conductive atomic force microscopic (c-AFM) measurement performed on (1) intact Ge nanowires after 30 s growth, (2) laterally fractured Ge nanowires, and (3) oxide-free Ge substrate. (b) Current–voltage response in c-AFM measurement for 1–3. Ga(*l*) nanodroplets were deposited on the wafer support by molecular beam epitaxy at 550 °C with a constant Ga beam equivalent pressure of 3.7×10^{-7} Torr for 10 s. ec-LLS conditions: $E_{app} = -1.6$ V vs Ag/AgCl, T = 40 ± 2 °C, 0.05 M GeO_2, and 0.01 M $Na_2B_4O_7$.

elevated temperatures/pressures, in contrast to the highly processed and partially-to-completely reduced chemical precursors in molecular beam epitaxy (MBE), chemical vapor deposition, and solution–liquid–solid crystal growth.[29,30] The ec-LLS process also stands apart from other electrochemical-based efforts to make crystalline semiconductor materials. For a covalent semiconductor like Ge, electrodeposition on a solid electrode at room temperature yields amorphous films with entrapped solvent since the factors that promote bulk crystal growth are not accessible. Specifically, movement of Ge adatoms to a crystal growth front on a Ge surface is much greater than kT at room temperature,[31] solvation by and re-precipitation out of the aqueous electrolyte of reduced Ge is not feasible, and templating substrate effects like those in electrochemical atomic layer epitaxy[32] do not readily translate into thick films.[33] Instead, solvation in the ec-LLS shown here by the liquid metal of elemental Ge lowers the energy for crystal nucleation and growth within the liquid metal. In this way, the identity of the liquid metal nanodroplets matters critically.

In this work, both complex (i.e. MBE) and simple (i.e. pulsed electrodeposition) protocols were used to prepare Ga initial nanodroplet electrode arrays without changes in the primary findings, i.e. epitaxial and single-crystalline nanowire electrodeposition. This indicates the critical steps of the ec-LLS process, i.e. electrochemical reduction of the ionic precursor, adsorption and dissolution of the reduced Ge^0 species, crystal nucleation and crystal growth are not affected by liquid metal (i.e. Ga) catalyst preparation. Such tolerance is advantageous for adaptation of ec-LLS to large scale production where heterogeneity in one synthetic step can lead to undesired results. In fact, simple electrodeposition of Ga nanodroplet catalysts (versus MBE preparation) completely mitigated apparent stacking fault defect formation in the Ge nanowires. This observed difference in growth orientation between Ge nanowires grown from MBE-prepared Ga droplets and electrodeposited Ga droplets suggest that the liquid metal/substrate interface plays a critical role in crystallographic twin formation. Assuming that the conditions at the three phase contact line (i.e. phase boundary between liquid electrolyte, liquid metal, and crystalline Ge) affect crystal growth, the wetting properties (i.e. surface tension) of the liquid metal nanodroplet, the solubility of Ge^0 in the liquid metal solvent, and the electrostatics of the double layer at the electrode/electrolyte interface could be factors in crystallographic defect formation in ec-LLS.

With respect to nanofabrication, ec-LLS with liquid metal nanodroplets also offers practical advantages. A single electrochemical step for the concerted synthesis and growth of nanowires is naturally compatible with the equipment already used for electroplating in microelectronics. For example, electrochemical plating of copper contacts at the wafer scale is presently performed with electrolyte baths (e.g., oxidized copper salts in water) and low process temperatures (e.g., 25 °C) consistent with the ec-LLS process reported here.[34] Further, with individually addressable liquid metal nanodroplets the possibility exists to fabricate nanowire-based circuits locally on a large device platform. While development of the ec-LLS process is still in the early stages, the work reported here in conjunction with recent breakthroughs for the ec-LLS preparation of covalent semiconductors like Si[18] and GaAs[16] suggests that ec-LLS with liquid metal nanodroplets could serve as a new method for conductive nanowire device construction and integration.

2.5. Conclusions

This chapter advanced the primary hypothesis that ec-LLS can facilitate epitaxial crystal growth when the liquid metal electrode thickness (volume) is smaller than the mean free path of solute diffusion before heterogeneous nucleation. In fact, this chapter marks the first report of a room temperature epitaxial growth process for a Group IV semiconductor in water. Although the nanowires were single crystal, the evolution of planar defects within the crystal gave rise to growth direction changes and kinking. The root cause of systematic defect formation in these nanostructures is particularly interesting from a nanoscale control perspective and is the focus of continued efforts beyond this work.

2.6. References

1. Ferain, I.; Colinge, C. A.; Colinge, J.-P. *Nature* **2011**, *479*, 310.
2. Goldberger, J.; Hochbaum, A. I.; Fan, R.; Yang, P. *Nano Lett.* **2006**, *6*, 973.
3. Larrieu, G.; Han, X. L. *Nanoscale* **2013**, *5*, 2437.
4. Lu, W.; Lieber, C. M. *Nat. Mater.* **2007**, *6*, 841.
5. Ng, H. T.; Han, J.; Yamada, T.; Nguyen, P.; Chen, Y. P.; Meyyappan, M. *Nano Lett.* **2004**, *4*, 1247.
6. Wang, D. W.; Wang, Q.; Javey, A.; Tu, R.; Dai, H. J.; Kim, H.; McIntyre, P. C.; Krishnamohan, T.; Saraswat, K. C. *Appl. Phys. Lett.* **2003**, *83*, 2432.
7. Moutanabbir, O.; Isheim, D.; Blumtritt, H.; Senz, S.; Pippel, E.; Seidman, D. N. *Nature* **2013**, *496*, 78.
8. Renard, V. T.; Jublot, M.; Gergaud, P.; Cherns, P.; Rouchon, D.; Chabli, A.; Jousseaume, V. *Nat. Nanotechol.* **2009**, *4*, 654.
9. Sedky, S.; Witvrouw, A.; Bender, H.; Baert, K. *IEEE Trans. Electron Devices* **2001**, *48*, 377.
10. Wang, Y.; Schmidt, V.; Senz, S.; Goesele, U. *Nat. Nanotechol.* **2006**, *1*, 186.
11. Andricacos, P. C.; Uzoh, C.; Dukovic, J. O.; Horkans, J.; Deligianni, H. *IBM J. Res. Dev.* **1998**, *42*, 567.
12. Rosenberg, R.; Edelstein, D. C.; Hu, C. K.; Rodbell, K. P. *Annu. Rev. Mater. Sci.* **2000**, *30*, 229.
13. Al-Salman, R.; Mallet, J.; Molinari, M.; Fricoteaux, P.; Martineau, F.; Troyon, M.; El Abedin, S. Z.; Endres, F. *Phys. Chem. Chem. Phys.* **2008**, *10*, 6233.
14. Mallet, J.; Molinari, M.; Martineau, F.; Delavoie, F.; Fricoteaux, P.; Troyon, M. *Nano Lett.* **2008**, *8*, 3468.
15. Carim, A. I.; Collins, S. M.; Foley, J. M.; Maldonado, S. *J. Am. Chem. Soc.* **2011**, *133*, 13292.
16. Fahrenkrug, E.; Gu, J.; Maldonado, S. *J. Am. Chem. Soc.* **2012**, *135*, 330.
17. Gu, J.; Collins, S. M.; Carim, A. I.; Hao, X.; Bartlett, B. M.; Maldonado, S. *Nano Lett.* **2012**, *12*, 4617.
18. Gu, J.; Fahrenkrug, E.; Maldonado, S. *J. Am. Chem. Soc.* **2013**, *135*, 1684.
19. Qian, F.; Gradecak, S.; Li, Y.; Wen, C. Y.; Lieber, C. M. *Nano Lett.* **2005**, *5*, 2287.
20. Wagner, R. S.; Ellis, W. C. *Appl. Phys. Lett.* **1964**, *4*, 89.
21. Hyde, M. E.; Compton, R. G. *J. Electroanal. Chem.* **2003**, *549*, 1.
22. Liang, Y. Q.; Zhen, C. G.; Zou, D. C.; Xu, D. S. *J. Am. Chem. Soc.* **2004**, *126*, 16338.
23. Fortuna, S. A.; Li, X. *Semicond. Sci. Technol.* **2010**, *25*.
24. Hom, T.; Kiszenick, W.; Post, B. *J. Appl. Crystallogr.* **1975**, *8*, 457.
25. Davidson, F. M.; Lee, D. C., III; Fanfair, D. D.; Korgel, B. A. *J. Phys. Chem. C* **2007**, *111*, 2929.
26. den Hertog, M. I.; Rouviere, J. L.; Dhalluin, F.; Gentile, P.; Ferret, P.; Baron, T. In *Microscopy of Semiconducting Materials 2007*; Cullis, A. G., Midgley, P. A., Eds. 2008; Vol. 120, p 217.
27. Tian, B.; Xie, P.; Kempa, T. J.; Bell, D. C.; Lieber, C. M. *Nat. Nanotechol.* **2009**, *4*, 824.
28. Lieten, R. R.; Degroote, S.; Kuijk, M.; Borghs, G. *Appl. Phys. Lett.* **2008**, *92*.

29. Barth, S.; Hernandez-Ramirez, F.; Holmes, J. D.; Romano-Rodriguez, A. *Prog. Mater. Sci.* **2010**, *55*, 563.
30. Kolasinski, K. W. *Curr. Opin. Solid State Mat. Sci.* **2006**, *10*, 182.
31. Buhro, W. E.; Hickman, K. M.; Trentler, T. J. *Adv. Mater.* **1996**, *8*, 685.
32. Gregory, B. W.; Stickney, J. L. *J. Electroanal. Chem.* **1991**, *300*, 543.
33. Liang, X.; Kim, Y.-G.; Gebergziabiher, D. K.; Stickney, J. L. *Langmuir* **2009**, *26*, 2877.
34. Moffat, T. P.; Bonevich, J. E.; Huber, W. H.; Stanishevsky, A.; Kelly, D. R.; Stafford, G. R.; Josell, D. *J. Electrochem. Soc.* **2000**, *147*, 4524.

CHAPTER 3

Direct Aqueous Electrodeposition of Crystalline Germanium Microwire Films on Hard and Soft Conductive Substrates

3.1. Introduction

This chapter details the advancement of the electrochemical liquid liquid solid (ec-LLS) crystal growth strategy toward the direct preparation of highly ordered crystalline Ge *microwire* arrays with individual diameters larger than 1 μm. The ec-LLS synthesis of Ge microwires was carried out in aqueous solutions at ambient pressure below the boiling point of water using only common lab equipment and non-toxic oxide precursors. A pertinent feature of this work is the use of a liquid metal patterning strategy which combines the utility of photolithography with the simplicity of doctor blading to produce macroscopic (> 1 cm^2) arrays of liquid metal microelectrodes. Scanning electron microscopy indicated the templated liquid metal microdroplets act as discrete sites for electrochemically-driven crystal growth of Ge microwires with controlled size and pitch. Compared with the individual volumes of the liquid Ga nanodroplets (~10^{-16} cm^3) employed for ec-LLS nanowire growth, significantly larger liquid metal electrodes (~10^{-10} cm^3) were fabricated and employed in this study. Optical and electron micrographs showed the compatibility of the liquid metal patterning process and subsequent ec-LLS microwire growth with a wide assortment of different conductive substrates including silicon, indium tin oxide (ITO), Cu foil, Ti foil, stainless steel and PEDOT:PSS polymers. Further, a simple chemical bath lift-off procedure was developed to fully remove the Ge microwire arrays embedded in SU8 photoresist without perturbing the order or quality of the material, resulting in a free-standing composite membrane. Data from energy dispersive spectroscopy, Auger nanoprobe spectroscopic mapping, and four-terminal single microwire electrical measurements indicated that the specific liquid metal used for ec-LLS impacts the morphology and electrical properties of the resultant Ge microwires. The

collective results define a precedent for ec-LLS as a simple strategy to produce high quality hybrid inorganic semiconductor/organic structures while also serving as a basis for future studies aimed at tuning ec-LLS crystal nucleation and growth for deterministic synthesis of high quality semiconductor materials.

Synthesis of group IV semiconductor microwire and nanowire films presently implies the use of high temperatures, caustic precursors,[1-5] and multiple processing steps if integration into an electronic device is required. As a result, combining crystalline semiconductor microwires onto thermally/chemically-sensitive substrates is tedious at the laboratory scale and difficult at large scales.[5-12] Alternative synthetic strategies that are benchtop (i.e. low temperature, requires only common solvents and reagents) and compatible with all types of support substrates would be germane to the development of low-cost energy conversion devices,[13] flexible electronics,[5,14-16] and chemical sensors.[1,17]

In this chapter we report a series of advancements involving a new hybrid electrochemical synthetic method for the direct preparation of crystalline covalent semiconductors. In an electrochemical liquid-liquid-solid (ec-LLS) process, a liquid metal is used both to provide electrons for heterogeneous electroreduction reactions and simultaneously as a solvent for three-dimensional semiconductor crystal growth.[18-26] We have previously validated the ec-LLS concept for the preparation of crystalline Si, GaAs, and Ge[20, 23, 25] at record low temperatures. However, all previous ec-LLS work has only demonstrated the growth of crystals on the nanoscale. Accordingly, a motivating factor for this work was to determine whether larger crystals could also be prepared via ec-LLS at low temperatures (i.e. below the boiling point of water).

This chapter tests four hypotheses regarding the development of a new synthetic tactic for crystalline semiconductor microstructures: (*1*) ec-LLS can be used to directly electrodeposit crystalline Ge microwires. (*2*) The identity of the liquid metal strongly influences Ge crystal growth in ec-LLS. (*3*) Crystal growth of Ge in ec-LLS can be controlled and performed in parallel over large (>1 cm^2) areas to produce films of crystalline microwires on virtually any type of conductive support. (*4*) Free-standing Ge microwire films embedded in an organic film can be lifted-off the growth substrate and transferred to any other surface under purely benchtop conditions.

3.2. Methods

Materials and Chemicals

Acetic acid (99.9%, Alfa Aesar), acetone (ACS grade, BDH), methanol (ACS grade, BDH), 2-propanol (ACS grade, BDH), tetrahydrofuran (Sigma Aldrich), pyridine (99%, Sigma Aldrich), n-butylamine (99.5%, Sigma Aldrich), ethylene glycol (>99%, Sigma-Aldrich), cyclopentanone (>99%, Sigma-Aldrich), Ga(*l*) (99.999%, Alfa Aesar), In(*s*) (99.98 – 99.99%, Alfa Aesar), GeO2 (99.999%, Alfa Aesar), hydrofluoric acid (49%, Transene Inc.), oxygen gas (Metro Welding, Detroit, MI), hexamethyldisilazane (HMDS, Fischer Scientific), titanium diisopropoxy-bis(atetylacetonate) (AP300, 75% in 2-propanol, Sigma-Aldrich), and poly(3,4-ethylenedioxythiophene) polystyrene sulfonate (PEDOT:PSS, 1.2% in water, Clevios P, Sigma) were used as received. Substrates for microfabrication and electrodeposition included Si(100) (Crysteco, <100> As-doped n-type, < 0.007 Ω·cm, 0.625 ± 0.020 mm thick), Si(111) (MEMC Electronic Materials Inc., <111>, As-doped n-type, 0.0030-0.0040 Ω·cm, 0.510 mm thick), Cu foil (110 grade, McMaster-Carr), stainless steel (303 grade, McMaster-Carr), titanium alloy foil (90% Ti, 6% Al, 4% V, McMaster-Carr), and indium-doped tin oxide (ITO)-coated glass (R_s< 12.1 Ω cm, Pilkington). Water was purified from a Barnstead Nanopure III purification system (>18 MΩ cm) and was used throughout.

Microfabrication, Liquid Metal Doctor Blading, & Lift-Off

Hole arrays with various diameter and pitch were patterned on all substrates using standard photolithographic procedures. Substrates (typically 10 x 10 mm and 0.6 mm thick) were degreased by sonicating for five minutes each in acetone, methanol, and water, then dried under a N_2(g) stream. Care was taken during sonication to minimize contact between wafers to prevent surface scratches by employing a custom wafer holder. [Appendix A.1] For Si wafers, the native oxide was removed by etching in 5% HF for 60 s, rinsing vigorously with water, and drying under N_2(g), immediately prior to fabrication. Hexamethyldisilazane (HMDS) was spin coated on the Si wafer to act as an adhesion promoter. Copper foils were instead etched with glacial acetic acid for 10 minutes to remove native CuO_x followed by immediate spin coating of titanium diisopropoxy-bis(atetylacetonate) (75% v/v in 2-propanol) as an adhesion promoter. Titanium, stainless

steel, ITO-coated glass and PEDOT:PSS on ITO were used without chemical etching or application of adhesion promoters.

A negative tone photoresist (SU8-2025, Microchem Corp.) was then diluted from 68.6 % to 52.5 % total dissolved solids in cyclopentanone and stirred while covered for 60 minutes. The diluted SU8 photoresist was spin-coated over the substrate and allowed to rest for two minutes at room temperature prior to soft baking on a hotplate at 95 °C for 3 minutes. The SU8 coated substrate (except for Cu foils) was placed on a vacuum chuck where the edge bead was manually removed with a razor blade by scraping ~1 mm inward along each edge. To prevent deformation of thin Cu foils during mechanical edge bead removal, a custom vacuum chuck accessory was fabricated to prevent edge bead formation entirely. [Appendix A.3] UV light exposure (OAI) for 11 s (Si), 16 s (ITO and PEDOT:PSS), 22 s (Cu, Ti, and stainless steel) at 26 W/cm^2 through a custom-made contact photomask (Fineline Imaging, Colorado Springs, CO) was used to transfer the hole array patterns to the photoresist layer. Substrates were subject to a post-exposure bake at 95 °C for 5 minutes on a hot plate. Development for 5 minutes under agitation with SU8 developer (Microchem. Corp.) removed the unexposed regions of the photoresist. After development, the substrate was rinsed vigorously with 2-propanol, dried under N_2(g) and then annealed in air at 135 °C for 20 minutes to fully cross-link the SU8 polymer. Substrates were then treated with an oxygen plasma at 20 sccm O_2(g) and 400 W (PE-50, Plasma Etch Inc.) for 3 minutes to remove un-crosslinked SU8 from the surface of the photoresist (i.e. descumming).

To fill hole arrays patterned on Si with liquid metal, the native oxide was again removed by soaking the patterned wafer in 5 % (v/v) HF for 60 s. No additional etching steps were required for titanium, stainless steel, ITO-coated glass and PEDOT:PSS on ITO. Either pure Ga(*l*) or InGa eutectic (EGaIn, 75% Ga, 25% In) was first heated to 100 °C in an oven to increase workability of the metal. Substrates were immobilized in a home-made vacuum chuck while ~200 µL of the heated liquid metal was dispensed on the surface of the hole array pattern. A lint-free towel (Kimtech W4, Fisher) was used to compress the liquid metal against the substrate and force it to wet the interior of each hole. The towel was continually rubbed across the template in all directions until all holes were filled.

Excess liquid metal was removed by applying methanol to a lint-free towel and wiping the substrate surface until the silver hue of the metal was visibly absent.

Lift-off of Ge microwire arrays embedded in SU8 photoresists was carried out through a wet chemical process adapted from previous work.[27] Briefly, substrates to be lifted-off were placed in a sealed glass vial containing 2:2:1 (parts by volume) pyridine, THF, and *n*-butylamine at 65 °C. The substrates were allowed to soak for ~15-30 min before complete delamination occurred. The lift-off solution was replaced with a more inert transfer solvent (i.e. acetone, methanol, water). The target substrate for transfer was placed under the floating SU8 layer. Excess liquid was slowly removed from the vial, allowing the film the gently transfer to the new underlying support. Transferred films were gently washed with methanol and water before drying under N_2(g).

Electrochemistry and Electrodeposition

After filling hole arrays with liquid metal, substrates were immediately assembled into custom single chamber PTFE cells with either 0.1 or 1.3 cm^2 exposed electrode area. Electrical contact to Si wafers was made by applying a thin layer of EGaIn to the back of the wafer and pressing it against a stainless steel electrode support. Conductive copper tape (Ted Pella) was used to make top contact to ITO-coated glass and PEDOT:PSS on ITO substrates. No special methods were employed for contacting metal foil substrates. A standard three-electrode configuration with a Pt mesh counter electrode and a Ag/AgCl (sat. KCl) reference electrode was employed. Metrohm Autolab PGSTAT302N, CHI420, and CHI760C electrochemical workstations were employed for electrodepositions and chronoamperometric measurements. All reported electrochemical potentials are with respect to *E*(Ag/AgCl, sat. KCl). Electrodeposition of Ge microwires was conducted potentiostatically at -1.6 V in a temperature-controlled water bath (Buchi Water bath, B-481) held at 80 °C.

Materials Characterization

Scanning electron microscopy (SEM) imaging and focused ion beam (FIB) milling were conducted in FEI NOVA Nanolab Dualbeam and FEI Helios Nanolab 650 Dualbeam workstations, both equipped with Schottky field emitters and Ga focused ion beams. For lift-out, Ge microwire arrays were first sonicated in ~1 mL methanol for 30 s and re-

dispersed on a 1 cm^2 Si wafer so the microwires were oriented on their sides. In the SEM/FIB workstation, an Omniprobe AutoProbe 200 micromanipulator equipped with a standard tungsten (W) probe tip (Ted Pella) was used to approach and contact single microwires on the substrate. A temporary Pt weld was made between the microwire and the W probe via electron beam assisted chemical vapor deposition (EBA-CVD) with a $C_5H_4CH_3Pt(CH_3)_3$ gas injection system. The micromanipulator was then retracted to lift-out the single microwire from the surface. Single wires were then individually placed across a custom-made four terminal electrical measurement device inside the SEM/FIB workstation. Each of the four Au electrical leads from the device substrate were Pt-welded to the Ge microwire using a low-resistivity FIB assisted Pt welding approach. After electrical contact was made, the temporary Pt weld between the W tip and the microwire was cut by the FIB. Special measures were exercised to ensure the Ge microwires were not exposed to the FIB beam during welding or milling. Powder X-ray diffraction (XRD) was performed using a Bruker D8 Advance X-ray diffractometer with a Cu K_α X-ray source (λ = 1.5406 Å). A 0.6 mm slit width was employed with a sampling rate of 20 data points per degree 2θ at 2 s $point^{-1}$. Auger spectroscopic analyses were conducted with a Physical Electronics Scanning Auger Nanoprobe 680 equipped with a field emission source, Everhart-Thornley secondary electron detector, cylindrical mirror analyzer, and an eight-channel detector. Sputtering depth profile experiments were performed with a PHI model 06-350E Ar^+ source biased at 1 keV. Laser diffraction experiments were conducted with a HeNe gas laser (λ = 632.8 nm) positioned 1 cm from the substrate with a measured spot size of 5 mm^2. The microwire pitch was calculated from eq 3.1:

$$d_{hole} = \frac{L\lambda\sqrt{2}}{\bar{x}} \qquad (3.1)$$

where d_{hole} is the experimental distance between holes in the array, L is the distance between the laser source and the diffracting object (L = 1 cm), λ is the laser wavelength (λ = 632.8 nm), and $\bar{x}$ is the average measured distance between the diffraction spots.

Electrical Characterization

Four terminal electrical characterization devices were photolithographically fabricated as discussed in a previous work.[18] An Alessi probe station with a Keithley 4200-SCS was used to measure electrical properties of single Ge microwire devices.

3.3. Results

Ge Microwires by ec-LLS

Figure 3.1a describes the three electrode electrochemical cell setup initially used to electrodeposit Ge microwires through ec-LLS. The electrically-contacted liquid metal microdroplets were prepared through one of two methods. Either a single, macroscopic liquid metal drop immersed in methanol was first sonicated to form a suspension of fine liquid metal droplets[28] which were then cast on to a conductive substrate or a single macroscopic liquid metal drop was physically smeared with a lint-free towel across a conductive substrate to form discrete microscopic droplets. Following decoration with liquid metal microdroplets, the conductive substrates were immersed in an aqueous solution containing 0.05 M $GeO_2(aq)$ and 0.01 M $Na_2B_4O_7(aq)$. Application of an electrochemical potential more negative than -1.6 V vs. Ag/AgCl triggered electrodeposition of Ge(*s*) selectively at the individual liquid metal microdroplets through reaction 1.

$$HGeO_3^-(aq) + 4e^- + 2H_2O \rightarrow Ge(s) + 5OH^-(aq)$$

Figure 3.1b summarizes the ec-LLS process.[19] The key distinction in this work is that the distance between the liquid electrolyte/liquid metal interface where $HGeO_3^-(aq)$ ions are electrochemically reduced to Ge(*s*) and the liquid metal/substrate interface where heterogeneous nucleation and crystal growth occurs is at least several microns. This is in contrast to previous work on Ge nanowire ec-LLS where liquid Ga nanodroplets were on the order of 0.1 μm in diameter. Figure 3.1c shows representative images of the resultant Ge microwires prepared by ec-LLS for two hours with liquid metal droplets of approximately 10 μm diameter. Two different liquid metal types, Ga(*l*) and a eutectic mixture of Ga and In (EGaIn) were used, with melting points of 29.4 °C and 24 °C, respectively. Both liquid metal types facilitated electrodeposition of Ge microwires, implying that supersaturation was achieved and that crystal nucleation was heterogeneous at the underlying substrate surface for each liquid metal type. However, the morphology of the Ge microwires electrodeposited was strongly sensitive to the liquid metal type. The Ge microwires prepared using Ga(*l*) had a smooth and rounded surface texture with various smaller protuberances along the length of the structure. These Ge microwires also had a

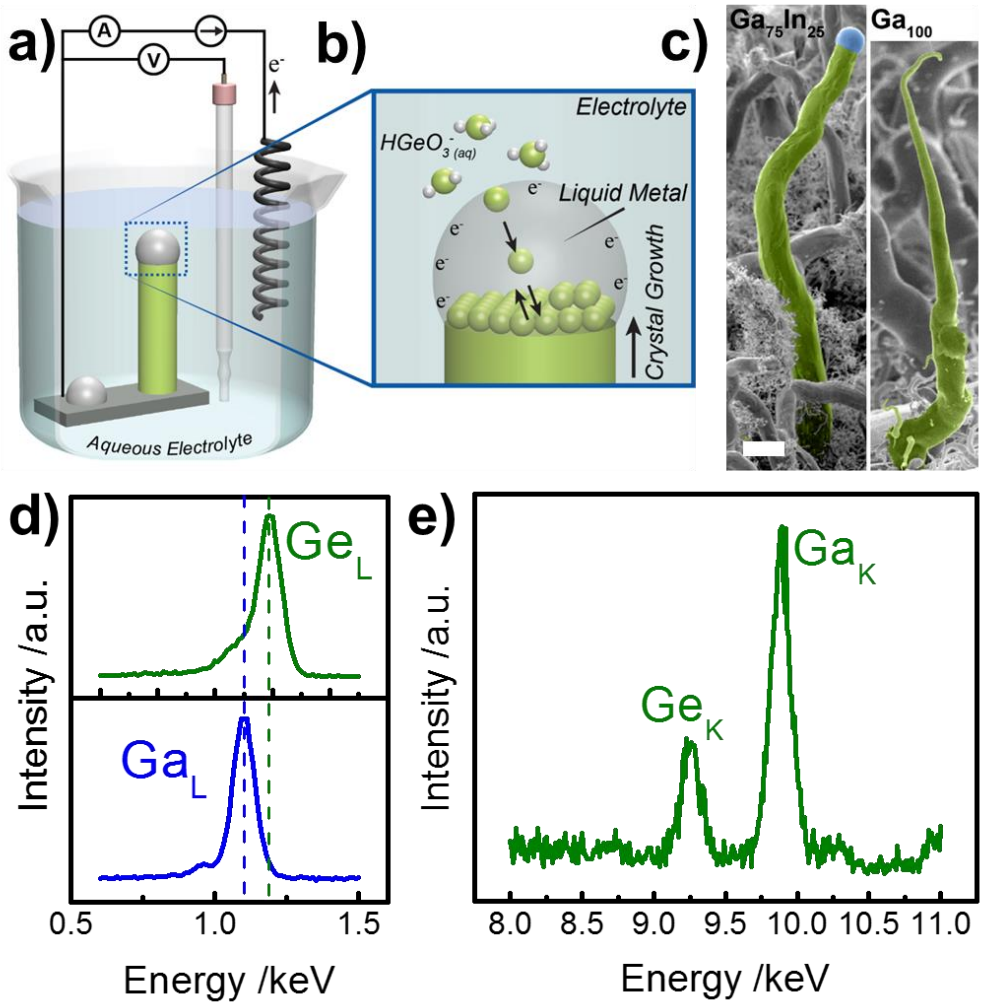

Figure 3.1. (a) Schematic depiction of three electrode electrochemical cell and beaker setup used for Ge microwire ec-LLS. (b) Zoomed in schematic of the tip of the Ge microwire pictured in a) showing the proposed ec-LLS microwire growth mechanism. Dissolved $HGeO_3^-(aq)$ ions are electrochemically reduced to Ge(*s*) which partitions into the liquid metal until supersaturation induces nucleation and concomitant heterogeneous crystal growth. (c) Tilted scanning electron micrographs of Ge microwires grown from EGaIn(*l*) (75% Ga, 25% In by wt.) and pure Ga(*l*) electrodes following ec-LLS growth at 80 °C for 120 minutes. Scale bar is 10 µm. (d) High resolution X-ray energy dispersive spectra (EDS) collected from the body (green) and tip (blue) of the Ge microwire grown from EGaIn pictured in c). (b) EDS spectrum collected from the body of a Ge microwire grown from a pure Ga(*l*) electrode pictured in (c).

pronounced taper (the diameter decreased from 10.2 to 0.8 μm over a total length 120.5μm; cone angle = 2.23°) and lacked an identifiable liquid metal 'cap', as noted previously in the electrodeposition of single-crystalline Ge nanowires.[19] In contrast, the Ge microwires produced with EGaIn microdroplets had faceted surfaces with no obvious side growths/branching. Further, these Ge microwires had much less apparent tapering (a diameter reduction from 10.1 to 6.5 μm over a total length of 124.9 μm; cone angle = 0.83°) and a round cap was clearly observed at the top (false colored in blue in Figure 3.1c). For the Ge microwires prepared with Ga(*l*) microdroplets, the length stopped increasing after a set amount of time (~45 min) and electrodepositions performed for longer times did not increase the Ge microwire lengths. Conversely, the length of the Ge microwires prepared with EGaIn was strongly sensitive to electrodeposition time even at long times (Figure 3.2).

Figure 3.1d shows localized energy dispersive X-ray spectroscopy (EDS) measurements collected from different points along the Ge microwire prepared with EGaIn. The spectrum collected from the Ge microwire body showed a strong signal centered at 1.2 keV, diagnostic of a Ge L line. Signals consistent with the In M- (0.4 – 0.7 keV), In L- (3 – 4.3 keV), and Ga L- (1 – 1.3 keV) transitions were not observed along the body of the Ge microwire. In contrast, the EDS spectrum collected from the cap at the end of the Ge microwire (Figure 3.1e) contained only Ga L- and In L transitions, indicating the metal cap was composed largely/entirely of liquid metal. Since EDS is inherently a bulk technique,[29] Auger nanoprobe spectroscopy was separately employed to investigate the surface composition of the Ge microwires (Figure 3.3) and the liquid metal electrode. The Auger surface compositional map of a single Ge microwire in Figure 3.3a largely mirrored the findings from EDS analyses, i.e. the majority of liquid metal was localized to the cap. Additional quantitative Auger analyses performed on the liquid microdroplet before and after ec-LLS (Figure 3.3c) showed a 20 % indium enrichment in the liquid metal composition from $Ga_{83}In_{17}$ to $Ga_{63}In_{37}$ (at. %) after 60 min. Although Auger analysis largely complemented the EDS data, three additional aspects were identified. First, the distribution of In and Ga in the liquid metal cap was not spatially uniform. Second, some isolated spots of Ga were detected on the surface of the Ge microwire. Third, the relative concentrations of Ga and In in the liquid metal droplet are not constant over the ec-LLS microwire growth duration.

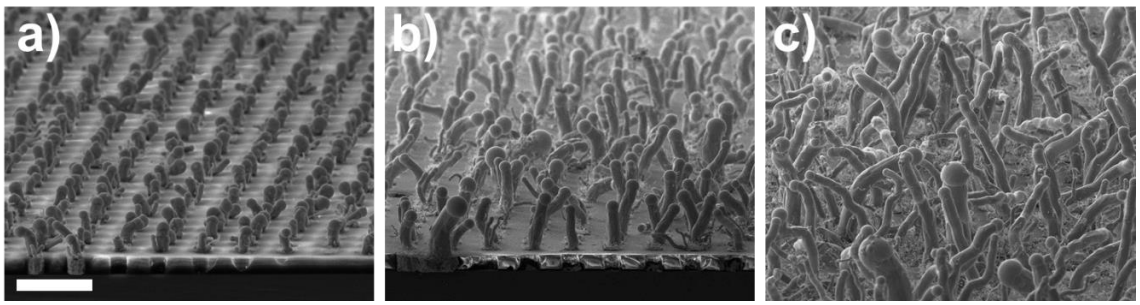

Figure 3.2. Tilted scanning electron micrographs collected after Ge microwire ec-LLS from EGaIn microdroplet electrodes in a 10 x 10 μm SU8 template after (a) 30, (b) 60, and (c) 120 min. Scale is 50 μm.

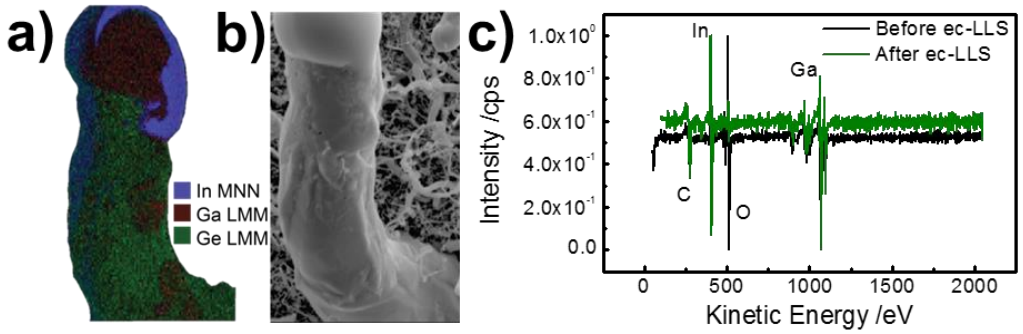

Figure 3.3. (a) Surface Auger nanoprobe spectroscopic compositional map of a single Ge microwire pictured in the corresponding electron micrograph in (b). Growth conducted at -1.6 V for 30 minutes at 80 °C. Scale is 10 µm. (c) Differentiated Auger spectra collected from an EGaIn microdroplet before (black) and after (green) ec-LLS Ge microwire growth for 30 min at 80 °C.

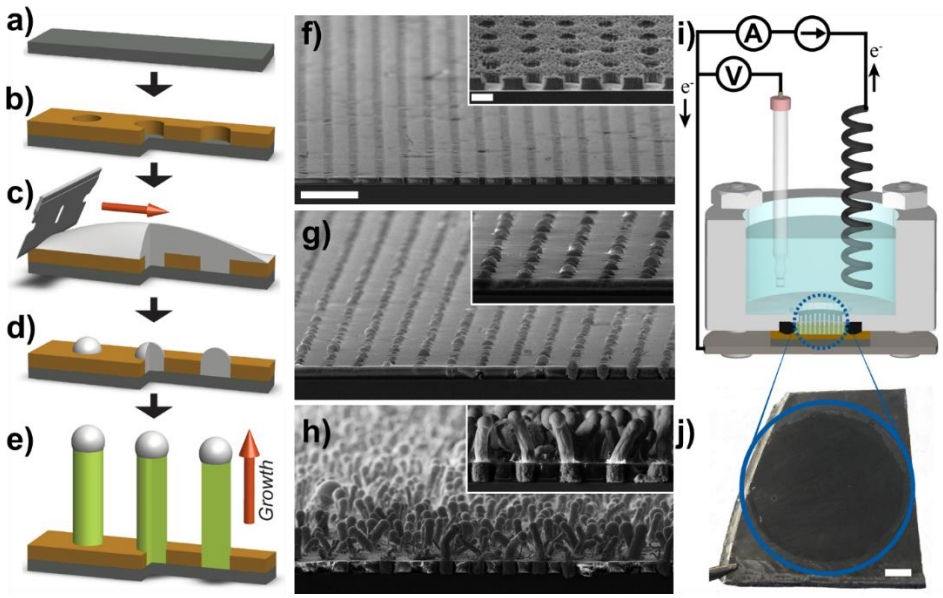

Figure 3.4. (a-e) Schematic of the liquid metal lithography sequence for preparing arrays of liquid metal microelectrodes. A flat conductive support (a) is photolithographically patterned leaving thru-holes of determinate size and pitch, (b). (c) Bulk liquid metal is doctor bladed repeatedly over the surface to fill the exposed holes. Excess liquid metal is removed methanol leaving (d) ordered arrays of discrete liquid metal microelectrodes for (e) subsequent ec-LLS microwire growth. (f-h) Tilted scanning electron micrographs of the steps depicted in (b), (d), and (e), respectively. Scale bar is 50 µm. Insets shown zoomed in features with a scale of 10 µm. (i) Cross-sectional schematic of the actual PTFE o-ring electrochemical cell employed for all ec-LLS Ge microwire growths. (j) Optical micrograph of the zoomed in region in (i) highlighting the circular o-ring imprint that defines the boundary of ec-LLS growth. Scale is 2 mm.

Subsequent Ge microwire ec-LLS experiments were performed with a refined preparation method developed for EGaIn microdroplets. Specifically, a protocol was developed to control liquid metal droplet diameter and pitch through a combination of conventional photolithography and doctor blading steps. Figures 3.4a-e describe the employed strategy, where liquid metal was doctor bladed into void spaces in photolithographically patterned negative photoresist (SU-8) films. A brief O_2(g) plasma etch was used to clean the pattern and assist wetting of the EGaIn. The specific plasma etch duration provided additional fine control over SU8 hole size (Figure 3.5). Excess liquid metal was removed with methanol and a lint-free wipe, leaving arrays of size- and pitch-controlled liquid metal microelectrode droplets. The thickness of the SU-8 layer and the dimensions of the patterned holes dictated the volume of the liquid metal droplets. Tilted scanning electron micrographs of the patterned photoresist before and after infiltration with liquid metal as well as after Ge ec-LLS are shown in Figures 3.4f-h. Figures 3.6a-g show the applicability of the doctor blading technique to virtually any diameter, thickness and hole pitch over large areas provided the dimensions are accessible by conventional photolithographic means. The EGaIn droplets were completely constrained to the patterned holes with no residual EGaIn on the surface of the photoresist. Due to the large inherent surface tension of the liquid metal, a small fraction of the droplet protrudes from the surface of the SU8 pattern. This is especially apparent as the aspect ratio of the SU8 patterned hole (hole depth divided hole diameter) decreases below unity (Figures 3.6a-f). Figure 3.4h shows Ge microwires electrodeposited at E_{app} = -1.6 V for 30 min at 80 °C. The recorded current response for the potentiostatic electrodeposition in Figure 3.4h was analyzed both in the absence and presence of dissolved GeO_2 precursor (Figure 3.7). In the absence of dissolved GeO_2, the current response follows the non-zero steady-state behavior expected for hemispherical diffusion-limited current at microelectrodes.[30] However, in the presence of GeO_2, the current increases monotonically over the entire 30 min ec-LLS microwire growth. For these ec-LLS experiments, a custom o-ring cell [Appendix A.4] was used to define the total surface area exposed to solution (Figures 3.4i). Each EGaIn microdroplet exposed to aqueous electrolyte yielded exactly one single Ge microwire (Figures 3.4h). Figures 3.4j shows the macroscopic uniformity of the electrodeposited Ge microwire film across the entire exposed area (~ 1.32 cm^2).

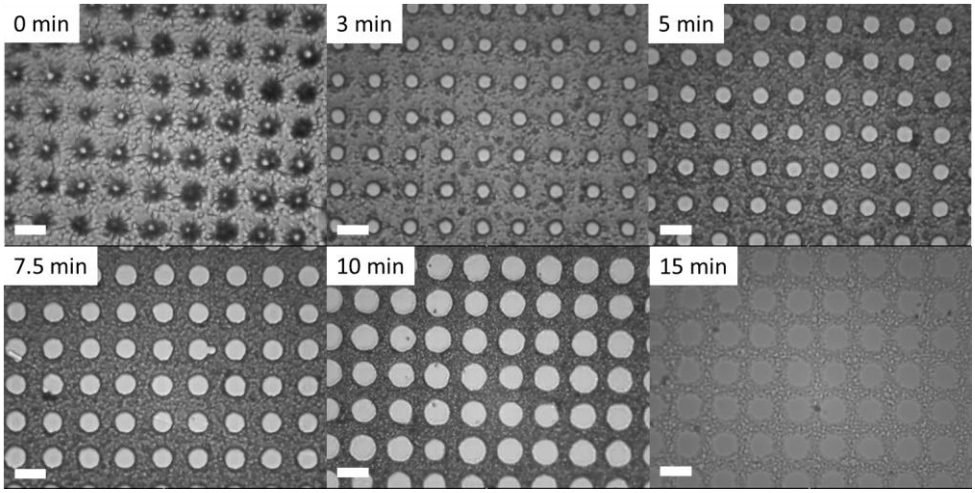

Figure 3.5. Plan-view optical micrographs collected from a single 10 μm thick SU8 2007 photoresist template with nominally 10 μm diameter holes after plasma etching in 20 SCCM O_2(g) at 400 W for (a) 0 min, (b) 3 min, (c) 5 min, (d) 7.5 min, (e) 10 min, and (f) 15 min.

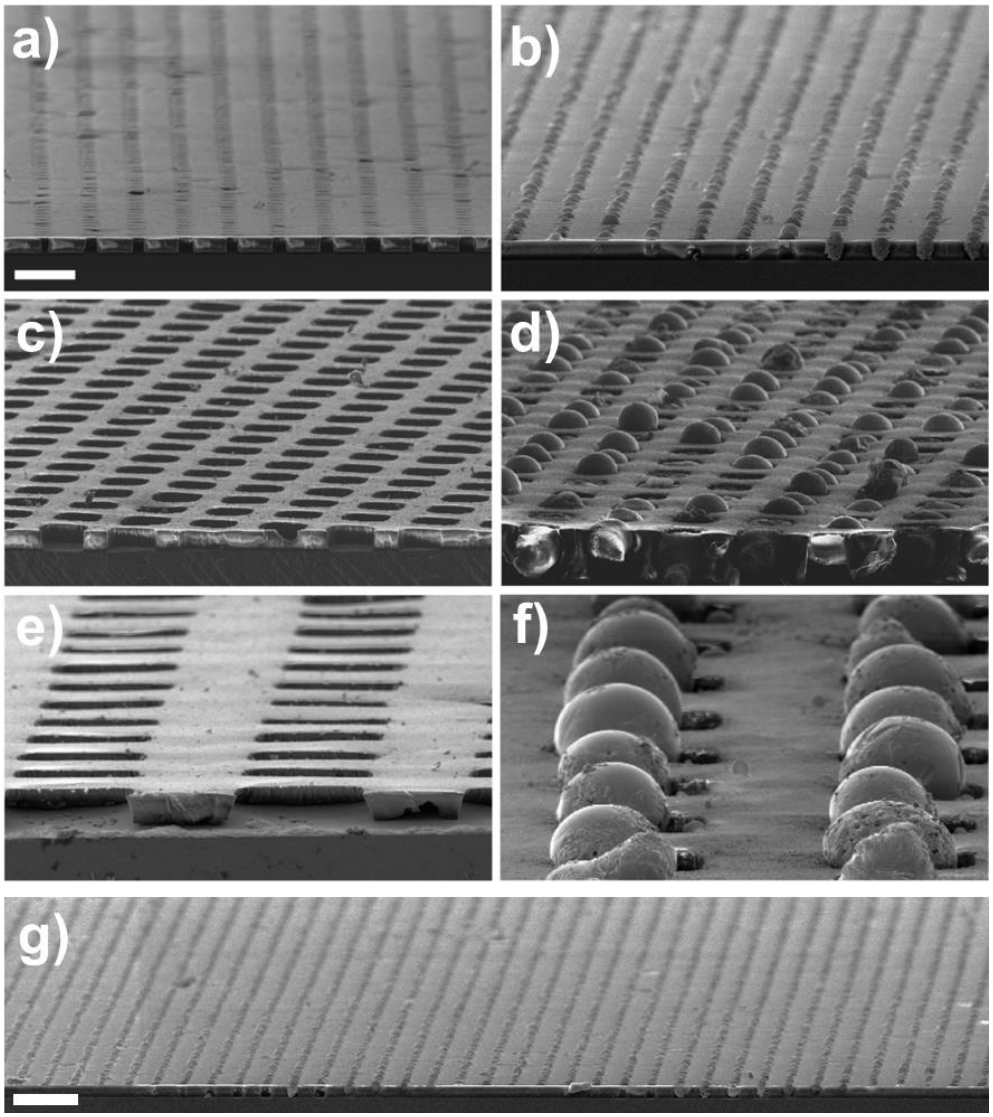

Figure 3.6. (a) Tilted scanning electron micrographs of photolithographically prepared SU8 patterns on n^+-Si(100) with 10 µm holes with 10 µm pitch before (a) and after (b) liquid metal doctor blading, 30 µm holes with 30 µm pitch before (c) and after (d) doctor blading, and 50 µm holes with 50 µm pitch before (e) and after (f) doctor blading. Scale is 10 µm. **(**g) Large field of view micrograph of the SU8 pattern shown in (a). Scale is 50 µm.

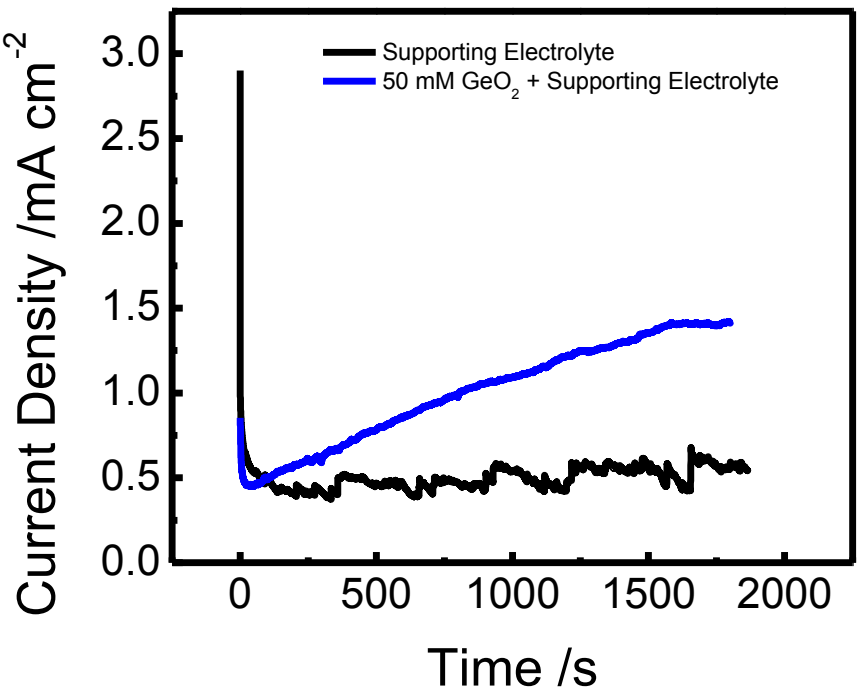

Figure 3.7. Current-time responses for a patterned EGaIn microdroplet array during 30 min ec-LLS at -1.6 V in the absence (black) and presence (blue) of the dissolved GeO_2 precursor. The supporting electrolyte was 0.01 M $Na_2B_4O_7$ in water.

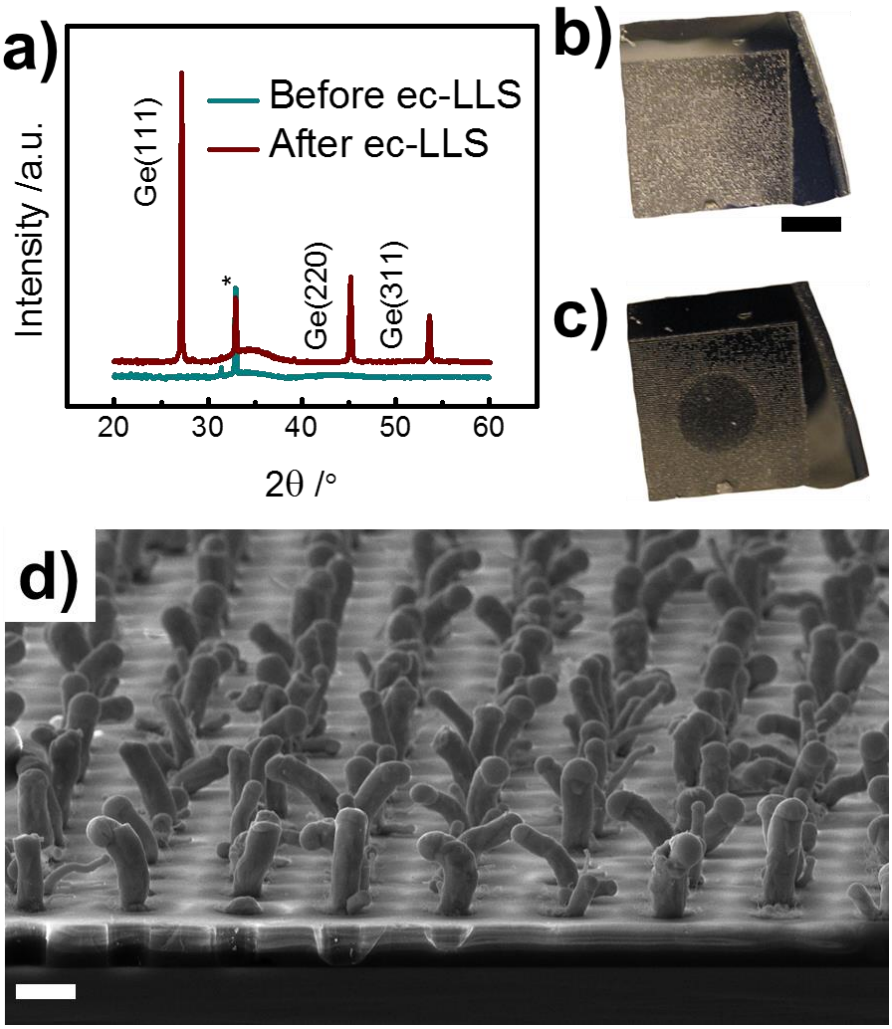

Figure 3.8. (a) Powder X-ray diffraction pattern collected from an EGaIn(*l*) microelectrode array templated in SU8 on Si(100) (red) and the corresponding pattern after Ge microwire ec-LLS for 30 minutes at 80 °C (green). The reflection at 32.5° highlighted with an asterisk is from the Si(100) background. Other labelled reflections are from diamond cubic Ge. Corresponding optical images of the EGaIn microelectrode array in SU8 and the resultant Ge microwire array are depicted in (b) and (c), respectively. Scale is 4 mm. (d) Cross-sectional electron micrograph of a Ge microwire array used for pXRD measurement in (a). Scale is 20 µm.

The crystallinity and orientation of as-prepared Ge microwires electrodeposited on a degenerately doped n^+-Si(100) substrate were assessed through powder X-ray diffraction (Figure 3.8a). Powder diffraction patterns measured on the liquid metal droplet arrays before (Figure 3.8b) and after (Figure 3.8c) the ec-LLS process are presented. Prior to ec-LLS, the substrates exhibited only a broad feature at 34.5° and a sharp but weak feature at 33° attributed to liquid EGaIn and the [100] signal of the Si substrate, respectively. After ec-LLS, the diffractograms showed an additional set of three sharp and intense reflections at 2θ = 27.2°, 45.2°, and 53.6°. These three peaks matched the expected [111], [220], and [311] lines for crystalline, diamond cubic Ge.[31] The corresponding linewidths for each Ge reflection were each too narrow to carry out Scherrer crystallite size analyses, indicating the crystalline domain size in each Ge microwire was in excess of 200 nm in each of the respective [111], [220], and [311] directions.[32] Comparison of peak area ratios of each *hkl* reflection with those of a standard pattern[31] indicated strong texturing of the microwires along the [111] direction. The electron micrograph shown in Figure 3.8d is in line with this observation, as the majority of microwires are tilted towards one of the [111] directions with respect to the substrate [100] surface orientation. These observations are broadly consistent with the preferred [111] growth direction observed previously for Ge nanowire growth by ec-LLS.[19]

Current Voltage Characteristics of Single Ge Microwires

The electrical resistivities of individual, as-deposited Ge microwires were assessed through four point probe measurements. Through a combination of focused ion beam lift-out and ion-beam welding, four separate Pt contacts were deposited on individual Ge microwires (Figure 3.9a). For each measurement, current was sourced through the outer terminals while measuring the voltage drop across the inner terminals to mitigate contact and lead resistance artifacts. The current-voltage (*I*-*V*) responses for separate Ge microwires collected from opposite sides of the same Ge microwire film array are shown in Figure 3.9b. Both microwires show nominally comparable *I*-*V* responses over three full voltage sweep cycles. For the employed conditions listed above, the average resistivity of as-prepared Ge microwires was 1.5 ± 0.1 Ω·cm. This resistivity value was too low to be consistent with the resistivity of intrinsic Ge. Instead, the value implies some level of doping in the as-prepared Ge microwires. Using resistivity-dopant concentration

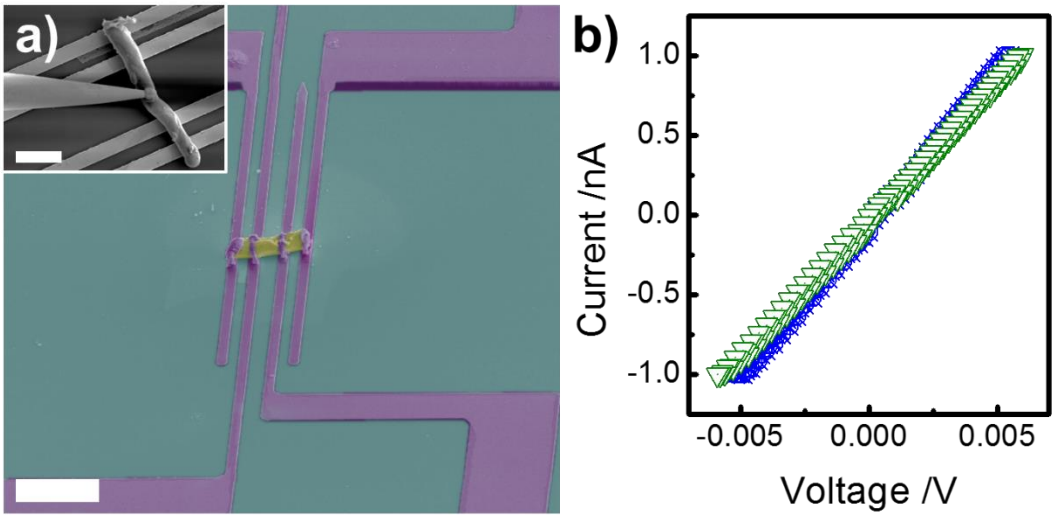

Figure 3.9. (a) Tilted scanning electron micrograph of a four-terminal electrical device used to measure resistivity of single Ge microwires. Scale is 20 µm. Inset shows an electron micrograph of a separate Ge microwire being placed across the terminals with a tungsten micromanipulator probe prior to Pt welding. Scale is 20 µm. (b) Corresponding current-voltage plots of the two Ge microwire devices pictured in (a).

correlations for bulk crystalline Ge,[33] this average resistivity value translated to an approximate dopant concentration of 2.3 x 10^{15} cm^{-3} (~10^{-7} at %). Indium impurities were likely not the main source of these dopants as In solubility in Ge at the temperatures employed here is not known[34] and no In signals were observed in the EDS spectra of the bulk of the microwires. Conversely, this inferred level of doping is consistent with incorporated Ga atoms acting as electrically active impurities. However, since the equilibrium solubility of Ga in Ge at T = 80 °C is 0.9 at. %,[35] the estimated doping level implied a comparatively low level of substituted Ga atoms within the Ge crystals.

Ge Microwire ec-LLS on Assorted Conductive Substrates

Since the ec-LLS process shown here does not involve excessively high process temperatures, direct growth of crystalline Ge microwires on both 'hard' and 'soft' conductive substrates should be possible. Accordingly, Ge microwire arrays were prepared by ec-LLS on a set of various conductive supports comprised of metal foils, a conductive oxide, and a conductive organic polymer. For each substrate, the exact same ec-LLS conditions were employed, i.e. E_{app} = -1.6 V vs. Ag/AgCl for 30 minutes at 80 °C in the aqueous electrolyte of 0.05 M GeO_2 and 0.01 M $Na_2B_4O_7$. Figure 3.10 shows tilted scanning electron micrographs of the resultant Ge microwire films prepared in this way on n^+-Si(100), Cu foil, stainless steel (type 303), a titanium alloy (6Al-4V), indium-doped tin oxide (ITO), and PEDOT:PSS. Optical images of the substrates after ec-LLS growth are shown in the insets. In every case, the overwhelming majority of EGaIn microdroplets yielded microwires with a liquid metal cap and the same nominal length. The fidelity of the patterned photoresist depended somewhat on the conductive substrate,[36] unintentionally increasing the polydispersity of the liquid metal droplet sizes. The high yield of Ge microwires on all substrates indicated so long as the EGaIn microdroplets were in intimate electrical contact with a conductive substrate, microwire growth by ec-LLS was possible. The Ge microwire morphology and size were nominally invariant to the type of substrate, suggesting the liquid metal composition was much more influential on these properties as compared to the substrate.

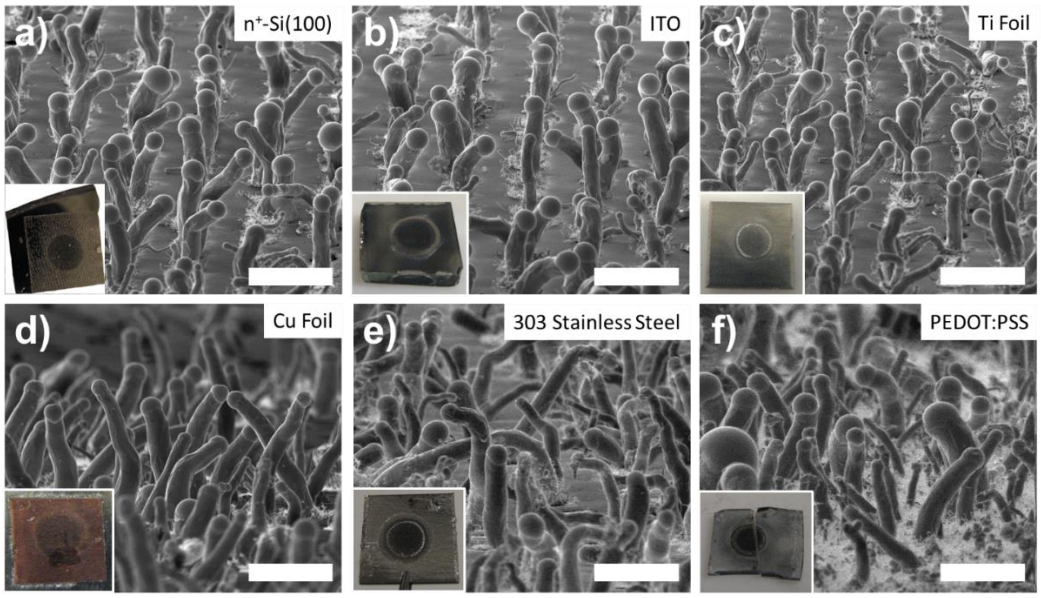

Figure 3.10. (a) Tilted scanning electron micrographs of Ge microwires after growth at 80 °C for 30 minutes on SU8 patterned a) n-Si(100), (b) indium tin oxide coated glass, (c) titanium 6Al-4V alloy foil, (d) Cu foil, and (e) stainless steel. (f) Scanning electron micrograph of Ge microwires prepared identically to those in (a-e) on a PEDOT:PSS film except no SU8 pattern was employed. Scale is 50 μm. Insets show optical images of the substrates after growth.

Lift-off of Embedded Ge Microwire Arrays

A consequence of doctor blading the liquid metal microdroplets into a photolithographically templated resist layer is that the ec-LLS process produced Ge microwires embedded in a thin plastic film. Unfortunately, cross-linked SU-8 is strongly adherent on Si[37] and strategies for non-destructive lift-off of SU-8 are not known, despite intense interest.[38] Nevertheless, if the polymer film could be lifted off without damage to the Ge microwires, then a freestanding hybrid inorganic-organic film would result. Such hybrid composite materials are being intensely explored for solar energy conversion/storage applications.[13,39,40] To this end, a series of experiments were conducted to remove the cross-linked SU-8 film from n^+-Si(100).

The existing literature on immersion of SU-8 films in organic solvents indicates that excess photo-activated acid initiator ($HSbF_6$) is released from the polymer and triggers further cross-linking and hardening.[27,41] Assuming an immersion solvent is basic enough to neutralize any $HSbF_6$, penetration into SU-8 should cause swelling and facile delamination from the substrate. Based on that premise, mixtures of tetrahydrofuran, pyridine, and *n*-butylamine were specifically studied. *n*-butylamine (pK_b = 3.41) was chosen to neutralize excess $HSbF_6$ while THF and pyridine were selected to stabilize the protonated form of *n*-butylamine. Importantly, this solvent mixture was also non-corrosive towards Ge. Exhaustive analyses showed that immersion of SU-8 films in 2:2:1 tetrahydrofuran/pyridine/*n*-butylamine for 15 minutes at 65 °C caused full delamination after 10-20 minutes. As a result, any patterned SU-8 film immersed in this solution gently floated off the original underlying Si substrate in one piece. Notably, no sacrificial layers[42] were needed. When this lift-off process was performed on SU-8 films containing Ge microwires produced by ec-LLS, composite inorganic-organic membranes were readily produced. These hybrid materials exhibited good flexibility and optical transparency. Figure 3.11a schematically depicts the process and Figures 3.11b and 3.11c show a micrograph and photograph, respectively, demonstrating the resultant, unsupported material. The viewing angle in the micrograph in Figure 3.11b was positioned below the lifted-off polymer layer so both the individual holes where electrical contact was originally made through the photoresist as well as the resulting microwires on the surface could be visualized.

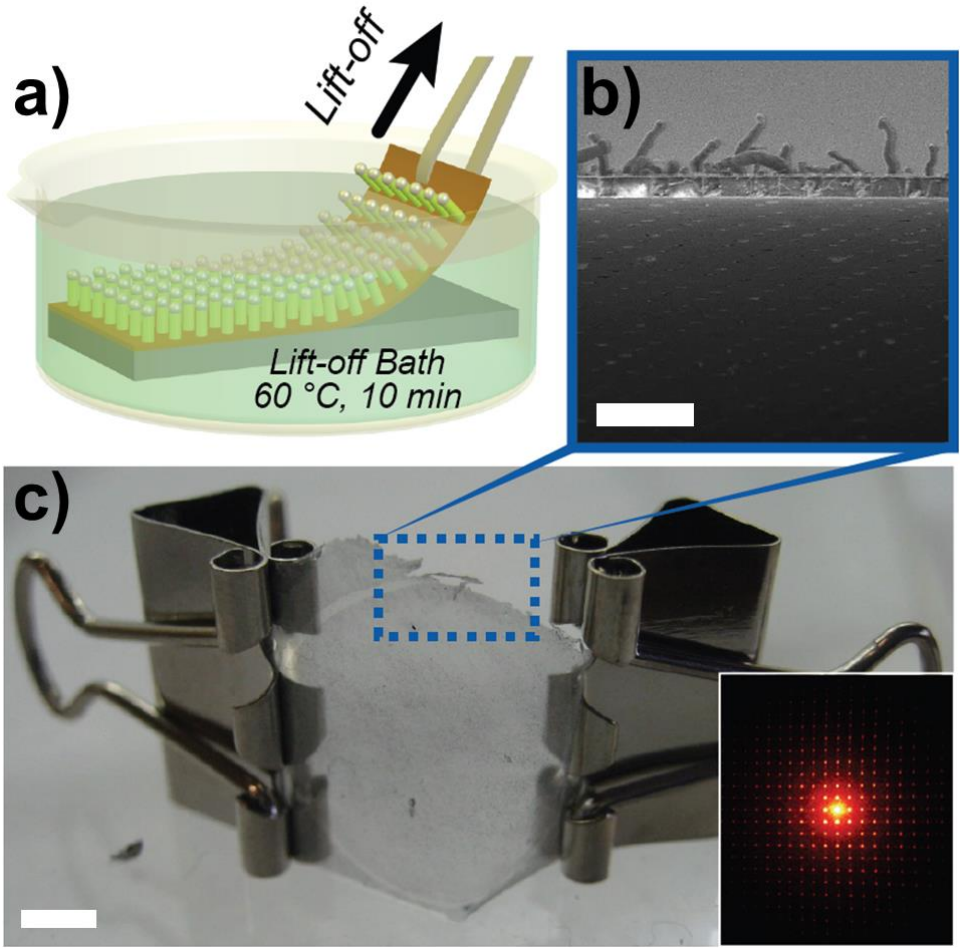

Figure 3.11. (a) Schematic of Ge microwire array lift-off procedure. (b) Cross-sectional scanning electron micrograph taken along the edge of the Ge microwire film highlighted in (c). Scale is 50 μm. (c) Free-standing Ge microwire array embedded in SU8 that is bent to show the flexibility. Scale is 1 cm. Inset is an optical diffraction pattern from a 632 nm HeNe laser through the Ge microwire array pictured in (c). Scale is 7 cm.

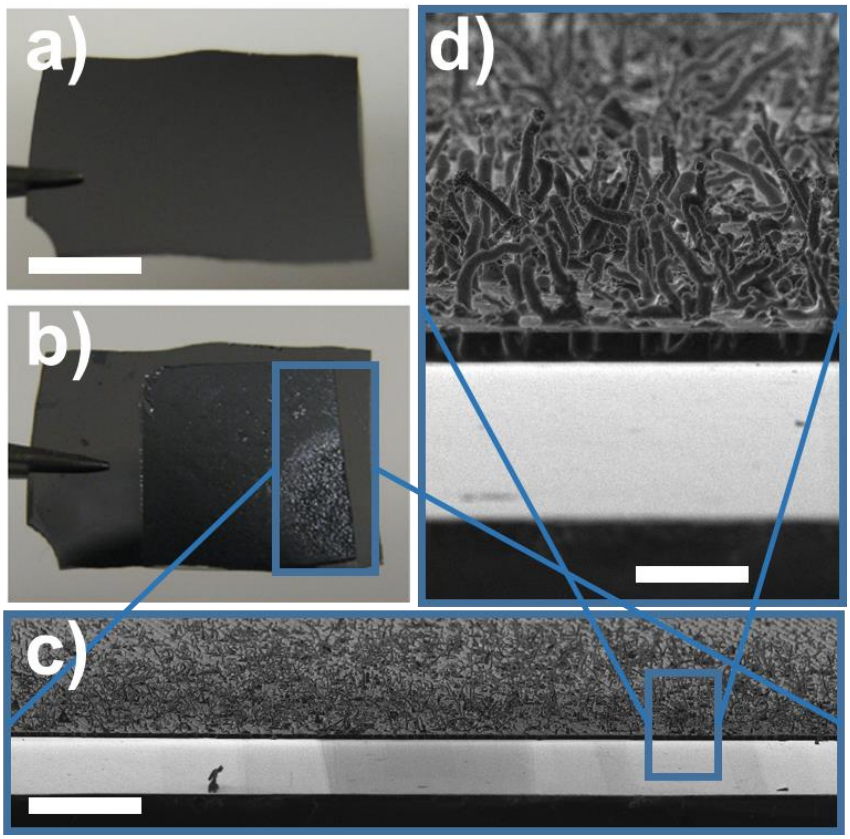

Figure 3.12. (a) Optical image of un-doped Si wafer before a) and after (b) transfer of a lifted-off Ge microwire array embedded in an SU8 film. Scale is 5 mm. (c) Corresponding scanning electron micrograph of the interface between the transferred array and the un-doped Si wafer. Scale is 0.1 mm. (d) Zoomed in area of (c). Scale is 40 μm.

The lift-off process did not change the net orientation of the microwires (i.e. oriented normal to the surface plane). Further, laser diffraction through the composite film (Figures 3.11c inset) showed a high degree of order (e.g. the 8th order of diffraction was easily observable) was retained in the free-standing composite material. Specifically, an average wire-to-wire distance of 10.1 ± 0.5 μm was estimated from the diffraction pattern, in good agreement with the 10 μm pitch of the original photolithography mask. Subsequent transfer of the free-standing Ge microwire/SU-8 polymer composite onto other substrates was also explored. Figures 3.12a and 3.12b show that the Ge microwire film could be float-transferred without wrinkling/folding onto a new flat substrate. The Ge microwires remained fully intact within the SU8 polymer layer and remained unperturbed by the lift-off conditions.

Ge ec-LLS in Arbitrary Patterned Shapes

Thus far, all Ge ec-LLS studies have focused on anisotropic growth of crystalline nanowire or microwire morphologies. To test the capacity of the ec-LLS technique for preparation of crystalline Ge thin films, a host of SU8 templates with various feature shapes and sizes were patterned via photolithography (Figure 3.13). The photoresist templates in Figure 3.13 were then filled with EGaIn by doctor blading and used for ec-LLS Ge crystal growth. The scanning electron micrographs in Figure 3.14 show four different free-standing Ge films with markedly different shape, size, and curvature following Ge ec-LLS for 30 min at 80 °C and subsequent removal of the original photoresist template. Close-up micrographs in Figure 3.15a show the as-deposited Ge films are comprised of heavily faceted grains in excess of 1 μm. The crystallinity of the film pictured in Figure 3.15a was further probed by powder X-ray diffraction. Figure 3.15b shows a series of incident angle-dependent diffraction patterns for the Ge film. At all incident angles, three intense and sharp reflections for diamond cubic Ge are observed at positions in accord with [111], [220], and [311] lines for crystalline, diamond cubic Ge.[31] The measured linewidths for each Ge reflection were too narrow to carry out Scherrer crystallite size analyses, indicating the crystalline domain size in the Ge films was in excess of 200 nm which is in accord with the microcrystalline domains observed by SEM (Figure 3.15a).[32] Comparison of peak area ratios of each *hkl* reflection with those of a standard pattern[31] indicated strong anisotropic

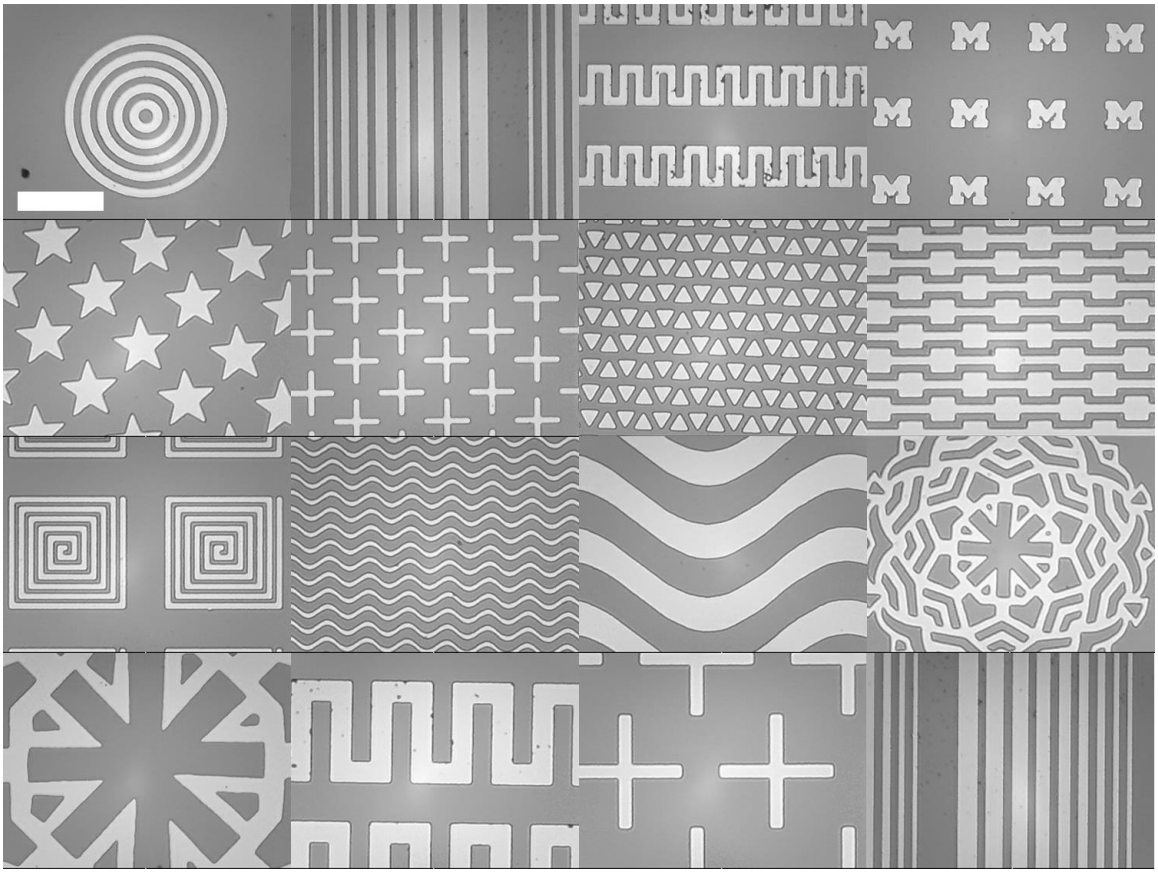

Figure 3.13. Plan-view optical micrographs of various photolithographic templates patterned in SU8 photoresist on n-Si(100) substrates for subsequent Ge ec-LLS growth. Scale is 0.25 mm.

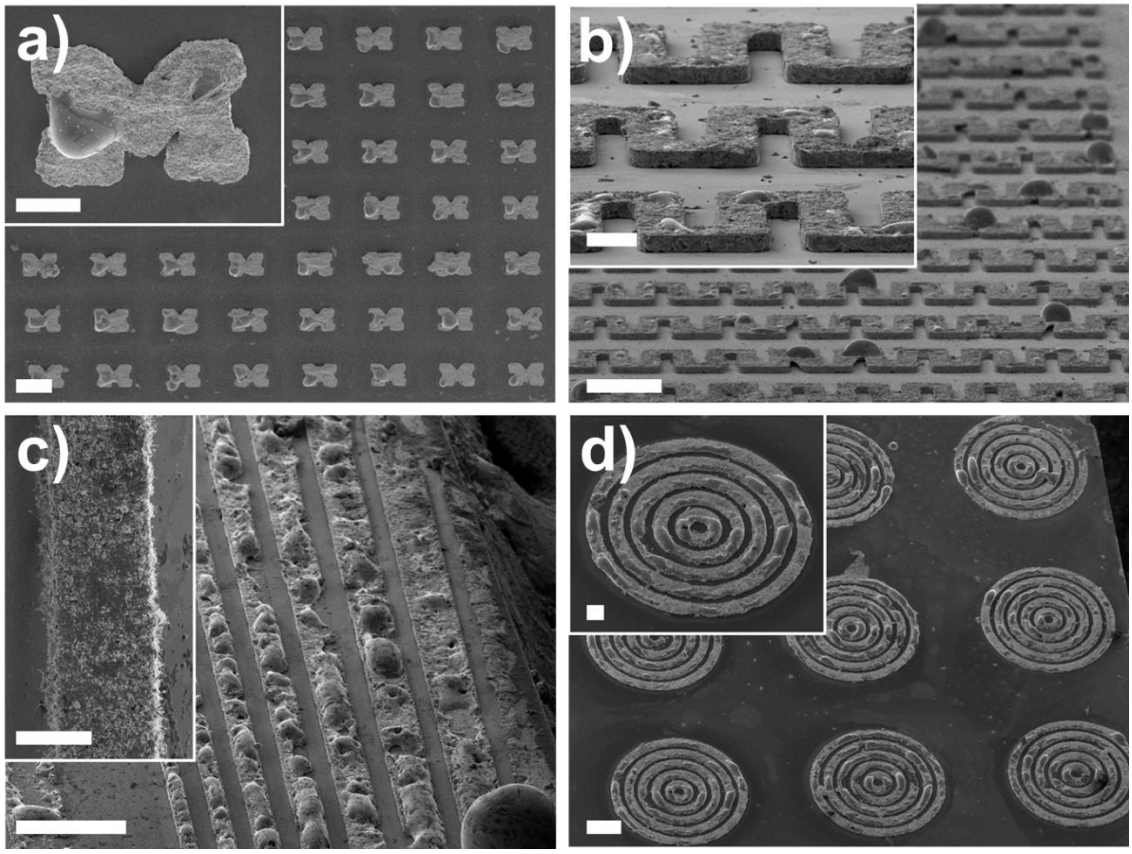

Figure 3.14. (a-d) Tilted cross-sectional scanning electron micrographs of various free-standing crystalline Ge films prepared by ec-LLS with EGaIn films patterned in photoresist templates. Scale is 100 μm. Inset scale is 25 μm.

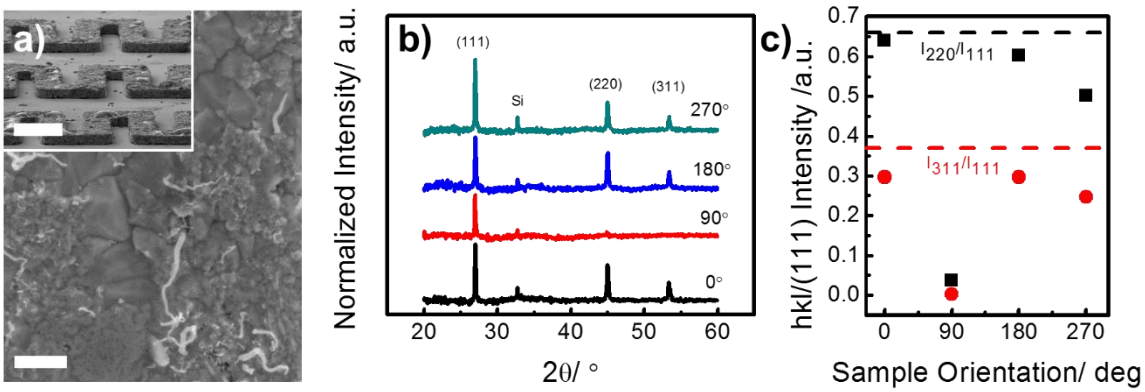

Figure 3.15. (a) Scanning electron micrograph of the close-up grain structure for the ec-LLS Ge film shown in the inset. Scale is 1 μm, inset is 50 μm. (b) Incident angle-dependent powder X-ray diffraction patterns collected from the Ge film shown in the inset of (a). (c) Plot of incident angle dependent diffraction intensity for (220) and (311) planes normalized to the respective (111) intensity from (b).

texturing of the crystalline films along the [111] direction. Further, the normalized diffraction intensities for the [220] and [311] planes (Figure 3.15c) reveal an angle dependence which is in accord with films under some crystallographic influence from the underlying growth substrate (i.e. epitaxy). For the films shown in Figure 3.14, the ec-LLS duration was chosen specifically to halt growth just before the Ge film reached the top of the photoresist template. Prolonged ec-LLS growth (t > 30 min) resulted in a distinct morphological transition from film-like Ge structures within the photoresist template, to microwire morphology once the film breached the surface plane of the template (Figure 3.16). This result is in accord with differences in liquid metal (i.e. EGaIn) wetting properties on the SU8 photoresist and the Ge film.

3.4. Discussion

The data presented here collectively support the main premise that Ge crystallites greater than one micrometer in size can be directly electrodeposited in water under mild temperatures by ec-LLS. More specifically, this work demonstrated several new concepts. *(1)* ec-LLS can be used to grow films of crystalline Ge microwires with high aspect ratios. *(2)* The structural and electrical properties of the resultant Ge microwires from ec-LLS are strongly impacted by the choice of liquid metal. *(3)* The ec-LLS tactic for crystalline semiconductor microwires is fully compatible with a wide array of substrate types. *(4)* A combination of conventional photolithography with doctor blading of liquid metal affords the ability to produce large-area arrays of uniform liquid metal microdroplet electrodes with control over their size and pitch. *(5)* A new lift-off protocol was developed here for SU-8 photoresist that allowed the preparation of free-standing flexible composites of Ge microwires embedded in a polymer membrane. This inorganic-organic composite could be seamlessly transferred to any arbitrary support, further widening the possible conductive substrates that can be accessed. *(6)* The liquid metal electrode patterning strategy can further be extended to non-spherical template shapes to effect free-standing microcrystalline Ge films of any geometry readily defined by photolithography.

As demonstrated here, ec-LLS with Ga-based liquid metals facilitates growth of crystalline Ge microwires at much lower temperatures than is typical for vapor phase deposition of analogous structures.[1,2,5]

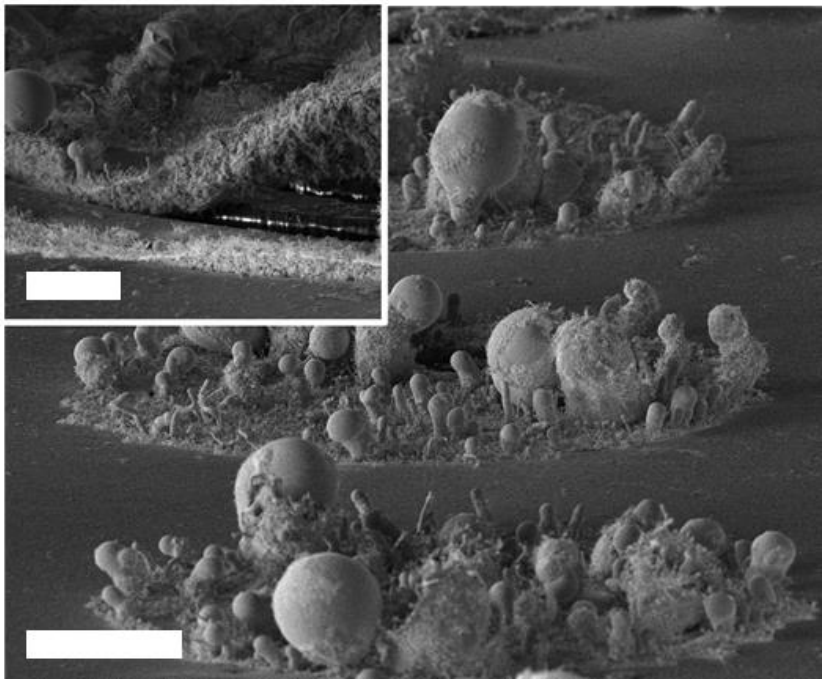

Figure 3.16. (a) Scanning electron micrograph of a Ge film prepared by ec-LLS from an EGaIn film constrained within a concentric circle SU8 template for 60 min at 80 °C. The inset shows a close-up of a portion of the Ge film delaminating from the substrate. Scale is 50 μm, inset is 30 μm.

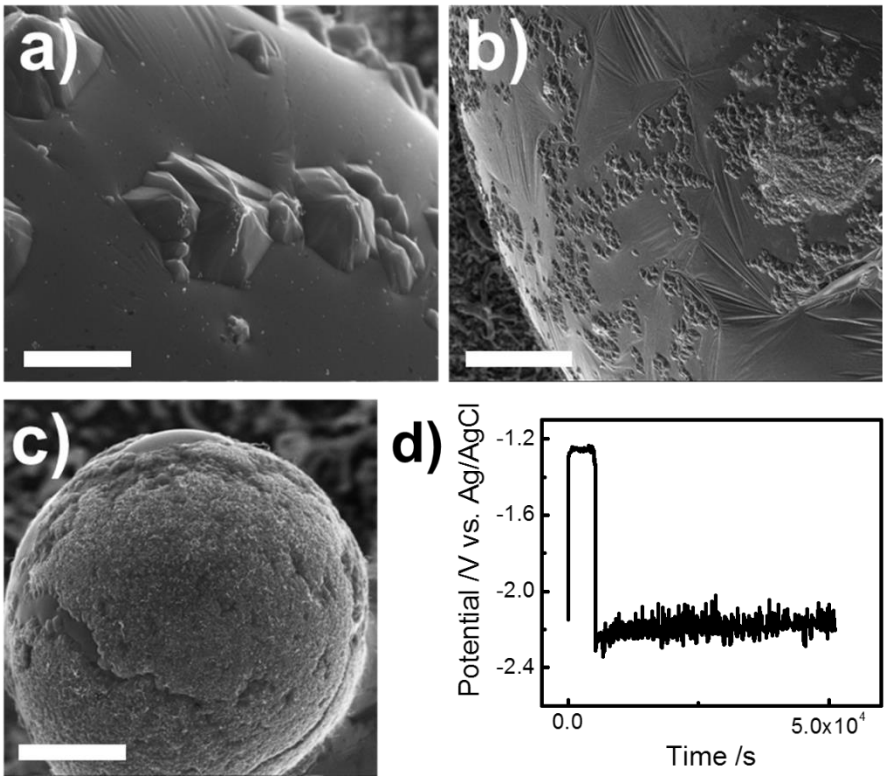

Figure 3.17. (a-c) Scanning electron micrographs of EGaIn droplets tips after ec-LLS growth of Ge microwires for 60 minutes at room temperature. Scales are 0.5, 1, and 5 µm, respectively. (d) Chronopotentiometry transient collected during galvanostatic ec-LLS of Ge microwires at i_{app} = 0.0001 A and 80 °C.

More specifically, in nano/microdroplet form, these liquid metals support heterogeneous nucleation of Ge crystals, i.e. crystal growth can initiate at the substrate/liquid metal interface rather than at/near the liquid metal/liquid electrolyte interface. The latter scenario has been consistently observed for ec-LLS processes using macro-scale liquid metal electrodes.[18,20,23] Therefore, a key conclusion from these new findings is that the size/volume of the liquid metals strongly dictates how crystal growth in ec-LLS begins. For at least Ga and EGaIn, when deleterious (with respect to microwire growth) homogeneous nucleation is sufficiently slow, heterogeneous nucleation and growth of microwires predominates. For example, for a given liquid metal microdroplet size, the initial rate of microwire growth was nominally invariant to the identity of the liquid metal (and support substrate). Moreover, when the microdroplet size was too large, no microwires were observed and only a polycrystalline film of Ge on the liquid metal surface was observed (Figures 3.17a-c). In that case, homogeneous nucleation in the bulk EGaIn dominated over heterogeneous crystal growth at the substrate/electrode interface resulting in a liquid metal surface passivated by Ge. This effect was apparent in the potential-time transient recorded during galvanostatic ec-LLS of Ge, where the measured potential decreased by over 1 V after the electrode surface was rendered inactive to ec-LLS due to surface passivation (Figure 3.17d). The probability of observing a microwire for each liquid metal droplet used in ec-LLS was temperature dependent. For comparatively large EGaIn microdroplets that yielded microwires at T = 80 °C, microwires were not obtained at room temperature (these droplets were instead covered by a polycrystalline Ge film on the surface). Thus, diffusional transport of newly electroreduced Ge to the substrate/liquid metal interface in the ec-LLS experiments appeared more influential in initiating and sustaining crystal growth than the identity of the support substrate. Since the respective densities (5.5 and 6.5 g cm^{-3}, respectively)[43] and viscosities (1.39 and 1.99 mPa·s, respectively)[44,45] of Ga and EGaIn are comparable, the diffusional transport properties of Ge within these liquid metals should be similar. Accordingly, both liquid metals were equally 'active' for nucleating Ge microwires by ec-LLS.

The identity of the liquid metal directly impacts the structural, morphological and electronic properties of the Ge microwires grown by ec-LLS, suggesting that the details of crystal growth following initial nucleation *are* sensitive to the chemistry of the liquid metal.

The preliminary findings shown here do not allow a microscopic understanding of the differences in ec-LLS crystal growth with Ga and EGaIn. Further dedicated study with these and other liquid metals is needed. Still, the observation that In was enriched at the EGaIn microdroplet surface suggests that the wetting properties and resulting surface tension between the liquid metal and Ge crystal are critical. In particular, the sticking coefficient of Ge on Ga seems to be decreased by the presence of In. Accordingly, other Ga alloys that further promote dewetting of the liquid metal from the crystal growth front of Ge in ec-LLS may yield Ge with different levels of crystallinity and purity. This notion is broadly in line with solute trapping models which predict the driving force for impurity inclusion in semiconductor crystal growth to be a strong function of the metal flux composition.[46,47] Work on this front is ongoing and will be reported elsewhere.

To this end, the development of the lithography/doctor blading technique is beneficial because patterning liquid metal droplets is challenging.[48,49] Aside from the initial approach used here to prepare discrete liquid metal microdroplets, other methods for obtaining highly uniform microdroplet arrays do not exist. Due to the refractory nature of Ga,[50] gallium cannot be easily sublimed[48,51,52] and simple electrodeposition is challenging[53-55] due to solubility and sensitivity to pH changes. Further, due to the marked differences in redox potential and sublimation conditions, both electroplating and vapor phase deposition lack the ability to controllably deposit metal alloys with compositional precision over large areas. Therefore, the refined approach developed here involving doctor blading into patterned polymer fills has tremendous value. Large area (> 1 cm^2) patterned hole arrays can be uniformly filled at room temperature on the benchtop in minutes. Since metal alloys for deposition are prepared gravimetrically, any liquid metal alloy can be patterned while preserving the intended stoichiometry. These factors make this approach invaluable for study of liquid metal alloys in ec-LLS.

The notion of covalent semiconductor crystal growth directly on malleable plastic supports is intriguing for various reasons but the primary novelty is that it is even possible through ec-LLS. Direct deposition of crystalline group IV semiconductors on a conductive polymer is wholly impossible through techniques such as chemical vapor deposition, molecular beam epitaxy, or solution-liquid-solid crystal growths. Further, the ability to transfer films of microwires prepared by ec-LLS to other substrates further extends the

complexity of architectures that can be realized without expensive or elaborate ancillary equipment. Although SU-8 was used here for the chemical lift off experiments, in principal other polymer photoresists materials could be used to impart additional functionality in composite inorganic-organic materials made in this way. Still, the development of a simple wet chemical lift-off procedure for SU-8 is by itself a noteworthy advancement that may appeal in general to the microfabrication communities.

The lithography/doctor blading technique in conjunction with Ge ec-LLS crystal growth is also shown to be applicable to virtually any patterned template accessible by photolithography (Figure 3.14). When the liquid metal is actively constrained within the sidewalls of the polymer photoresist template, the structure of the resultant ec-LLS Ge film is an exact replicate of the original template shape. However, as the Ge film thickness exceeds the thickness of the photoresist layer, the liquid metal 'film' dewets from the sidewalls of the photoresist leaving individual microdroplet electrodes that act as sites for Ge microwire growth, as shown in Figure 3.16. These results further support the notion that surface tension and wetting properties of the liquid metal interface are critical to deterministic control of crystal morphology by the ec-LLS strategy. The lithographic/doctor blading approach is a unique platform to probe surface and line tension forces in ec-LLS and how they relate to size and shape of the liquid metal electrode. Current fabrication restrictions limit the minimum feature size to a few micrometers, but combining the liquid metal doctor blading approach with templates prepared by nanoimprint or electron beam lithography could further extend ec-LLS to previously unexplored size regimes.

3.5. Conclusions

The cumulative data in this chapter show that ordered arrays of crystalline Ge microwires with diameters larger than 1 μm can be directly prepared in water via ec-LLS. A salient feature of this work is the use of a liquid metal patterning process that combines the utility of photolithography with the simplicity of doctor blading to produce macroscopic arrays of liquid metal microelectrodes with defined size and pitch. Subsequent use of the templated liquid metal electrodes as individual sites for ec-LLS yielded large arrays of Ge microwires with a high degree of uniformity and fidelity. This work demonstrates the proof of concept that both the patterning process and ec-LLS microwire

growth can be adapted simply to any conductive substrate with no change in the resultant material. The cumulative data also explicitly highlight the impacts of liquid metal electrode composition on the morphology and electrical properties of the resultant Ge microwires. These results serve as the basis for future studies aimed at controlling crystal nucleation and crystal growth in ec-LLS so as to produce the highest possible quality crystalline semiconductor materials.

3.6. References

1. McAlpine, M. C.; Ahmad, H.; Wang, D.; Heath, J. R. *Nat Mater* **2007**, *6*, 379.
2. Greene, L. E.; Law, M.; Goldberger, J.; Kim, F.; Johnson, J. C.; Zhang, Y.; Saykally, R. J.; Yang, P. *Angew. Chem., Int. Ed.* **2003**, *42*, 3031.
3. Kamins, T. I.; Li, X.; Williams, R. S.; Liu, X. *Nano Lett.* **2004**, *4*, 503.
4. Kim, B. H.; Kwon, J. W. *Sci. Rep.* **2014**, *4*, 4379.
5. Stauth, S. A.; Parviz, B. A. *Proc. Natl. Acad. Sci.* **2006**, *103*, 13922.
6. Noda, S.; Tomoda, K.; Yamamoto, N.; Chutinan, A. *Science* **2000**, *289*, 604.
7. Fuhrer, M. S.; Nygård, J.; Shih, L.; Forero, M.; Yoon, Y.-G.; Mazzoni, M. S. C.; Choi, H. J.; Ihm, J.; Louie, S. G.; Zettl, A.; McEuen, P. L. *Science* **2000**, *288*, 494.
8. Huang, Y.; Duan, X.; Cui, Y.; Lauhon, L. J.; Kim, K.-H.; Lieber, C. M. *Science* **2001**, *294*, 1313.
9. Eric , J. S.; John, C.; Gordon , S. W. C. *Jpn. J. Appl. Phys., Part 1* **2002**, *41*, 4366.
10. Shiu, S.-C.; Hung, S.-C.; Chao, J.-J.; Lin, C.-F. *Appl. Surf. Sci.* **2009**, *255*, 8566.
11. Logeeswaran, V. J.; Katzenmeyer, A. M.; Islam, M. S. *IEEE Trans. Electron Devices* **2010**, *57*, 1856.
12. Ahn, J.-H.; Kim, H.-S.; Lee, K. J.; Jeon, S.; Kang, S. J.; Sun, Y.; Nuzzo, R. G.; Rogers, J. A. *Science* **2006**, *314*, 1754.
13. Hochbaum, A. I.; Yang, P. *Chem. Rev.* **2010**, *110*, 527.
14. Pang, C.; Cui, H.; Yang, G.; Wang, C. *Nano Lett.* **2013**, *13*, 4708.
15. Weisse, J. M.; Lee, C. H.; Kim, D. R.; Zheng, X. *Nano Lett.* **2012**, *12*, 3339.
16. Wu, L.; Li, S.; He, W.; Teng, D.; Wang, K.; Ye, C. *Sci. Rep.* **2014**, *4*, 3940.
17. McAlpine, M. C.; Friedman, R. S.; Lieber, C. M. *P. IEEE* **2005**, *93*, 1357.
18. Carim, A. I.; Collins, S. M.; Foley, J. M.; Maldonado, S. *J. Am. Chem. Soc.* **2011**, *133*, 13292.
19. Fahrenkrug, E.; Gu, J.; Jeon, S.; Veneman, P. A.; Goldman, R. S.; Maldonado, S. *Nano Lett.* **2014**, *14*, 847.
20. Fahrenkrug, E.; Gu, J.; Maldonado, S. *J. Am. Chem. Soc.* **2013**, *135*, 330.
21. Fahrenkrug, E.; Gu, J.; Maldonado, S. *Chem. Mater.* **2014**, *26*, 4535.
22. Gu, J.; Collins, S. M.; Carim, A. I.; Hao, X.; Bartlett, B. M.; Maldonado, S. *Nano Lett.* **2012**, *12*, 4617.
23. Gu, J.; Fahrenkrug, E.; Maldonado, S. *J. Am. Chem. Soc.* **2013**, *135*, 1684.
24. Ma, L.; Gu, J.; Fahrenkrug, E.; Maldonado, S. *J. Electrochem. Soc.* **2014**, *161*, D3044.
25. Mahenderkar, N. K.; Liu, Y.-C.; Koza, J. A.; Switzer, J. A. *ACS Nano* **2014**, *8*, 9524.
26. Lahiri, A.; Olschewski, M.; Carstens, T.; El Abedin, S. Z.; Endres, F. *ChemElectroChem* **2015**, *2*, 571.
27. Joye, C. D.; Calame, J. P.; Garven, M.; Levush, B. *J. Micromech. Microeng.* **2010**, *20*, 1.
28. Thelen, J.; Dickey, M. D.; Ward, T. *Lab on a Chip* **2012**, *12*, 3961.
29. Williams, D. B.; Carter, C. B. *Transmission electron microscopy: a textbook for materials science*; Plenum Press: New York, 1996.
30. Bard, A. J.; Faulkner, L. R. *Electrochemical Methods*; 2nd ed.; John Wiley & Sons: UK, 2004.
31. Hom, T.; Kiszenik, W.; Post, B. *J. Appl. Crystallogr.* **1975**, *8*, 457.

32. Langford, J. I.; Wilson, A. J. C. *J. Appl. Crystallogr.* **1978**, *11*, 102.
33. Cuttriss, D. B. *Bell Syst. Tech. J.* **1961**, *40*, 509.
34. Olesinki, R. W.; Kanani, N.; Abbaschian, G. J. *Bull. Alloy Phase Diagr.* **1985**, *6*, 536.
35. Olesinski, R. W.; Abbaschian, G. J. *Bull. Alloy Phase Diagr.* **1985**, *6*, 258.
36. Carballo, V. M. B.; Melai, J.; Salm, C.; Schmitz, J. *Microelectron. Eng.* **2009**, *86*, 765.
37. Benjamin, R.; Véronique, B.; Jean-Baptiste, D.; Emmanuelle, D.; Thierry, C.; Maëlenn, A.; Alain, L.; Claire, T. *Japanese Journal of Applied Physics* **2014**, *53*, 08MC03.
38. Dentinger, P. M.; Clift, W. M.; Goods, S. H. *Microelectron. Eng.* **2002**, *61–62*, 993.
39. He, L.; Jiang, C.; Wang, H.; Lai, D.; Rusli *ACS Appl. Mater. Interfaces* **2012**, *4*, 1704.
40. McAlpine, M. C.; Friedman, R. S.; Jin, S.; Lin, K.-h.; Wang, W. U.; Lieber, C. M. *Nano Lett.* **2003**, *3*, 1531.
41. Rodrigo, M.-D.; Marc, J. M. In *Microfluidics and Nanofluidics Handbook*; CRC Press: 2011, p 231.
42. Bohl, B.; Steger, R.; Zengerle, R.; Koltay, P. *J. Micromech. Microeng.* **2005**, *15*, 1125.
43. Xu, Q.; Oudalov, N.; Guo, Q.; Jaeger, H. M.; Brown, E. *Phys. Fluids* **2012**, *24*, 063101.
44. Dickey, M. D.; Chiechi, R. C.; Larsen, R. J.; Weiss, E. A.; Weitz, D. A.; Whitesides, G. M. *Adv. Func. Mat.* **2008**, *18*, 1097.
45. Assael, M. J.; Armyra, I. J.; Brillo, J.; Stankus, S. V.; Wu, J.; Wakeham, W. A. *J. Phys. Chem. Ref. Data* **2012**, *41*.
46. Evans, P. V.; Vitta, S.; Hamerton, R. G.; Greer, A. L.; Turnbulls, D. *Acta Metall. Mater.* **1990**, *38*, 233.
47. Hurle, D. T. J. *Solid-State Electron.* **1961**, *3*, 37.
48. Guo, C.; Yu, Y.; Liu, J. *J. Mat. Chem. B* **2014**, *2*, 5739.
49. Dickey, M. D. *ACS Appl. Mater. Interfaces* **2014**, *6*, 18369.
50. Cochran, C. N.; Foster, L. M. *J. Electrochem. Soc.* **1962**, *109*, 144.
51. Meléndrez, M. F.; Cárdenas, G.; Arbiol, J. *J. Colloid Interface Sci.* **2010**, *346*, 279.
52. Vivekchand, S. R. C.; Engel, C. J.; Lubin, S. M.; Blaber, M. G.; Zhou, W.; Suh, J. Y.; Schatz, G. C.; Odom, T. W. *Nano Lett.* **2012**, *12*, 4324.
53. Kenny, S.; Dambrowsky, N.; Mann, O. In *Microsystems, Packaging, Assembly and Circuits Technology Conference (IMPACT), 2012 7th International* 2012, p 251.
54. Dow, W. P.; Huang, H. S. *J. Electrochem. Soc.* **2005**, *152*, C67.
55. Spiesshoefer, S.; Rahman, Z.; Vangara, G.; Polamreddy, S.; Burkett, S.; Schaper, L. *J. Vac. Sci. Technol. A* **2005**, *23*, 824.

CHAPTER 4

Electrodeposition of Crystalline GaAs on Liquid Gallium Electrodes in Aqueous Electrolytes

4.1. Introduction

Crystalline gallium arsenide (c-GaAs) possesses many desirable optoelectronic properties suited for solar energy conversion,[1] light and radiation detection,[2] chemical sensing,[3] lighting,[4] and high speed electronics.[5] One considerable challenge with GaAs technologies at scale is the existing methods for the preparation of c-GaAs(*s*) are energy-, time-, and resource-intensive.[6] For example, molecular beam epitaxy (MBE) and metal-organic chemical vapor deposition (MOCVD) require ultra-high vacuum (UHV) equipment, highly refined reagents such as arsine gas, and process temperatures in excess of 600 °C.[7,8] Similarly, liquid phase epitaxy (LPE) and the liquid encapsulated Czochralski (LEC) processes rely on temperatures in excess of 700 °C, require complex furnace designs to minimize loss of As(*g*) at elevated temperatures, and unavoidably result in crystals with high defect densities.[9-12] Accordingly, although single and multi-junction GaAs photovoltaics (PV) are the most efficient solar-to-electricity conversion devices to date,[13] GaAs-based PVs require energy payback times on the order of five years.[14] In this regard, simple, low temperature, and non-resource-intensive c-GaAs(*s*) preparation strategies are appealing.

Previous work in our group has shown that crystalline inorganic semiconductors can be prepared under bench-top conditions by an electrodeposition process in aqueous solutions without any physical or chemical templates. Specifically, liquid metals can be used simultaneously both as a conventional electrodes for electrodeposition and as solvents for crystalline semiconductor growth at room temperature.[15]

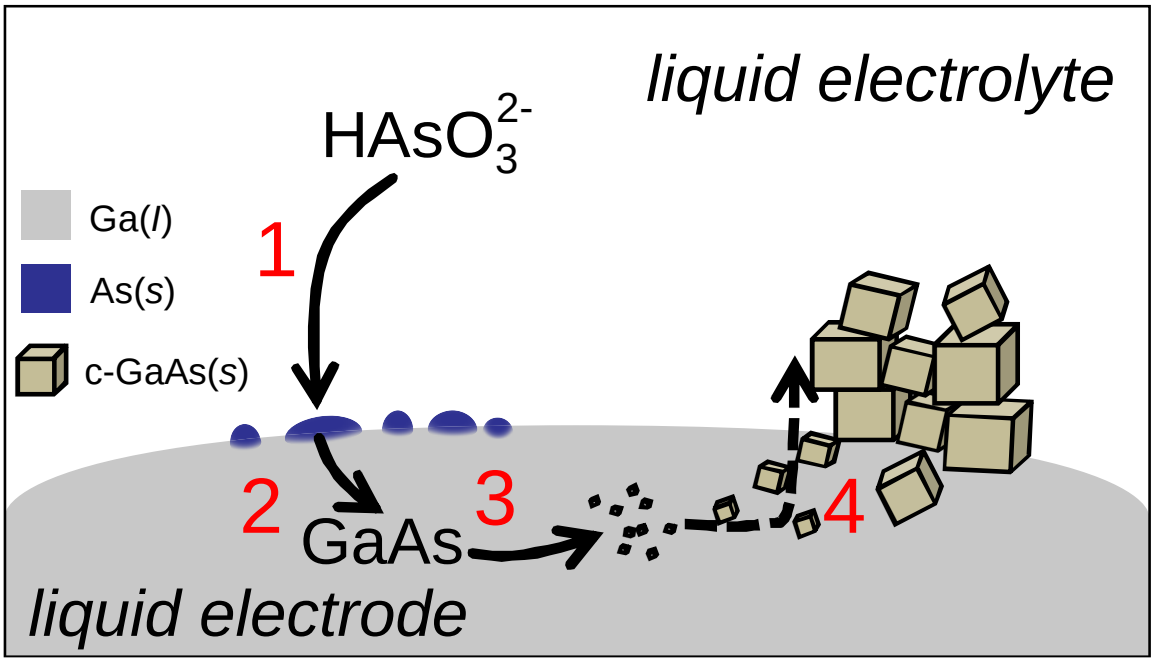

Figure 4.1. Schematic depiction of GaAs ec-LLS constituted by four principal steps. (*1*) Electroreduction of dissolved As_2O_3 to As(*s*) at the Ga(*l*) pool electrode surface. (*2*) Dissolution of As(*s*) into the Ga(*l*) pool and concurrent alloying to form an intermetallic GaAs phase. (*3*) Crystallite nucleation of dissolved GaAs. (*4*) GaAs crystal growth and phase separation from the bulk Ga(*l*) melt.

The advantage of this electrochemical liquid-liquid-solid (ec-LLS) process is the possibility to prepare directly a functional, crystalline semiconductor material without the need for heavily refined precursors, elaborate equipment, and high temperatures.

The hypothesis tested in this chapter is that c-GaAs(*s*) can be prepared simply via an embodiment of the ec-LLS process with a liquid gallium (Ga(*l*)) pool which serves simultaneously as an electrode, solvent, and as a co-reactant (Figure 4.1). In contrast to conflicting previous reports on the electrodeposition of GaAs,[16,17] we posit that c-GaAs(s) can be synthesized predictably through the electrodeposition of As from dissolved As_2O_3 specifically on a Ga(*l*) electrode at modest temperatures in water. A series of Raman, X-ray diffraction and electron microscopy data are shown that highlight the critical parameters associated with c-GaAs(*s*) formation. These data are discussed in the context of controlling the ec-LLS process and reconciling aspects of the earlier literature on GaAs electrodeposition from aqueous solutions.

4.2. Methods

Chemicals and Materials

Ga(*l*) (99.999%) and platinum (Pt) wire (99.9%) were obtained from Alfa Aesar. Prior to use, surface-based Ga oxides were mechanically removed via glass pipette tip. As_2O_3(*s*) powder (99.95%, Mallinkrodt), anhydrous Na_2SO_4 (99%, EMD), and NaOH (98%, Fisher) were used as received. H_2O that was obtained from a Barnstead Nanopure III purification system (>18 MΩ cm) was used for all solutions. Ar(*g*) (99.998%) was obtained from Detroit Metro Welding.

Electrodeposition and Electrochemical Measurements

CHI420A and CHI760C (CH Instruments) workstations were used for electrochemical experiments. All electrochemical data collected below 100 °C were acquired under open atmosphere in 100 mL Pyrex cells with a three electrode configuration featuring a 200 μL Ga(*l*) pool working electrode, a Pt flag (2 cm^2) counter electrode, and a Pt wire quasi-reference electrode. Due to electrocapillary effects, electrical contact to the working electrode was made through a small piece of platinum mesh/coil connected to a copper wire insulated by polytetrafluoroethylene (PTFE) that was pushed down through the center of the top of the Ga(*l*) pool. Electrodepositions performed at temperatures

exceeding 100 °C were carried out in a custom-built electrochemical reactor pressurized with Ar(*g*) to 27.5 bar to minimize solvent vaporization. The reactor was purged with a steady flow of Ar(*g*) for 10 minutes prior to heating with heat tape at a rate of 1 °C min^{-1}. The anodic wave featured at -1.375 V vs. Ag/AgCl in voltammetry collected at 30 °C was used to correct all quasi-referenced potentials to the Ag/AgCl couple. All electrochemical data are plotted with posit4e currents indicating net reduction processes and negative currents corresponding to net oxidation processes.

Fabrication and Assembly of a Pressurized Electrochemical Cell

The custom pressurized electrochemical reaction vessel was composed of a stainless steel jacketed exterior with isolated electrical, gas and thermocouple feedthroughs (Figure 4.2). [Appendix A.5] Reactor bodies, caps and compression rings were machined from 304 grade stainless steel round stock (McMaster-Carr) and assembled in-house. PTFE round stock (McMaster-Carr) was used to fabricate gaskets for the static pressure seal. Electrical connections were made through a hermetically sealed 4-pin feedthrough (Pascal Technologies) that was vacuum welded through the reactor cap. Each isolated stainless steel pin was attached directly to individual electrodes through a section of PTFE heat-shrink tubing (McMaster-Carr). A 24" x 0.5" section of heat tape (Amptek) was used to supply and control heat input. Internal cell temperature was monitored with a K-type stainless steel thermocouple probe (Omega Engineering).

Materials Characterization

Raman spectra were obtained using a Renishaw RM Series Raman microscope equipped with a Nikon LU Plan 20x objective (*NA* = 0.4) and edge filters to reject the 785 nm excitation line. The excitation source and CCD detector (578 x 400) were positioned in a 180° backscatter geometry. No polarizing collection optics were used for spectral acquisition. A 785 nm diode laser was used as the incident excitation at a total radiant power of 1.12 mW over a 20 μm^2 spot to minimize local heating of the sample. In a typical spectral collection, the collected signal was integrated for 30 seconds and spectra were scan-averaged over five repetitions. Reported Raman data are representative of a collection of spectra acquired over at least ten spots covering the surface of each measured sample.

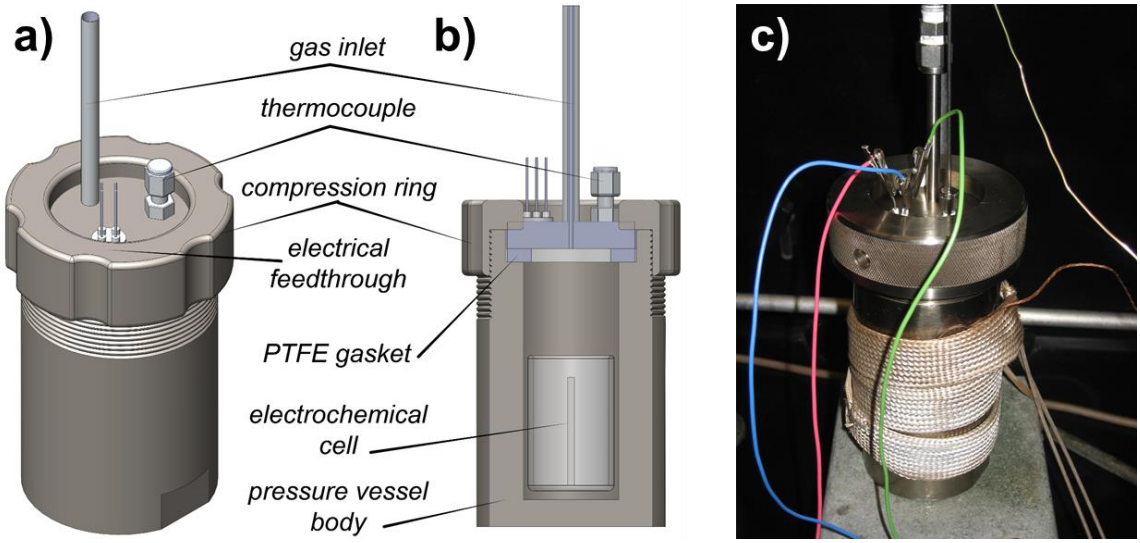

Figure 4.2. (a) Isometric model, (b) Cross-sectional model and (c) photograph of the pressurized electrochemical vessel designed and fabricated for ec-LLS at elevated temperatures in aqueous and non-aqueous solutions. The system is capable of conducting electrodepositions up to 250 °C and 200 bar.

Time-dependent *in-situ* Raman spectra were collected in a custom PTFE cell that can accommodate horizontally positioned electrodes designed to fit within the working distance of the objective. Single 10 second spectral acquisitions were sequentially acquired with a 0.8 second delay between collections.

Powder X-ray diffractograms were obtained using a Bruker D8 Advance X-ray diffractometer with a Cu Kα X-ray source (λ = 1.5406 Å). A 2.0 mm slit width was employed with a sampling rate of 20 data points/degree 2θ at 1 s point^{-1}. For XRD heating experiments, as-deposited samples were placed on a standard glass slide which sat on top of a copper heating element embedded in a ceramic heating block. The temperature was controlled via PID feedback with a custom temperature controller (Omega Engineering). Temperature-dependent diffractograms were collected after annealing for 15 minutes at each temperature point.

High-resolution transmission electron microscopy (HRTEM) and selected area electron diffraction (SAED) were conducted with a JEOL 3011 TEM equipped with a LaB_6 electron source operating at 300 kV. Samples were prepared by first freezing the Ga(*l*) electrode immediately after electrodeposition, followed by gently mechanically removing the electrodeposited film with a razor blade, then washing the collected material in a plastic vial with CH_3OH(*l*) (190 proof, ACS spectrophotometric grade, Aldrich), followed by centrifugation for 60 s at 9G, then decanting all but 1 mL of the ethanol supernatant, then re-suspending the particulates by sonication for 60 s, and finally drop-casting 3 µL onto a 400 mesh copper TEM grid coated with an ultra-thin carbon support (Ted Pella).

Scanning electron microscopy (SEM) was performed with a Philips XL30 SEM equipped with a Schottky field emission gun (FEG) operated at 15 kV. Cross-sections of the as-deposited GaAs film on top of a Ga(*l*) electrode were prepared by freezing the Ga(*l*) electrode which induced natural fractures in the GaAs film. After the Ga(*s*) was placed on a clean Si substrate, the electrode/film was thawed and the bulk Ga(*l*) was removed via pipet leaving a cracked thin film on the Si substrate. ImageJ software was used to assess the film thickness from scanning electron cross-sectional micrographs. Delineation between the deposited GaAs film and the Ga(*l*) electrode substrate was established by energy dispersive spectroscopy (EDS) of the film/electrode interface. An average thickness value was reported after measuring ten points along the film/electrode interface.

Inductively coupled plasma atomic emission spectroscopy (ICP-AES) elemental analysis for As was obtained using a Perkin-Elmer Optima 2000DV instrument. Samples were prepared by dissolving the as-deposited GaAs film and the Ga(*l*) electrode in 12 mL of aqua regia (3:1 37%(*aq*) hydrochloric acid and 68–70%(*aq*) nitric acid, Fisher Scientific) for 24 hours at room temperature. Samples and standards were fortified with 1 ppm yttrium (Y) internal standard which was used to correct measured As intensities for matrix and sampling differences among samples. Samples were measured directly using emission lines at 371.029 and 228.812 nm for Y and As, respectively. A linear calibration curve (R = 0.9998) was constructed over the As concentration range of 0 - 10 mg L^{-1}.

Photocurrent Measurements

The electrodeposited GaAs film was prepared at 90 °C at E = -1.58 V onto a Ga(*l*) electrode immersed in 1 mM As_2O_3 solution for two hours. As-deposited films were subject to immediate photoelectrochemical analyses conducted under white light illumination using a tungsten halogen lamp light source (ELH, Osram) equipped with a quartz diffuser. The illumination power density measured by a thermopile (S302A, Thorlabs) was 200 W cm^{-2} with the film positioned 10 cm from the lamp source. A glass cell, a Pt mesh counter electrode and a Ag/AgCl reference electrode were used to collect photoelectrochemical data with a digital potentiostat (PGSTAT302N, Metrohm Autolab). An aqueous 1 M KCl (99%, Sigma) solution was used as the electrolyte.

Peak Fitting and Modeling

Raman spectra were fit in Origin 8.0 using >500 fit iterations with a 1 x 10^{-15} tolerance using a maximum of three peaks corresponding to the transverse and longitudinal optical phonon modes (TO and LO, respectively) and the overtone of the LO mode (2LO). As noted in previous reports,[18-21] the empirical line shape of the LO mode observed in nanocrystalline GaAs exhibits an asymmetric character, therefore this mode was best fit with an asymmetric double sigmoidal function. The line shape of both the TO and 2LO modes were best fit with a Voigt function. The full width at half maximum of the TO mode was constrained to 15 cm^{-1} for all fits.

The phonon confinement (PC) model[20] has been previously used to interpret optical phonon frequency shifts and peak broadening with the effective crystallite size of the GaAs.

In this work, estimates from the PC model were used to assess the measured spectral features of the LO mode from electrodeposited c-GaAs. In the PC model, the lineshape of the LO phonon mode is given by,[20]

$$I(\omega) \cong \int_0^1 \frac{\left|C(0,q)\right|^2 d^3q}{(\omega - \omega(q))^2 + (\Gamma_0/2)^2} \tag{4.1}$$

where vector $\boldsymbol{q}$ is in the units of $2\pi/a$, a is the lattice constant of GaAs (5.653 Å),[22] $d^3\boldsymbol{q}$ is the volume element in spherical coordinates, and Γ_0 = 3 cm^{-1} is the natural line width for the LO phonon of GaAs.[21] For an isotropic microcrystal, the phonon confinement can be described by a Gaussian weighting function that yields Fourier coefficients,[18]

$$\left|C(0,q)\right|^2 = e^{-q^2L^2/4a^2} \tag{4.2}$$

where L is the phonon confinement length. The phonon dispersion curve for GaAs is given by Equation 4.3,[21]

$$\omega(q) = A + B\cos(\pi q) \tag{4.3}$$

where A and B (269.5 cm^{-1} and 22.5 cm^{-1}, respectively) are fitting constants specific to GaAs.

4.3. Results

Figure 4.3 illustrates the current-potential characteristics for Ga(l) electrodes in an aqueous solution containing 1 mM As_2O_3, 100 mM NaOH and 100 mM Na_2SO_4. In the absence of dissolved As_2O_3 (Figure 4.3a), the multi-electron oxidation of bulk Ga(l) was observable at potentials more positive than -1.15 V vs. Ag/AgCl .[23] During scans to potentials more *negative* than the open circuit rest potential, a separate and 'inverted' voltammetric wave (i.e. the current sign implied a net oxidative process during a cathodic sweep) near -1.375 V vs. Ag/AgCl was noted. Analogous 'inverted' voltammetric waves have been noted previously with metal electrodes that exhibit transpassivity.[23,24] Extended (10 min) potential step experiments with a Ga(l) electrode biased at the peak potential of the inverted voltammetric wave showed a sustained, oxidative process (Figure 4.4a), arguing against a contaminant dissolved in the electrolyte as the source of this redox process.

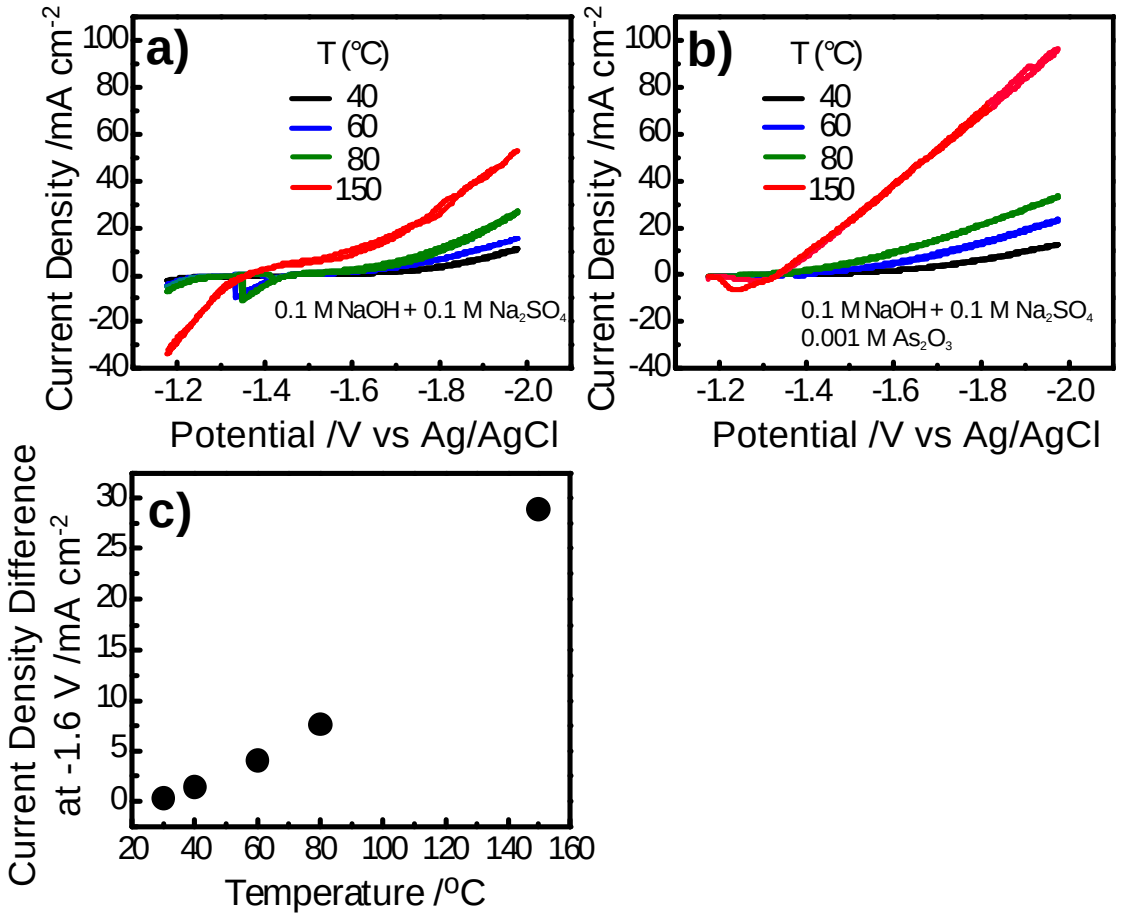

Figure 4.3. Temperature-dependent cyclic voltammetric responses collected at a Ga(*l*) pool electrode immersed in an aqueous solution containing a) 0.1 M NaOH and 0.1 M Na_2SO_4 and b) 0.1 M NaOH, 0.1 M Na_2SO_4, and 0.001 M As_2O_3. Scan rate: 0.01 V s^{-1}. c) Difference in measured current density with and without a formal concentration of 0.001 M As_2O_3 in the electrolyte at an applied potential of -1.6 V vs. Ag/AgCl as a function of temperature.

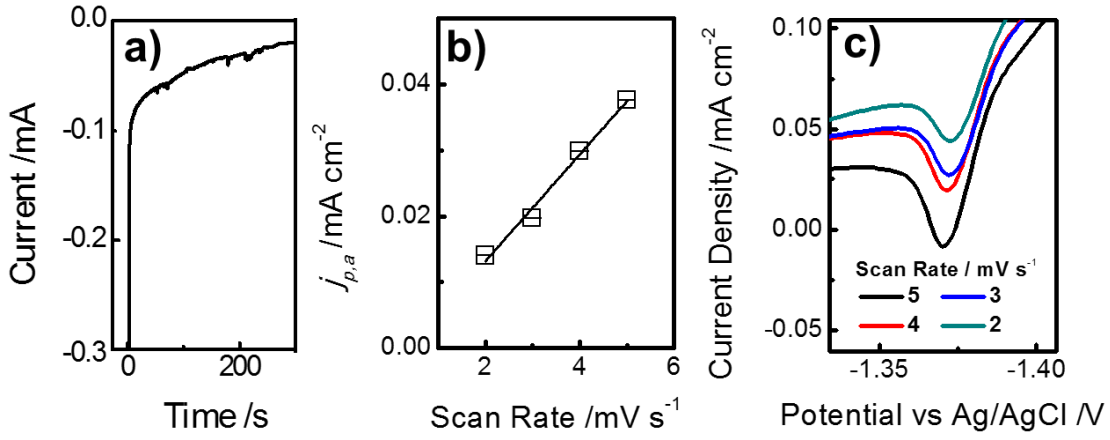

Figure 4.4. (a) Current-time transient for potential step measurement where the potential was held at -1.375 V vs Ag/AgCl, the peak position of the inverted voltammetric wave at 30 °C. The measurement was conducted at a Ga(*l*) electrode immersed in an unstirred solution of 0.1 M NaOH and 0.1 M Na_2SO_4. (b) Linear scan rate dependence of peak anodic current for the 'inverted' voltammetric wave. (c) Raw voltammetry data for the wave at a variety of scan rates in an aqueous solution of 0.1 M NaOH and 0.1 M Na_2SO_4.

The linear dependence of the peak current with scan rate (Figures 4.4b-c) was consistent with behavior expected from a redox process at the Ga(*l*) surface. All electrodepositions were performed at potentials more negative than the peak potential for this 'inverted' wave ensuring an oxide-free Ga(*l*) surface.

Figure 4.3 describes the observed voltammetry for a Ga(*l*) electrode immersed in a solution containing dissolved As_2O_3. At pH=13, the predominant species in solution was $HAsO_3^{2-}$.[25] At low formal concentrations of As_2O_3, the voltammetric response for sweeps to more negative potentials lacked a well-defined peak. At high (≥50 mM) formal concentrations of As_2O_3, the voltammetric response looked similar but also included a small cathodic wave with a peak at –1.4 V vs. Ag/AgCl (Figure 4.5). The absence of a clear reductive wave indicated an electroreduction at Ga(*l*) electrodes limited by a kinetic process rather than mass-transport.[26] A similar observation has been made previously for As^{3+} reduction in alkaline solutions at both solid and liquid metal electrodes.[27-29] As a result and as indicated in Figure 4.3a, the difference between current for film formation and $H_2(g)$ evolution was slight at room temperature at low overpotentials. However, at potentials more negative than -1.5 V vs. Ag/AgCl, the difference between the current measured with and without dissolved As_2O_3 increased. Figure 4.3c illustrates the competition between the two processes at a given potential was a strong function of temperature, with an apparent increase in inferred Faradaic efficiency for reduction of dissolved As_2O_3 at higher temperatures.

Chronoamperometric experiments were performed to effect formation of c-GaAs(*s*) through As electrodeposition onto Ga(*l*). To monitor the nature of the deposit, Raman spectra were obtained at the Ga(*l*)/electrolyte interface during electrodeposition. The first order Raman spectrum for bulk crystalline GaAs shows two optical phonon modes (TO at 266 and LO at 292 cm^{-1})[30] that are distinguishable from the primary signatures for amorphous GaAs (150-250 cm^{-1}),[31,32] crystalline As_2O_3 (379, 417, 428, 458, 576, 644, and 750 cm^{-1}),[33,34] amorphous As_2O_3 (450-470 cm^{-1}),[33,34] crystalline As(*s*) (198 and 257 cm^{-1}),[35-37] and amorphous As(*s*) (115, 145, 200, 235, 283 and 340 cm^{-1}).[38-40] Figure 4.6a shows time-dependent Raman spectra for a potential step experiment conducted at room

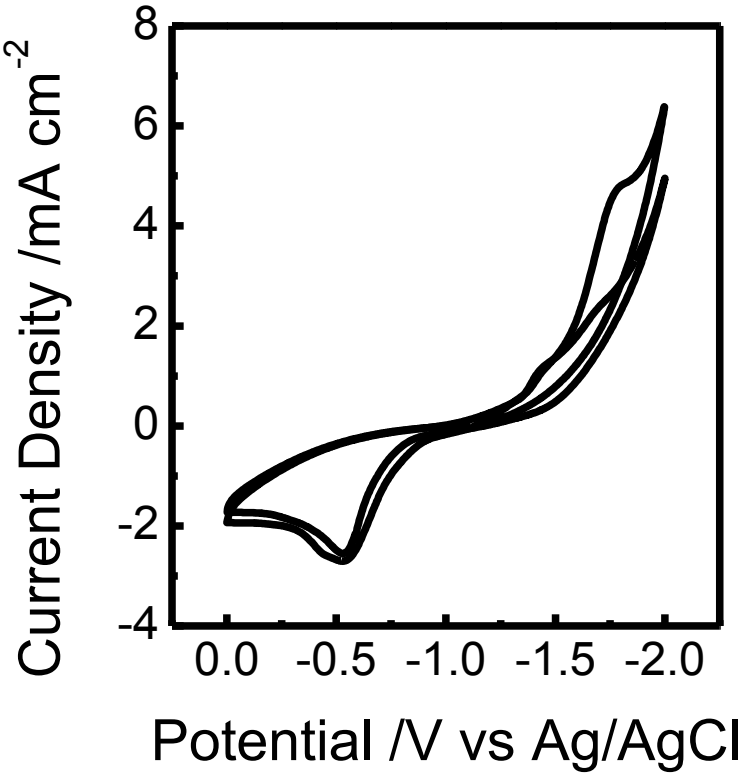

Figure 4.5. Cyclic voltammetry for a Ga(*l*) electrode submerged in an aqueous solution containing 0.05 M As_2O_3, 0.1 M NaOH, and 0.1 M Na_2SO_4. Voltammetry was collected at 30 °C at a scan rate of 25 mVs^{-1}.

temperature with 40 mM As_2O_3 and an applied bias of -1.0 V vs. Ag/AgCl. Several signatures were evident after 76 s. Under these electrodeposition conditions, the observed signatures were inconsistent with either crystalline or amorphous GaAs, crystalline or amorphous As_2O_3, and crystalline As(*s*).[31-40] Instead, the spectral features were uniformly in accord with amorphous As(*s*).[38-40] The sharpness of the Raman mode at 200 cm^{-1}, as well the presence of the less intense modes at 115, 145, 283, and 340 cm^{-1}, matched separate reports of amorphous As(*s*) films with some long range order (as compared to purely amorphous As(*s*) films prepared through sputter deposition).[38,39] The intensity of these modes continued to increase monotonically before reaching a maximum after 130 s, consistent with an electrodeposition process that ultimately attains a thickness greater than the Raman probe depth. Similar Raman spectra were collected for As(*s*) electrodeposition on solid copper electrodes from identical electrolyte solutions (Figure 4.6b). Raman modes for c-GaAs were never observed during or following potential step experiments conducted with Ga(*l*) electrodes in solutions of 40 mM As_2O_3 at room temperature.

Subsequent thermal annealing of electrodeposited amorphous As(*s*) films on Ga(*l*) was performed to elucidate the critical temperature for thermal alloying and metallurgical formation of c-GaAs. Figure 4.7a summarizes a set of X-ray diffractograms collected after holding a single sample for 15 min at several temperatures. Reflections at 43.5 and 50.4° in the diffractograms corresponded to the copper heating element positioned beneath the films and reflections at 25.6 and 29.5 ° in the diffractograms corresponded to the ceramic heating block. X-ray diffraction data collected immediately after electrodeposition without any annealing indicated the film on the Ga(*l*) electrode possessed no crystallinity, in accord with the collected Raman spectra. Samples heated between 20 and 150 °C similarly showed no evidence of crystalline character for As(*s*), GaAs(*s*), or As_2O_3(*s*). Reflections consistent with only zincblende c-GaAs(*s*) were apparent in diffractograms collected at 200 °C and above. Analogous annealing experiments analyzed with Raman yielded a similarly high critical annealing temperature (Figure 4.7b). This threshold temperature observed here is in accord with previous reports on purposely annealing co-electrodeposited As and Ga films to induce a metallurgical alloying to produce c-GaAs.[17,41-44]

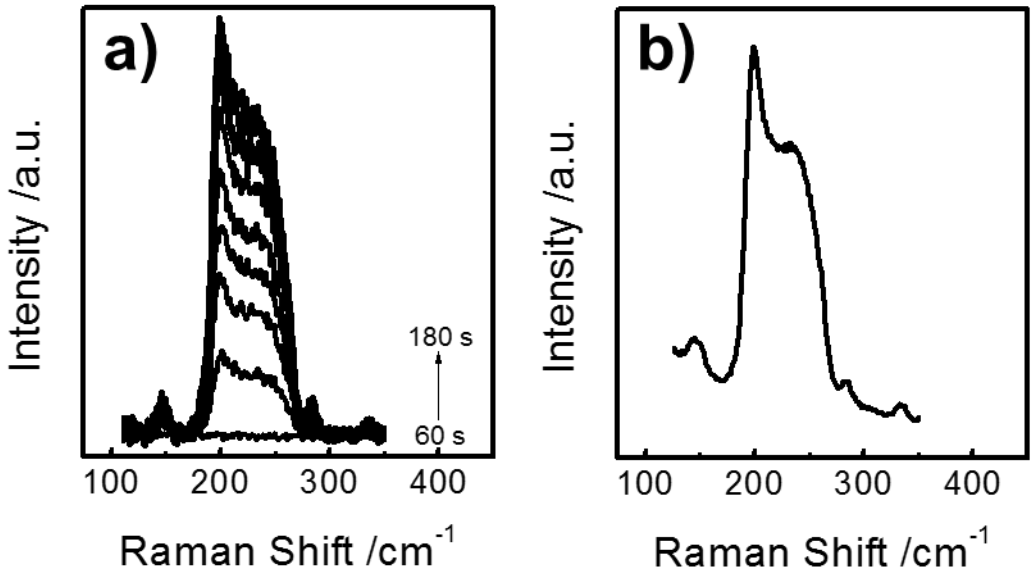

Figure 4.6. (a) Time-dependent Raman spectra collected every 10.8 s at Ga(*l*) pool electrodes immersed in an aqueous solution containing 0.1 M NaOH, 0.1 M Na_2SO_4, and 0.04 M As_2O_3 and polarized at -1.0 V vs. Ag/AgCl. Spectra acquired in first 60 s had no Raman features and are not shown. Spectra not intentionally offset. (b) Raman spectrum collected from As(*s*) films deposited at Cu(*s*) flag electrode from a 0.05 M As_2O_3 solution containing 0.1 M NaOH and 0.1 M Na_2SO_4 at 40 °C.

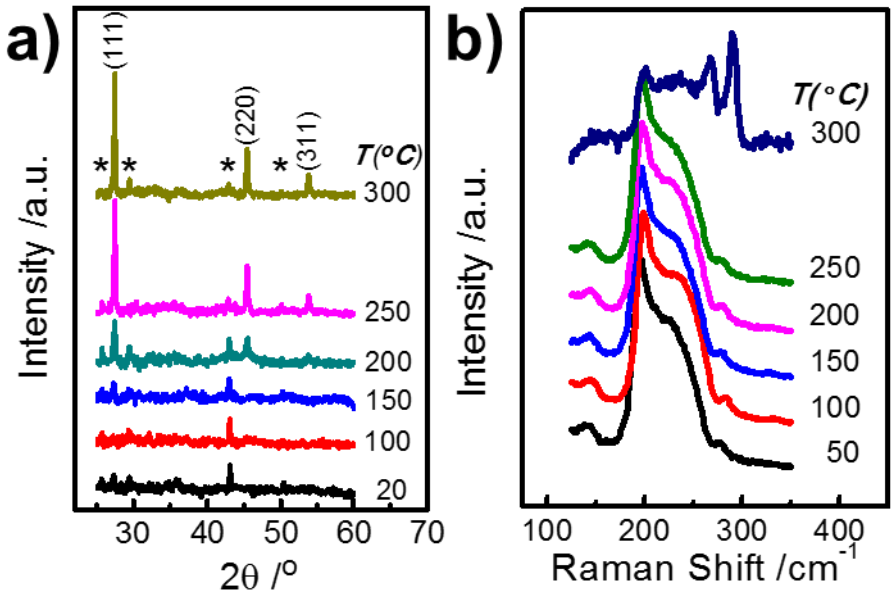

Figure 4.7. (a) Powder X-ray diffractograms obtained during annealing of an electrodeposited As(*s*) film on a Ga(*l*) pool electrode prepared from an aqueous solution containing 0.1 M NaOH, 0.1 M Na_2SO_4, and 0.01 mM As_2O_3 at 40 °C. Indexed peaks correspond to zincblende GaAs. Peaks denoted with '*' correspond to the copper heating element. Diffractograms are offset for clarity. (b) Raman spectra obtained during annealing of a thin As(*s*) film after a prior electrodeposition on a Ga(*l*) cathode from a 0.05 M As_2O_3 solution at 40 °C for two hours. As-prepared films were heated for 15 minutes before collecting the spectrum at each temperature.

Based on the data in Figures 4.2-4.6, additional electrodeposition experiments were performed at elevated temperatures to determine whether electroreduction of dissolved As_2O_3 could directly affect c-GaAs(*s*). A custom pressurized electrochemical vessel was utilized for electrodeposition at temperatures exceeding the boiling point of water (Figure 4.2, Appendix A.5). Figure 4.8 contains Raman spectra collected both for electrodeposition experiments held at a constant applied bias and for electrodeposition experiments held at a constant temperature with a Ga(*l*) electrode immersed in alkaline solution containing a formal concentration of 10 mM As_2O_3. Figure 4.8a presents Raman spectra collected after electrodeposition at several applied potentials and at a constant temperature of 90 °C. These spectra showed features indicative of only amorphous As(*s*). At applied potentials more negative than -1.68 V vs. Ag/AgCl the evolution of $H_2(g)$ was substantial and mechanically perturbed the as-electrodeposited film. Raman signatures for amorphous As(*s*) were also observed at this temperature with the Ga(*l*) electrode at the open-circuit rest potential (i.e. in the absence of an applied bias), although the observable film quantity was minimal even after long times ($t \geq 120$ min). The inset in Figure 4.8b shows an optical image of the amorphous As(*s*) film on a Ga(*l*) electrode just after electrodeposition. This characteristic dull black was consistent throughout an electrodeposition (i.e. thin or thick film), transitioning only from pale to progressively more opaque. Figure 4.8b shows Raman spectra collected for electrodeposited films prepared at various temperature at a constant bias of -1.58V vs. Ag/AgCl. Over the entire temperature range of 40-150 °C, the Raman spectra indicated only amorphous As(*s*) after electrodeposition for two hours. These collective experiments indicated the primary product of electroreduction of dissolved As_2O_3 at high concentrations (10 mM) and elevated temperatures at Ga(*l*) electrodes was amorphous As(*s*).

To effectively limit the overall rate and amount of As electrodeposited onto the surface of Ga(*l*), separate electrodeposition experiments were performed with more dilute concentrations of dissolved As_2O_3. Figure 4.9 illustrates a time-lapse sequence of optical images of a Ga(*l*) pool electrode housed in a glass bowl throughout a two hour electrodeposition with an alkaline solution containing a formal concentration of only 1 mM As_2O_3 at 90 °C at an applied bias of -1.58 V vs. Ag/AgCl. Unlike the dark film featured in the inset of Figure 4.8b, the hue of the electrodeposited film on Ga(*l*) in this experiment

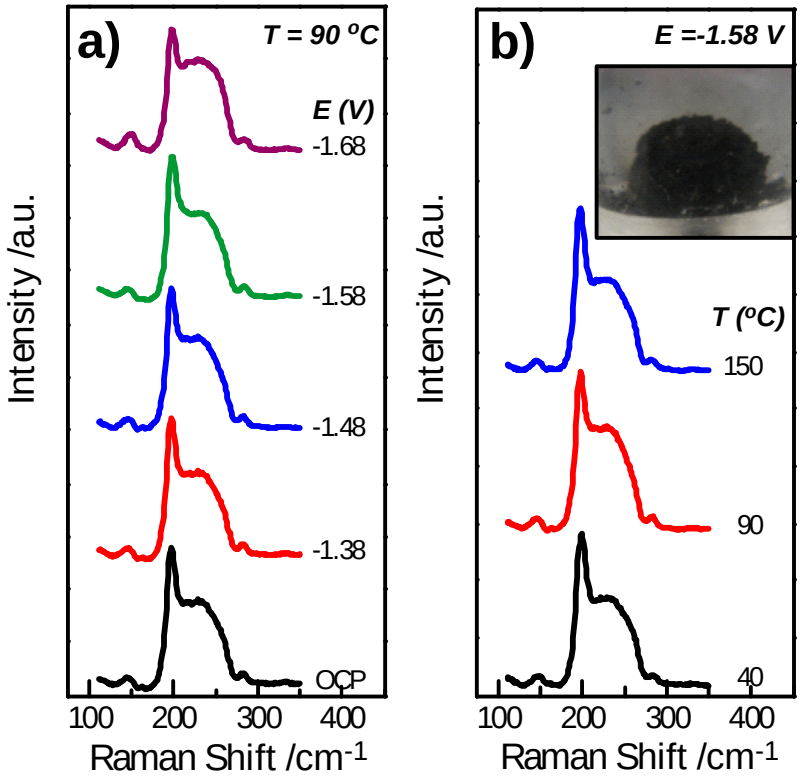

Figure 4.8. (a) Raman spectra for films deposited at Ga(*l*) pool electrodes immersed in an aqueous solution containing 0.1 M NaOH, 0.1 M Na_2SO_4, and 0.01 M As_2O_3 at 90 °C for two hours at several different applied biases. For this set of experiments, the open circuit rest potential (OCP) was -1.20 V vs Ag/AgCl. Inset: Optical photograph highlighting appearance of electrodeposited film at 90 °C at an applied potential of –1.58 V vs Ag/AgCl for 2 hours. (b) Raman spectra for films deposited at Ga(*l*) pool electrodes immersed in an aqueous solution containing 0.1 M NaOH, 0.1 M Na_2SO_4, and 0.01 M As_2O_3 at an applied bias of -1.58 V vs. Ag/AgCl for two hours at several different electrodeposition temperatures. Spectra are offset for clarity.

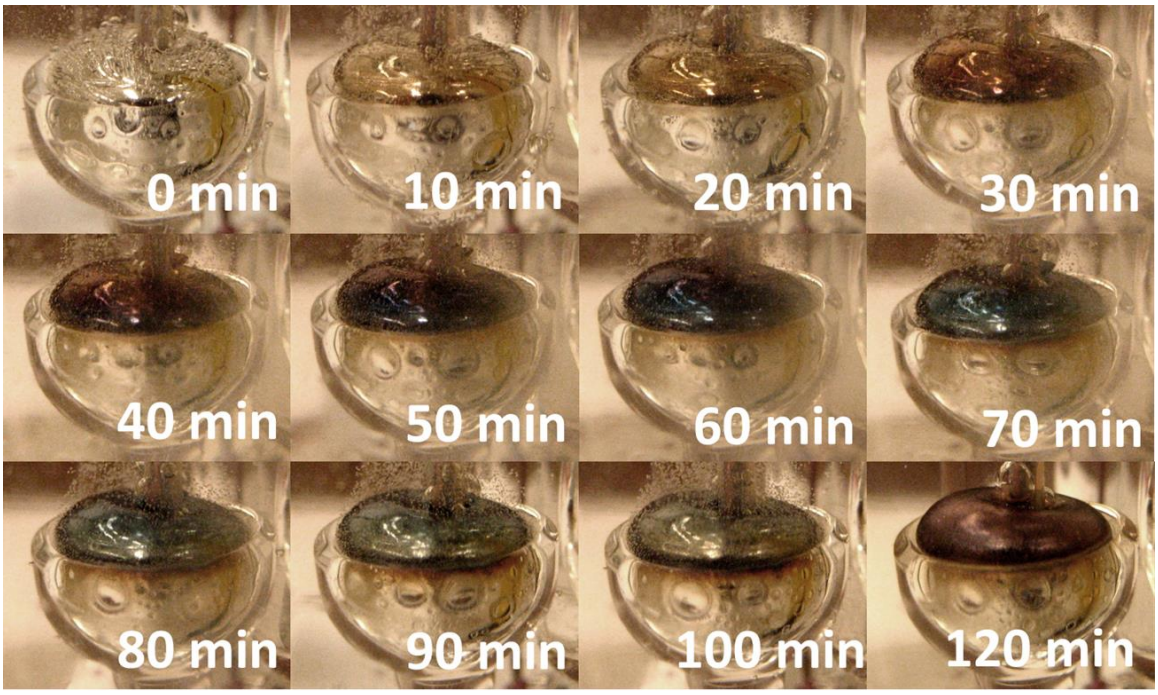

Figure 4.9. Optical images of a Ga(*l*) pool electrode immersed in an aqueous solution containing 0.1 M NaOH, 0.1 M Na_2SO_4, and 0.001 M As_2O_3 at 90 °C while biased at –1.58 V vs. Ag/AgCl for 0, 30, 60, 90, and 120 min.

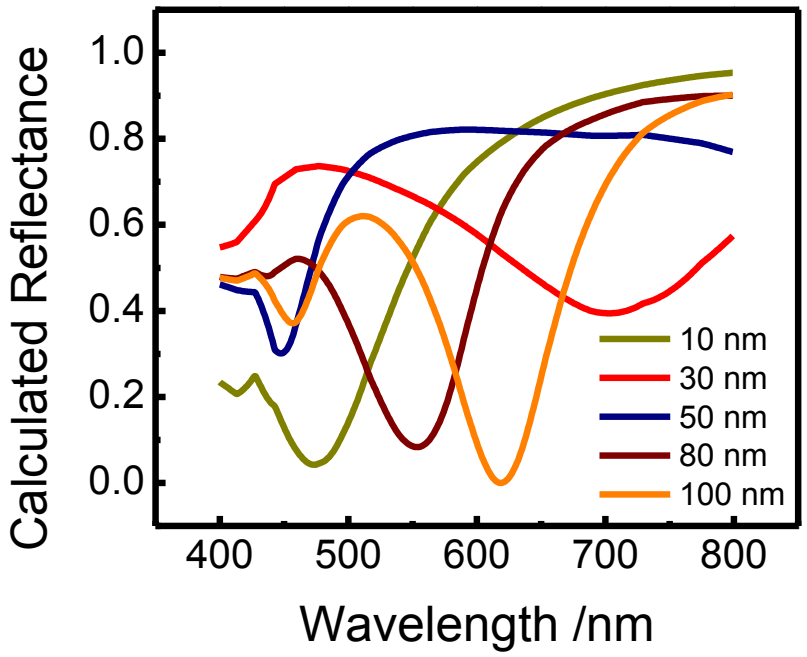

Figure 4.10. Calculated wavelength-dependent reflectance of GaAs thin films of varying thickness positioned on a Ga electrode in air. Expressions based on the complex-matrix form of the Fresnel equations were used to calculate the reflectance of 10, 30, 50, 80 and 100 nm GaAs films (n = 3.312) on a gallium substrate (n = 1.5) through air (n = 1).

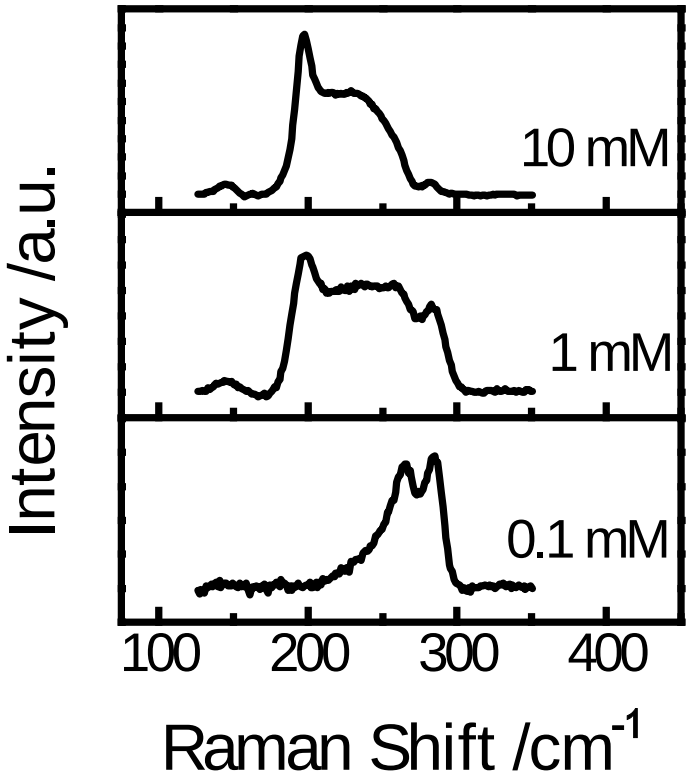

Figure 4.11. Raman spectra for films deposited at Ga(*l*) pool electrodes immersed in an aqueous solution containing 0.1 M NaOH, 0.1 M Na_2SO_4 at 80 °C with an applied bias of -1.58 V vs. Ag/AgCl as a function of the formal concentration of As_2O_3.

was a uniform gold after ten minutes. At longer times, the color of the film transitioned through shades of amber, blue, green, and then back to a darker amber. The apparent color of an ultrathin (<100 nm) GaAs film (i.e., the spectral profile of the reflected visible light) should change as the film thickness increases (Figure 4.10). The color change stopped if the electrodeposition was stopped, indicating the color change was a function of the quantity (thickness) of the electrodeposited film. Further experiments confirmed the nature of the electrodeposited film was not amorphous As(*s*) at lowered concentrations of dissolved As_2O_3. Figure 4.11 contains Raman spectra for a set of three electrodeposited films at 80 °C at E = -1.58 V vs. Ag/AgCl onto Ga(*l*) electrodes immersed in solutions with dissolved As_2O_3 concentrations spanning two orders of magnitude (10 mM to 0.1 mM). In Figure 4.11, the Raman spectra show a transition in the composition of the electrodeposited film from pure amorphous As(*s*) to pure crystalline c-GaAs(*s*) as the dissolved As_2O_3 concentration decreased. Specifically, the disappearance of the modes associated with amorphous As(*s*) and the prominent appearance of the TO and LO modes characteristic for c-GaAs(*s*) was apparent and consistent across the entire film surfaces prepared at 1 and 0.1 mM. The uniformity of the spectral features across randomly selected regions on the as-prepared films indicated a homogeneous film composition.

Figure 4.12 displays the temperature- and potential-dependent Raman spectra collected after electroreduction for 120 minutes in an alkaline solution with a formal As_2O_3 concentration of 1 mM. Raman spectra collected after electrodeposition at a constant temperature of 90 °C showed no clear signatures for amorphous As(*s*) at any investigated applied potential. Instead, the Raman spectra were dominated by the two peaks for the c-GaAs(*s*) TO and LO modes centered at 266 and 286.5 cm^{-1}, respectively. At this temperature, changes in the applied potential between -1.48 V and -1.68 V vs. Ag/AgCl did not result in substantial changes in the collected Raman spectra. The number of peaks, peak centers, and peak widths remained unchanged (Table 4.1). At -1.38 V vs. Ag/AgCl, the same qualitative spectral features consistent with c-GaAs(*s*) were apparent, albeit with much lower signal to noise. However, the specific applied potential used for electrodeposition did negatively impact the adherence of the c-GaAs(*s*) film to the Ga(*l*)

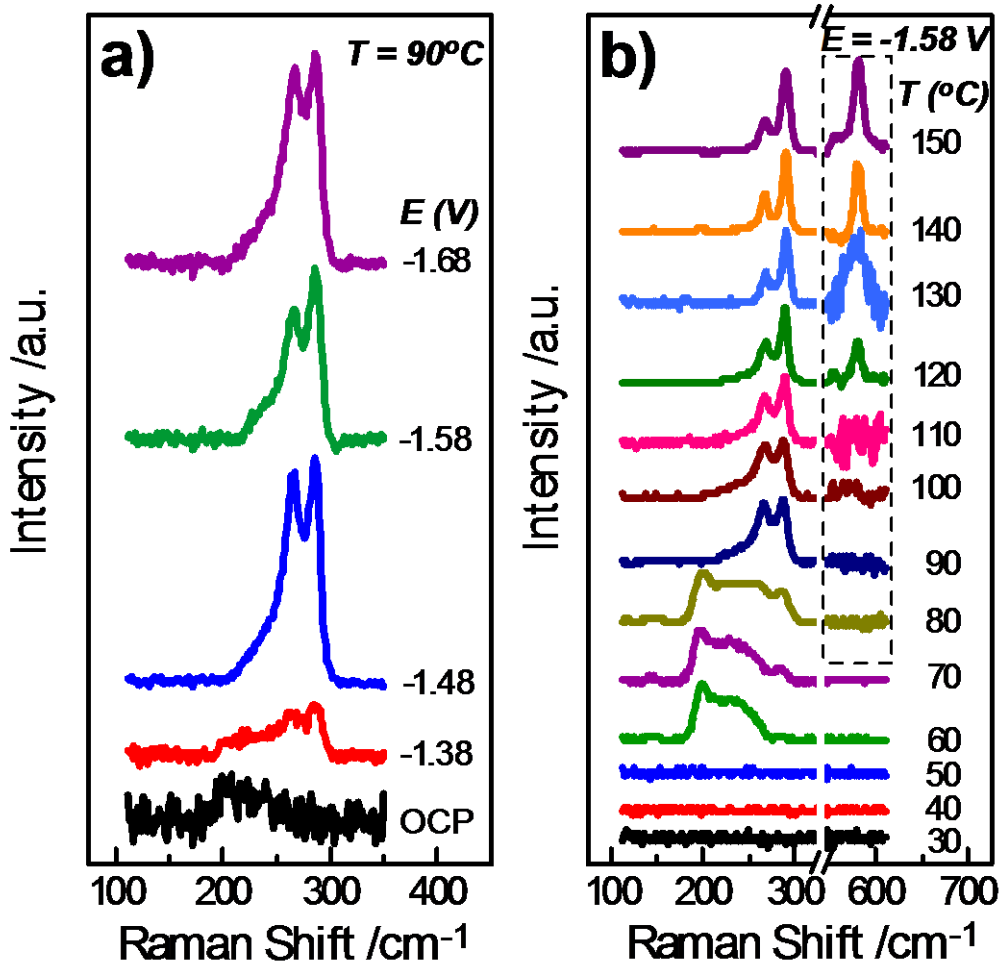

Figure 4.12. (a) Raman spectra for films deposited at Ga(*l*) pool electrodes immersed in an aqueous solution containing 0.1 M NaOH, 0.1 M Na_2SO_4, and 0.001 M As_2O_3 at 90 °C for two hours at several different applied biases. For this set of experiments, the open circuit rest potential (OCP) was -1.28 V vs Ag/AgCl. (b) Raman spectra for films deposited at Ga(*l*) pool electrodes immersed in an aqueous solution containing 0.1 M NaOH, 0.1 M Na_2SO_4, and 0.001 M As_2O_3 at an applied bias of -1.58 V vs. Ag/AgCl for two hours at several different electrodeposition temperatures. The dashed box denotes data scaled by an additional factor of 10. Spectra are offset for clarity.

Table 4.1. Raman spectral features for c-GaAs prepared[a] at various applied potentials

	Applied	TO[c,d]	LO	TO:LO
Conc. /mM	Potential[b] /V	Peak Position /cm^{-1}	Peak Position /cm^{-1}	Peak Intensity Ratio
	-1.48	266.1 (15)	285.5 (14.1)	100:110
0.1 mM	-1.58	265.8 (15)	285.6 (14.8)	100:97
	-1.68	266.1 (15)	286.0 (14.4)	100:101
	-1.38	265.4 (15)	285.9 (14.6)	100:117
1 mM	-1.48	266.0 (15)	286.1 (14.4)	100:106
	-1.58	265.8 (15)	285.8 (14.4)	100:134
	-1.68	266.2 (15)	286.1 (14.8)	100:107

[a] Prepared at an electrodeposition temperature of 90 °C. [b] vs. Ag/AgCl. [c] Value in parentheses corresponds to full width at half maximum for given peak. [d] Full width at half maximum value for TO mode constrained to 15 cm^{-1} during peak fitting.

Table 4.2. Raman spectral features prepared[a] at various temperatures

		TO[b,c]	LO	2LO	TO:LO:2LO
Conc. /mM	**Temp/ °C**	**Peak Position /cm^{-1}**	**Peak Position /cm^{-1}**	**Peak Position /cm^{-1}**	**Peak Intensity Ratio**
0.1 mM	80	264.9 (15)	284.7 (15.0)	—	100:101:0
	90	265.6 (15)	285.6 (14.3)	—	100:111:0
	100	265.3 (15)	286.5 (13.3)	—	100:98:0
	110	266.3 (15)	287.6 (11.8)	—	100:110:0
	120	266.9 (15)	288.5 (11.2)	580.2 (25)	100:112:13
	130	266.7 (15)	289.3 (10.7)	579.6 (22)	100:189:12
	140	266.9 (15)	289.3 (10.6)	580.0 (18)	100:193:21
	150	267.0 (15)	289.3 (10.5)	581.4 (15)	100:215:24
1 mM	80	260.3 (15)	284.3 (15.6)	—	100:94:0
	90	265.5 (15)	285.4 (14.5)	—	100:106:0
	100	265.9 (15)	286.2 (13.6)	—	100:104:0
	110	266.4 (15)	287.3 (11.5)	—	100:134:0
	120	266.7 (15)	288.1 (10.6)	578.0 (20)	100:182:12
	130	267.2 (15)	288.8 (10.7)	579.7 (22)	100:204:13
	140	266.1 (15)	288.4 (10.7)	579.4 (15)	100:206:15
	150	267.0 (15)	288.5 (10.9)	580.0 (15)	100:246:29

[a] Prepared at an applied potential of -1.58 V vs. Ag/AgCl. [b] Value in parentheses corresponds to full width at half maximum for given peak.
[c] Full width at half maximum value for TO mode constrained to 15 cm^{-1} during peak fitting.

electrode surface and reduced the total quantity produced. Experiments performed under the same conditions but in the absence of an applied bias resulted in Raman spectra with no discernible spectral features above the baseline indicating no detectable deposit of any kind.

Figure 4.12b shows representative Raman spectra for electrodeposited films on a Ga(*l*) electrode prepared in alkaline solution containing 1 mM dissolved As_2O_3 at -1.58 V vs. Ag/AgCl for 120 min at several temperatures. At or below 50 °C, no Raman features were observed above the background in the collected Raman spectra. At 60 °C, the collected Raman spectra showed the characteristic features for amorphous As(*s*) only. At 70°C, the Raman spectra showed more spectral signatures, with a slight peak at 282.5 cm^{-1} consistent with the LO mode for c-GaAs(*s*) in addition to the modes indicative of amorphous As(*s*). A similar combination of signatures for both As(*s*) and c-GaAs(*s*) was evident in data collected at 80 °C, with an increased intensity and blue shift for the observed c-GaAs(*s*) LO mode. At 90 °C and higher temperatures, the collected Raman spectra showed only the two prominent c-GaAs(*s*) TO and LO modes and a total absence of any amorphous As(*s*) or amorphous GaAs signatures.[31,32,38-40] As the electrodeposition temperature was increased, the collected Raman spectra showed an increase in the relative intensity of the LO mode, a blue-shift in the peak center of the LO mode, and a decrease in the full width at half maximum (FWHM) of the LO mode. These changes are explicitly listed in Table 4.2. As the electrodeposition temperature increased, the absolute and relative intensities of the first overtone of the LO mode (2LO) at 580 cm^{-1} increased substantially, typically a hallmark of increased levels of semiconductor crystallinity.[45,46]

Two additional orthogonal analyses were conducted to verify separately the crystallinity of the as-prepared GaAs films. X-ray diffraction patterns were collected for films electrodeposited at 150 °C (Figure 4.13). Reflections indexed to the zincblende unit cell for GaAs were observed in the as-prepared films. Separate transmission electron microscopy data also indicated crystalline character in the electrodeposited films. Figure 4.14 shows a high magnification transmission electron micrograph for GaAs prepared at 120 °C in an alkaline solution containing 1 mM As_2O_3. The HRTEM image in Figure 4.14a displays the lattice fringes with grain sizes around 5 nm. Figure 4.14b presents a magnified image of a single as-deposited c-GaAs crystallite.

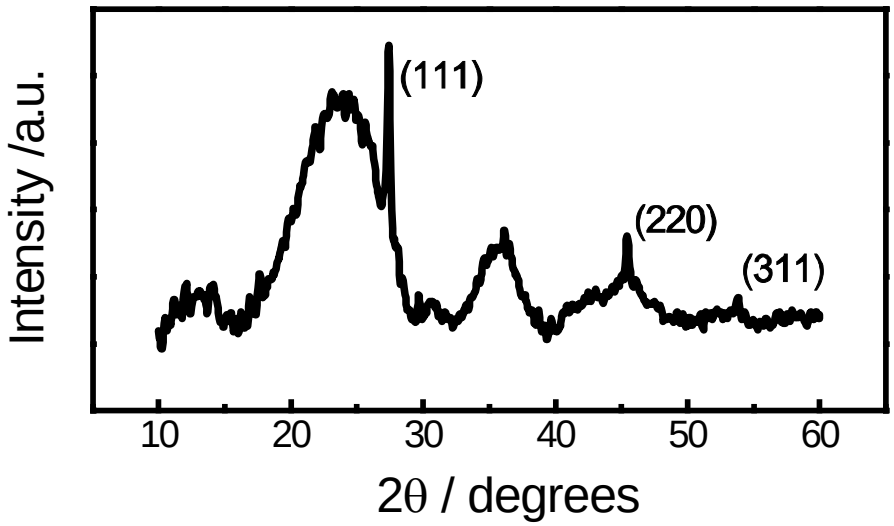

Figure 4.13. Powder X-ray diffractogram collected from an as-prepared film electrodeposited from 0.0001 M As_2O_3 at 150 °C. Indexed peaks correspond to zincblende GaAs.

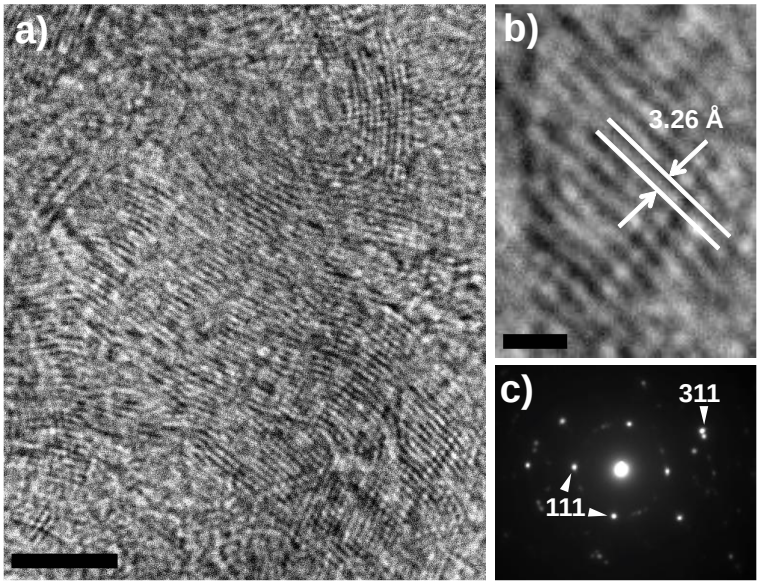

Figure 4.14. (a) High resolution transmission electron micrograph of c-GaAs prepared at at a Ga(*l*) pool electrode immersed in an aqueous solution containing 0.1 M NaOH, 0.1 M Na_2SO_4, and 0.001 M As_2O_3 and biased at –1.58 V vs. Ag/AgCl for 120 min. Scale bar is 5 nm. (b) High magnification electron micrograph showing lattice fringes with a 3.26 Å spacing. Scale bar is 1 nm. (c) Selected area electron diffraction pattern for the same sample in (a). Points positioned on inner and outer rings match expected spacings for zincblende GaAs (111) and (311) planes, respectively.

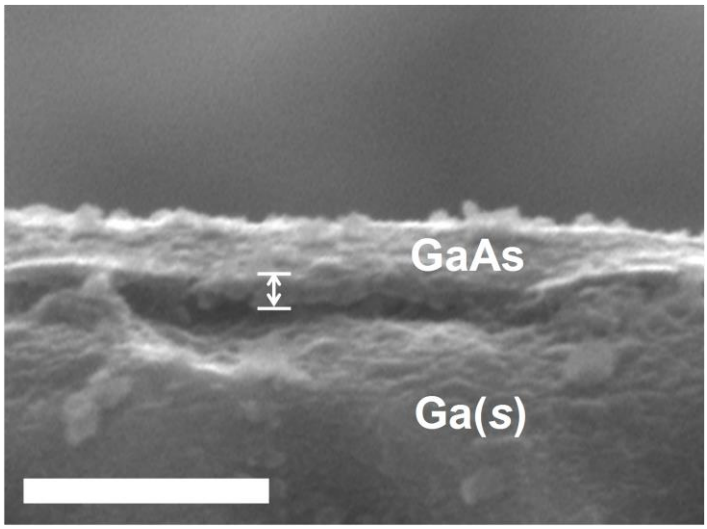

Figure 4.15. Scanning electron micrograph cross-section of a GaAs film electrodeposited (E = -1.58V) on a Ga(l) electrode from a 0.001 M As_2O_3 solution at 80 °C for two hours. Thickness measurements were conducted along the GaAs film/Ga electrode interface as indicated by the arrows. Scale bar is 500 nm.

The *d*-spacing measured at 3.26 Å from Figure 4.14b was in accord with the (111) spacing for bulk c-GaAs(*s*).[22] Figure 4.14c presents a SAED pattern for the sample shown in Figure 4.14a,b. The SAED pattern contained diffraction spots that also indexed to the (111) and (311) planes of zincblende GaAs, with measured *d*-spacing values of 3.27 and 1.70 Å, respectively. Corresponding scanning electron micrographs of cross-sectioned samples indicated the GaAs films were approximately 65 nm in thickness (Figure 4.15). This thickness value was separately corroborated by inductively coupled plasma (ICP)–atomic emission spectroscopy analysis (Figure 4.16).

Figure 4.17 shows Raman spectra for c-GaAs(*s*) films prepared from electrolytes containing 0.1 mM of dissolved As_2O_3. As shown in Figure 4.17a, a negative applied potential of at least -1.48V vs. Ag/AgCl was required for deposition of c-GaAs. As observed for films prepared with 1 mM dissolved As_2O_3, changes in the applied potential beyond the threshold for electrodeposition did not impact the measured Raman spectra. All of these spectra showed the same LO and TO features and no signatures for amorphous As(*s*), irrespective of the applied bias. The Raman spectra in Figure 4.17b further showed that amorphous As(*s*) was not deposited at any temperature with 0.1 mM dissolved As_2O_3. At this dissolved As_2O_3 concentration, there also was no spectroscopic evidence for either As(*s*) or c-GaAs(*s*) for electrodepositions performed at or below 60 °C. At these conditions, there was no visible change to the surface of the Ga(*l*) electrode. However, at 80 °C and higher, a colored film was deposited onto the Ga(*l*) electrode. Further, the collected Raman spectra showed that the relative intensities of both the LO and 2LO phonon modes increased at elevated temperatures. The TO peak centers and FWHM values did not vary with electrodeposition temperature. Figure 4.18 collects and compares the LO phonon mode features for both sets of spectra in Figures 4.12b and 4.17b. Figure 4.18a summarizes the shift in LO peak position, $\Delta\nu_{LO}$, relative to the LO position for bulk c-GaAs. The two datasets for electrodepositions performed at 1 mM and 0.1 mM dissolved As_2O_3, respectively, showed comparable values of $\Delta\nu_{LO}$ as a function of temperature up until 120 °C. For electrodeposition temperatures spanning 120-150 °C, the $\Delta\nu_{LO}$ values remained constant for both datasets. Figure 4.18b shows the relation between $\Delta\nu_{LO}$ and the LO peak FWHM ($FWHM_{LO}$) for the spectra in Figures 4.12b and 4.17b. For nanostructured c-GaAs, $\Delta\nu_{LO}$ and $FWHM_{LO}$ are correlated.[21]

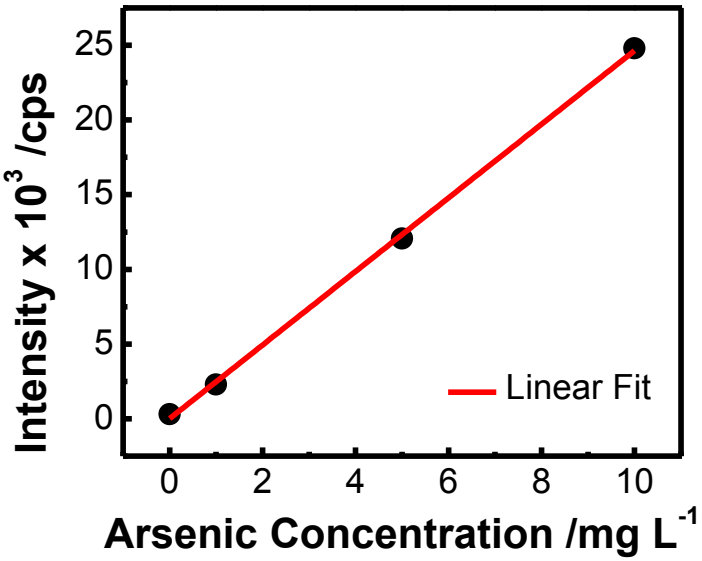

Figure 4.16. Calibration curve of emission intensity at 228.12 nm vs. dissolved As concentration over the 0 – 10 mg L^{-1} concentration range. A linear fit (red) was applied with a resulting correlation coefficient of 0.9998. The total electrodeposited As was determined from a GaAs film prepared on a Ga(*l*) electrode at 90 °C held at a potentiostatic bias of -1.58 V for two hours in a 1 mM As_2O_3 solution. The ICP-AES calibration curve shown here was constructed over the As concentration range of 0-10 mg L^{-1} and used for subsequent determination of As concentration in samples of dissolved GaAs films. Measured As concentrations and total extraction volumes were used to calculate the total electrodeposited As mass. The theoretical As mass was calculated using Faraday's Law and the total charge passed during the two hour electrodeposition. Dividing the measured As mass by the calculated mass provided an estimate of the Faradaic efficiency. The measured surface area of the Ga(*l*) electrode (0.6 cm^2) and the GaAs density (5.32 g cm^{-3}) was used to estimate the total deposit thickness over the electrode surface. A measured mass of 0.025 mg dispersed evenly over the electrode surface area equates to a thickness of 78 nm.

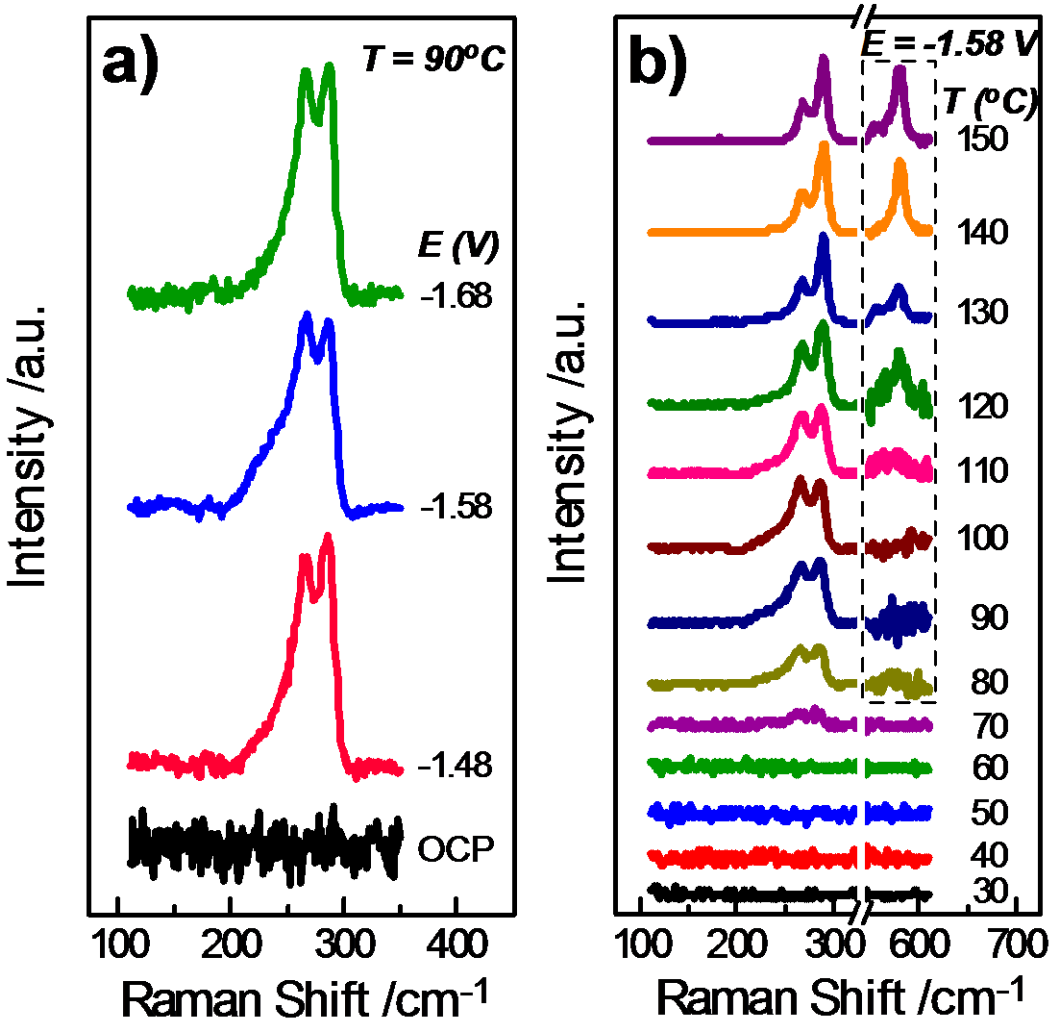

Figure 4.17. (a) Raman spectra for films deposited at Ga(*l*) pool electrodes immersed in an aqueous solution containing 0.1 M NaOH, 0.1 M Na_2SO_4, and 0.0001 M As_2O_3 at 90 °C for two hours at several different applied biases. For this set of experiments, the open circuit rest potential (OCP) was -1.35 V vs Ag/AgCl. (b) Raman spectra for films deposited at Ga(*l*) pool electrodes immersed in an aqueous solution containing 0.1 M NaOH, 0.1 M Na_2SO_4, and 0.0001 M As_2O_3 at an applied bias of -1.58 V vs. Ag/AgCl for two hours at several different electrodeposition temperatures. The dashed box denotes data scaled by an additional factor of 10. Spectra are offset for clarity.

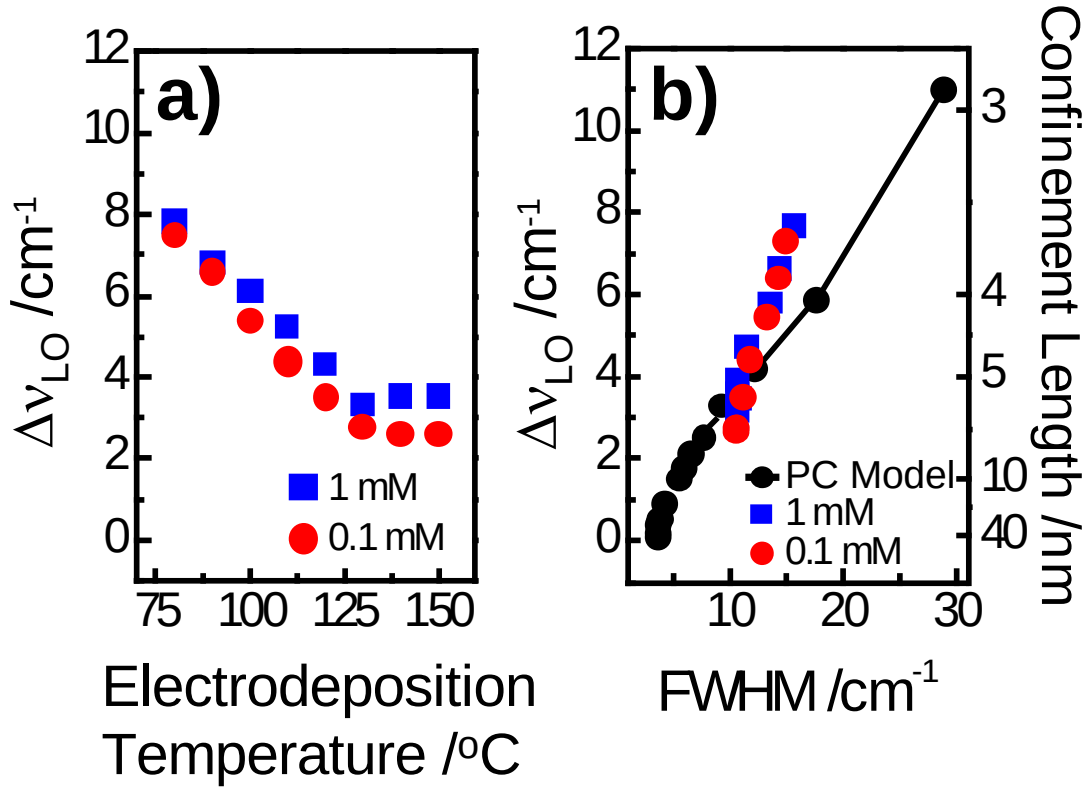

Figure 4.18. (a) Measured shifts in c-GaAs LO phonon mode ($\Delta\nu_{LO}$) relative to the bulk GaAs LO phonon mode (ν_{LO} = 292 cm^{-1}) as a function of electrodeposition temperature. Formal concentrations of As_2O_3 of (blue squares) 0.001 M and (red circles) 0.0001 M. (b) Measured c-GaAs LO phonon mode shifts plotted against the measured c-GaAs LO phonon line width. The black line represents the c-GaAs LO phonon shift and peak width relation predicted by the Phonon Confinement Model assuming an isotropic crystal with a Gaussian weighting function. The confinement length is indicated on the right-hand y-axis.

Figure 4.18b illustrates the predicted LO phonon shift and FWHM relationship given by the Phonon Confinement model[47] for a GaAs crystallite with isotropic and Gaussian-type phonon confinement as a function of the phonon confinement length. Following these model parameters, the measured $\Delta\nu_{LO}$ and $FWHM_{LO}$ values for c-GaAs films deposited both in 1 mM and 0.1 mM dissolved As_2O_3 solutions implied confinement lengths < 10 nm in the as-prepared c-GaAs films.

4.4. Discussion

The collected data validate the hypothesis that c-GaAs(*s*) can be controllably prepared through electroreduction of dissolved As_2O_3 at Ga(*l*) electrodes at mild temperatures in water. The presented results illustrate that crystallinity in as-prepared GaAs can be achieved without separate thermal annealing. This work represents the first dataset describing an ec-LLS process where a liquid metal electrode explicitly serves simultaneously as an electrode, solvent and co-reactant to produce a crystalline binary semiconductor. The key aspects impacting this ec-LLS process for GaAs are a clean Ga(*l*)/electrolyte interface, a sufficiently negative bias to reduce dissolved As_2O_3, a low concentration of dissolved As_2O_3, and only moderately elevated temperatures. These points are detailed below.

The measurements shown here indicate controllable and predictable behavior of Ga(*l*) electrodes in this GaAs ec-LLS process. For example, a set of 10 replicate electrodepositions at 80 °C and an applied bias of -1.58 V vs. Ag/AgCl in 1 mM As_2O_3 solutions produced films identical in color, crystallinity, and quantity. Although Ga(*l*) electrodes have been previously noted as less reproducible than Hg(*l*) electrodes for electroanalytical applications,[23,48] the consistency of the voltammetric responses collected here support the contention that Ga(*l*) electrodes are not compromised by thick, blocking films in this electrolyte at the employed potentials. Specifically, we posit that the passivating oxides (≤ 10 Å) previously noted on Ga(*l*) surfaces exposed to air through x-ray reflective measurements were not stable at the negative applied biases used here, as suggested previously.[49,50] Three empirical observations are in accord with a pristine Ga(*l*)/electrolyte interface for the conditions employed here. First, the linear scan rate dependence of the 'inverted' voltammetric wave suggests a surface-based process. Second,

the sustained anodic current implies continuous Ga(*l*) dissolution at the peak potential of the 'inverted' voltammetric wave. Third, the potential of the 'inverted' voltammetric wave is proximal to the transition potential from corrosion susceptibility to stability for Ga(*l*) electrodes predicted by electrode potential-pH equilibrium diagrams.[50,51] We posit that potential-dependent removal of a passivating oxide film exposes the surface of bare Ga(*l*) to electrolyte and is unstable until more negative applied potentials. Additionally, the appearance and shape of the Ga(*l*) pool electrodes were inconsistent with an interface dictated by surface oxides. Ga(*l*) pools exposed to humid air attain a slightly dull, grey appearance and appear semi-flat (compressed). Upon immersion in these alkaline electrolytes, Ga(*l*) pool surfaces attained a crisp, mirror finish with a convex contour, in accord with literature descriptions of the increased a surface tension/shape of a Ga(*l*) pool following mechanical removal of an interfacial oxide(s).[52,53]

The synthesis of c-GaAs(*s*) shown here required an applied bias more negative than –0.982 V vs. Ag/AgCl, the standard potential of the $HAsO_3^{2-}$/As redox couple. In all experiments where the electrochemical cell was charged with both Ga(*l*) and dissolved As_2O_3 but no bias was applied, c-GaAs(s) was not observed. At all concentrations and at temperatures below 50 °C, there was no visible or detectable film deposited on the Ga(*l*) pool. At high dissolved As_2O_3 concentrations and high temperatures, a film composed exclusively of amorphous As(*s*) was detectable by Raman. Accordingly, the available evidence clearly indicates that electroreduction of As_2O_3 to As(*s*) is a key and necessary step in this preparation of c-GaAs(*s*). However, the impact that the *rate* at which As(*s*) is electrodeposited onto Ga(*l*) is less clear.

In a cathodic electrodeposition process under kinetic control, the two principle factors that govern the rate (J_{dep}, expressed as a current density) of material deposition are the concentration of the reducible species (C) and the applied bias (E_{app}) used to perform the electroreduction,

$$J_{dep} = nFCk^0 e^{-\frac{\alpha F\left(E^0 - E_{app}\right)}{RT}} \tag{4.4}$$

where J_{dep} is the measured electrodeposition current density, k^0 is the standard rate constant for electroreduction of the species being deposited, α is the charge-transfer coefficient, E^0 is the standard potential for the species to be deposited, and the other terms have their usual electrochemical meanings.[26] Equation 4.4 follows a Butler-Volmer formalism and should be generally valid for the data shown here since none of the voltammetry for the electroreduction of dissolved As_2O_3 indicated a transition to mass-transport limited conditions (i.e. a 'peak' in the net voltammetric response for As_2O_3 electroreduction). Equation 4.4 predicts that the electrodeposition rate is a stronger function of the applied bias than the dissolved As_2O_3 concentration. However, the collected data implicate the dissolved As_2O_3 concentration as the factor that more strongly determined whether c-GaAs(*s*) was formed over amorphous As(*s*). Specifically, at a given temperature, a transition in the composition of the resultant film on the Ga(*l*) electrode from amorphous As(*s*) to c-GaAs(s) occurred as the formal concentration of As_2O_3 was varied by two orders of magnitude. However, at a given temperature and formal As_2O_3 concentration, variation in the applied bias by as much as 0.3 V did not change any measurable feature in the Raman spectra, i.e. the apparent film composition was the same. Assuming a nominal transfer coefficient of 0.5, a 0.3 V change in the applied potential should also effect approximately a two order of magnitude increase in the rate of electrodeposition. The apparent rate of film electrodeposition as inferred from visible inspection did increase at more negative potentials. Accordingly, the data suggest the absolute rate of As(*s*) electrodeposition was not itself a primary controlling factor in facilitating this ec-LLS process.

One alternative possibility regarding apparently strong sensitivity of the formation of c-GaAs towards the concentration of dissolved As_2O_3 is that the concentration of dissolved As_2O_3 could more strongly impacts the *form* of the initial electrodeposit. The dissolving power of a liquid melt towards a solid is known to be strongly sensitive to the morphology of the solid.[54] At a constant mass, a solid will dissolve more quickly and readily when presented as a fine, high surface area powder rather than a single, large object. Specifically, for any binary system composed of a solid dissolving into a liquid, the rate of dissolution of the solid into the liquid phase is given by Equation 4.5,[55]

$$\frac{dC}{dt} = k_{diss}\frac{s}{V}(C_{sat} - C_{diss}) \tag{4.5}$$

where k_{diss} is the dissolution rate constant, s is the surface area of the solid in contact with the liquid, V is the volume of the liquid, C_{sat} is the solubility of the solid in the liquid, and C_{diss} is the concentration of the dissolved solid in the bulk of the liquid phase. In the case of electrodeposition, the morphology of deposited films begins typically as discrete nuclei/islands.[56] After sufficient time, the discrete clusters coalesce and eventually form a continuous phase. At a given applied potential, the size, density, and average spacing of the initial electrodeposited clusters can depend on several factors. Analytical expressions are known for interpreting these parameters from chronoamperometric data for electrodepositions performed under mass-transport limitations.[57-59] Although equivalent expressions have not been determined for electrodepositions performed under purely kinetic limitations,[56] similar functional forms are expected with parameters such as concentration. Notably, the island density of electrodeposited films scales as $C^{3/2}$.[56] Accordingly, electrodepositions performed at higher concentrations will generally be both faster and have high nucleation densities that can coalesce into a continuous film quickly. A coalesced film should result in low effective s/V for the electrodeposited solid. Conversely, electrodeposition in more dilute solutions will not only deposit more slowly but also result in less dense, discretized amorphous islands that favor larger s/V ratios.

We hypothesize that subsequent formation of c-GaAs(s) requires controlled dissolution of As(s). At room temperature, the equilibrium solubility of As in Ga is sparing (10^{-13} at %).[60,61]The binary phase diagram for Ga and As mixtures indicates that the equilibrium mixture composition at high mole fractions of Ga is Ga(l) and GaAs(s).[62] As a result, formation first of a stable, solvated As species within Ga(l) is not expected. Instead, the formation of dissolved GaAs most likely occurs as a result of, or concomitant with, As(s) dissolution. Precipitation of c-GaAs(s) should then follow earlier ec-LLS descriptions,[15,63] where crystallization results from supersaturation of the liquid metal electrode with GaAs. Assuming classical nucleation theory,[64] the size of the precipitating nuclei from a supersaturated solution should increase at higher temperatures where solubility is greater. The increase in effective domain size implied by the blue shifts and

narrowed peak widths in collected Raman spectra at higher temperatures supports this general premise.

Figure 4.1 summarizes the proposed ec-LLS model for GaAs. The multi-step sequence inherently places a large emphasis on the interplay between the individual electrochemical, chemical, metallurgical and physical growth steps. If As(*s*) is electrodeposited in a manner that exceeds the dissolution and alloying reaction rates, then an excess of amorphous As(*s*) will accumulate and prevent formation of c-GaAs as the primary product at any temperature. If As(*s*) is electrodeposited in a fashion that facilitates fast dissolution into Ga(*l*) and reaction to form GaAs, then c-GaAs(*s*) will ultimately be produced. According to the collected data, the crystalline grain size, as inferred from the Raman measurements, of the resultant c-GaAs(*s*) follows temperature more strongly than changes in dissolved As_2O_3 concentration and applied potential.

This work demonstrates the proof of concept of the GaAs ec-LLS process but does not define the full extent this tactic can be leveraged. A more quantitative development of the interplay between the various processes identified in Figure 4.1 is needed. Accordingly, a better understanding of several aspects of the operation of liquid metal electrodes is paramount. First, electrodeposition at liquid metal electrodes is not comprehensively understood. On solid electrodes, the role of adatom surface diffusion on the electrodeposited nuclei density, size, and shape has only recently been recognized.[65,66] Electrodeposition studies with liquid metal electrodes, where surface transport could be fast, have yet to address this aspect.[67,68] Second, chemical dissolution and reaction rate constants at the interface between solid and liquid metals are not well described. Although discussed in the context of solders,[54] a more comprehensive understanding of these rate constants would give greater predictive power in designing better ec-LLS processes. Third, nucleation within, and crystal growth out of, a liquid metal electrode under applied bias is not well described. Liquid phase electro-epitaxial crystal growth at high temperatures (>850 °C) and under large current densities (2-10 A cm^{-2}) has been attempted,[69] but the analogies between that process and this ec-LLS sequence have yet to be established.

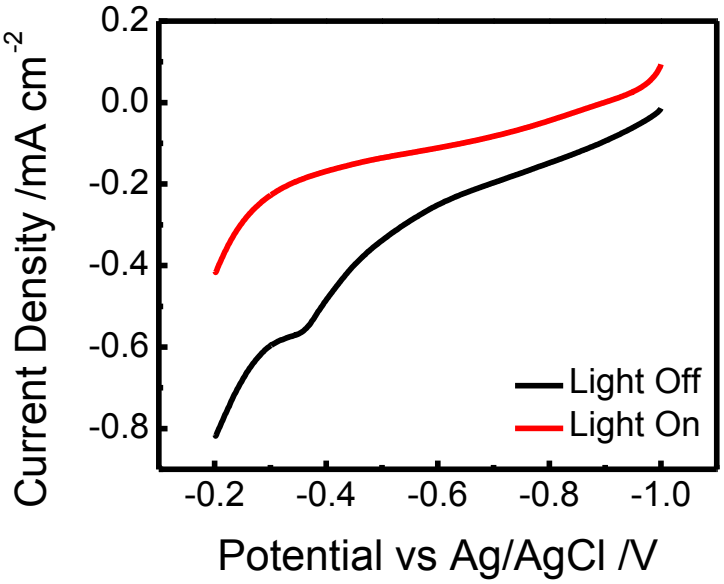

Figure 4.19. Steady state current-potential response for a GaAs film under white light illumination in 1 M KCl electrolyte. The GaAs film was prepared at 90 °C on a Ga(*l*) electrode under potentiostatic bias (E = -1.58 V) for two hours in a 0.001 M As_2O_3 solution.

Further, as implied by Equation 4.5, the physical properties of the liquid metal should impact the ec-LLS process. More work is needed to identify how features relating to the physical size/shape of the liquid metal electrode influence the c-GaAs produced through ec-LLS. In this preliminary stage, we have observed that c-GaAs shows some innate n-type responsivity to white light illumination (Figure 4.19). However, it is unclear whether this observation is an intrinsic property of this particular GaAs ec-LLS process or is a result of extrinsic measurements conditions. A better understanding of the microscopic role of Ga(l) in this ec-LLS process is necessary. In addition, identification of other low melting point metals and metal alloys that could be employed as liquid metal electrodes for ec-LLS is needed to synthesize other crystalline binary and/or ternary semiconductors.

The work presented here not only represents an explicit demonstration of an ec-LLS process for GaAs but also provides insight to rationalize the existing GaAs electrodeposition literature. Most reports indicate that co-electrodeposition of Ga and As from aqueous electrolytes cannot yield c-GaAs without subsequent annealing at high temperatures ($T \geq 250$ °C).[17,41-44] Typically, the net product at room temperature of co-electrodeposition of Ga and As is not crystalline or stoichiometric GaAs(*s*) but instead an amorphous, physical mixture of Ga and As. However, select reports do indicate some level of crystallinity in GaAs(*s*) from Ga and As co-electrodeposition at mild temperatures.[16,70,71] In co-electrodeposition, it is possible that microscopic Ga(*l*) droplets are formed initially that could then facilitate some type of ec-LLS as described here. We have recently demonstrated that ec-LLS is in fact possible with discrete metal nanoparticles.[63] However, as the data here demonstrate, the ec-LLS strategy for GaAs is sensitive to many processes and unless each is tightly regulated, a high yield of highly crystalline GaAs at mild temperatures is difficult. Still, the development of electrochemical reactors that exploit this particular ec-LLS process represents an exciting new strategy for preparing GaAs-based technologies.

4.5. Conclusions

The cumulative data in this chapter demonstrate that c-GaAs(*s*) can be directly electrodeposited on Ga(*l*) pool electrodes in aqueous solutions under mild conditions without requiring annealing, expensive precursors, or multiple process steps. Raman spectroscopy, powder X-ray diffraction and transmission electron microscopy analyses

independently and collectively confirmed the c-GaAs films are polycrystalline as prepared. The salient feature of this work is the demonstration of an ec-LLS sequence where a liquid metal serves simultaneously as an electrode substrate, crystal growth solvent/medium, *and* a co-reactant for the electrochemical preparation of c-GaAs from dissolved oxides in water. The data shown here establish a precedent for an alternative methodology for the preparation of c-GaAs that does not require vacuum or high-temperature equipment, potent gaseous precursors, or exotic solvents. Based on the results described here, the future work required to develop this process to produce functional c-GaAs materials and devices is described.

4.6. References

1. Bosi, M.; Pelosi, C. *Prog. Photovoltaics* **2007**, *15*, 51.
2. Buttar, C. M. *Nucl. Instrum. Methods Phys. Res., Sect. A* **1997**, *395*, 1.
3. Charlton, C.; Giovannini, M.; Faist, J.; Mizaikoff, B. *Anal. Chem.* **2006**, *78*, 4224.
4. Hayashi, I.; Panish, M. B.; Foy, P. W.; Sumski, S. *Appl. Phys. Lett.* **1970**, *17*, 109.
5. Hung, H. L. A.; Hegazi, G. M.; Lee, T. T.; Phelleps, F. R.; Singer, J. L.; Huang, H. C. *IEEE Trans. Microwave Theory Tech.* **1988**, *36*, 1966.
6. Cowley, A. H.; Jones, R. A. *Angew. Chem., Int. Ed. Engl.* **1989**, *28*, 1208.
7. Nakanisi, T. *J. Cryst. Growth* **1984**, *68*, 282.
8. Manasevi.Hm *Appl. Phys. Lett.* **1968**, *12*, 156.
9. Jurisch, M.; Eichler, S. In *3rd Czochralski Symposium* Kcynia, Poland, 2003.
10. Thomas, R. N.; Hobgood, H. M.; Eldridge, G. W.; Barrett, D. L.; Braggins, T. T.; Ta, L. B.; Wang, S. K. *Semicond Semimetals* **1984**, *20*, 1.
11. Weiner, M. E.; Lassota, D. T.; Schwartz, B. *J. Electrochem. Soc.* **1971**, *118*, 301.
12. Hicks, H. G. B.; Manley, D. F. *Solid State Commun.* **1969**, *7*, 1463.
13. Green, M. A.; Emery, K.; Hishikawa, Y.; Warta, W.; Dunlop, E. D. *Prog. Photovoltaics* **2012**, *20*, 12.
14. Mohr, N. J.; Schermer, J. J.; Huijbregts, M. A. J.; Meijer, A.; Reijnders, L. *Prog. Photovoltaics* **2007**, *15*, 163.
15. Carim, A. I.; Collins, S. M.; Foley, J. M.; Maldonado, S. *J. Am. Chem. Soc.* **2011**, *133*, 13292.
16. Chandra, S.; Khare, N. *Semicond. Sci. Technol.* **1987**, *2*, 214.
17. Yang, M. C.; Landau, U.; Angus, J. C. *J. Electrochem. Soc.* **1992**, *139*, 3480.
18. Campbell, I. H.; Fauchet, P. M. *Solid State Commun.* **1986**, *58*, 739.
19. Huang, Y. H.; Yu, P. Y.; Charasse, M. N.; Lo, Y. H.; Wang, S. *Appl. Phys. Lett.* **1987**, *51*, 192.
20. Richter, H.; Wang, Z. P.; Ley, L. *Solid State Commun.* **1981**, *39*, 625.
21. Tiong, K. K.; Amirtharaj, P. M.; Pollak, F. H.; Aspnes, D. E. *Applied Physics Letters* **1984**, *44*, 122.
22. Cho, A. Y.; Dernier, P. D. *J. Appl. Phys.* **1978**, *49*, 3328.
23. Varadharaj, A.; Rao, G. P. *Proc. - Indian Acad. of Sci., Chem. Sci.* **1990**, *102*, 177.
24. Stirrup, B. N.; Hampson, N. A. *J. Electroanal. Chem.* **1976**, *67*, 45.
25. Tomilov, A. P.; Smetanin, A. V.; Chernykh, I. N.; Smirnov, M. K. *Russ. J. Electrochem.* **2001**, *37*, 997.
26. Bard, A. J.; Faulkner, L. R. *Electrochemical Methods*; 2nd ed.; John Wiley & Sons: UK, 2004.
27. Arnold, J. P.; Johnson, R. M. *Talanta* **1969**, *16*, 1191.
28. Bayerle, V. *Recl. Trav. Chim. Pays-Bas* **1925**, *44*, 514.
29. Bejan, D.; Bunce, N. J. *J. Appl. Electrochem.* **2003**, *33*, 483.
30. Abstreiter, G.; Bauser, E.; Fischer, A.; Ploog, K. *Appl. Phys.* **1978**, *16*, 345.
31. da Silva, S. W.; Lubyshev, D. I.; Basmaji, P.; Pusep, Y. A.; Pizani, P. S.; Galzerani, J. C.; Katiyar, R. S.; Morell, G. *J. Appl. Phys.* **1997**, *82*, 6247.
32. Desnica, I. D.; Ivanda, M.; Kranjcec, M.; Murri, R.; Pinto, N. *J. Non-Cryst. Solids* **1994**, *170*, 263.
33. Ashby, C. I. H.; Sullivan, J. P.; Newcomer, P. P.; Missert, N. A.; Hou, H. Q.; Hammons, B. E.; Hafich, M. J.; Baca, A. G. *Appl. Phys. Lett.* **1997**, *70*, 2443.

34. Li, X.; Bohn, P. W. *J. Electrochem. Soc.* **2000**, *147*, 1740.
35. Calleja, J. M.; Lannin, J. S.; Cardona, M.; Schonher.E *Bull. Am. Phys. Soc.* **1974**, *19*, 227.
36. Schwartz, G. P.; Dutt, B. V.; Gualtieri, G. J. *Appl. Phys. Lett.* **1981**, *39*, 52.
37. Schwartz, G. P.; Schwartz, B.; Distefano, D.; Gualtieri, G. J.; Griffiths, J. E. *Appl. Phys. Lett.* **1979**, *34*, 205.
38. Lannin, J. S. *B. Am. Phys. Soc.* **1976**, *21*, 461.
39. Lannin, J. S. *Phys. Rev. B* **1977**, *15*, 3863.
40. Nemanich, R. J.; Lucovsky, G.; Pollard, W.; Joannopoulos, J. D. *Solid State Commun.* **1978**, *26*, 137.
41. Gheorghies, C.; Gheorghies, L.; Fetecau, G. *J. Optoelectron. Adv. M.* **2007**, *9*, 2795.
42. Mahalingam, T.; Lee, S.; Lim, H.; Moon, H.; Kim, Y. D. *Sol. Energy Mater.* **2006**, *90*, 2456.
43. Kozlov, V. M.; Bozzini, B.; Bicelli, L. P. *J. Alloys Compd.* **2004**, *379*, 209.
44. Mengoli, G.; Musiani, M. M.; Paolucci, F. *J. Electroanal. Chem.* **1992**, *332*, 199.
45. Wagner, J.; Hoffman, C. *Appl. Phys. Lett.* **1987**, *50*, 682.
46. Hardtdegen, H.; Hollfelder, M.; Meyer, R.; Carius, R.; Munder, H.; Frohnhoff, S.; Szynka, D.; Luth, H. *J. Cryst. Growth* **1992**, *124*, 420.
47. Gouadec, G.; Colomban, P. *Prog. Cryst. Growth Ch.* **2007**, *53*, 1.
48. Lezhava, T. I.; Vagramyan, A. I. *Russ. Chem. Bull.* **1964**, *13*, 409.
49. Korshunov, V. N.; Safonov, V. A. *Russ. J. Electrochem.* **2001**, *37*, 1089.
50. Pourbaix, M. *Atlas of Electrochemical Equilibria*; 2nd ed.; National Association of Corrosion Engineers: Houston, TX, 1974.
51. Pourbaix, M. *Biomaterials* **1984**, *5*, 122.
52. Dickey, M. D.; Chiechi, R. C.; Larsen, R. J.; Weiss, E. A.; Weitz, D. A.; Whitesides, G. M. *Adv. Func. Mat.* **2008**, *18*, 1097.
53. Larsen, R. J.; Dickey, M. D.; Whitesides, G. M.; Weitz, D. A. *J. Rheol.* **2009**, *53*, 1305.
54. Dybkov, V. I. *Reaction Diffusion and Solid State Chemical Kinetics*; IPMS: Kyiv, 2002.
55. Dokoumetzidis, A.; Macheras, P. *Int. J. Pharm.* **2006**, *321*, 1.
56. Guo, L.; Oskam, G.; Radisic, A.; Hoffmann, P. M.; Searson, P. C. *J. Phys. D: Appl. Phys.* **2011**, *44*, 44301.
57. Palomar-Pardave, M.; Scharifker, B. R.; Arce, E. M.; Romero-Romo, M. *Electrochim. Acta* **2005**, *50*, 4736.
58. Scharifker, B.; Hills, G. *Electrochim. Acta* **1983**, *28*, 879.
59. Scharifker, B.; Mostany, J. *J. Electroanal. Chem.* **1984**, *177*, 13.
60. Hall, R. N. *J. Electrochem. Soc.* **1963**, *110*, 385.
61. Thurmond, C. D. *J. Phys. Chem. Solids* **1965**, *26*, 785.
62. Tmar, M.; Gabriel, A.; Chatillon, C.; Ansara, I. *J. Cryst. Growth* **1984**, *69*, 421.
63. Gu, J.; Collins, S. M.; Carim, A. I.; Hao, X.; Bartlett, B. M.; Maldonado, S. *Nano Lett.* **2012**, *12*, 4617.
64. Kumar, S.; Nann, T. *Small* **2006**, *2*, 316.
65. Guo, L.; Searson, P. C. *Electrochimica Acta* **2010**, *55*, 4086.
66. Radisic, A.; Vereecken, P. M.; Hannon, J. B.; Searson, P. C.; Ross, F. M. *Nano Lett.* **2006**, *6*, 238.

67. Astley, D. J.; Harrison, J. A. *Electrochim. Acta* **1970**, *15*, 2007.
68. Fleischmann, J.; Harrison, J. A.; Thirsk, H. R. *Trans. Faraday Soc.* **1965**, *61*, 2742.
69. Bryskiewicz, T.; Boucher, C. F.; Lagowski, J.; Gatos, H. C. *J. Cryst. Growth* **1987**, *82*, 279.
70. Gao, Y. K.; Han, A. Z.; Lin, Y. Q.; Zhao, Y. C.; Zhang, J. D. *J. Appl. Phys.* **1994**, *75*, 549.
71. Murali, K. R.; Subramanian, V.; Rangarajan, N.; Lakshmanan, A. S.; Rangarajan, S. K. *J. Mater. Sci.: Mater. Electron.* **1991**, *2*, 149.

CHAPTER 5

Electrochemically-Gated Alloy Formation of Crystalline InAs Thin Films at Room Temperature in Aqueous Electrolytes

5.1. Introduction

Large scale production of crystalline thin films of III-V semiconductors is challenging in two ways. First, the majority of synthetic methods are energy- and resource-intensive.[1-3] For example, vapor phase crystal growth techniques such as metal-organic vapor phase epitaxy (MOVPE) and molecular beam epitaxy (MBE) involve ultra-high vacuum (UHV) equipment and temperatures above 400 °C.[1,3] Similarly, liquid phase epitaxy requires sustained temperatures in excess of 750 °C and pressurized furnaces.[2] Second, these same fabrication methods can be difficult to incorporate directly into device fabrication processes. For example, the high temperatures and corrosive reagents used in LPE, MOCVD, and MBE can damage delicate electronic device architectures (e.g. complementary metal-oxide-semiconductor (CMOS)) and sensitive platforms (e.g. plastics). As a result, cumbersome and costly transfer and integration steps are necessary.[4]

An ongoing frontier in materials science is thus the discovery and development of synthetic strategies for III-V semiconductors that mitigate these aforementioned challenges while not sacrificing crystalline quality, material purity, process controllability, and reproducibility. In this vein, gas-phase[5,6] and solution-phase[7] conversion of metals into compound semiconductors have been studied as possible synthetic alternatives.[5-7] These methods offer the potential for fewer fabrication steps and potentially simpler device integration, albeit still with the requirement of high temperatures and caustic environments. Separately, electrodeposition of III-V semiconductors has been extensively investigated since electrochemistry offers precise control of (heterogeneous) reaction rates and simple process electronics and equipment (i.e. a current or potential source and a beaker).[8-13] However, stoichiometry, purity, and crystallinity have proven difficult to control.

Our group recently identified new electrodeposition processes like electrochemical liquid-liquid-solid (ec-LLS) crystal growth where the electrode material serves multiple functions. In one sense, the metallic electrode is the familiar source of electrons for heterogeneous redox reactions; but, in another sense, it serves as a separate medium for crystal formation.[14] In this capacity, we have discovered that covalent groups IV and III-V semiconductors can be prepared in crystalline form under benchtop conditions.

The hypothesis tested in this work is that crystalline InAs, useful for light and radiation detection[15], chemical sensing[16], plasmonics[17], and high speed electronics[18], can be synthesized controllably through a new hybrid electrodeposition-alloying process. In this report, we show that, under certain cathodic conditions, controlled electrodeposition of As(*s*) from the reduction of dissolved As_2O_3(*aq*) onto indium (In) metal electrodes can drive an alloying reaction between In^0 and As^0 to form crystalline InAs under ambient conditions. A proposed schematic for the alloying process and setup geometry is depicted in Figure 5.1. The underlying premise is that, as long as In^0 and As^0 are brought in to intimate contact, this reaction will occur spontaneously even at room temperature (In(*s*) + As(*s*) → InAs(*s*), $\Delta G_{formation}$ = -53.6 kJ mol^{-1}).[19] We demonstrate the key elements for the process: a rigorously clean (i.e. oxide free) In electrode and a deliberately slow deposition of As^0. Data for a series of materials characterizations are shown that illustrate the uniformity and crystallinity of as-prepared films of polycrystalline InAs. The data are further contextualized with regards to the unique features and advantages of this new synthetic approach for the preparation of crystalline InAs.

5.2. Methods

Chemicals and Materials

In(*s*) foil (0.127 mm thick, 99.99%) was obtained from Alfa Aesar and used as received. Arsenic trioxide powder (As_2O_3(*s*), 99.95%, Mallinckrodt), anhydrous Na_2SO_4 (99%, EMD), and NaOH (98%, Fisher) were used as received. Water was purified from a Barnstead Nanopure III purification system (>18 MΩ cm) and was used for all solutions.

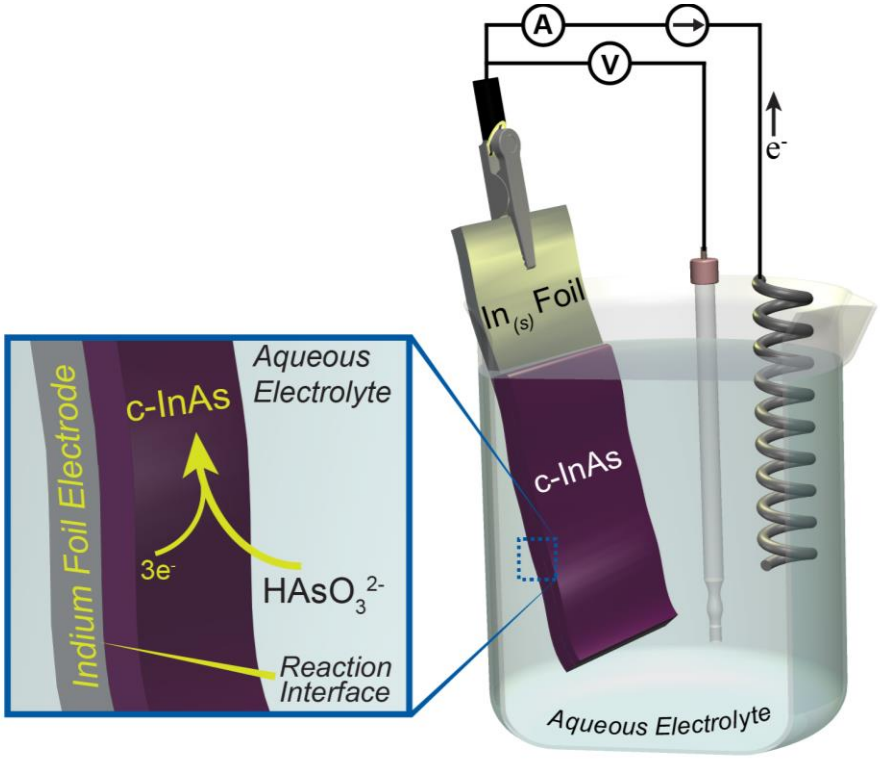

Figure 5.1. Schematic of proposed electrochemically-gated alloying reaction between electrodeposited As(*s*) on In(*s*) foil electrodes to form crystalline InAs thin films. The In(*s*) foil electrode serves as the cathode in an aqueous solution of dilute dissolved As_2O_3.

Electrodeposition and Electrochemical Measurements

CHI420A and CHI760C (CH Instruments) workstations were used for electrochemical experiments. All electrochemical data were acquired under open atmosphere in a standard glass electrochemical cell with a three electrode configuration featuring a ~0.5 cm^2 In(*s*) foil working electrode, a Pt mesh (2 cm^2) counter electrode, and a Ag/AgCl reference electrode. In(*s*) foil electrodes were fabricated by first cutting a small section of foil from a larger sheet using a razor blade. Electrical contact between the In(s) foil and a 10 cm section of 24 AWG copper wire was made using ~1 μL silver paint (GC Electronics) and dried at 40 °C for 30 min. A glass shroud was epoxied (Loctite 1C Hysol) around the Cu conductor leaving only the In(*s*) exposed to solution. All potentials are reported with respect to *E*(Ag/AgCl, sat. KCl). All electrochemical data are plotted with positive and negative currents indicating net reduction and oxidation reactions, respectively.

Materials Characterization

High-resolution transmission electron microscopy (HRTEM) and selected area electron diffraction (SAED) measurements were performed with a JEOL 3011 TEM equipped with a LaB_6 electron source operating at 300 keV. Samples were prepared by first gently scraping the as-deposited film from the surface of the In(*s*) foil electrode with a glass Pasteur pipet tip. Care was taken to avoid removing excess substrate from the soft In(*s*) underlayer. The collected film was dispersed in a minimum volume (< 500 μL) of CH_3OH (190 proof, ACS spectrophotometric grade, Aldrich) and sonicated for 60 s. Three separate 3 μL aliquots of the suspension were cast successively over a 400 mesh copper TEM grid coated with an ultrathin carbon support (Ted Pella). Scanning electron micrographs were collected with an FEI NOVA Nanolab Dualbeam Workstation with a Schottky field emitter operated at 15 keV beam voltage and a 0.14 nA beam current coupled with a through-the-lens detector (TLD). Electron diffraction patterns for InAs were simulated with SingleCrystal software in the $F\bar{4}3m$ space group (a = 6.0583 Å).[20]

Steady state and time-dependent Raman spectra were obtained using a Renishaw RM series Raman microscope equipped with a Nikon LU Plan 20x objective (NA = 0.4) and edge filters to reject the 785 nm excitation line. The excitation source and CCD detector

(578 x 400) were positioned in 180° backscatter geometry. No polarizing collection optics were used for spectral acquisition. A 785 nm diode laser was used as the incident excitation. Neutral density filters were placed in the optical path to limit the total radiant power to 1.12 mW over a 20 μm^2 spot. In a typical spectral collection, the collected signal was integrated for 30 s, and spectra were scan-averaged over three repetitions. Reported Raman data are representative of a collection of spectra acquired over at least 10 spots covering the surface of each measured sample. Time-dependent in-situ Raman spectra were collected in a custom Pyrex cell with a quartz viewing window that can accommodate horizontally positioned electrodes designed to fit within the working distance (*WD* = 13 mm) of the objective. Ten spectra (10 s per acquisition) were sequentially collected and averaged at each time point with 0.8 s delay between collections. For clarity, time-dependent spectra in this paper are shown every 1200 s over the experiment duration.

Raman spectral maps were collected with a Renishaw inVia equipped with a 785 nm excitation line source and a Renishaw MS20 100 nm encoded stage. A single ten second acquisition was collected at each pixel through a 50x (Olympus) objective. The magnitude between the spectral baseline and the longitudinal optical (LO) phonon peak position for InAs at = 234 cm^{-1} was used to plot the corresponding pixel color intensities.

Inductively coupled plasma atomic emission spectroscopy (ICP-AES) elemental analysis for As was obtained using a Perkin-Elmer Optima 2000DV instrument. Samples were prepared by dissolving the as-deposited InAs film in 12 mL aqua regia (3:1, 37% hydrochloric acid and 68-70% nitric acid, Fisher Scientific) for 24 hours at room temperature. Samples and standards were fortified with 1 ppm yttrium (Y) internal standard which was used to correct measured As intensities for matrix and sampling difference among samples and replicates. Samples were measured directly using emission lines at 371.029 and 228.812 nm for Y and As, respectively. A linear calibration curve (R = 0.999) was constructed over the As concentration range of 0 – 10 mg L^{-1}. The measured As concentration and total extraction volumes were then used in conjunction with the measured In(*s*) electrode surface area and the InAs density (5.68 g cm^{-3}) to calculate the total deposit thickness over the electrode surface.

Auger spectroscopic analyses were conducted with a Physical Electronics Scanning Auger Nanoprobe 680 equipped with a field emission source, Everhart-Thornley secondary

electron detector, cylindrical mirror analyzer, and an 8-channel detector. Sputtering depth profile experiments were performed with a PHI Model 06-350E Ar^+ source biased at 1 keV. The experimentally determined InAs sputtering rate on this instrumental geometry was 14 ± 3 nm min^{-1}.

Powder X-ray diffraction (XRD) was performed using a Bruker D8 Advance X-ray diffractometer with a Cu Kα X-ray source (λ = 1.5406 Å). A 0.6 mm slit width was employed with a sampling rate of 20 data points per degree 2θ at 2 s $point^{-1}$. Crystallite size analysis was conducted using Equation 5.1,

$$\overline{D_{hkl}} = \frac{K\lambda}{\beta \cos\theta} \tag{5.1}$$

where D_{hkl} is the crystallite size perpendicular to the *hkl* plane, *K* is a dimensionless shape factor of 0.88, λ is the X-ray source wavelength (Cu Kα , λ = 1.5406 Å), β is the line broadening at half maximum intensity of the *hkl* reflection (FWHM), and θ is the Bragg angle.

5.3. Results

Figure 5.2 shows the current-potential characteristics of native In(*s*) electrodes immersed in aqueous electrolytes in 0.1 M Na_2SO_4 and 0.1 M NaOH containing As_2O_3 dissolved. At pH 13, the predominant As-containing species in solution is $HAsO_3^{2-}$.[21] At this pH, the reduction of $HAsO_3^{2-}$ is expected to occur at *E* = -0.98 V vs Ag/AgCl.[21]

$$HAsO_3^{2-}(aq) + 3e^- + 2H_2O(l) \rightarrow As(s) + 5OH^-(aq) \tag{5.2}$$

However, at low (≤ 0.001 M) formal concentrations of dissolved arsenate species, the voltammetric responses lacked any identifiable cathodic feature diagnostic of Reaction 1 at this potential. In fact, no voltammetric feature suggestive of a mass-transport-limited reduction of $HAsO_3^{2-}$ was seen out to the cathodic window edge of water. Still, at potentials more negative than -1.2 V, the onset of current for H_2 evolution was consistently larger in the presence of dissolved As_2O_3 than without, suggesting some reduction of $HAsO_3^{2-}$ to As^0. Similar voltammetric observations were reported for reduction of arsenates in dilute alkaline solutions on both liquid[14,22] and solid metal electrodes.[23]

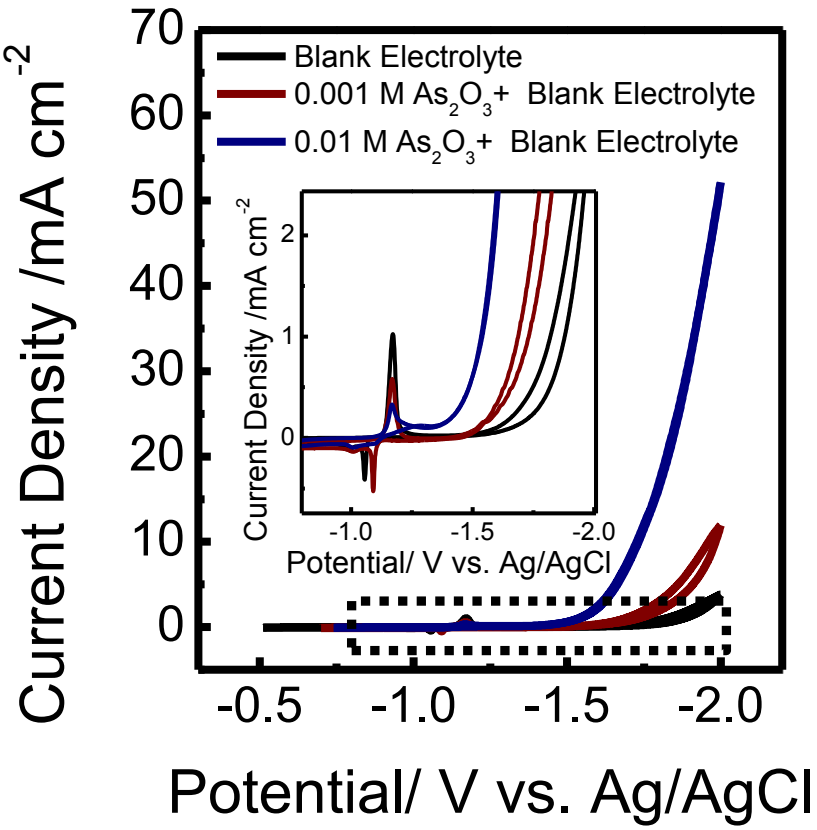

Figure 5.2. Cyclic voltammetric responses recorded with In electrodes submerged in an aqueous electrolyte containing 0.1 M Na_2SO_4 and 0.1 M NaOH and either (red) 0.01 M or (blue) 0.001 M As_2O_3. T = 25 °C; scan rate: 0.025 V s^{-1}. Inset: A more detailed view of the region enclosed within the dashed line box.

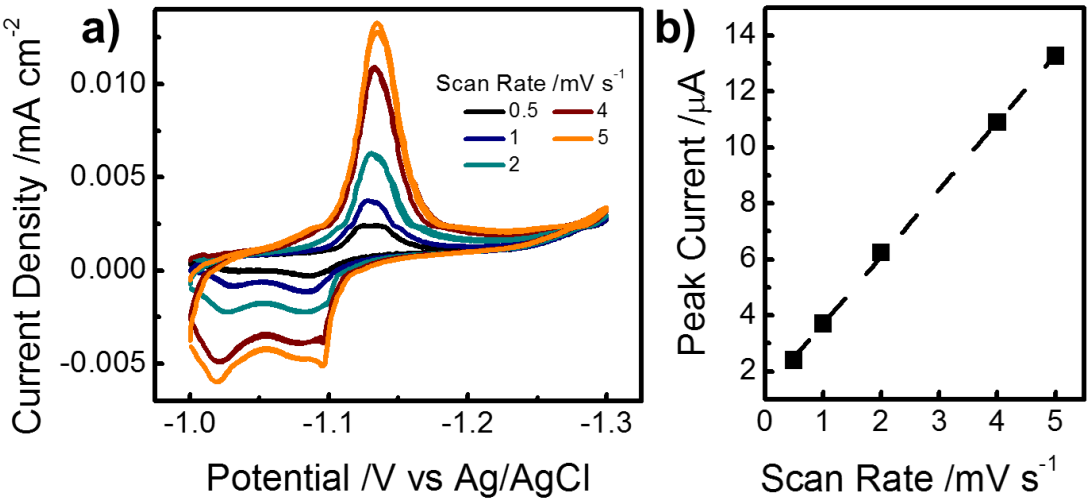

Figure 5.3. (a) Scan rate dependent cyclic voltammetric response for an In(*s*) electrode submerged in a quiescent electrolyte containing 0.1 M Na_2SO_4 and 0.1 M NaOH at room temperature. (b) Linear scan rate dependence of the peak current of the cathodic wave positioned at -1.13 V.

Both in the absence and presence of dissolved As_2O_3, the voltammetric responses included a sharp symmetrical wave near -1.15 V that was followed by two anodic features on the return sweep near -1.1 V (Figure 5.2) that showed a linear dependence with scan-rate (Figure 5.3a,b). In the blank electrolyte, this redox process corresponded to an optical transition in the surface of the In electrode from a dull grey color to a bright, more reflective appearance. The half wave potentials and total integrated cathodic and anodic charges for this feature were consistent with the electrochemical reduction/removal of an insoluble[21] oxide from the In(*s*) electrode surface that could be re-formed anodically.[24,25]

Since cathodic currents significantly increased once the surface oxide was stripped, further experiments were conducted to determine whether the native oxide also was a determining factor for the formation of InAs on to the In electrode surface. Specifically, potential step experiments were conducted with In(*s*) electrodes immersed in solutions with a 0.01 M formal concentration of arsenates at potentials that were both more negative than $E^0(HAsO_3^{2-}/As)$ *and* that bracketed the cathodic stripping of the surface oxide. Figure 5.4a shows that when E_{app} = -1.1 V, there was no visible change in the appearance of the In electrode (i.e. retained metallic silver hue) after 30 min. Further, Raman spectra collected from In electrodes biased at -1.1 V showed no spectroscopic signature of either As or InAs. Extending the potential step experiments for t > 48 h effected no changes in these observations (Figure 5.5a,b). However, when the potential was stepped to E_{app} = -1.25 V, the In electrode color changed to a deep purple tint after only five minutes. The collected Raman spectrum in Figure 5.4a for this experiment showed two prominent and sharp features at 215.6 and 234.4 cm^{-1} that were consistent with the transverse optical (TO) and LO phonon modes of crystalline InAs. The peaks were red-shifted ~1.5 cm^{-1} from the expected phonon frequencies of bulk InAs,[26] indicating the InAs film on the In electrodes was polycrystalline with domains on the order of 10 nm. No Raman features indicative of either amorphous[27] or crystalline[28] As^0 were seen even after 60 minutes E_{app} = -1.25 V, indicating all electrodeposited As^0 alloyed with the In electrode to form crystalline InAs. Further, the collected Raman spectra were devoid of any features that implicated amorphous InAs[29], re-precipitated As_2O_3[30], or In_2O_3[31] in the film.

Figure 5.4 also shows results from two additional experiments that probed the identity and composition of the red film on the In electrodes.

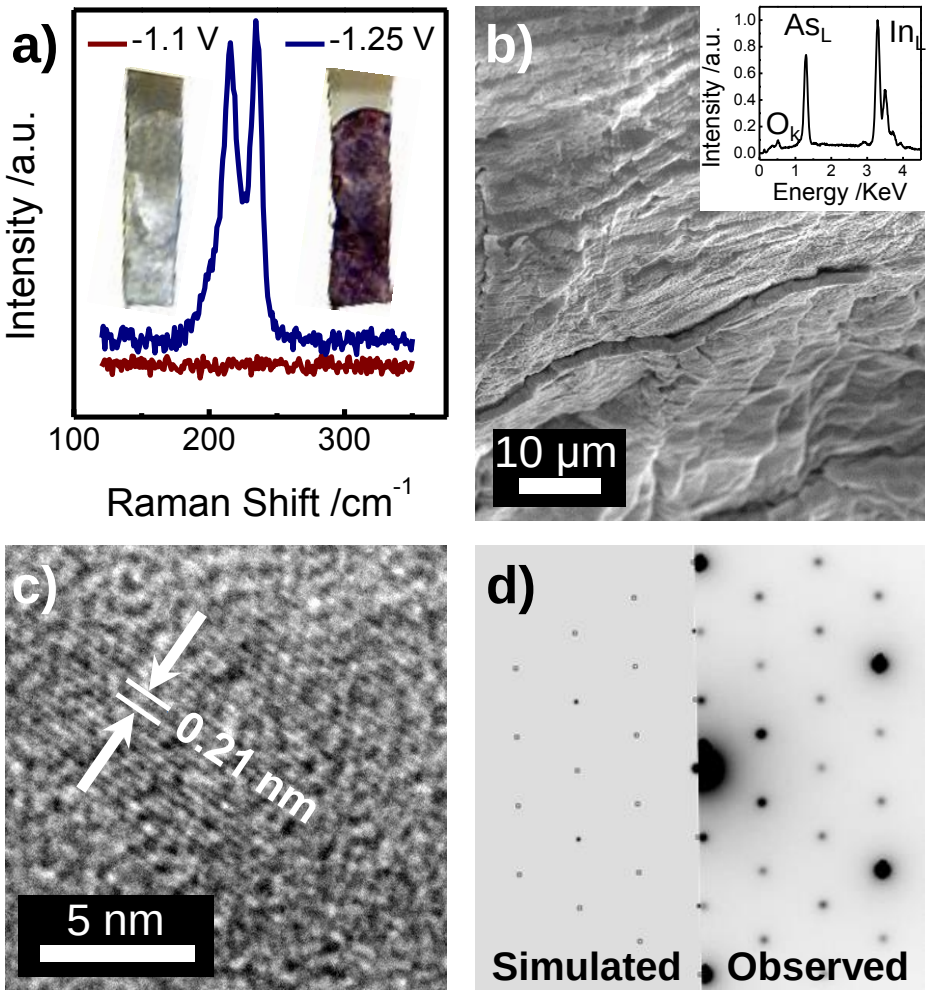

Figure 5.4. (a) Steady state Raman spectra collected at two In electrodes, both immersed in a room temperature aqueous solution containing 0.01 M As_2O_3, 0.1 M Na_2SO_4, and 0.1 M NaOH for 30 minutes at two different applied potentials. Inset shows optical images of the corresponding In electrodes after treatment. (b) Scanning electron micrograph of an the as-deposited film on the colored electrode in (a). Inset: X-ray energy dispersive spectrum collected from the film pictured in (a). (c) High resolution transmission electron micrograph of a section of a film prepared on an In electrode biased at -1.3 V for 30 minutes in a solution containing 0.01 M As_2O_3, 0.1 M Na_2SO_4, and 0.1 M NaOH. T= 25 °C. d) Selected-area electron diffraction pattern from the sample in (c) collected near the [111] zone axis.

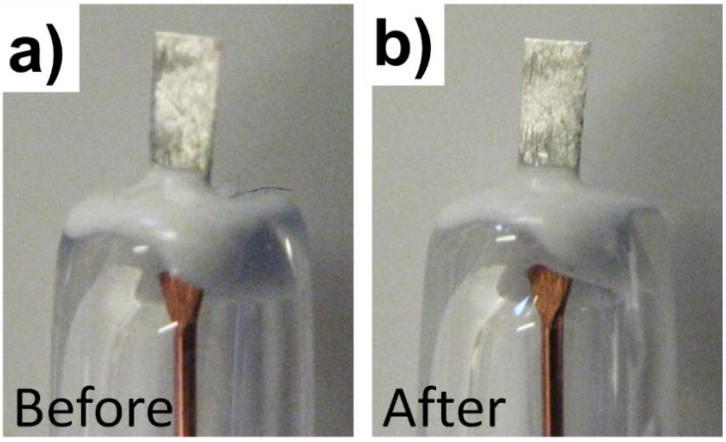

Figure 5.5. Optical images of In(*s*) foil electrodes collected a) before and b) after a potential step experiment at -1.1 V for 48 h in 0.01 M As_2O_3.

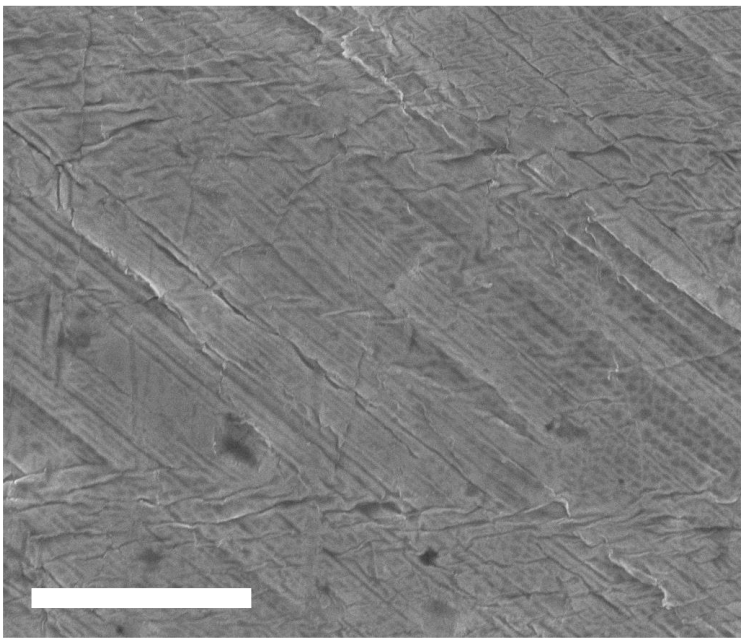

Figure 5.6. Scanning electron micrograph of a native In(*s*) foil electrode prior to InAs electrodeposition. Scale bar is 5 μm.

Figure 5.4b highlights a scanning electron micrograph that details the morphology of the as-deposited red film on In. The films on the In electrodes were continuous and flat when prepared potentiostatically at -1.3 V for 60 min in 10 mM As_2O_3. No meso-structures or large three dimensional clusters/particles were observed. In fact, the microscopic texture of the In electrode surfaces in the scanning electron micrographs was not perceptively altered after formation of the red film (Figure 5.6). The inset in Figure 5.4b shows an X-ray energy dispersive spectrum (XEDS) for this film containing prominent signatures for As and In, with the small feature at 0.5 keV consistent with oxide formation after storage of films in ambient air. Quantitative Auger Microprobe analysis (Figure 5.7) indicates the as-prepared InAs film is stoichiometric within the uncertainty of the Auger measurement. Figure 5.4c presents a high resolution transmission electron micrograph (HRTEM) of a section of the resultant film on the In electrode after biasing at E_{app} = -1.30 V in 0.01 M As_2O_3 for 30 minutes at room temperature. The lattice spacing measured in the HRTEM image was consistent with the d_{220} plane spacing of zincblende crystalline InAs.[32] In turn, the selected area electron diffraction (SAED) pattern collected from the InAs film (Figure 5.4d) was in agreement with the simulated SAED pattern for a zincblende InAs crystal viewed along the [111] zone axis.[32] Diffuse rings or satellite diffraction spots were not observed, consistent with a pure crystalline material as opposed to a crystalline/amorphous mixture. A low magnification TEM image (Figure 5.8a) shows a mechanically removed InAs film agglomerate composed of many small grains. The corresponding SAED pattern (Figure 5.8b) collected over the entire field of view reveals multiple diffraction rings characteristic of the indexed polycrystalline zincblende InAs phase. X-ray diffraction of the very thin (< 60 nm) InAs films is in fact observed (Figure 5.9) in the standard Bragg-Brentano geometry, however due to the bulk probing nature of X-rays, intense reflections from the underlying In(*s*) foil are most dominant. For that reason, Powder X-ray diffraction was used only as a secondary confirmation of structure and as a qualitative probe of crystallite size. InAs films grown at room temperature for 60 minutes clearly show diffraction reflections for the (111), (220) and (311) planes expected for the zincblende phase observed in HRTEM. Scherrer analysis of both the native In(*s*) foil (Figures 5.10, 5.11 and Table 5.2) and the InAs thin film on In(*s*) foil structure (Figures 5.9 and Table 1) reveal the grain sizes to be on average 45.4 and 16.4 nm, respectively.

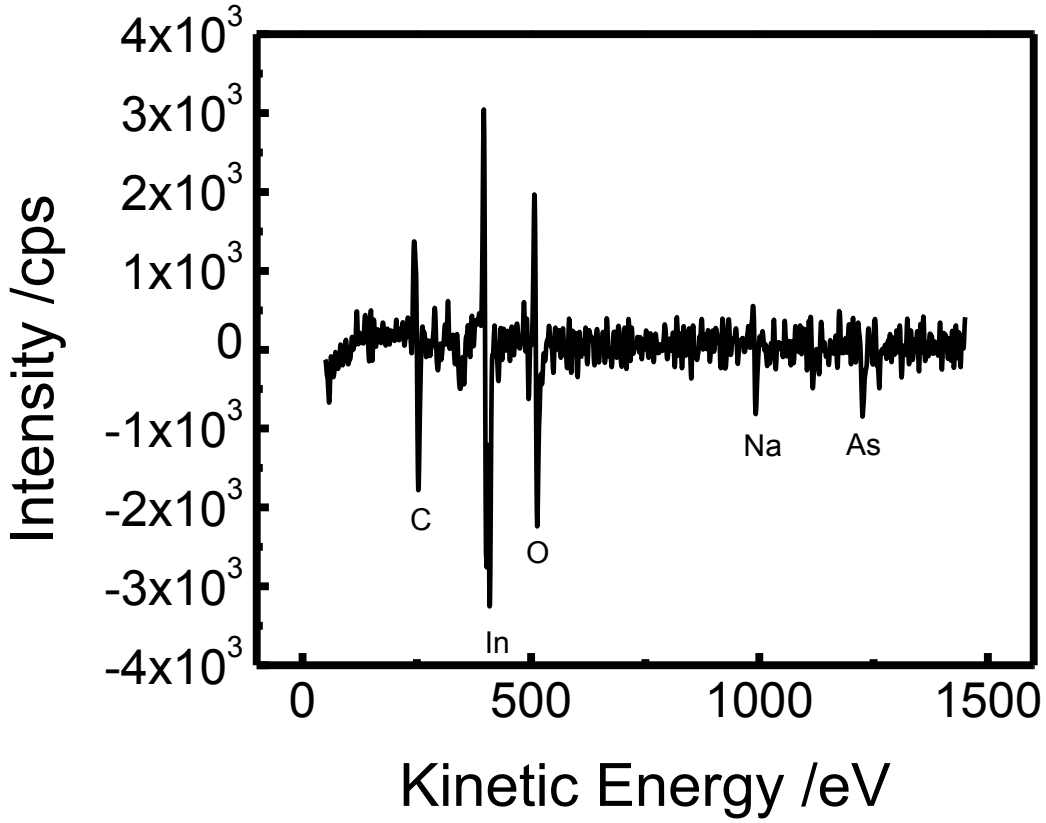

Figure 5.7. Differentiated Auger spectrum collected from an InAs film prepared for 60 minutes at -1.3 V from 0.01 M As_2O_3, 0.1 M NaOH, and 0.1 M Na_2SO_4 electrolyte.

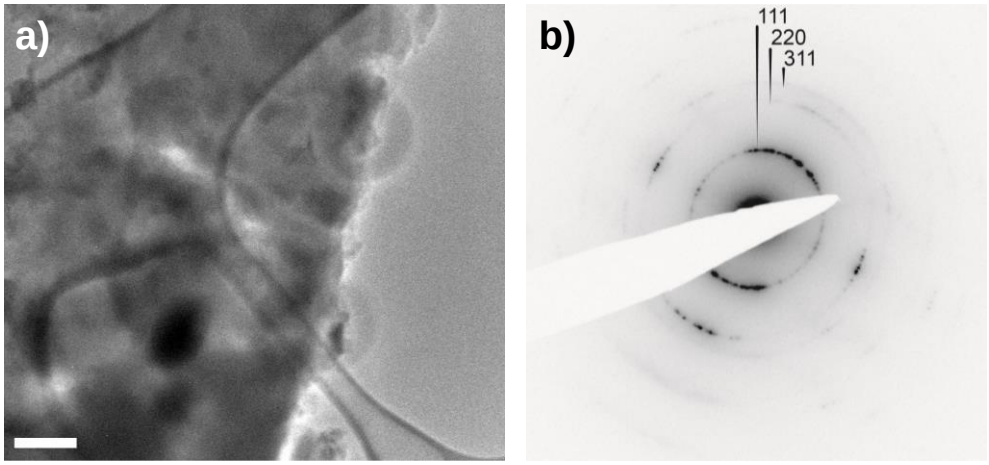

Figure 5.8. (a) Low magnification bright field TEM image of an InAs agglomerate after mechanical scraping from the indium foil substrate and (b) the corresponding large field of view selected area electron diffraction pattern collected from the agglomerate shown in (a). The scale is 200 nm.

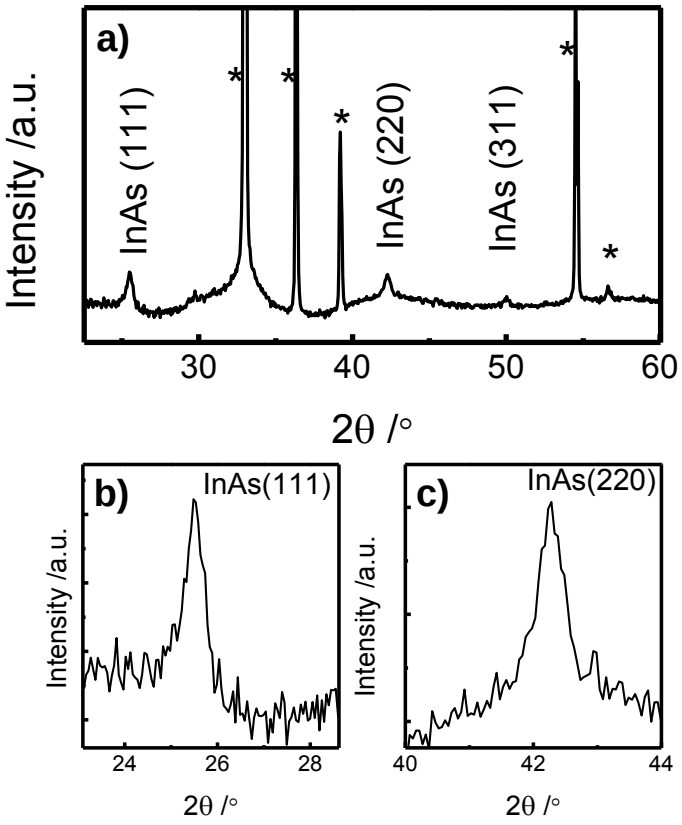

Figure 5.9. (a) Powder X-ray diffraction pattern collected from an InAs film prepared on an In(*s*) foil for 60 min at room temperature from a 0.01 M As_2O_3 solution. Asterisks denote reflections from the bulk tetragonal In(*s*) substrate (I4/mmm). Magnified views of the (a) InAs (111) and (b) InAs (220) reflections used for Scherrer crystallite size analysis.

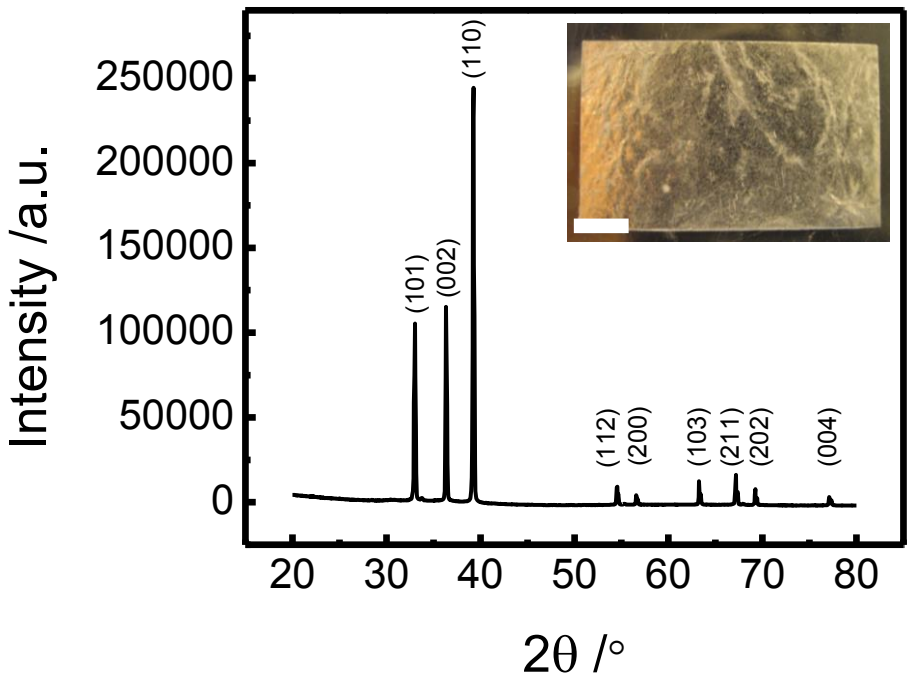

Figure 5.10. Powder X-ray diffraction pattern collected from the native In(*s*) foil substrate pictured in the inset. Inset scale is 2 mm.

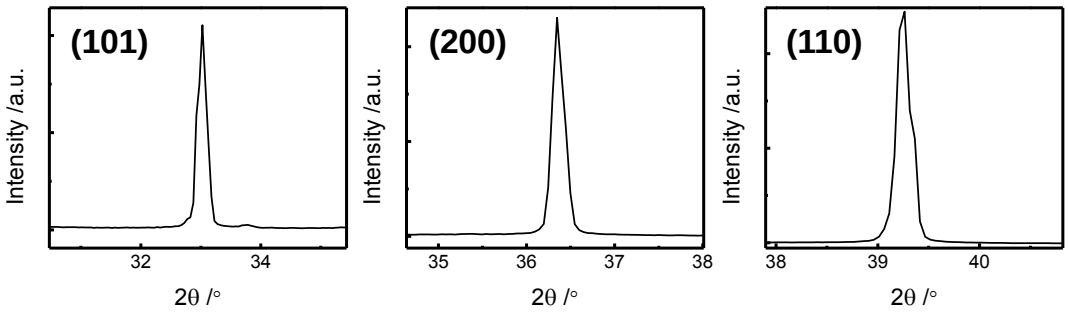

Figure 5.11. Magnified views of the powder X-ray diffraction pattern segments from the In(*s*) foil pictured in Figure 5.10 for the (a) (101), (b) (200), and (c) (110) reflections of tetragonal indium metal (I4/mmm).

Table 5.1. Tabulated InAs X-ray Diffraction Data for Scherrer Analysis

hkl	**2θ /°**	**FWHM /rad**	**D_{hkl} /nm[a]**
111	25.4820	0.008775	15.8
220	42.2814	0.008583	16.9

[a] Thickness ⊥ to *hkl* plane

Table 5.2. Tabulated In Foil X-ray Diffraction Data for Scherrer Analysis

hkl	**2θ /°**	**FWHM /rad**	**D_{hkl} /nm[a]**
101	33.0270	0.003626	39.0
200	36.3464	0.002997	47.6
110	39.2636	0.002901	49.6

[a] Thickness ⊥ to *hkl* plane

The homogeneity of the putative crystalline InAs films as a function of dissolved As_2O_3 concentration in solution was probed. Since film uniformity was difficult to assess by electron microscopy and conventional X-ray diffraction, Raman mapping of the InAs TO phonon mode at 216 cm^{-1} was used. Figure 5.12 shows two Raman spectral color intensity maps collected over 50 x 50 μm spots from two different In electrodes biased at E_{app} = -1.3V with 0.01 M and 0.001 M of dissolved As_2O_3. The Raman map in Figure 5.12a was collected from an InAs film prepared under a potentiostatic bias of -1.30 V for 5 minutes in a 0.001 M As_2O_3 solution. The color intensity over the map is non-uniform (the relative standard deviation in pixel intensity was ± 39.4 %) and the average intensity of the LO mode was relatively low above the background noise ($S/N \leq 4.5$), indicating a thin, discontinuous InAs film. Figure 5.12b shows a Raman intensity map for an In electrode biased at -1.30 V in a 0.01 M As_2O_3 solution for 60 min. This film showed uniform color intensity over the probed area (relative standard deviation in pixel intensity was 4.1 %) and the signal to noise was significantly higher ($S/N \leq 42.5$), implying a thicker and more uniform InAs film. Electrodeposition from the dilute 0.001 M As_2O_3 electrolyte for longer durations (> 90 min) revealed more uniform purple films similar to those deposited from 0.01 M As_2O_3 electrolytes at shorter durations (Figure 5.13).

Time-lapse optical photographs of In electrodes were collected throughout a 12 hr potential step experiment with E_{app} = -1.3 V in 0.01 M As_2O_3 (Figure 5.14a). The initial silver hue of the clean In foil changed to a light orange after 10 min and then progressed through shades of dark amber, violet, and eventually green after 12 hours at E_{app} = -1.3 V. A cessation in the apparent color change occurred only if the electrodeposition was halted, indicating the film formation was being gated electrochemically. As-prepared InAs films at various time points during the first hour were separately washed and then dissolved in acid so as to estimate the film thickness from the total As content, as measured with inductively coupled plasma atomic emission spectroscopic (ICP-AES). The total measured As mass, in conjunction with the density of InAs, was then used to calculate the average InAs film thicknesses for three separate electrodes at each time point with the assumption the film was homogenous over the entire electrode surface. Figure 5.14b shows that the apparent InAs film thickness increased steadily as a function of electrodeposition time, attaining a thickness of approximately 60 nm after 1 hr.

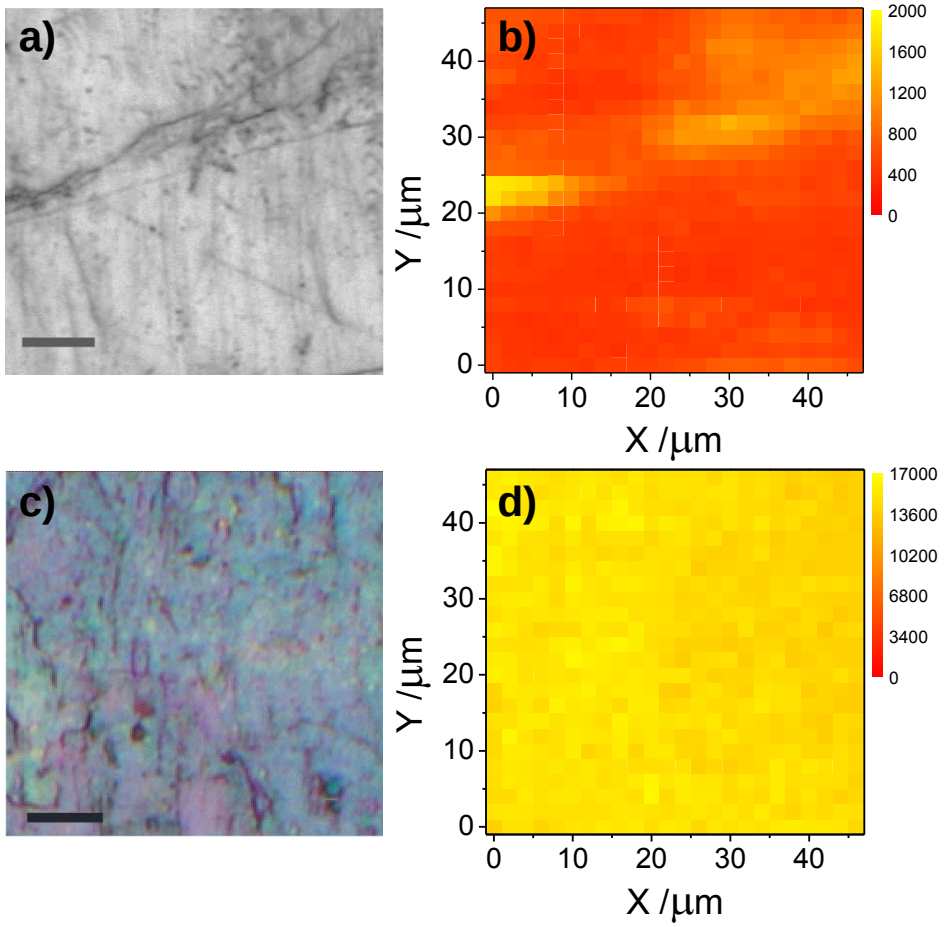

Figure 5.12. Optical micrographs (a, c) of two In electrodes after treatment and the corresponding Raman color maps (b, d) for the signal measured at 216 cm^{-1} (i.e. InAs TO phonon mode). The In electrodes were biased at -1.3 V in an aqueous 0.1 M Na_2SO_4, and 0.1 M NaOH solution containing either (a, b) 0.001 M As_2O_3 for 5 min or (c, d) 0.01 M As_2O_3 for 60 min. Scale bar: 10 µm.

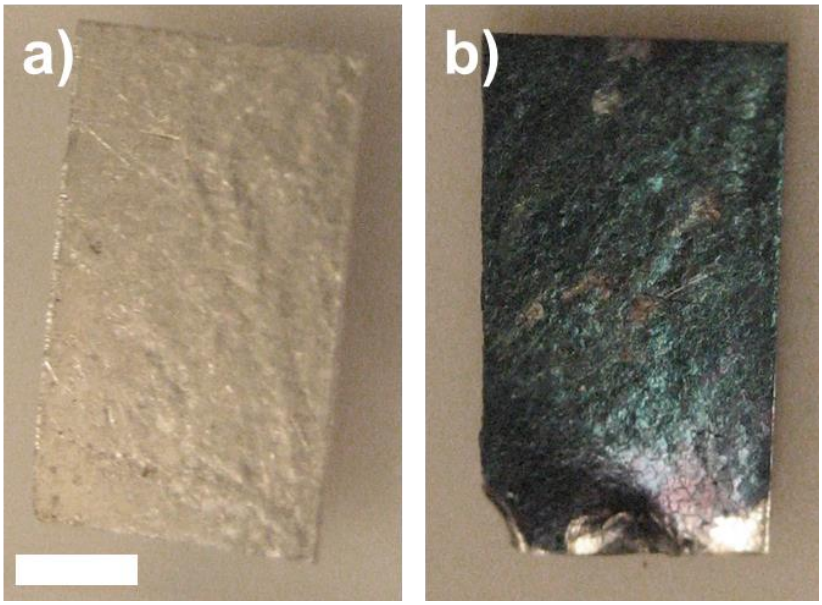

Figure 5.13. Optical micrographs collected from an In(*s*) foil (a) before and (b) after InAs electrodeposition from a 0.001 M As_2O_3 solution at -1.3 V for 120 minutes. Scale is 2 mm.

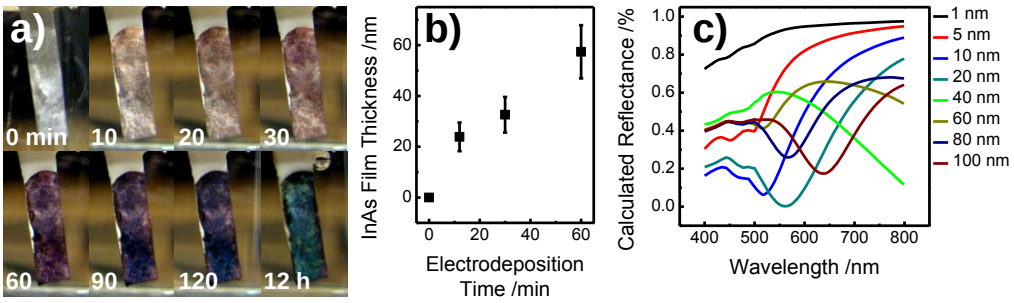

Figure 5.14. (a) Optical images of an In electrode immersed in an aqueous solution containing 0.01 M As_2O_3, 0.1 M Na_2SO_4, and 0.1 M NaOH and biased at -1.3 V for 0, 10, 20, 30, 60, 90, 120, and 720 min. Experiments were performed at T = 25 °C. (b) InAs film thicknesses measured by inductively coupled plasma atomic emission spectroscopy as a function of electrodeposition time for 0, 15, 30, and 60 min. (c) Calculated wavelength-dependent reflectance of InAs thin films as a function of thickness on a reflective substrate in air.

A one-dimensional thin film optical model based on the complex matrix form of the Fresnel equations was used to calculate the total reflectance (i.e. color) of uniform InAs films on the In foil (Figure 5.14c) as a function of thickness. The red color of the 60 nm InAs film was in accord with predictions from the optical model. The thickness of the as-prepared InAs films was also probed by collecting compositional depth profiles in a Scanning Auger Microprobe equipped with a focused Ar^+ ion sputtering beam (Figure 5.15a). The depth profile indicates a constant In/As ratio with depth until 85 ± 3 nm after which the As signal decays to zero, and only the bulk In(*s*) foil is probed. After sputtering the InAs film completely, the electrode color changed from blue back to the native silver hue of pure In(*s*) foil (Figure 5.15b,c). Taken together, the data in Figures 5.14 and 5.15 indicate a slow but continuous growth of a crystalline InAs film under these electrochemical conditions.

The ICP-AES measurements were sufficiently tedious and the thickness-dependent color change of the growing InAs films was complex enough that neither approach proved expedient for estimating any potential-dependent kinetic information about the InAs formation. Instead, a different descriptor was used to assess the time-dependence of this electrochemical process. The formation of InAs was probed with time-dependent Raman spectra collected during the course of several potential step experiments. A custom short working distance spectroelectrochemical cell was designed and fabricated to (1) minimize solvent evaporation and (2) avoid scattering losses through the electrolyte layer.[Appendix A.6] The experimental setup is illustrated schematically in Figure 5.16. For analysis of a thin film on a thick substrate, the measured Raman intensity for the thin film reports on the film thickness when the Raman probe depth extends well beyond the thin film,[33-35] That is, the measured Raman signal is a linear descriptor of InAs film thickness. Figures 5.17a-c show the time-dependent Raman spectra for three potential-step experiments conducted at room temperature with 0.01 M As_2O_3 and E_{app} = -1.25, -1.30 and -1.35 V, respectively. In all three spectral series, the TO and LO phonon modes were observed within 20 min. Both signatures for the TO and LO modes increased in intensity over time but the peak positions and peak widths remained unchanged with time, implying the film quality (i.e. crystallite size) was independent of both the electrodeposition time and applied potential.

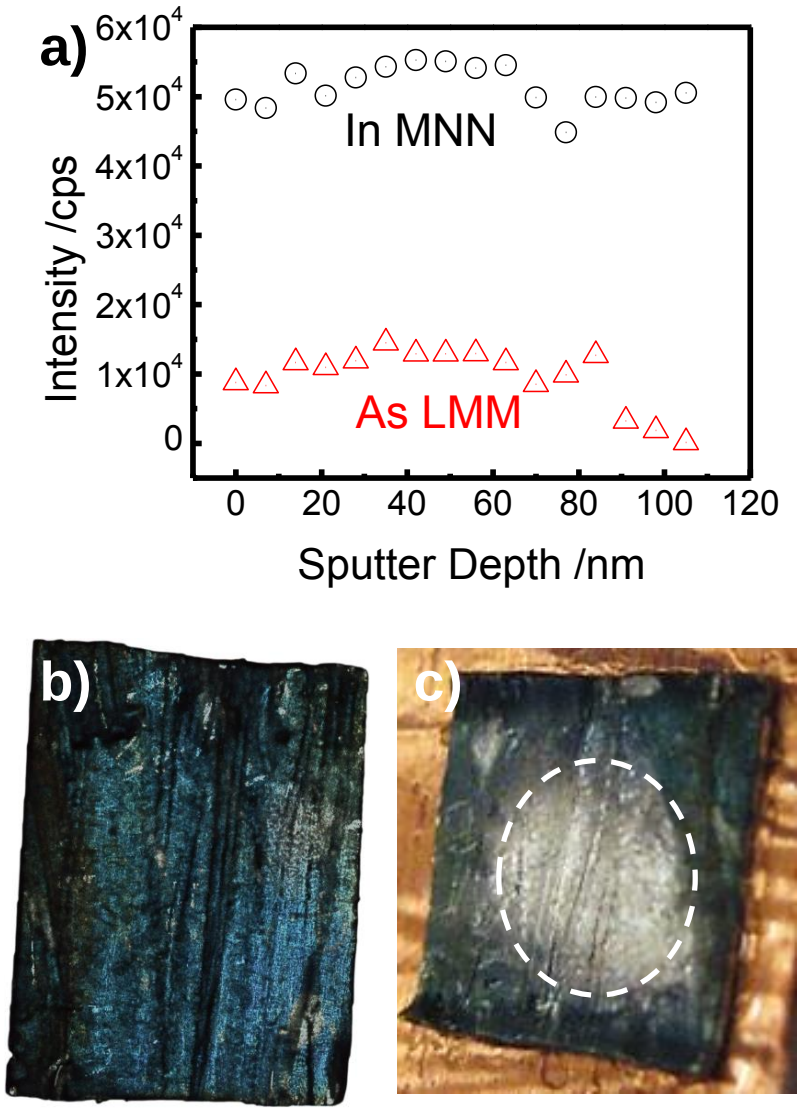

Figure 5.15. (a) Scanning Auger Nanoprobe sputtering depth profile of InAs thin film prepared on an In(*s*) foil substrate at -1.3 V for 60 minutes in 0.01 M As_2O_3. Corresponding optical image of the as-prepared InAs film (a) before sputtering and (b) after 110 nm sputtering depth. The dashed line in (c) indicates the location of the sputter probe.

The intensity of these modes reached a maximum at approximately 160 min. At longer times, two additional spectral features emerged at 200 cm^{-1} and 240-270 cm^{-1}. These new features were consistent with the formation of amorphous As(*s*).[36,37] The intensity of the amorphous As(*s*) Raman signature also increased after 160 min but remained unchanged if the applied bias was removed, i.e. spontaneous conversion of crystalline InAs(*s*) to amorphous As(*s*) was not observed. Figure 5.17d presents the time-dependent progression of the measured intensity for the InAs TO mode in Figures 5.17a-c. Over this 100 mV potential range, the three time-dependent profiles were nominally identical, with the measured intensity for the TO increasing monotonically for the first 160 min. These data imply that the formation of InAs, as probed by Raman, was not a strong function of the applied potential.

The time-dependences in Figure 5.17d were fit with a one dimensional model that describes a solid-state reaction between two contacting phases that react to form one alloy with 1:1 stoichiometry (Figure 5.18).[38,39] If InAs formation occurs by reduced As atoms/clusters that diffuse into and react with In(*s*), then the thickness of the InAs layer (x_{InAs}) as a function of reaction time (t) should be a function of both the reaction rate constant, k (cm s^{-1}), between In and As as well as the diffusivity of As in In, D_{As} (3.3 x 10^{-15} cm^2 s^{-1}).[19,38-44]

$$\frac{dx_{InAs}}{dt} = \frac{kD_{As}}{D_{As} + kx_{inAs}} \tag{5.3}$$

Integrating Equation 5.3 with the initial condition $x_{InAs} = 0$ at $t = 0$ yields the following explicit time dependent relationship for x_{InAs}.

$$x_{InAs}(t) = -\frac{D_{As}}{k} + \sqrt{\frac{{D_{As}}^2}{k^2} + 2D_{As}t} \tag{5.4}$$

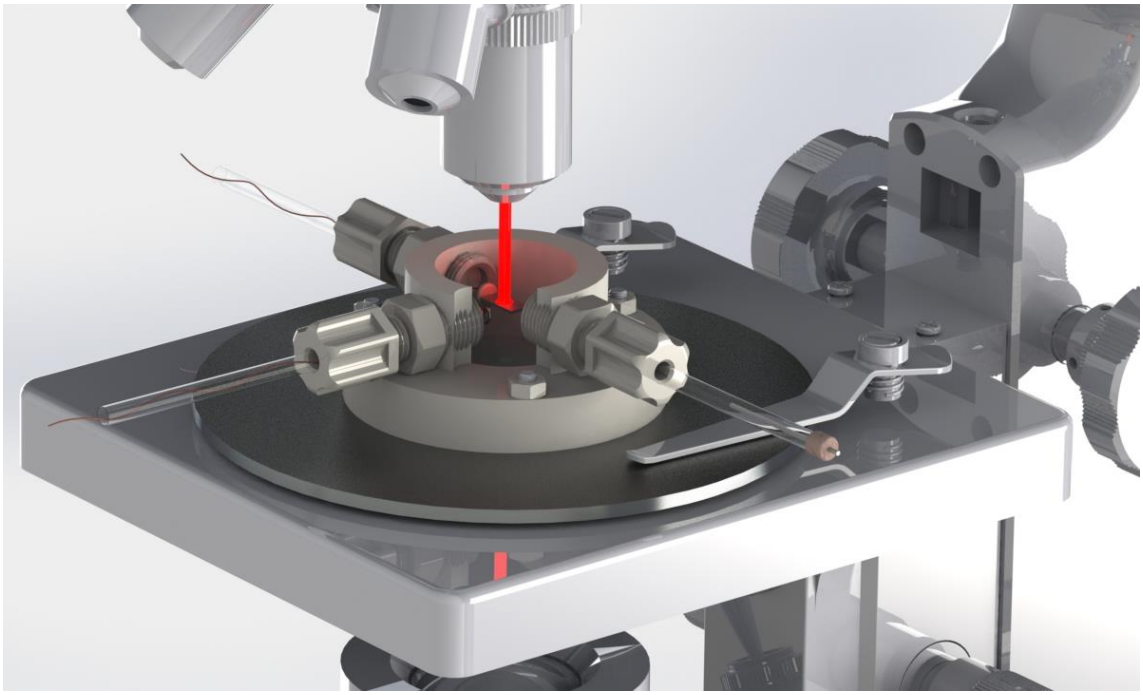

Figure 5.16. Rendered schematic of the in-situ spectroelectrochemical cell designed, fabricated, and employed for observing InAs formation in real-time.

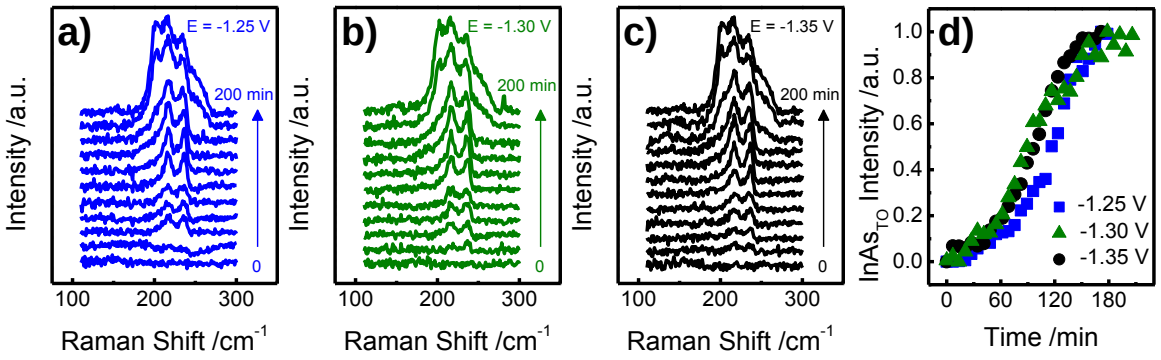

Figure 5.17. Raman spectra collected every 20 min at In electrode immersed in an aqueous solution containing 0.01 M As_2O_3, 0.1 M Na_2SO_4, and 0.1 M NaOH at *E* = (a)-1.25 V, (b)-1.30 V, and (c)-1.35 V. Experiments were performed at *T* = 25 °C. (d) Intensity of the TO mode at 216 cm^{-1} as a function of time at each applied potential. Intensities were normalized to the value recorded at *t* = 200 min.

Using Equation 5.4, the rising portions of the datasets in Figure 5.17 yielded values of 3 x 10^{-9}, 4 x 10^{-9}, and 4 x 10^{-9} cm $s^{-1}$for k at E = -1.25, -1.30 and -1.35 V, respectively.

5.4. Discussion

The collective data strongly support the hypothesis that InAs films can be prepared electrochemically from an aqueous bath at room temperature. The as-prepared InAs films did not require thermal annealing and instead were crystalline as-produced. The application of an external electrochemical bias provided a means to form (and maintain) a clean In interface that was reactive towards As, even while submerged in water, representing a new tactic for performing desirable alloying reactions like the spontaneous interaction of In(*s*) and As(*s*). In this way, this new method for synthesizing a III-V semiconductor film has both some parallels to and strong advantages over other synthetic methods.

Although the presented work is electrochemical in nature, it differs significantly from typical electrodeposition strategies for the preparation of InAs. In conventional electrodeposition, InAs is formed through the co-electrodeposition of In and As from an electrolyte bath containing dissolved (oxidized) precursors for each element.[8-10] Simultaneous co-electrodeposition of In and As on a current collector is problematic for three reasons. First, simultaneous co-electrodeposition of In and As from their parent oxides is difficult due to marked differences in their respective standard reduction potentials (ΔE > 500 mV), narrowing the possible electrolyte conditions (e.g. pH).[45] Second, the product InAs is often non-stoichiometric since balancing the rates of In and As deposition precisely is challenging.[46-49] Third, as-deposited films are more akin to physical mixtures of the individual elements[49-51] or amorphous alloys. Crystalline InAs cannot be directly obtained by this method.[50,52] In contrast, the results shown here indicate that requiring only the deposition of As onto a pre-existing clean In electrode circumvents all three issues entirely. Electrochemical atomic layer epitaxy (ECALE) is one notable electrodeposition exception. ECALE consists of sequential underpotential deposition of In and As monolayers to form ordered InAs on a noble metal electrode.[11-13] With ECALE, thick (> 10-20 monolayers) InAs films are difficult to obtain without significant three-dimensional growth and the possibility of oxide formation between the layered deposition

steps. In these aspects, the electrochemical alloying tactic presented here can grow thick semiconductor films relatively quickly without fear of oxide formation.

Apart from electrodeposition strategies, the presented work here superficially resembles the electrochemical method first reported by Miller and Heller, i.e. controlled anodization of metal (Cd) electrodes in sulfide-containing electrolytes to produce metal sulfide (e.g. CdS) films.[53] Subsequent work along this vein showed that several Cd-VI semiconductors could be made in this way. This anodization process involves positive applied potentials where the metal (Cd) electrode is oxidized and partially dissolved in the electrolyte.[54,55] The resultant sulfide/selenide/telluride films the form through a controlled precipitation reaction adjacent to/on the electrode surface,[56] first nucleating and then depositing as individual clusters unevenly on the electrode surface. Accordingly, semiconductor films with sufficient quality for high performance photovoltaic applications has not been achieved[55] and has accordingly fell out of favor. In contrast, the work presented here for InAs synthesis does **not** utilize oxidizing conditions that cause dissolution of the (In) electrode. Instead, substantially negative potentials are used to *reduce* dissolved species and cathodically protect the electrode material, i.e. the applied potential thermodynamically favors In^0 and As^0. Figure 5.19 explicitly shows the Pourbaix diagrams (i.e. three-dimensional plots depicting the most stable species at each possible set of potential and pH values) calculated through the Materials Project (https://materialsproject.org)[57] for the In-H_2O and In-As-H_2O systems. As indicated in Figure 5.19a, in alkaline solution, an oxide is formed on In at positive potentials. In_2O_3 is not soluble at high pH,[58] implying little to no dissolved In species in solution in the experiments performed here. Accordingly, the conditions employed here argue against a precipitation of InAs from a homogeneous reaction between dissolved In and As species.

For perspective, the results demonstrated here more directly relate to alloying reactions performed at high temperature under strong vacuum conditions. Specifically, the spontaneous formation of InAs by dosing As(g) onto an ultra-clean In surface (maintained by vacuum) was first demonstrated decades ago.[5,6] The method demonstrated that InAs would form spontaneously if a clean In/As interface could be maintained.

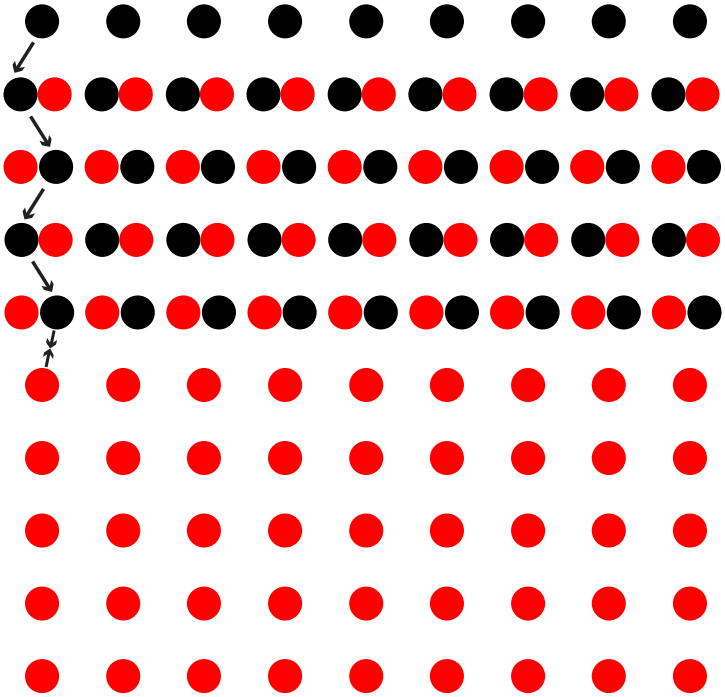

Figure 5.18. Schematic depiction of the growth of a 1:1 binary alloy between (red) atoms in a metal substrate and (black) adatoms on the surface. The alloying reaction is presumed to occur precisely at the interface between adatoms that diffuse to the underlying substrate.

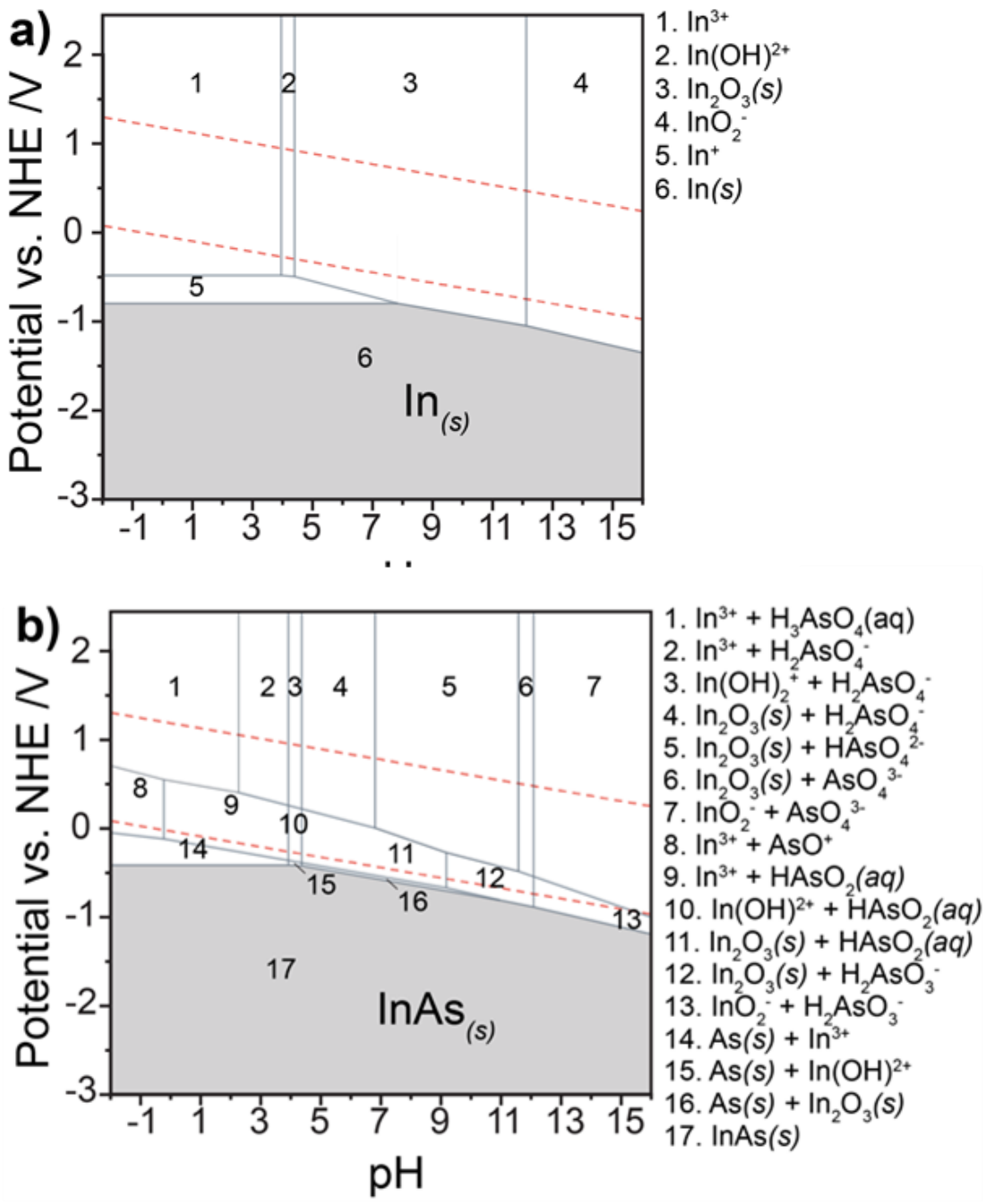

Figure 5.19. Pourbaix diagrams for a) In-H_2O and b) In-As-H_2O depicting the most stable chemical species at each corresponding pH and potential value. The grey regions indicate potential-pH combinations where In(*s*) and InAs(*s*) are thermodynamically stable, respectively. Vertical lines delineate acid/base transitions and horizontal lines depict redox reactions. Dashed red lines indicate the standard potentials for water reduction and water oxidation. The numbered regions of the plots corresponded to the list of stable species to the right of each plot.

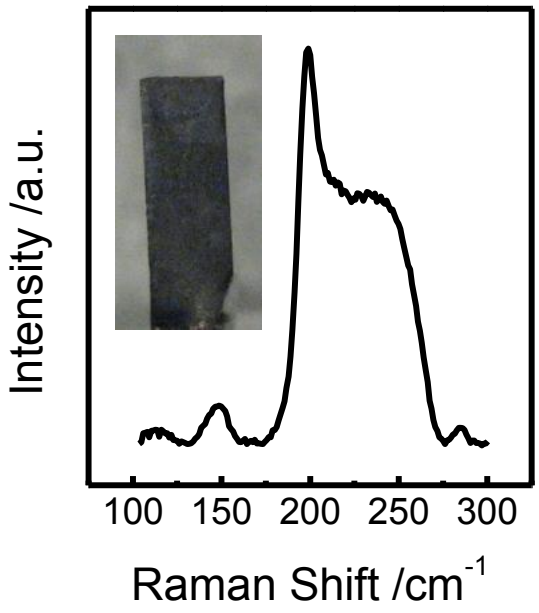

Figure 5.20. Raman spectrum for film deposited at an In(*s*) electrode biased at -1.3 V for 30 min in a room temperature aqueous solution containing 0.1 M As_2O_3, 0.1 M Na_2SO_4 and 0.1 M NaOH. The inset shows an optical image of the corresponding film.

Subsequent attempts at attaining this condition have involved a combination of higher temperatures and/or environments chemically corrosive to the oxides of In and As. The same effect was achieved here but using only an applied negative potential. As indicated on the In-H_2O Pourbaix diagram (Figure 5.19) and confirmed by our voltammetric measurements (Figures 5.2 and 5.3a), biasing the In electrodes at potentials more negative than the oxide stripping wave effected a clean, fully reduced In surface that spontaneously reacted with electrodeposited As. This feature is deceptively powerful, as the desirable metallurgical reaction to form InAs occurred at a clean In interface *in water* eliminating the need for the equipment/reagents for reductive gaseous ambients, high temperatures, and high vacuum.

Beyond simply 'gating' the reactability of the In electrode surface towards alloying reactions, electrochemical arsenate reduction also afforded control of the introduction of As onto In(*s*). Based on the collected data, both the concentration of dissolved arsenates and the electrodeposition time have measurable impact on the formation of InAs electrochemically. At high ($\geq$ 0.1 M) formal concentrations of arsenates, dull black amorphous As(*s*) was the predominant phase detected on the electrode surface at short and long experiment times (Figure 5.20). In more dilute (0.01 M) arsenate solutions, a surplus of amorphous As was detected on top of the newly formed InAs films after long (t > 160 min) experiment times. At short (t < 160 min) times, this electrolyte concentration yielded films that were smooth and pure crystalline InAs without detectable amorphous As(*s*). Further, performing the electrodeposition experiments for short times in 0.001 M arsenate solutions yielded crystalline InAs without amorphous As, but with spotty and uneven coverage as evidenced by Raman spectral mapping. However, if the electrodeposition was continued for longer periods of time (t > 90 min), the film uniformity began to resemble films grown from higher concentration As_2O_3 for shorter durations (Figure 5.13). Hence, we posit that dilute concentrations of dissolved As_2O_3 should favor a slow and controlled formation of As(*s*) adatoms/clusters on the In(*s*) electrode surface where two dimensional As films are favored over large three dimensional As^0 clusters.[59] Higher densities of discrete As nuclei lead to more uniform growth of InAs films. Similarly, when As is electrodeposited sufficiently slow so that excess As does not accumulate on the surface, pure InAs films are the only product. Electrodeposition from increasingly more dilute

solutions did not change the identity or uniformity of the deposit, only the rate at which film homogeneity was achieved. In this capacity, the results here demonstrate electrochemical 'dosing' control not possible in wet chemical alloy conversion reactions[60] and with more precision and simpler control equipment than in high vacuum/high temperature alloying reactions.

To be clear, the electrochemical potential used for the electroreduction of arsenates onto In did not change the shape or intensity of the collected Raman spectra, implying no role of the applied potential on crystallization. Further, the apparent rate constants for InAs film growth were invariant towards the applied potential. These observations stand in contrast to conventional electrodeposition processes that follow standard electrochemical kinetic models (e.g. Butler-Volmer) where the rate is strongly activated by the applied potential.[61] Instead, the data argue that one or both of the non-electrochemical processes (i.e. the alloying reaction, the diffusion of As in In, and the nucleation/crystallization) are the rate-limiting steps in the InAs synthesis presented here. Since the measured film thicknesses of InAs of 58 ± 4 nm after a 60 min experiment are consistent with the thickness expected based on the diffusivity of As in In(*s*), the data implicate diffusion rather than the kinetics of alloying or the speed of crystal formation as the rate limiting process.

5.5. Conclusions

The cumulative data in this chapter show that crystalline InAs films can be directly prepared by an electrochemically-controlled alloying reaction between In(*s*) electrodes and electrodeposited As nuclei. The demonstrated work was performed entirely in aqueous solutions at room temperature and ambient pressure without additional annealing or subsequent process steps. The cumulative measurements showed crystallinity unattainable by other electrochemical methods and simplicity unmatched by any other known process. Specifically, a salient feature of this work is the precedent for a III-V semiconductor preparation strategy that does not require vacuum or sophisticated furnaces, toxic gaseous precursors like arsine, or exotic solvents. This preliminary work demonstrates the proof of concept for direct preparation of crystalline InAs in an electrochemically gated alloy process but does not define the full extent possible. Although not tested explicitly here, this reactive electrodeposition process should be amenable to complete conversion of thin In(*s*) films to InAs films. A potential advantage of the electrochemical strategy shown here is

tight thickness control since applied potential/current waveforms can be performed with a high degree of temporal precision. More work is needed to identify what aspects control InAs crystallization so as both to produce the highest possible quality InAs and more generally to define the extent that electrode alloying can be used to form useful semiconductors.

5.6. References

1. Dick, K. A.; Deppert, K.; Martensson, T.; Mandl, B.; Samuelson, L.; Seifert, W. *Nano Lett.* **2005**, *5*, 761.
2. Krier, A.; Gao, H. H.; Sherstnev, V. V. *J. Appl. Phys.* **1999**, *85*, 8419.
3. Ye, H.; Li, L.; Hinkey, R. T.; Yang, R. Q.; Mishima, T. D.; Keay, J. C.; Santos, M. B.; Johnson, M. B. *J. Vac. Sci. Technol., B.* **2013**, *31*.
4. Mårtensson, T.; Wagner, J. B.; Hilner, E.; Mikkelsen, A.; Thelander, C.; Stangl, J.; Ohlsson, B. J.; Gustafsson, A.; Lundgren, E.; Samuelson, L.; Seifert, W. *Adv. Mater.* **2007**, *19*, 1801.
5. Godinho, N.; Brunnsch.A *Solid-State Electron.* **1970**, *13*, 47.
6. Epstein, M. *J. Appl. Phys.* **1965**, *36*, 2590.
7. Xie, Y.; Yan, P.; Lu, J.; Wang, W. Z.; Qian, Y. T. *Chem. Mat.* **1999**, *11*, 2619.
8. Dalchiele, E.; Cattarin, S.; Musiani, M.; Casellato, U.; Guerriero, P.; Rossetto, G. *J. Electroanal. Chem.* **1996**, *418*, 83.
9. Mengoli, G.; Musiani, M. M.; Paolucci, F. *J. Electroanal. Chem.* **1992**, *332*, 199.
10. Ortega, J.; Herrero, J. *J. Electrochem. Soc.* **1989**, *136*, 3388.
11. Innocenti, M.; Forni, F.; Pezzatini, G.; Raiteri, R.; Loglio, F.; Foresti, M. L. *J. Electroanal. Chem.* **2001**, *514*, 75.
12. Wade, T. L.; Vaidyanathan, R.; Happek, U.; Stickney, J. L. *J. Electroanal. Chem.* **2001**, *500*, 322.
13. Wade, T. L.; Ward, L. C.; Maddox, C. B.; Happek, U.; Stickney, J. L. *Electrochem. Solid-State Lett.* **1999**, *2*, 616.
14. Fahrenkrug, E.; Gu, J.; Maldonado, S. *J. Am. Chem. Soc.* **2013**, *135*, 330.
15. Rogalski, A.; Antoszewski, J.; Faraone, L. *J. Appl. Phys.* **2009**, *105*.
16. Du, J.; Liang, D.; Tang, H.; Gao, X. P. A. *Nano Lett.* **2009**, *9*, 4348.
17. Chang, C.-C.; Sharma, Y. D.; Kim, Y.-S.; Bur, J. A.; Shenoi, R. V.; Krishna, S.; Huang, D.; Lin, S.-Y. *Nano Lett.* **2010**, *10*, 1704.
18. Milnes, A. G.; Polyakov, A. Y. *Mater. Sci. Eng., B* **1993**, *18*, 237.
19. Kozlov, V. M.; Bozzini, B.; Bicelli, L. P. *J. Alloys Compd.* **2004**, *366*, 152.
20. Kegel, I.; Metzger, T. H.; Lorke, A.; Peisl, J.; Stangl, J.; Bauer, G.; Garcia, J. M.; Petroff, P. M. *Phys. Rev. Lett.* **2000**, *85*, 1694.
21. Pourbaix, M. *Atlas of Electrochemical Equilibria*; 2nd ed.; National Association of Corrosion Engineers: Houston, TX, 1974.
22. Arnold, J. P.; Johnson, R. M. *Talanta* **1969**, *16*, 1191.
23. Bejan, D.; Bunce, N. J. *J. Appl. Electrochem.* **2003**, *33*, 483.
24. Omanović, S.; Metikoš-Huković, M. *Thin Solid Films* **1995**, *266*, 31.
25. Omanovic´, S.; MetikoŠ-HukoviČ, M. *J. Appl. Electrochem.* **1997**, *27*, 35.
26. Cantoro, M.; Klekachev, A. V.; Nourbakhsh, A.; Soree, B.; Heyns, M. M.; De Gendt, S. *European Physical Journal B* **2011**, *79*, 423.
27. Schwartz, G. P.; Dutt, B. V.; Gualtieri, G. J. *Appl. Phys. Lett.* **1981**, *39*, 52.
28. Lannin, J. S. *Phys. Rev. B* **1977**, *15*, 3863.
29. Wihl, M.; Cardona, M.; Tauc, J. *J. Non-Cryst. Solids* **1972**, *8–10*, 172.
30. Ashby, C. I. H.; Sullivan, J. P.; Newcomer, P. P.; Missert, N. A.; Hou, H. Q.; Hammons, B. E.; Hafich, M. J.; Baca, A. G. *Appl. Phys. Lett.* **1997**, *70*, 2443.
31. Supangat, A.; Bryant, G.; Belcher, W.; Dastoor, P. *Mater. Res. Innov.* **2012**, *16*, 101.

32. Tomioka, K.; Motohisa, J.; Hara, S.; Fukui, T. *Jpn. J. Appl. Phys. 2* **2007**, *46*, L1102.
33. Aspnes, D. E.; Studna, A. A. *Phys. Rev. B* **1983**, *27*, 985.
34. Cheetham, K. J.; Carrington, P. J.; Krier, A.; Patel, I. I.; Martin, F. L. *Semicond. Sci. Technol.* **2012**, *27*, 015004.
35. McCreery, R. L. *Raman spectroscopy for chemical analysis*; John Wiley & Sons: New York, 2000.
36. Lannin, J. S. *B. Am. Phys. Soc.* **1976**, *21*, 461.
37. Lannin, J. S. *Phys. Rev. B* **1977**, *15*, 3863.
38. Dybkov, V. I. *J. Mater. Sci. Lett.* **1990**, *9*, 1459.
39. Dybkov, V. I. *J. Phys. Chem. Solids* **1992**, *53*, 703.
40. Natan, M.; Duncan, S. W. *Thin Solid Films* **1985**, *123*, 69.
41. Lien, C. D.; Nicolet, M. A.; Lau, S. S. *Thin Solid Films* **1986**, *143*, 63.
42. Tu, K. N.; Thompson, R. D. *Acta Metall. Mater.* **1982**, *30*, 947.
43. Wohlert, S.; Bormann, R. *J. Appl. Phys.* **1999**, *85*, 825.
44. Kleinkne.Hp *J. Appl. Phys.* **1966**, *37*, 2116.
45. Bard, A. J.; Parsons, R.; Jordan, J.; International Union of, P.; Applied, C. *Standard potentials in aqueous solution*; M. Dekker: New York, 1985.
46. Chandra, S.; Khare, N. *Semicond. Sci. Technol.* **1987**, *2*, 214.
47. Mahalingam, T.; Lee, S.; Lim, H.; Moon, H.; Kim, Y. D. *Sol. Energy Mater.* **2006**, *90*, 2456.
48. Yang, M. C.; Landau, U.; Angus, J. C. *J. Electrochem. Soc.* **1992**, *139*, 3480.
49. Dalchiele, E.; Cattarin, S.; Musiani, M.; Casellato, U.; Guerriero, P.; Rossetto, G. *J. Electroanal. Chem.* **1996**, *418*, 83.
50. Murali, K. R.; Trivedi, D. C. *J. Phys. Chem. Solids* **2006**, *67*, 1432.
51. Gheorghies, C.; Gheorghies, L.; Fetecau, G. *J. Optoelectron. Adv. M.* **2007**, *9*, 2795.
52. Lajnef, M.; Ezzaouia, H.; Chtourou, R. *J. Phys. D-Appl. Phys.* **2008**, *41*.
53. Miller, B.; Heller, A. *Nature* **1976**, *262*, 680.
54. Ham, D.; Son, Y.; Mishra, K. K.; Rajeshwar, K. *J. Electroanal. Chem.* **1991**, *310*, 417.
55. Rajeshwar, K. *Adv. Mater.* **1992**, *4*, 23.
56. Ham, D.; Mishra, K. K.; Rajeshwar, K. *J. Electrochem. Soc.* **1991**, *138*, 100.
57. Persson, K. A.; Waldwick, B.; Lazic, P.; Ceder, G. *Phys. Rev. B* **2012**, *85*.
58. Schweitzer, G. K.; Pesterfield, L. L. *The aqueous chemistry of the elements*; Oxford University Press: Oxford ; New York, 2010.
59. Guo, L.; Oskam, G.; Radisic, A.; Hoffmann, P. M.; Searson, P. C. *J. Phys. D-Appl. Phys.* **2011**, *44*.
60. Henkes, A. E.; Vasquez, Y.; Schaak, R. E. *J. Am. Chem. Soc.* **2007**, *129*, 1896.
61. Bard, A. J.; Faulkner, L. R. *Electrochemical Methods*; 2nd ed.; John Wiley & Sons: UK, 2004.

CHAPTER 6

Conclusions and Prospects for ec-LLS

6.1. Conclusions

This thesis details growth of covalent semiconductor crystals at record low temperatures with just simple, benchtop setups. From this perspective, ec-LLS already occupies a unique place in materials science and is a new step towards non-energy intensive manufacturing of technologically-relevant semiconductors. Still, more work is needed to make ec-LLS a disruptive process at relevant scales. Many simple but practical questions remain regarding the limits of ec-LLS in this context. Can ec-LLS be used to make large area epitaxial thin films? Can photovoltaic-grade heterojunction thin films be made directly through ec-LLS? To what extent can the liquid metal electrode be cleanly separated from the crystals? What are the relevant energetics and kinetics that dictate successful ec-LLS growth? The answers to these questions will determine the value of ec-LLS to the semiconductor industry.

Irrespective of the answers to these questions, ec-LLS may prove generally valuable for materials chemistry. Microscopic understanding of ec-LLS will not only lead to better resultant materials but should also inform our basic understanding of how crystals (of any type) nucleate and grow. In a separate context, ec-LLS could become useful for the synthesis of compositionally complex inorganic solids. The reactivity of metals dissolved in liquid metal electrodes has been recognized for decades,[1] but mostly as an unwanted complication in polarographic sensing methods. In this way, ec-LLS may be a versatile synthetic method that complements traditional inorganic flux syntheses.[2]

There are two research directions going forward from this thesis. First, extending ec-LLS to prepare thin film materials would provide simpler integration of resultant materials into existing processing schemes (i.e. CMOS). In that way, routes to direct adoption of the ec-LLS technology could be simpler. Second, both a theoretical and

empirical understanding of the energetics and kinetics of ec-LLS crystal nucleation and growth at the relevant temporal and spatial scales is required to deterministically assign design criteria. One aspect would include the development and use of tools that can probe nanoscale electrocrystallization in *operando*. In that context, the purpose of this thesis is to define the potential of ec-LLS and guide future users along the most fortuitous paths.

6.2. Future Work

Thin Film ec-LLS

The single crystal wafer growth substrate contributes significantly to the balance of systems costs for III-V based solar cells.[3,4] One strategy to lower production costs is through an epitaxial lift-off (ELO) process where extremely thin GaAs layers are deposited and carefully removed and transferred to a separate device platform allowing reuse of the substrate. ELO does remunerate some of the cost, but is ultimately limited to a finite number of growth cycles[5,6] and still relies on expensive GaAs wafer substrates.[7] The small lattice mismatch makes Ge a particularly useful substrate for epitaxial GaAs growth. In that regard, the ability to employ ec-LLS to prepare cheaper epi-ready Ge wafers for subsequent GaAs ELO has the potential of being a truly impactful technology.

As described in Chapters 2 and 3, the size (thickness) of the liquid metal electrode determines the primary nucleation mode. If the total thickness of the liquid metal exceeds the diffusional mean free path of the solute, homogenous nucleation will dominate, and Ge will accumulate at the liquid metal/electrolyte interface rather than by epitaxy at the substrate interface.

The main challenge with preparing thin liquid metal films is their large inherent surface tension which drives them to form spherical droplets to minimize overall surface energy. Thin, unconstrained, and oxide-free Ga films will always break up into discontinuous droplets over the film area.

One option is to design and construct a new liquid metal microfluidic cell that physically constrains a pressurized liquid metal thin film over a wafer substrate for ec-LLS deposition. Three distinct systems constraints were identified to guide cell design.

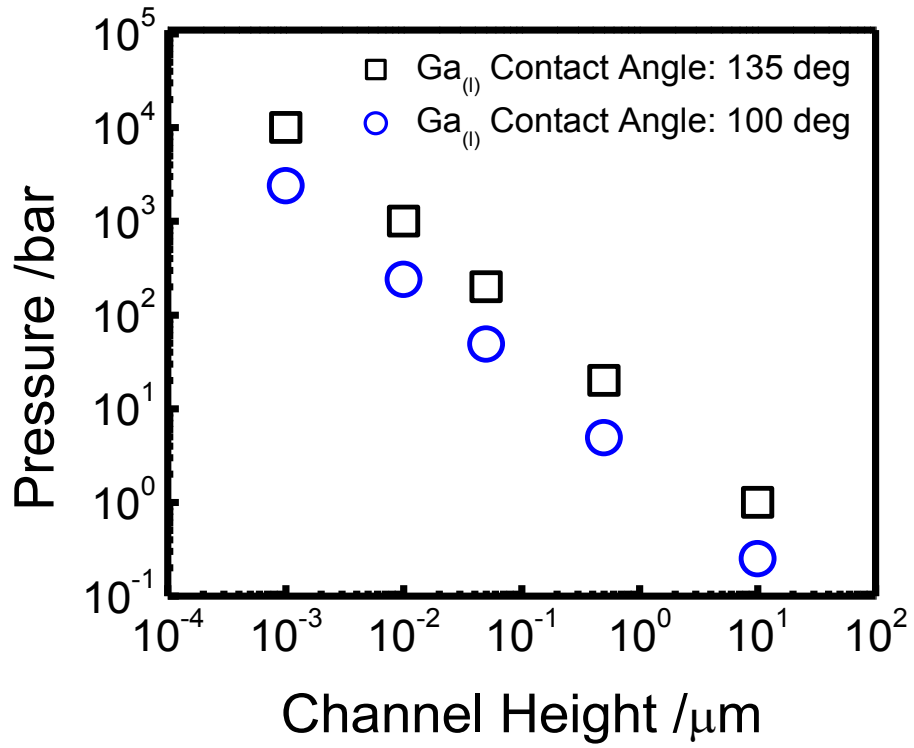

Figure 6.1. Calculated intrusion pressure for liquid gallium as a function of channel height for two different contact angles (surface tensions).

First, based on results in Chapter 3, the liquid metal thickness needed to be carefully controlled to < 20 μm to promote Ge epitaxial ec-LLS. Second, the system design must be able to accommodate the forces required to pressurize and confine high surface tension liquid metals to very thin films. Figure 6.1 indicates calculated pressures of 1 to 10 bar are required to intrude Ga into a 20 μm thick channel. Third, and arguably most critical, a membrane must be used to constrain the liquid metal electrode while simultaneously providing access to liquid electrolyte. This criterion can be further broken down into five subcategories: (*1*) the membrane must be chemically and physically robust to withstand multi-hour depositions in near-boiling alkaline water under compressive and tensile forces, (*2*) the pore size must still facilitate rapid electrolyte diffusion to minimize Ohmic losses, (*3*) the surface in contact with the liquid metal must be flat enough to form a hermetic seal to the substrate, (*4*) the edges of the membrane must be able to seal to prevent electrolyte from leaking through the membrane to the external environment, and (*5*) the membrane material must be non-conductive so it doesn't participate in the electrochemistry.

Each of the design criteria was addressed explicitly and individually in the engineering of the cell depicted in Figure 6.2 (Appendix A.7-A.11). The general concept is a compressive microfluidic device. The wafer growth substrate is lithographically patterned with a high-modulus polymer photoresist or SiO_x layer which defines the electrodeposition area and the liquid metal thickness with high precision. A hierarchically nanoporous silicon carbide (SiC) membrane is compressed against the templated substrate creating a thin channel for the liquid metal to reside under pressure. SiC satisfies the membrane criteria as it is non-conductive (1E10 Ω·cm), has a large compressive strength (1.3 GPa), and has the ability to be made porous and flat.[8] The liquid electrolyte is then contained in a reservoir atop the membrane where it can permeate through the SiC to the liquid metal interface for electrochemical reduction. Electrolyte leaking through the sides of the membrane is prevented by infiltrating the SiC pores with an inert polymer like polydimethylsiloxane (PDMS) using the homemade vacuum infiltration device in Figure 6.3 (Appendix A.12). A discrete and reproducible electrolyte channel can be simply defined with this process. Pressure control is imperative for ensuring a contiguous liquid metal film through the duration of the deposition and can be controlled through the custom constant-pressure (rather than constant-flow) syringe pump shown in Figure 6.4.

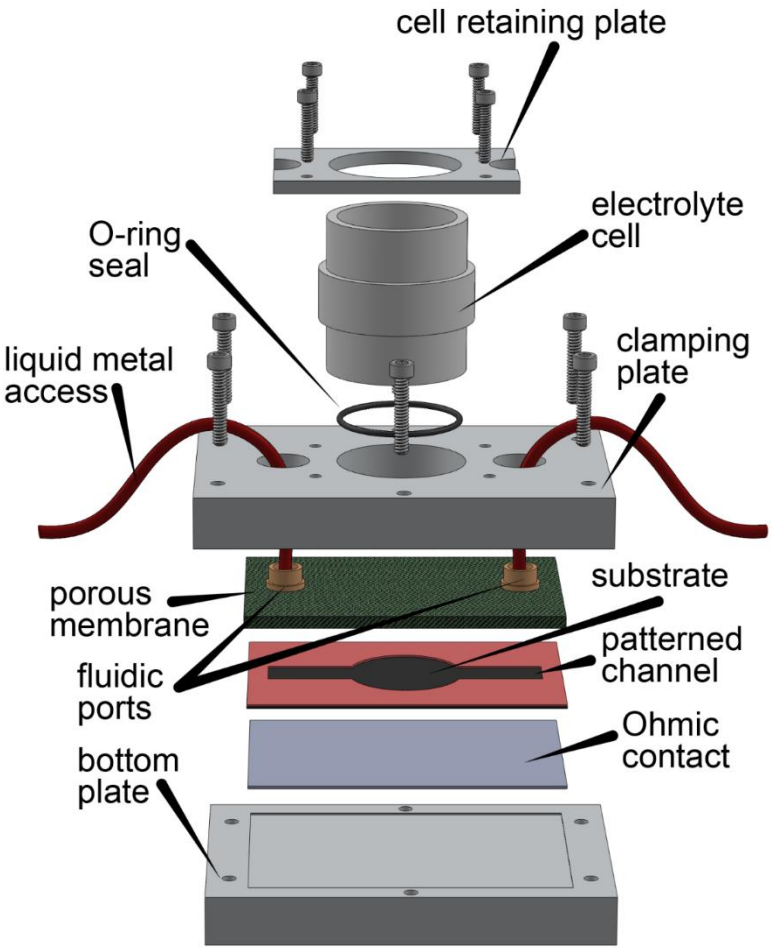

Figure 6.2. Schematic prototype of a liquid metal microfluidic device to accommodate thin film ec-LLS over 1 in^2.

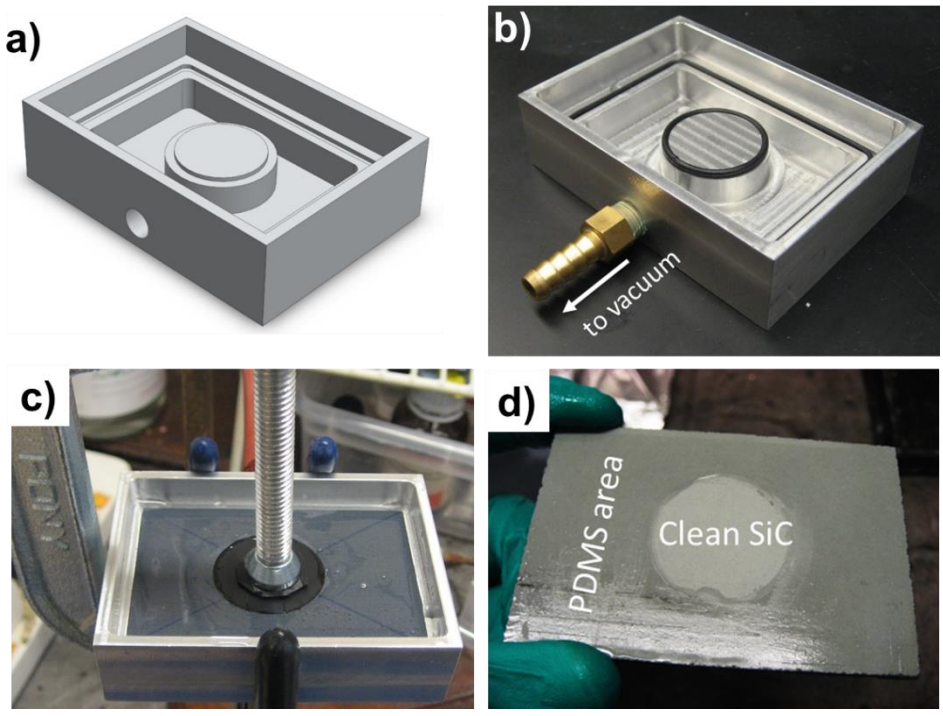

Figure 6.3. (a) Schematic concept and (b) optical image of a vacuum device to selectively infiltrate porous SiC membranes. (c) Device in use. (d) Porous SiC membrane following infiltration with PDMS.

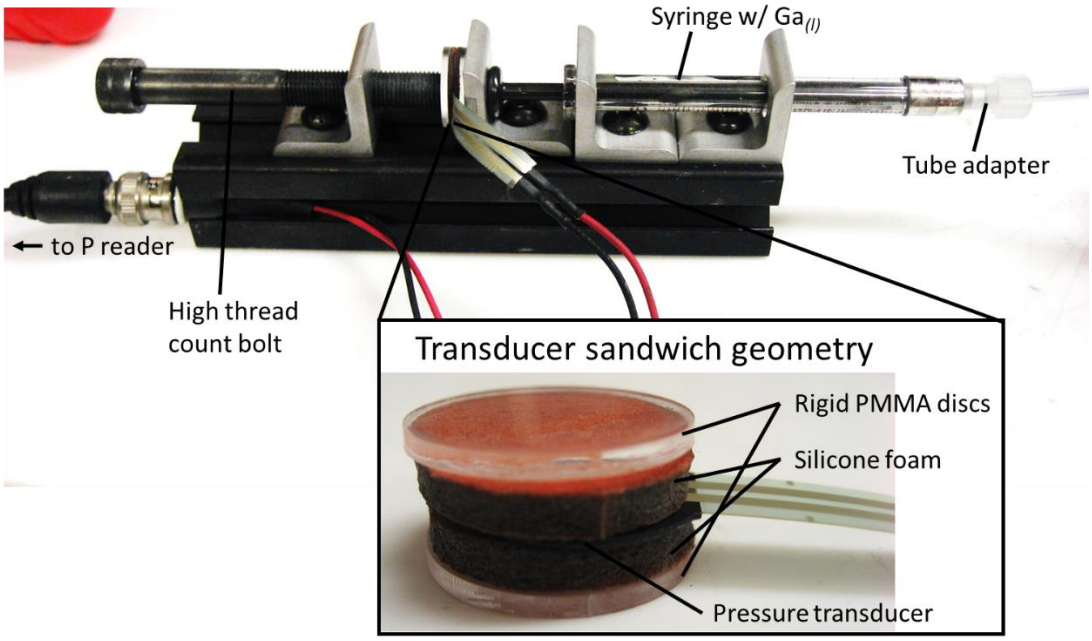

Figure 6.4. Custom constant-pressure syringe pump used to regulate input pressure of the liquid metal into to the thin film cell depicted in Figure 6.2. Inset shows the thin film resistive transducer geometry.

Electrodeposition at nominally 10 μm thick EGaIn film electrodes using the cell in Figure 6.2 results in growth of a thin Ge film over the 1 in^2 active area. Electron microscopy was used to investigate the microstructure and crystallography of the resulting films. Figure 6.5a shows a cross-section scanning electron micrograph of a film deposited at 90 °C. After two hours, the film thickness was nominally 1 μm and the surface was optically flat over large areas. The inset in Figure 6.5b shows the symmetric microstructure expected for an epitaxial film. Cross-sectional transmission electron microscopy was used to probe the interface between the Si(111) substrate and Ge film interface. Figure 6.5c shows a low magnification micrograph of the interface. The film is continuous across the interface with no apparent voids. Due to the 4% lattice mismatch between the Si/Ge, both bending contours and interfacial defects contribute to the observed contrast. Regardless, the selected area electron diffraction patterns for each layer (insets) are superimposable indicating a clean epitaxial relationship and a single crystal Ge film. Dark field scanning transmission electron microscopy (STEM-ADF) in Figure 6.5d shows continuous contrast in the Ge phase without grain boundaries or voids. The corresponding atomically-resolved image from the interface shows a defect free lattice continuity, further supporting the notion of clean epitaxy (Figure 6.4f). Elemental mapping through energy dispersive spectroscopy in STEM also cleanly distinguishes the distinct Ge epi-film from the original Si substrate (Figure 6.4e).

The cumulative results confirm the thin film ec-LLS concept while providing a new layer of intriguing research questions. Can this process be used to deposit semiconductors on non-conductive substrates like SiO_2, sapphire, or other ceramics? Can the electronics of the material be controlled with any fidelity to effect useful heterostructures? Could this method be used to grow ‘thick’ wafers or ingots? More generally, what are the areal and thickness limits of this process? Efforts towards thin film ec-LLS over full 4 inch wafers have been recently attempted with a new cell design shown in Figure 6.6 (Appendix A13-A20).

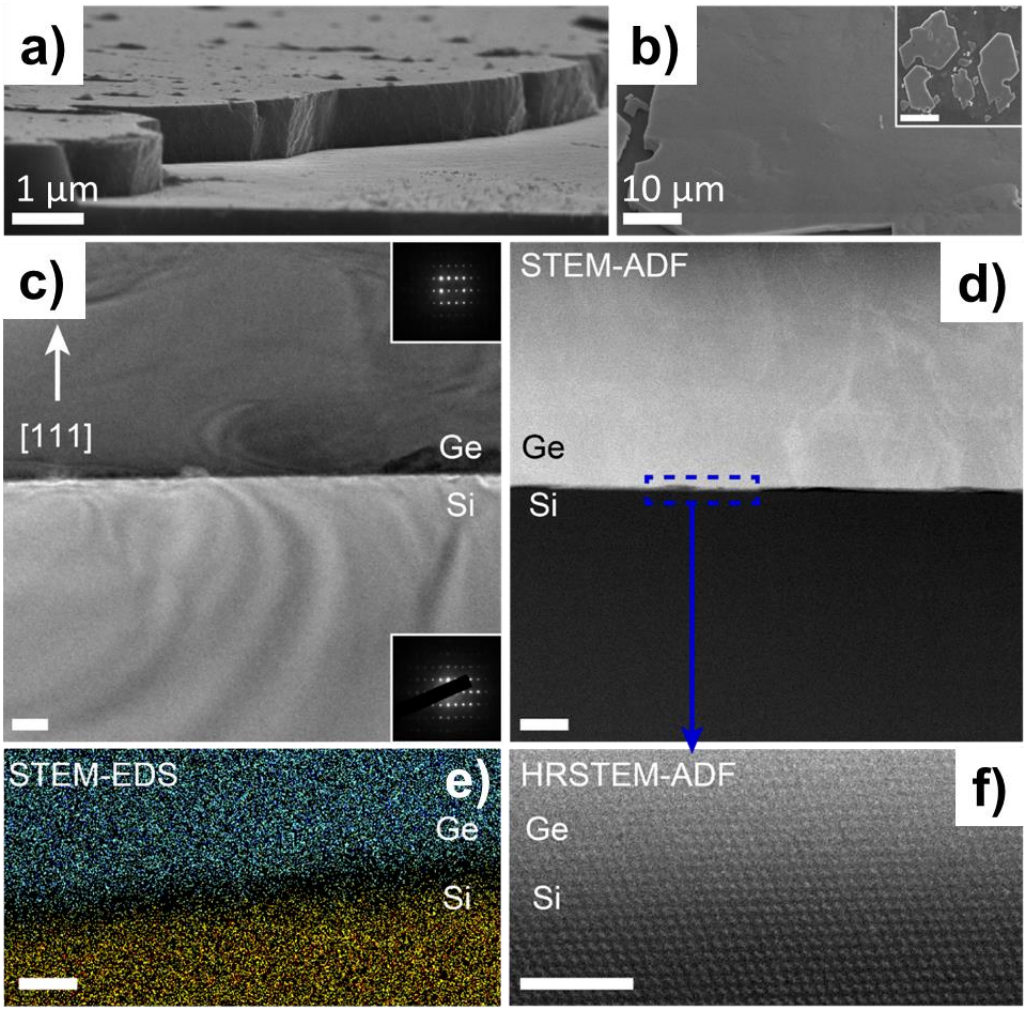

Figure 6.5. (a) Cross sectional scanning electron micrograph of a Ge film produced by thin film ec-LLS for 2 h at -1.4 V vs. Ag/AgCl in 50 mM GeO_2 and 10 mM $Na_2B_4O_7$. (b) Plan view image of the film in (b). Cross sectional TEM image of an epitaxial Ge film grown from Si(111) wafer substrate. Insets show selected area electron diffraction patterns from the respected film layers. (d) Corresponding scanning transmission electron annular dark field image of the interface in (c). (e) Energy dispersive spectroscopic map of the thin film Ge/Si interface. (f) Atomically-resolved dark field STEM image from the interface in (d). Scale bars are clockwise from top left: 1, 10, 0.1, 0.002, 0.1, 0.1 µm.

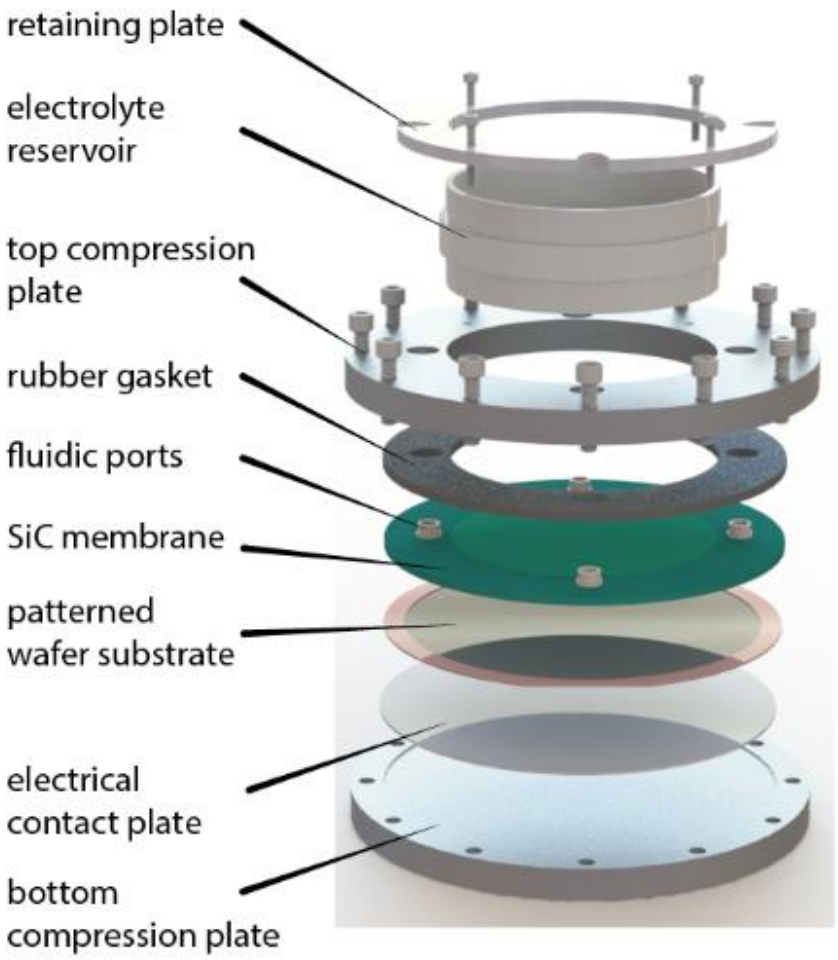

Figure 6.6. 3D CAD rendering of a thin film ec-LLS cell capable of growth over full 4" wafer substrates.

Although thin film ec-LLS is an exciting engineering feat, practical application of the technology requires a better fundamental understanding of the key energetic and kinetic parameters that actually govern ec-LLS. Answering the latter will most certainly answer the former.

Direct Visualization of ec-LLS by in-situ TEM

Although academically rich, the utility of ec-LLS as an alternative semiconductor fabrication method requires a more comprehensive understanding of the energetics and kinetics that govern or even constrain the process over wide experimental ranges. At this point, largely phenomenological results have been reported. A general model that connects independent results and describes the limitation of the ec-LLS system as a whole is imperative.

As a hybrid technology, ec-LLS borrows aspects from number of synthetic methodologies including vapor liquid solid (VLS) growth, electrodeposition, and liquid phase epitaxy (LPE). By stitching key components of these respective models together, a general set of guidelines for ec-LLS can be rendered. Although coarse models can be generated in this fashion either analytically or through finite element simulations, empirical validation remains elusive. The primary challenge for experimental visualization of the ec-LLS process is the stringent requirement of a characterization tool that simultaneously satisfies the high spatial and temporal resolutions required for direct observation while preserving experimental fidelity. In fact, the mechanism for the analogous VLS method was not empirically validated until almost 40 years after its discovery.[9,10]

One method for direct visualization of ec-LLS Ge nanowire growth is through the use of *in-situ* electrochemical transmission electron microscopy (ec-TEM). Technological advancements facilitated by precision machining and nanofabrication have allowed the field of *in-situ* TEM to enter the realm of liquid, gas, and even electrochemical systems in the last decade.[11-25] Since the typical operating pressures of a conventional TEM are in the 10^{-8} to 10^{-11} mbar range, standard liquid-based electrochemical experiments require special equipment. Figure 6.7 shows the tip of a TEM sample holder used for electrochemical experiments. A variety of isolated electrical leads and fluidic lines supply liquid and facilitate electrochemical bias to microfabricated chips housed at the front of the tip.

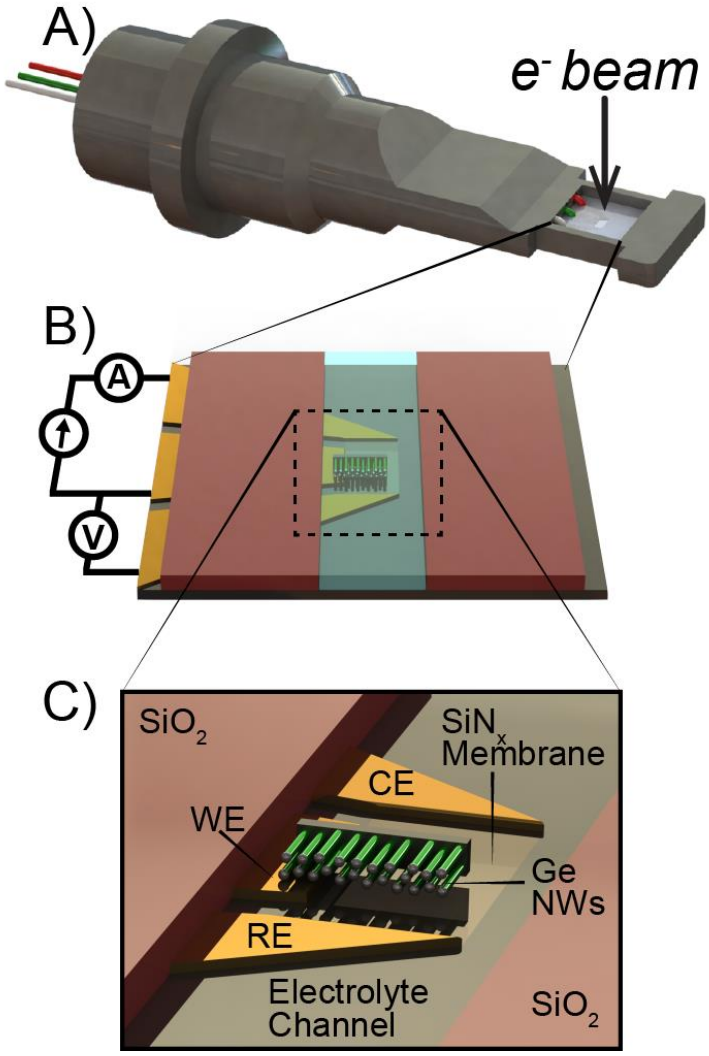

Figure 6.7. Rendering of a sample holder tip used in liquid cell electrochemical TEM (ec-TEM) experiments. (b) Blow-up of the microfabricated chips used in the ec-TEM experiment. One chip is patterned with thin film metal electrodes, while the mating chip is patterned with thin SiO_x spacers to form the liquid channel. Both chips have a thin (50 nm) SiN_x window at the center where the TEM beam passes with minimal scattering. (c) Zoom in of where the ec-LLS experiment will take place on-chip.

The chips shown in Figure 6.7b are typically patterned with thin film electrodes for electrochemistry and spacers to define liquid channels for flow. Each silicon chip is back-etched through the entire chip up to a thin amorphous SiN_x etch-stop layer on the surface. This forms a ~50 nm thick 'window' that is roughly 25 x 250 μm in size for the electron beam to pass with minimal scattering contribution.

One of the most challenging aspects of any *in-situ* TEM experiment is sample preparation. To observe ec-LLS growth of single Ge nanowires in TEM, a very thin slice of a single crystal Ge wafer substrate decorated with Ga nanodroplets must be precisely placed on one of the thin film electrodes over the SiN window in Figure 6.7c. A new focused ion beam (FIB) milling and nanomanipulation sequence was developed for this task. In general, the key challenges associated with using FIB liftout for this particular application are (*1*) beam damage and amorphization of the Ge slice (lamella), (*2*) chemical damage from the Pt precursor gas during Pt welding, and (*3*) damage or rupture of the 50 nm thick SiN window during placement and welding of the Ge lamella over the window area. To address these challenges, a new 'blind' cross-section FIB liftout method was developed. The general microscope geometry is depicted in Figure 6.8a. The starting Ga-decorated Ge(111) wafer is secured to a custom lift-out stub [Appendix A.21-A23] in a cross-section orientation with the Ga droplet face positioned normal to the e-beam and 52° tilted from the ion beam. The key concept here is that all milling and Pt welding steps occur with the wafer face hidden from the ion beam and gas injection systems. The first step shown in Figure 6.8b is the rapid milling of a wedge shaped lamella from cross-section. A nanomanipulator probe is then welded to the free end of the lamella, a release cut is made to the opposite lamella side, and the wedge is removed from the original wafer substrate. The lamella is then carefully positioned over the chip window in the inset of Figure 6.8c, where it is ion beam welded to the thin film electrode. Special care must be taken in this step to avoid ion beam damage of the chip, rupture of the window, or chemical passivation of the Ga nanodroplets with the Pt precursor gas. To validate that the final device structure in Figure 6.8c still facilitates Ge nanowire growth by ec-LLS, the chips were assembled into the tip in Figure 6.7 and tested outside of the TEM. Figure 6.8d shows multiple Ge nanowires after growth from the face of the thin Ge lamella.

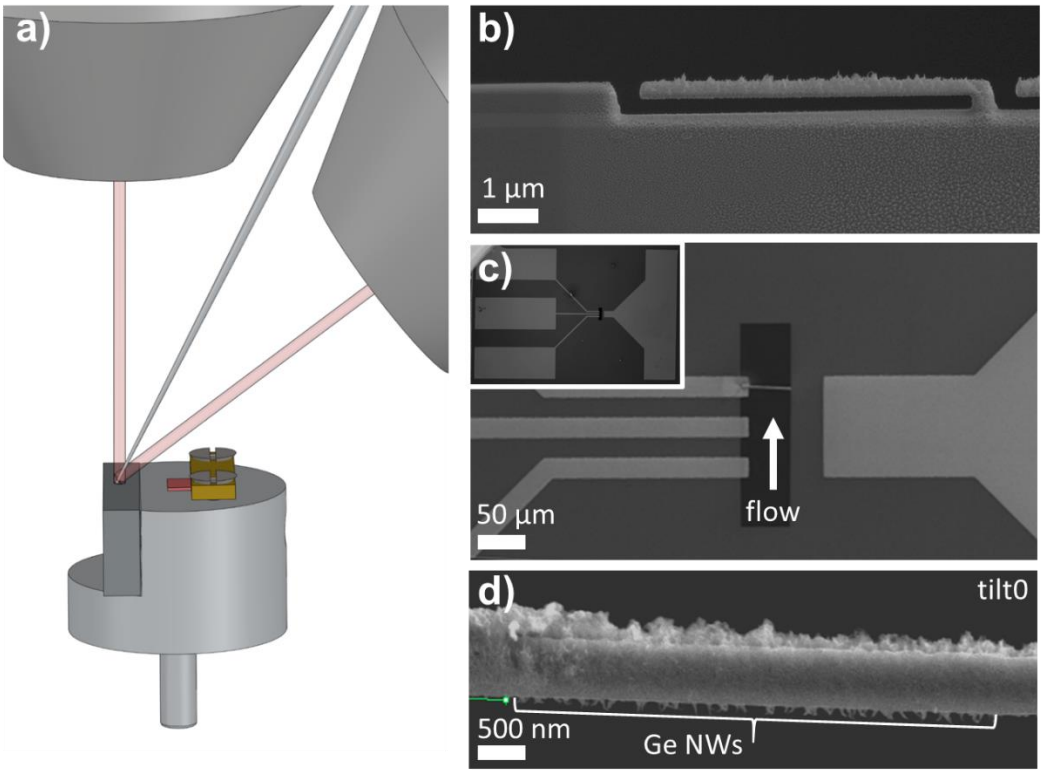

Figure 6.8. (a) Beam geometry used in the hybrid cross-sectional lift-out sample preparation. The vertical pole piece is the e-beam and the pole at 52 degrees is the FIB. (b) SEM image of the cross-sectional Ge wafer in (a) after the first angled FIB cut to generate the free-standing lamella. (c) SEM of the chip with the Pt-welded lamella. Inset is a zoomed out micrograph of the same chip. (d) High magnification micrograph of the lamella in (c) after an ex-situ ec-LLS nanowire growth process.

Two distinct observations were made while attempting ec-LLS inside the TEM. First, the contrast of the thin Ge lamella changed dynamically while under bias in the electrolyte of 50 mM GeO_2 and 10 mM $Na_2B_4O_7$. Gallium ions are known to incorporate into the lamella lattice during FIB milling.[26] The apparent contrast changes can be rationalized through Ga ion electromigration through the length of the lamella.[27,28] Second, growth of Ge nanowires from Ga nanoparticles was observed away from the lamella or electrode. This implies a growth process that is independent of the applied bias. It's possible that the Ga nanoparticles evolved from the Ga-doped lamella into solution under bias, which then served as sites for electron beam induced ec-LLS deposition. In other words, the applied potential induced Ga nanoparticle growth, but Ge nanowire growth was a result of the potential induced from the impingent electron beam. The interaction of the e-beam with the aqueous electrolyte is known to generate highly transient reducing species like solvated electrons, hydrogen radicals, and hydroxyl radicals.[29-31] We posit that solvated electron species provide the driving force for electrochemical reduction of the GeO_2 precursor at the Ga nanoparticles. Extracted frames from the resulting videos are shown in Figure 6.9. White outlines are used to train the eye. At 0 s, uniform contrast is observed over the Ga nanodroplet. At 6.1s, the contrast remains uniform but the volume of the particle has grown significantly as the GeO_2 is reduced to Ge and solvated by the Ga droplet. At 7.05 s, a discrete boundary is apparent which signifies a phase separation event of the Ge crystal from the Ga solvent. The resulting Ge crystal diameter is nominally the same as the Ga droplet. Over the next 21 s, the Ge crystal grows to a length of over 150 nm before be swept away by the flowing electrolyte solution. By converting the projected areas in the video frames to volumes, the extent of Ge solubility in Ga can be qualitatively estimated at the onset of phase separation. In this case, roughly 1 at. % Ge is present before two phases emerge. This experimental value is significantly larger than that predicted by the Ge-Ga equilibrium phase diagram in Figure 6.10.

There are a couple possible explanations for the large discrepancy in equilibrium solubility. First, volumes are inferred from projected areas which can lead to some deviation in the measured value. Assuming the measured solubility is accurate within an order of magnitude, the value is still over two orders of magnitude larger than the equilibrium solubility.

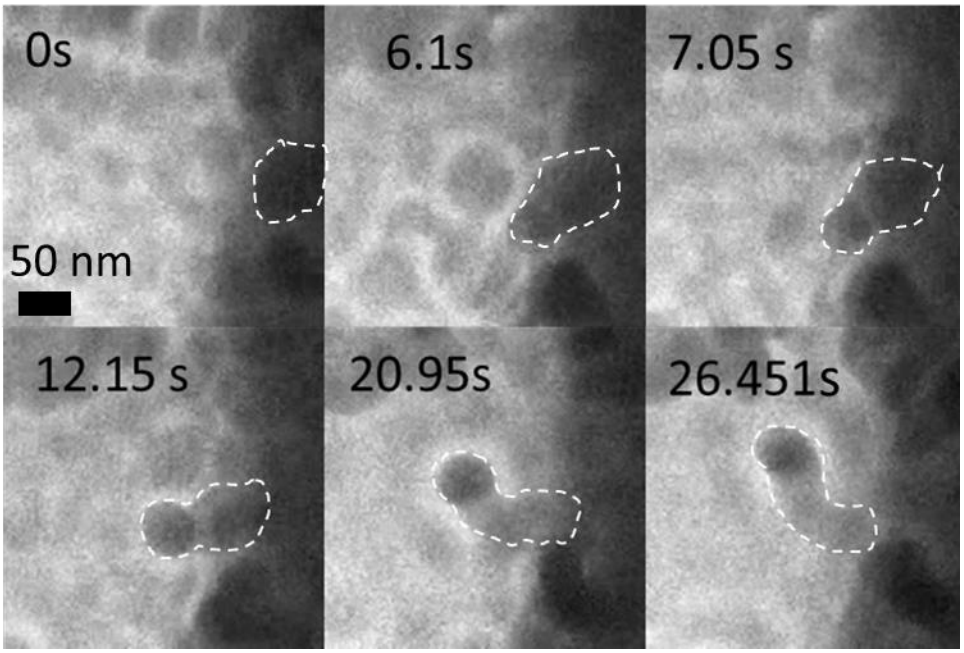

Figure 6.9. Time-lapse video frames extracted from an in-situ ec-LLS Ge nanowire growth experiment conducted inside a TEM.

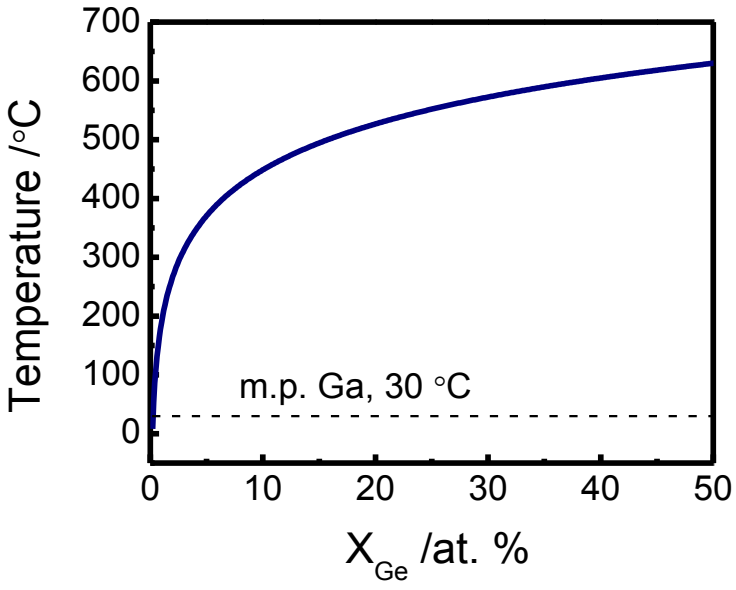

Figure 6.10. Binary compositional phase diagram for the Ga-Ge system as a function of temperature. Plot only extends to 50 at. % Ge for clarity.

Second, the low temperature region of the Ge-Ga binary phase diagram is very difficult to measure with traditional techniques since the mass change due to Ge solvation in Ga is very small and prone to error. In other words, it's possible that room temperature solubility used for comparison is not accurate. These data should be replicated many times to establish greater measurement precision. At the same time, control experiments with pre-synthesized Ga nanodroplets could help decouple the electromigration effects and focus exclusively on the e-beam induced ec-LLS process. Although preliminary, the data point to ec-LLS as a crystal growth method that operates at very large supersaturations. That concept is not unprecedented. In fact, it is well known in the vapor liquid solid and solution liquid solid fields, crystal growth occurs in a kinetically defined regime far from equilibrium.[32] Moreover, such large supersaturations could help rationalize the small nucleation barriers that facilitate semiconductor crystal growth at room temperature and at appreciable rates. Continued work on the electrochemical TEM system could provide fruitful insights into underpinnings of ec-LLS crystal growth.

6.3. References

1. Kemula, W.; Kublik, Z.; Galus, Z. *Nature* **1959**, *184*, B.A.56.
2. Kanatzidis, M. G.; Pöttgen, R.; Jeitschko, W. *Angew. Chem., Int. Ed.* **2005**, *44*, 6996.
3. Horowitz, K. A. W.; Woodhouse, M.; Lee, H.; Smestad, G. P. In *11th International Conference on Concentrator Photovoltaic Systems*; Siefer, G., Baudrit, M., Anton, I., Eds. 2015; Vol. 1679.
4. Zheng, M.; Horowitz, K.; Woodhouse, M.; Battaglia, C.; Kapadia, R.; Javey, A. *Prog. Photovolt: Res. Appl.* **2016**, *24*, 871.
5. van Geelen, A.; Hageman, P. R.; Bauhuis, G. J.; van Rijsingen, P. C.; Schmidt, P.; Giling, L. J. *Mater. Sci. Eng. B* **1997**, *45*, 162.
6. Bauhuis, G. J.; Mulder, P.; Haverkamp, E. J.; Schermer, J. J.; Bongers, E.; Oomen, G.; Köstler, W.; Strobl, G. *Prog. Photovolt: Res. Appl.* **2010**, *18*, 155.
7. Choi, W.; Kim, C. Z.; Kim, C. S.; Heo, W.; Joo, T.; Ryu, S. Y.; Kim, H.; Kim, H.; Kang, H. K.; Jo, S. *Adv. Energy Mater.* **2014**, *4*, n/a.
8. Suwanmethanond, V.; Goo, E.; Liu, P. K. T.; Johnston, G.; Sahimi, M.; Tsotsis, T. T. *Ind. Eng. Chem. Res.* **2000**, *39*, 3264.
9. Wu, Y.; Yang, P. *J. Am. Chem. Soc.* **2001**, *123*, 3165.
10. Wagner, R. S.; Ellis, W. C. *App. Phys. Lett.* **1964**, *4*, 89.
11. de Jonge, N.; Ross, F. M. *Nat. Nanotechnol.* **2011**, *6*, 695.
12. de Jonge, N.; Poirier-Demers, N.; Demers, H.; Peckys, D. B.; Drouin, D. *Ultramicroscopy* **2010**, *110*, 1114.
13. Gu, M.; Parent, L. R.; Mehdi, B. L.; Unocic, R. R.; McDowell, M. T.; Sacci, R. L.; Xu, W.; Connell, J. G.; Xu, P.; Abellan, P.; Chen, X.; Zhang, Y.; Perea, D. E.; Evans, J. E.; Lauhon, L. J.; Zhang, J.-G.; Liu, J.; Browning, N. D.; Cui, Y.; Arslan, I.; Wang, C.-M. *Nano Lett.* **2013**, *13*, 6106.
14. Liao, H.-G.; Zheng, H. *J. Am. Chem. Soc.* **2013**, *135*, 5038.
15. Nie, A.; Gan, L.-Y.; Chong, Y.; Asayesh-Ardakani, H.; Li, Q.; Dong, C.; Tao, R.; Mashayek, F.; Wang, H.-T.; Schwingenschloegl, U.; Klie, R. F.; Yassar, R. S. *ACS Nano* **2013**, *7*, 6203.
16. Park, J.; Zheng, H.; Lee, W. C.; Geissler, P. L.; Rabani, E.; Alivisatos, A. P. *ACS Nano* **2012**, *6*, 2078.
17. Radisic, A.; Ross, F. M.; Searson, P. C. *J. Phys. Chem. B* **2006**, *110*, 7862.
18. Radisic, A.; Vereecken, P. M.; Hannon, J. B.; Searson, P. C.; Ross, F. M. *Nano Lett.* **2006**, *6*, 238.
19. Ring, E. A.; de Jonge, N. *Microsc. Microanal.* **2010**, *16*, 622.
20. Ross, F. M. *Microsc. Microanal.* **2010**, *16*, 326.
21. White, E. R.; Singer, S. B.; Augustyn, V.; Hubbard, W. A.; Mecklenburg, M.; Dunn, B.; Regan, B. C. *ACS Nano* **2012**, *6*, 6308.
22. Yuk, J. M.; Park, J.; Ercius, P.; Kim, K.; Hellebusch, D. J.; Crommie, M. F.; Lee, J. Y.; Zettl, A.; Alivisatos, A. P. *Science* **2012**, *336*, 61.
23. Liu, X. H.; Huang, J. Y. *Energy Environ. Sci.* **2011**, *4*, 3844.
24. Liu, X. H.; Wang, J. W.; Huang, S.; Fan, F.; Huang, X.; Liu, Y.; Krylyuk, S.; Yoo, J.; Dayeh, S. A.; Davydov, A. V.; Mao, S. X.; Picraux, S. T.; Zhang, S.; Li, J.; Zhu, T.; Huang, J. Y. *Nat. Nanotechnol.* **2012**, *7*, 749.
25. Ross, F. M. *Mater. Today* **2006**, *9*, 54.

26. Rubanov, S.; Munroe, P. R. *Micron* **2004**, *35*, 549.
27. Strachan, D. R.; Johnston, D. E.; Guiton, B. S.; Datta, S. S.; Davies, P. K.; Bonnell, D. A.; Johnson, A. T. C. *Phys. Rev. Lett.* **2008**, *100*, 056805.
28. Tatiana, K.; Maria, R.; Henny, W. Z. *Nanotechnol.* **2013**, *24*, 505708.
29. Park, J. H.; Schneider, N. M.; Grogan, J. M.; Reuter, M. C.; Bau, H. H.; Kodambaka, S.; Ross, F. M. *Nano Lett.* **2015**, *15*, 5314.
30. Schneider, N. M.; Norton, M. M.; Mendel, B. J.; Grogan, J. M.; Ross, F. M.; Bau, H. H. *J. Phys. Chem. C* **2014**, *118*, 22373.
31. Schneider, N. M.; Norton, M. M.; Mendel, B. J.; Grogan, J. M.; Ross, F. M.; Bau, H. H. *Microsc. Microanal.* **2014**, *20*, 1516.
32. Wu, Y. Y.; Yang, P. D. *J. Am. Chem. Soc.* **2001**, *123*, 3165.

APPENDIX A

CAD Drawings

This appendix contains a variety of custom designed and fabricated tools, electrochemical cells, and pressure vessels, which contributed to this thesis. All CAD drawings were developed in the SolidWorks software platform.

A. 0. Slotted insert for T-tool thin film TEM sample polishing

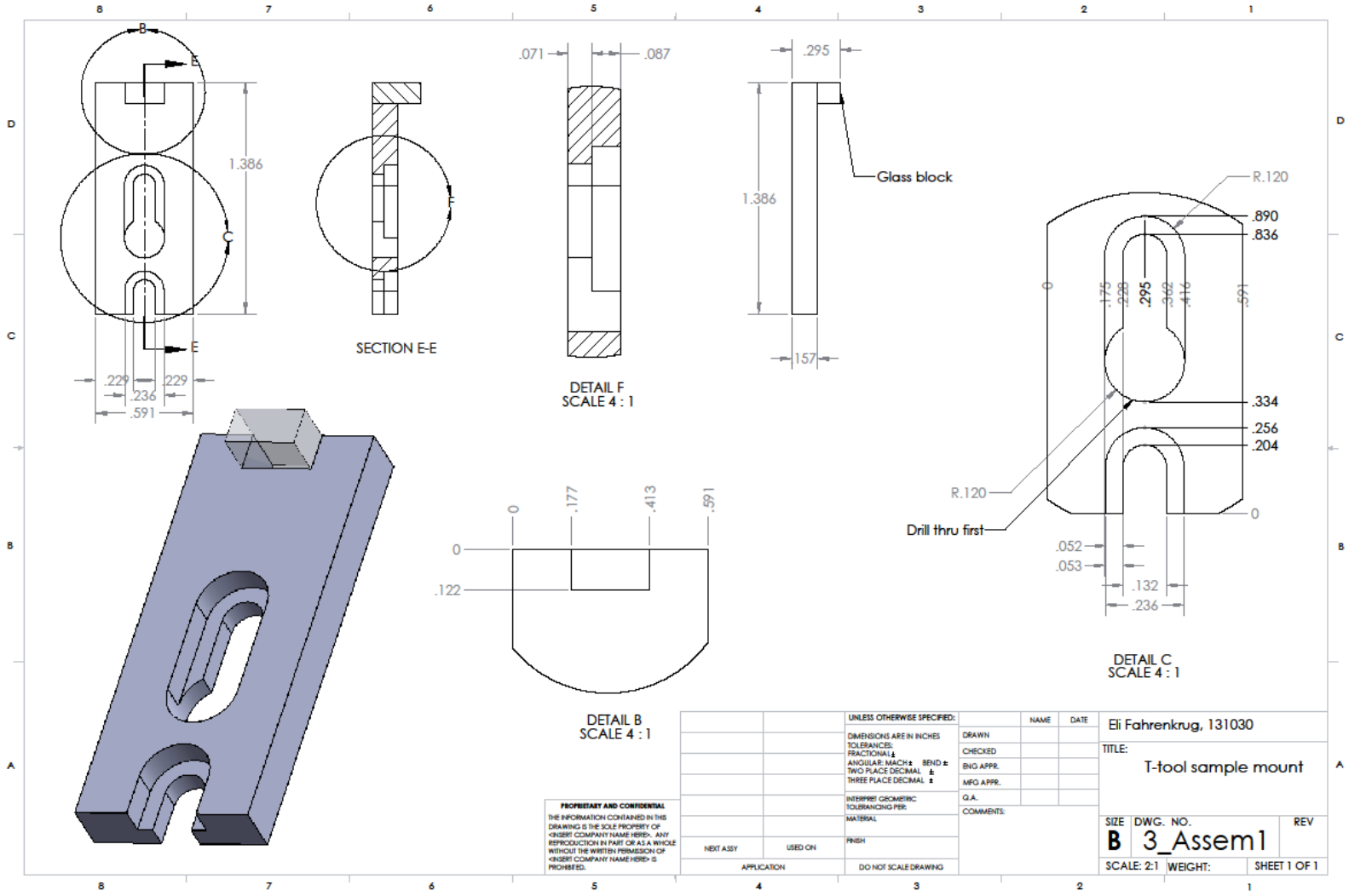

A. 1. Slotted wafer holder for degreasing – small (< 1 in^2)

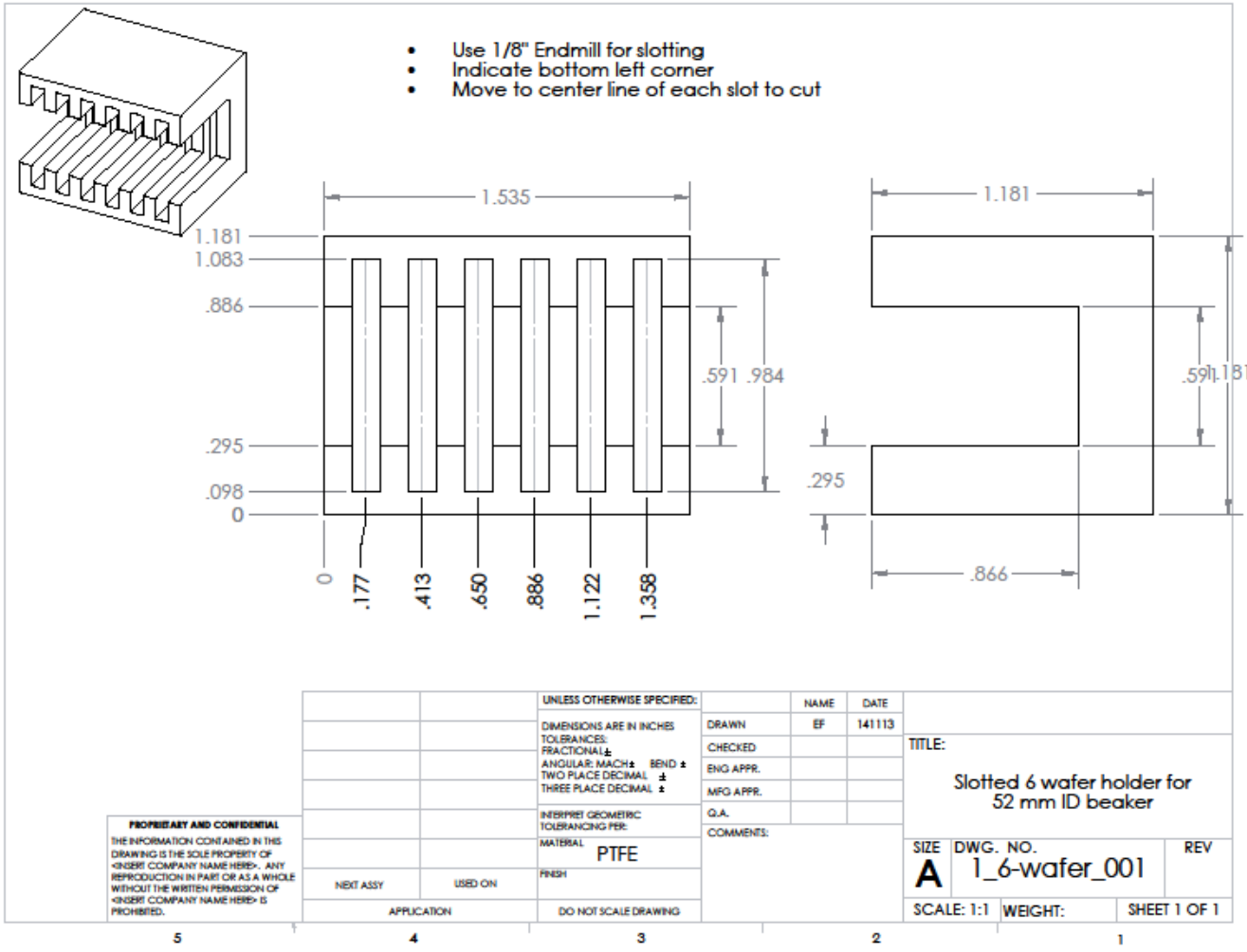

A. 2. Slotted wafer holder for degreasing – large (> 1 in^2)

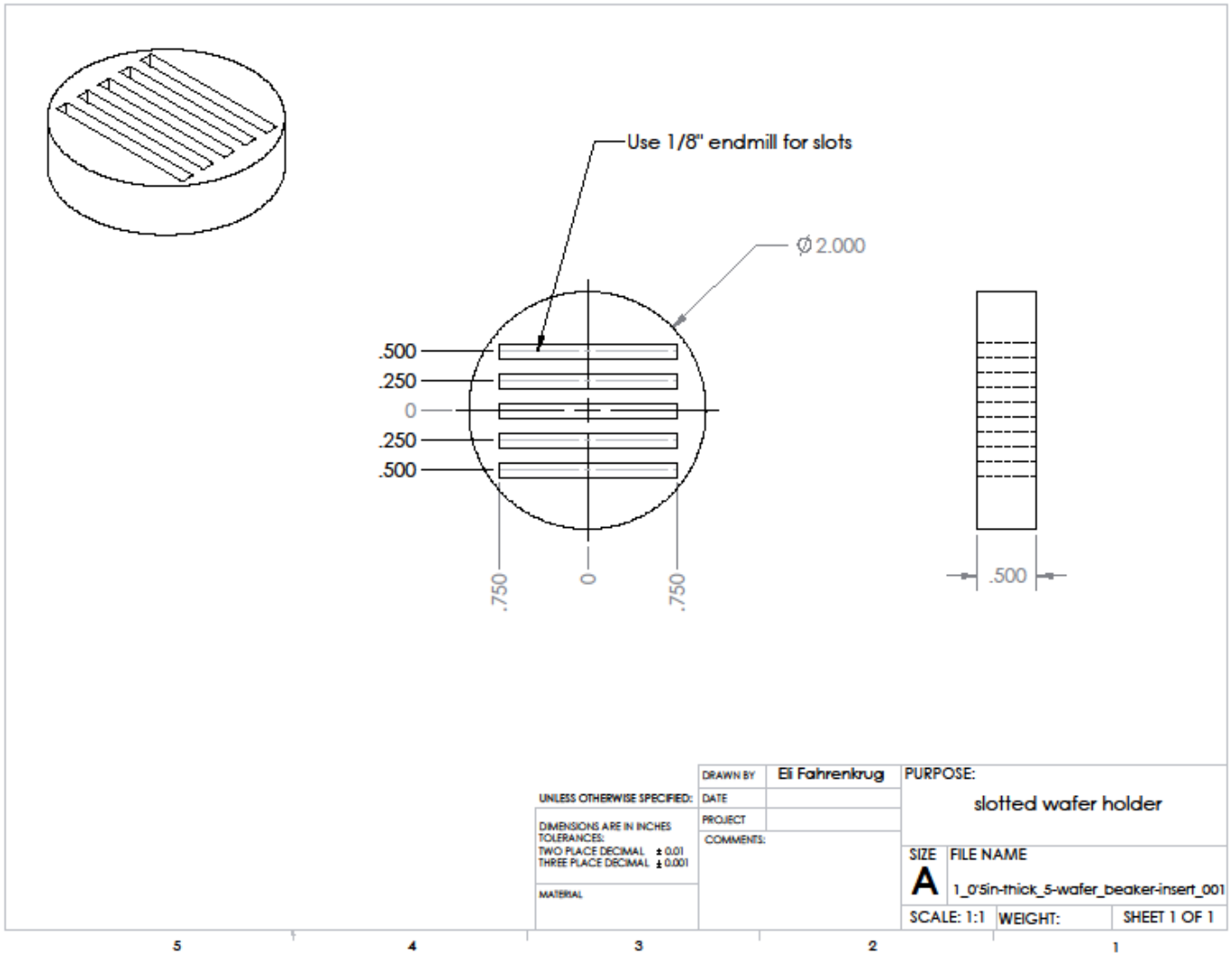

A. 3. Vacuum chuck for spinning photoresist on thin metal foils

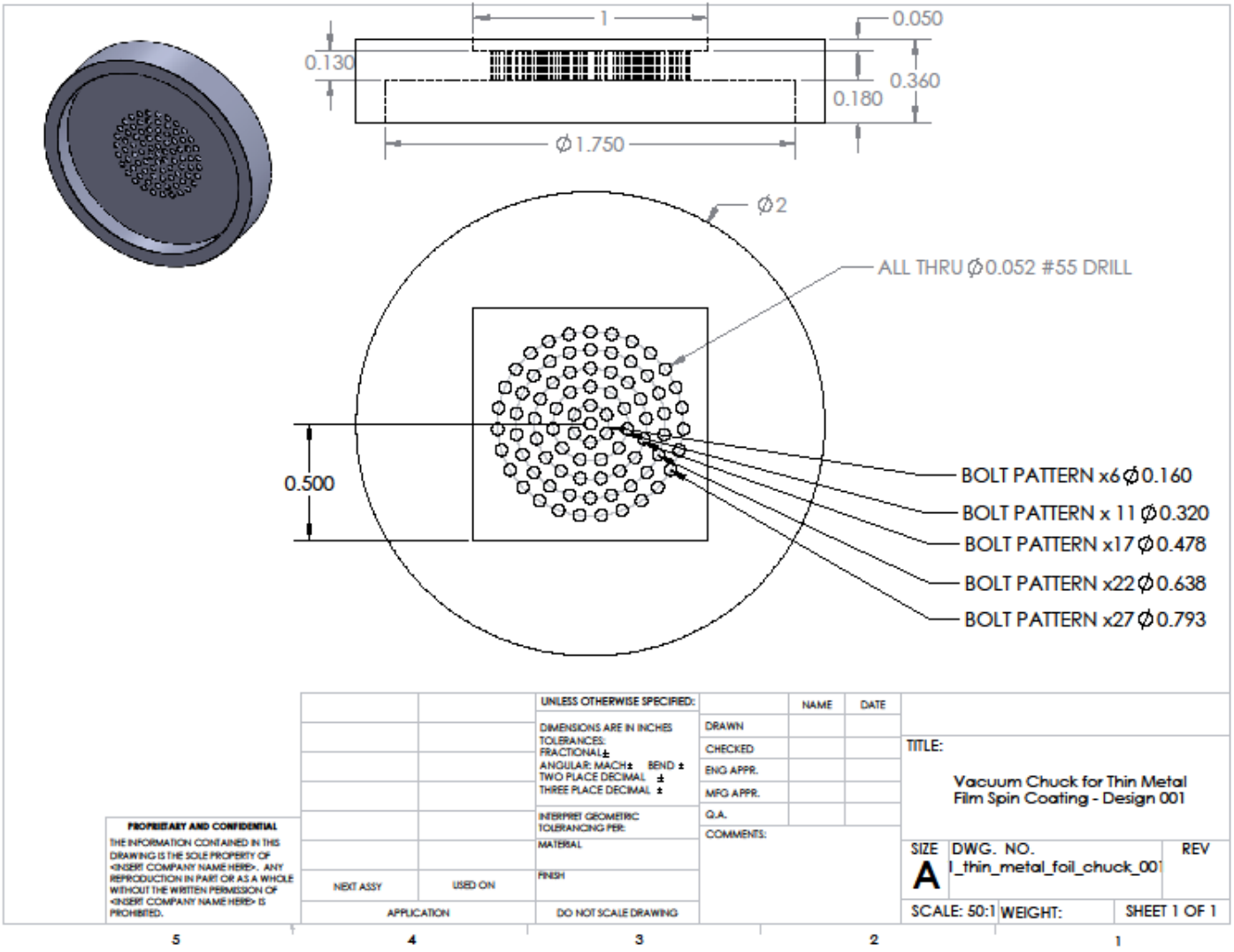

A. 4. Standard O-ring Cell

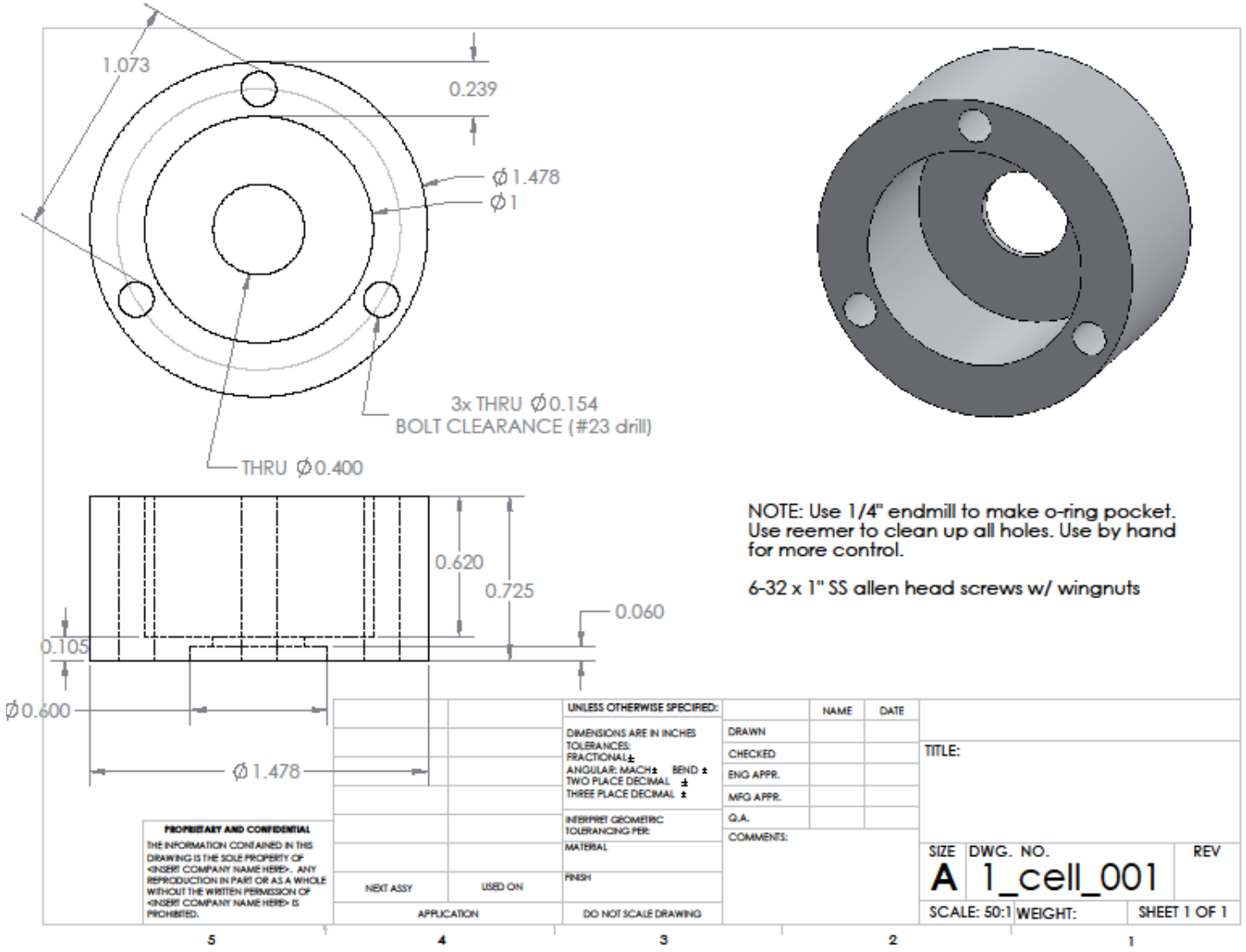

A. 5. Electrochemical Pressure Vessel

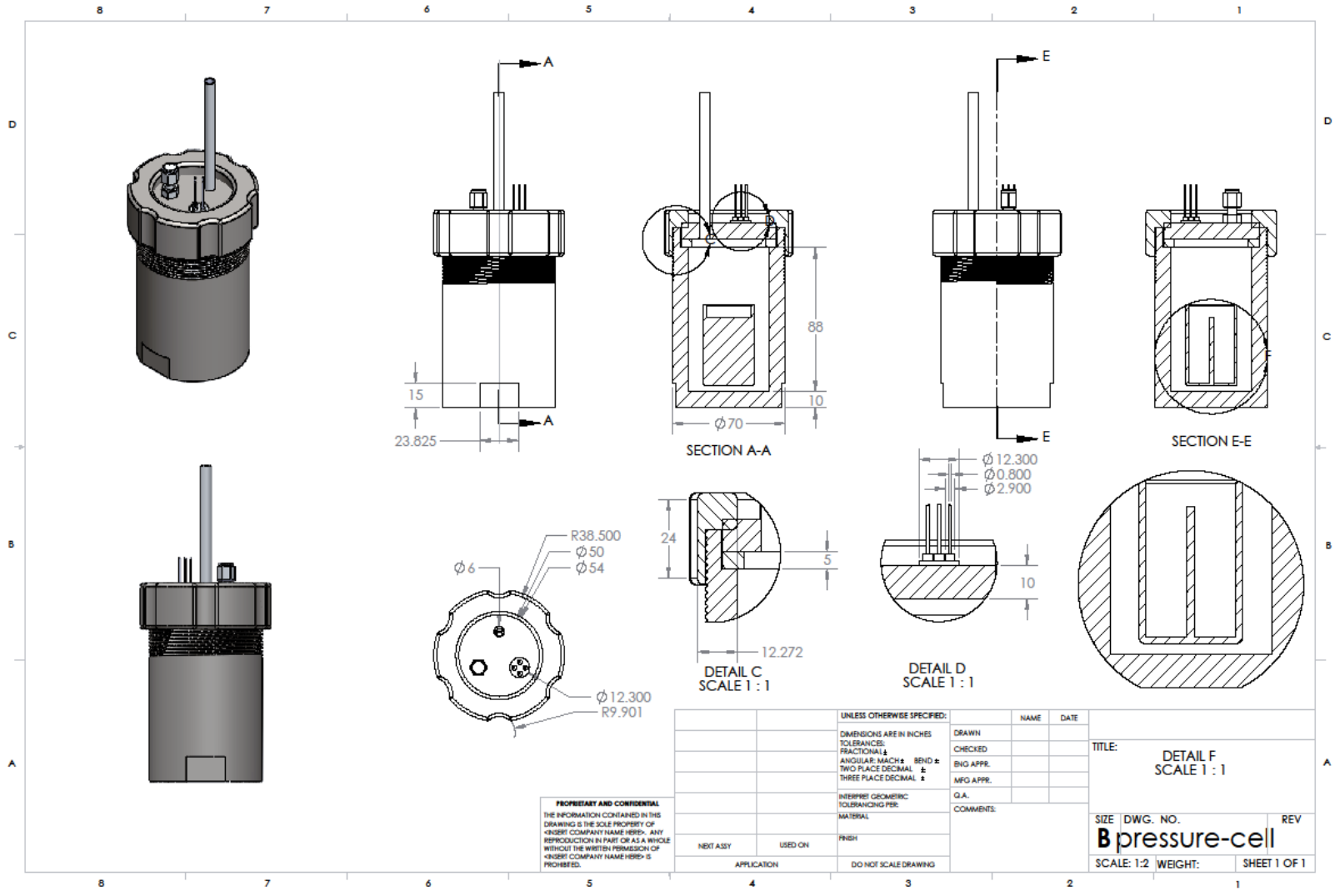

A. 6. In-situ Raman spectroelectrochemical cell

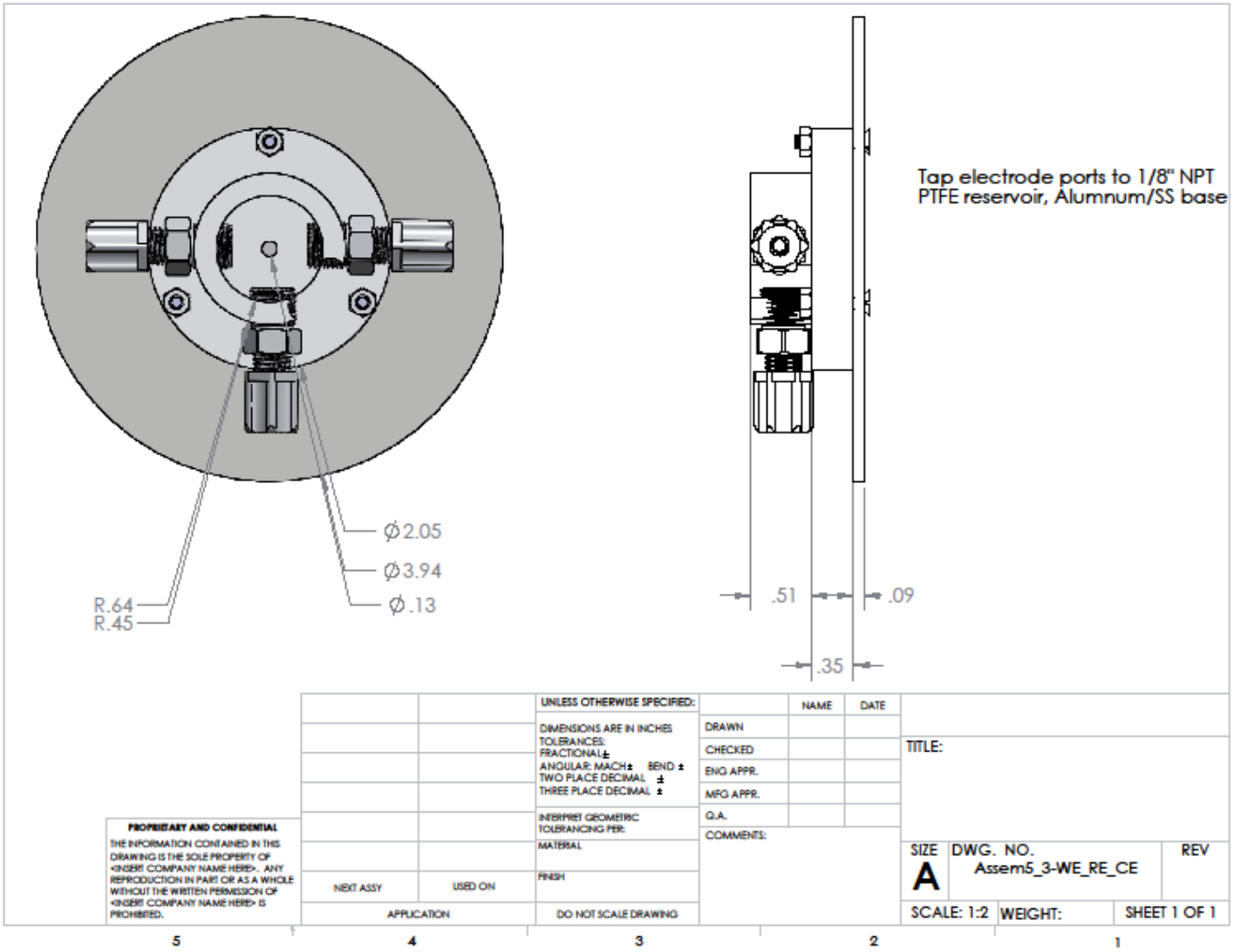

A. 7. Thin film ec-LLS cell – electrolyte reservoir

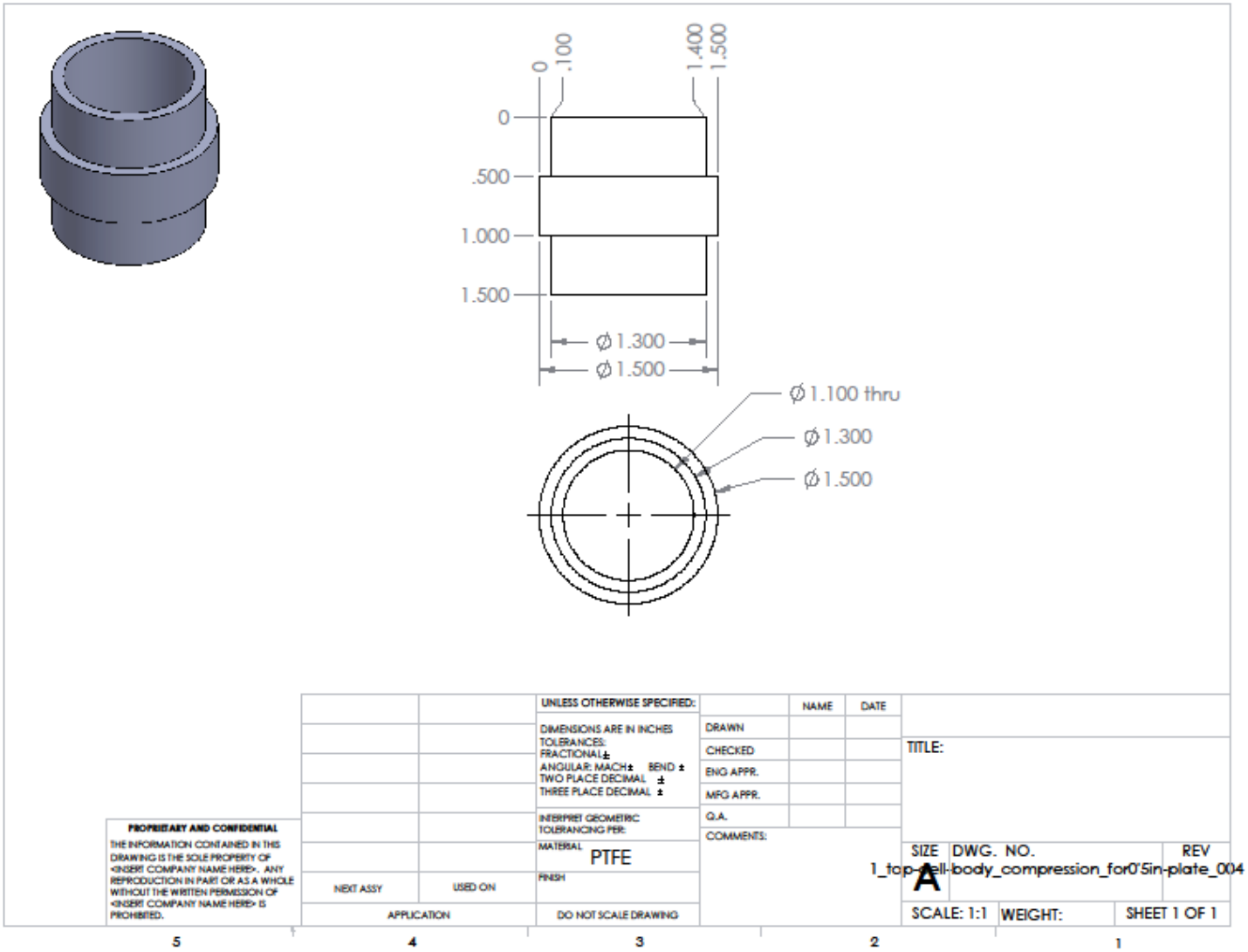

A. 8. Thin film ec-LLS cell – top compression plate

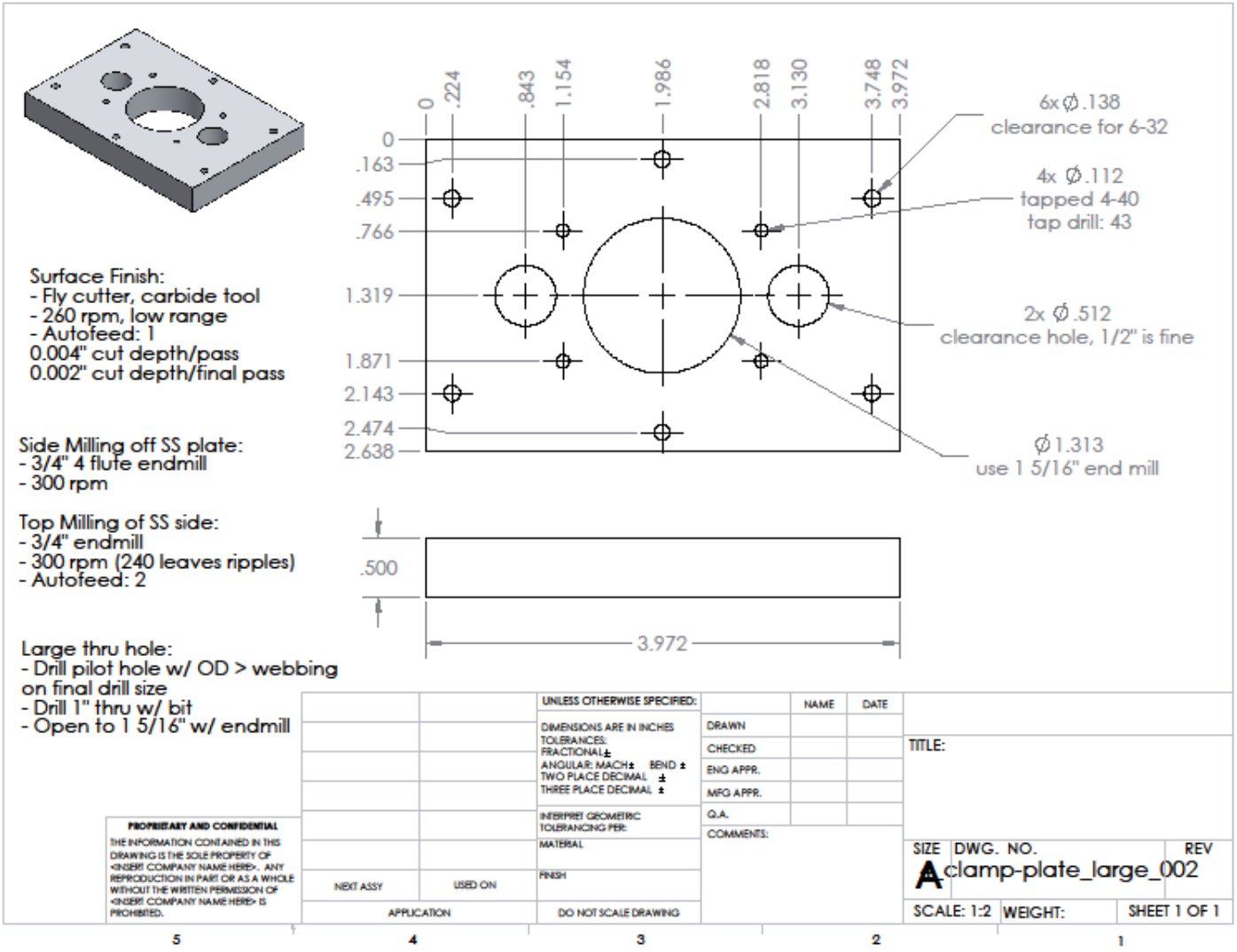

A. 9. Thin film ec-LLS cell – bottom compression plate

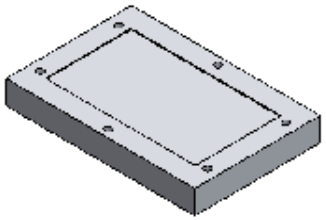

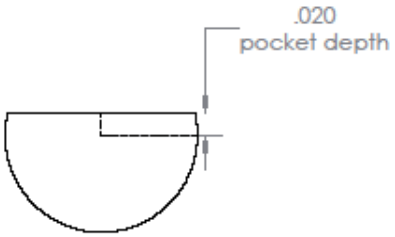

DETAIL A
SCALE 8 : 1

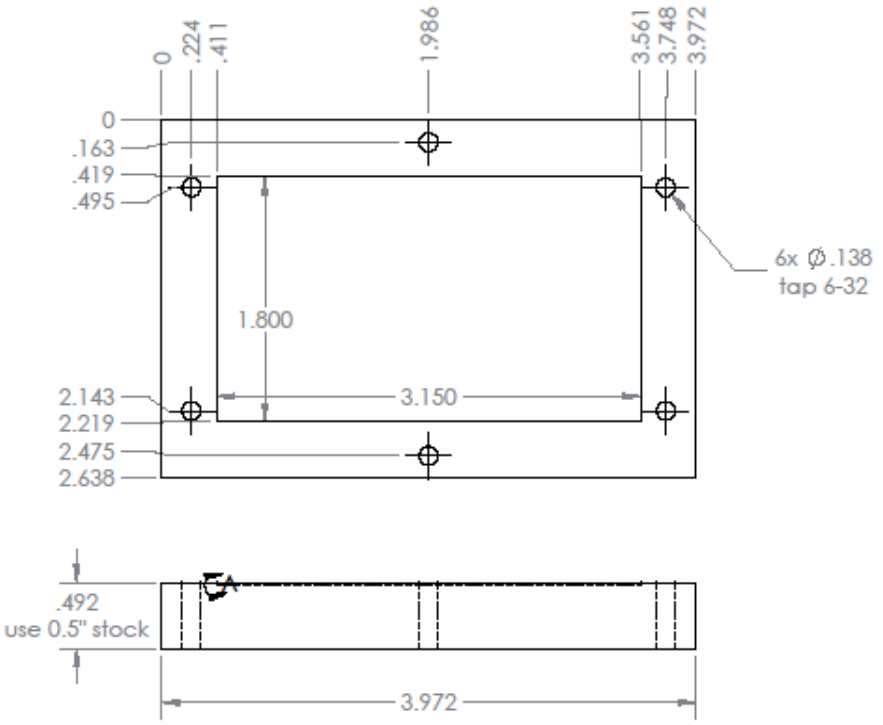

		UNLESS OTHERWISE SPECIFIED:		NAME	DATE
		DIMENSIONS ARE IN INCHES	DRAWN		
		TOLERANCES: FRACTIONAL ±	CHECKED		
		ANGULAR: MACH ± BEND ±	ENG APPR.		
		TWO PLACE DECIMAL ±	MFG APPR.		
		THREE PLACE DECIMAL ±	Q.A.		
		INTERPRET GEOMETRIC TOLERANCING PER:	COMMENTS:		
		MATERIAL 303 SS			
NEXT ASSY	USED ON	FINISH			
APPLICATION		DO NOT SCALE DRAWING			

TITLE:

SIZE	DWG. NO.	REV
A	5_bottom-plate_recess_001	
SCALE: 1:2	WEIGHT:	SHEET 1 OF 1

5 4 3 2 1

A. 10. Thin film ec-LLS cell - retainer

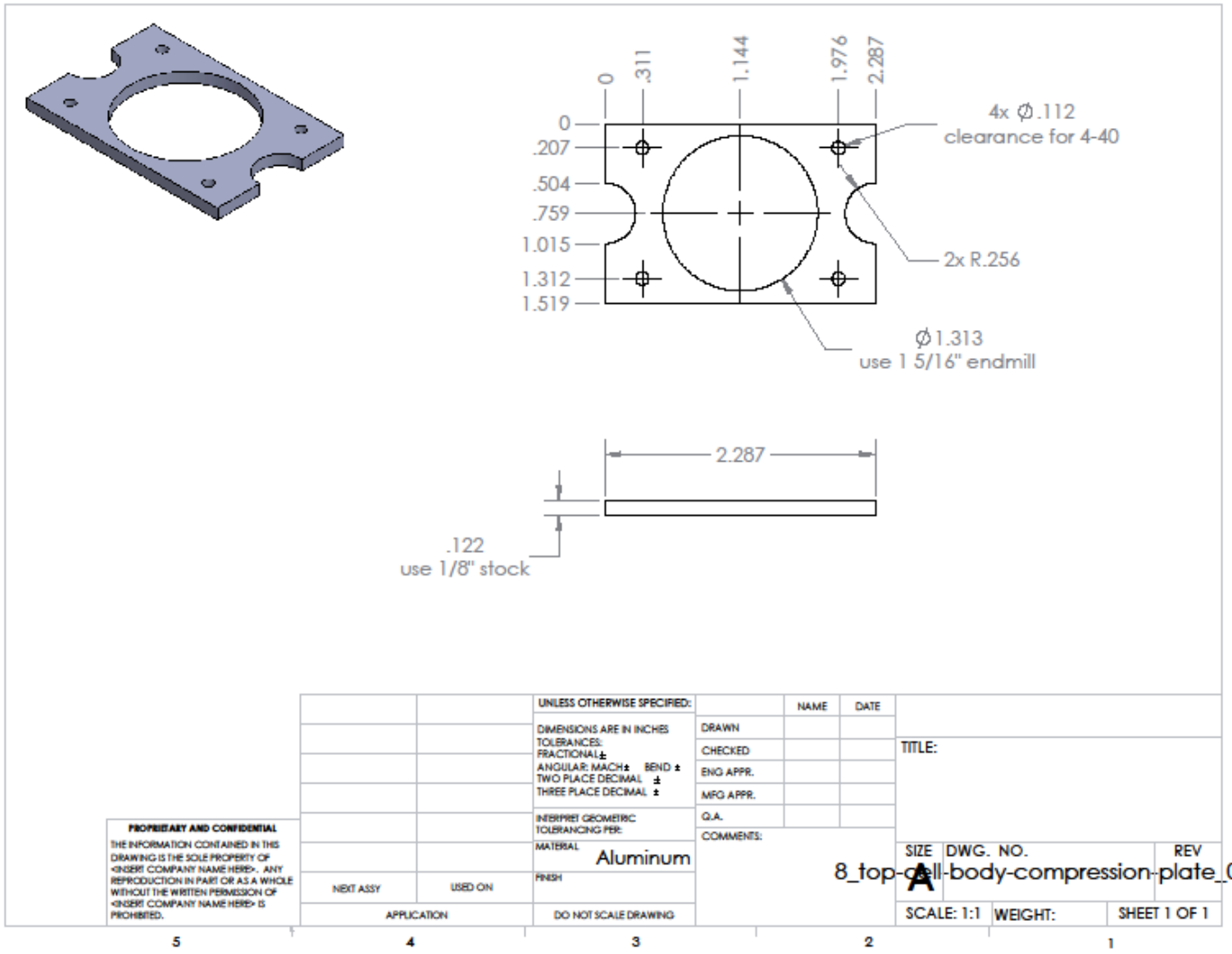

A. 2. Thin film ec-LLS cell – SiC template

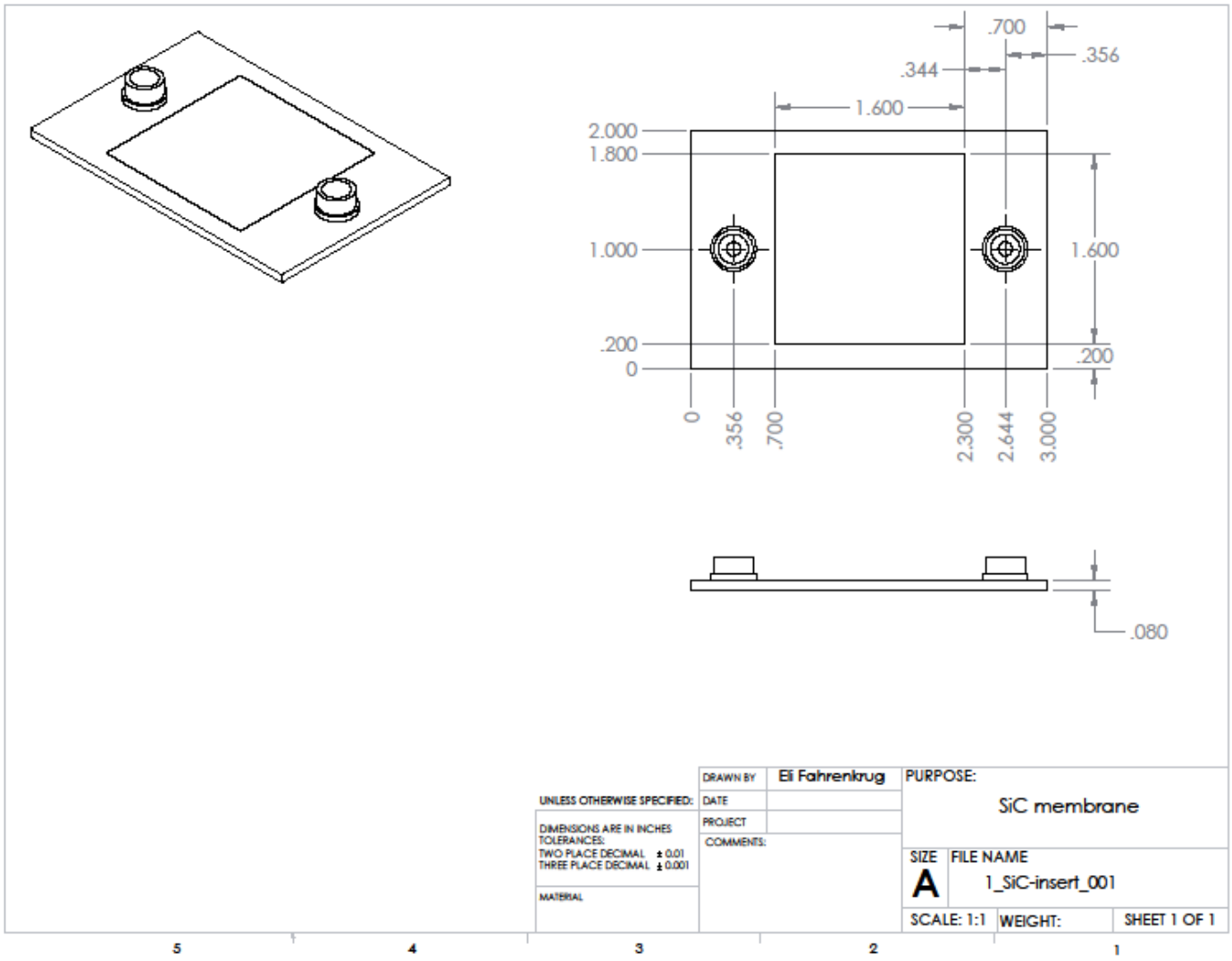

A. 3. Thin film ec-LLS cell – vacuum infiltration device

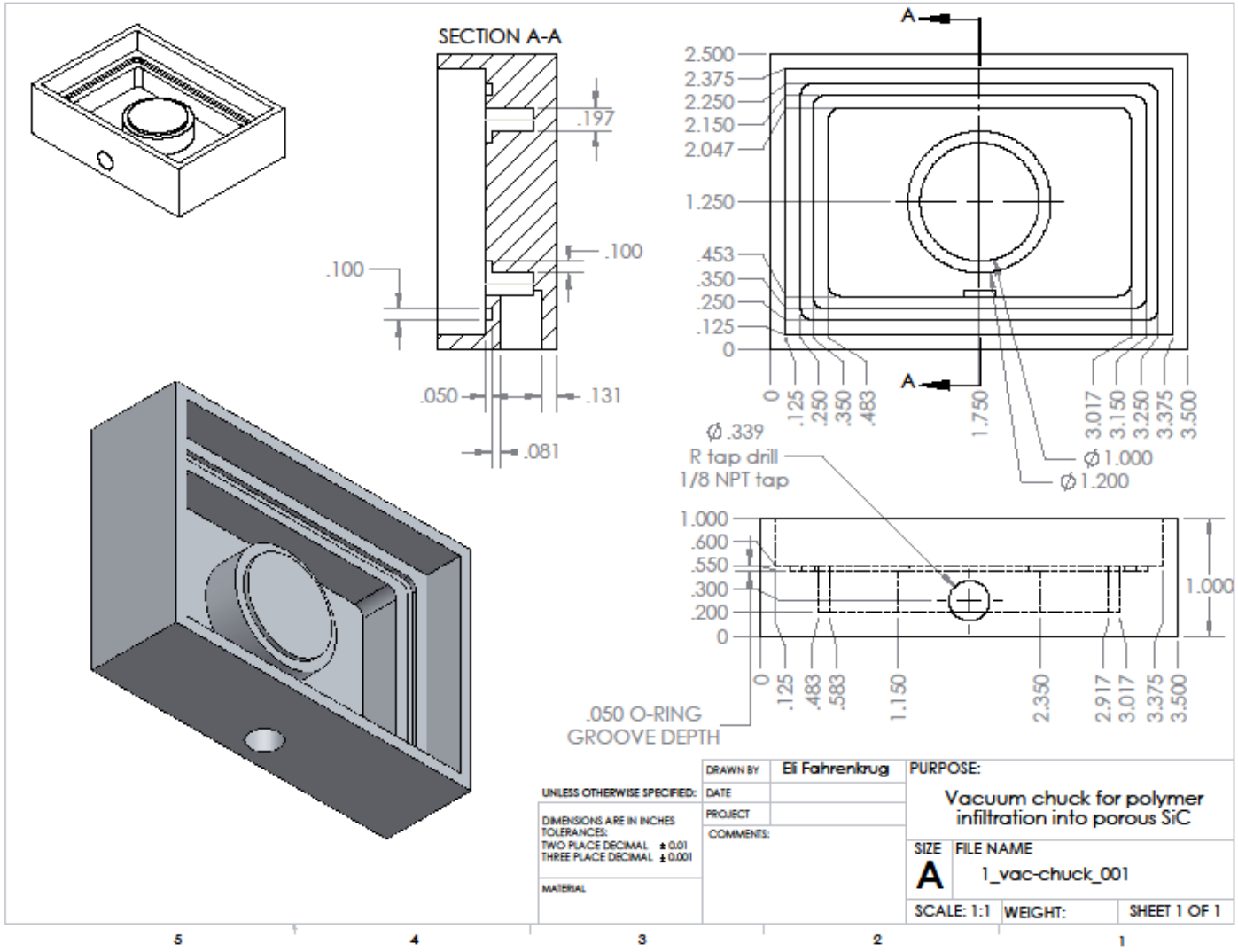

A. 4. Thin film ec-LLS, 4 inch wafer – Bottom compression plate

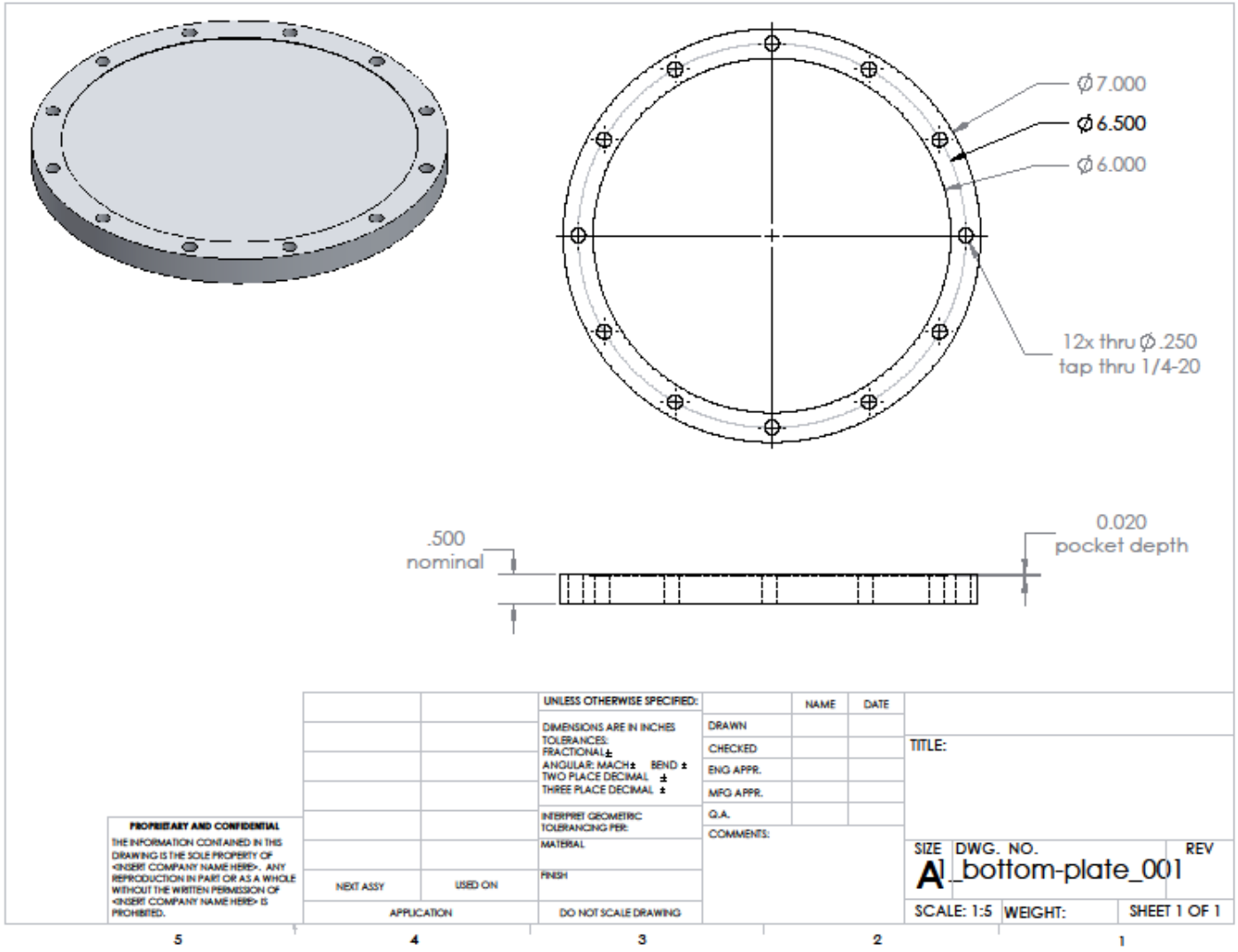

A. 5. Thin film ec-LLS, 4 inch wafer – Ohmic contact insert plate

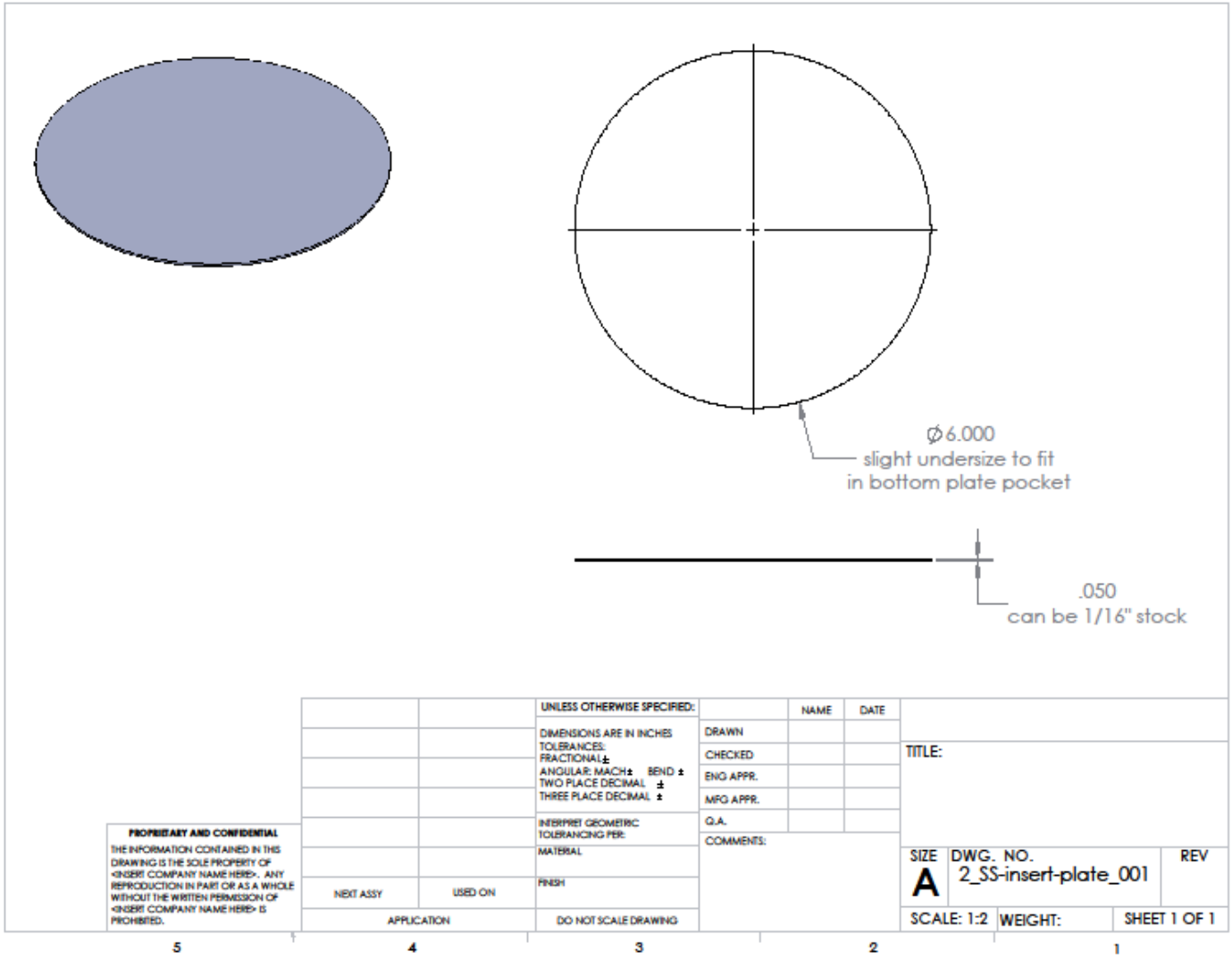

A. 6. Thin film ec-LLS, 4 inch wafer – Top compression plate

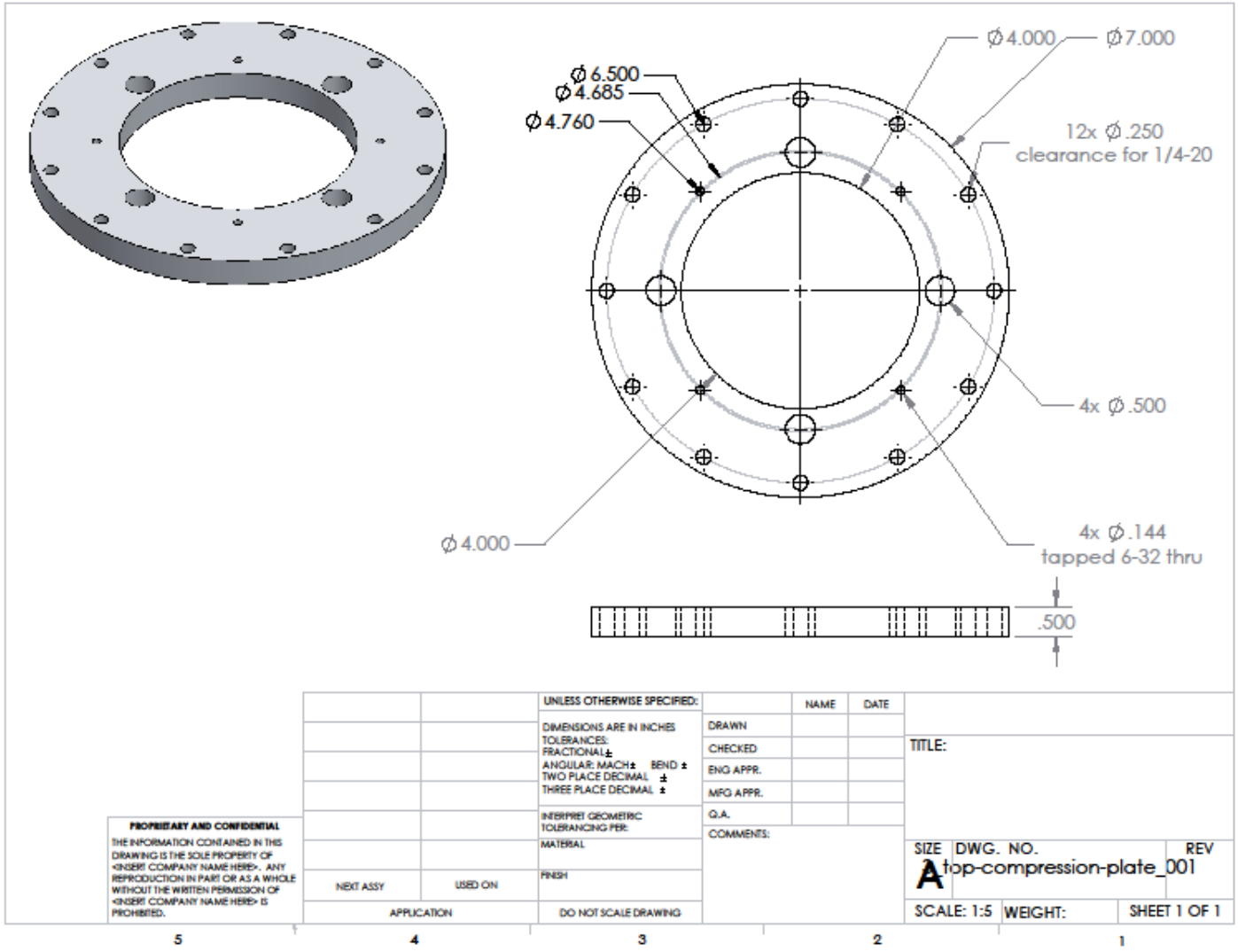

A. 7. Thin film ec-LLS, 4 inch wafer – SiC template

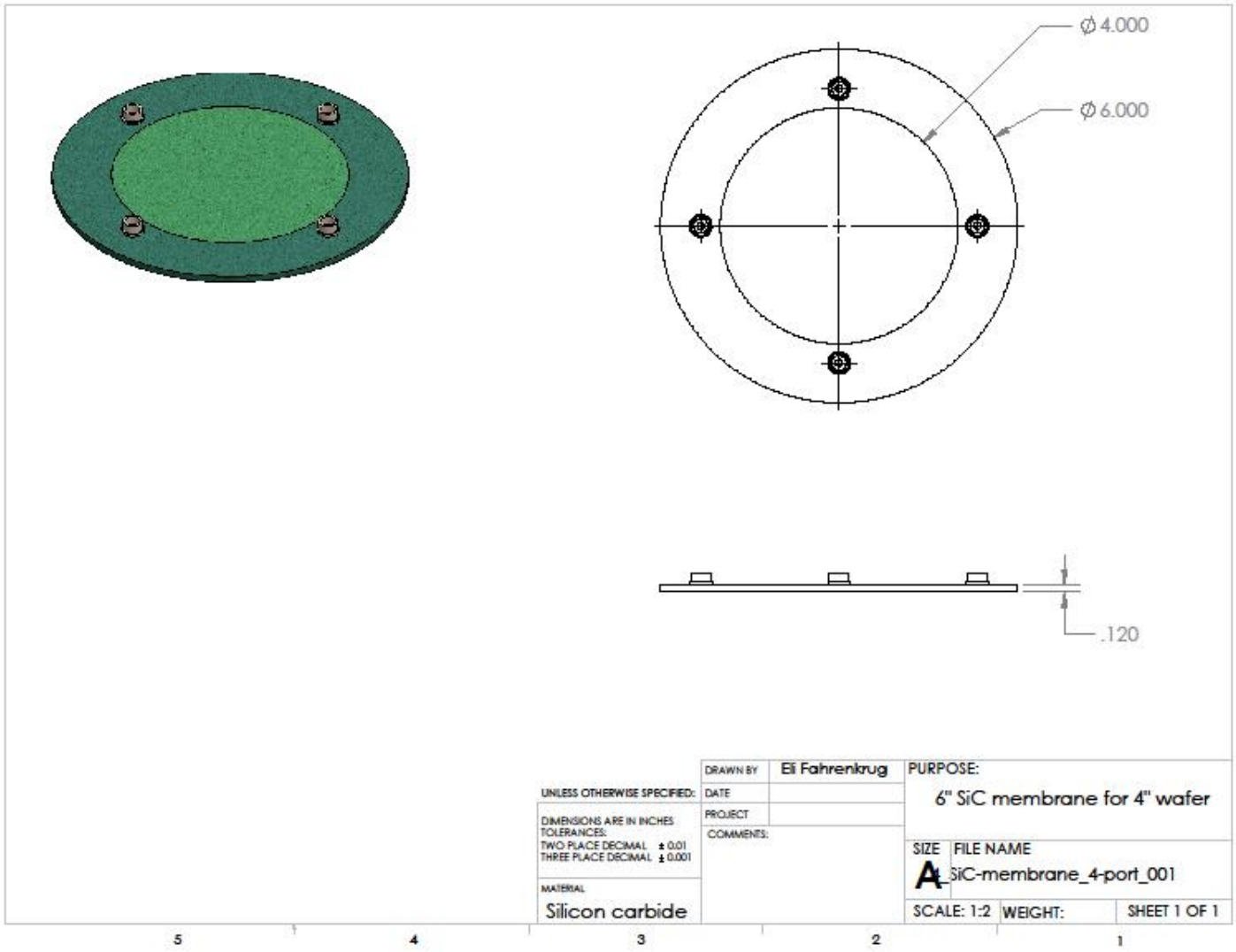

A. 8. Thin film ec-LLS, 4 inch wafer – electrolyte reservoir

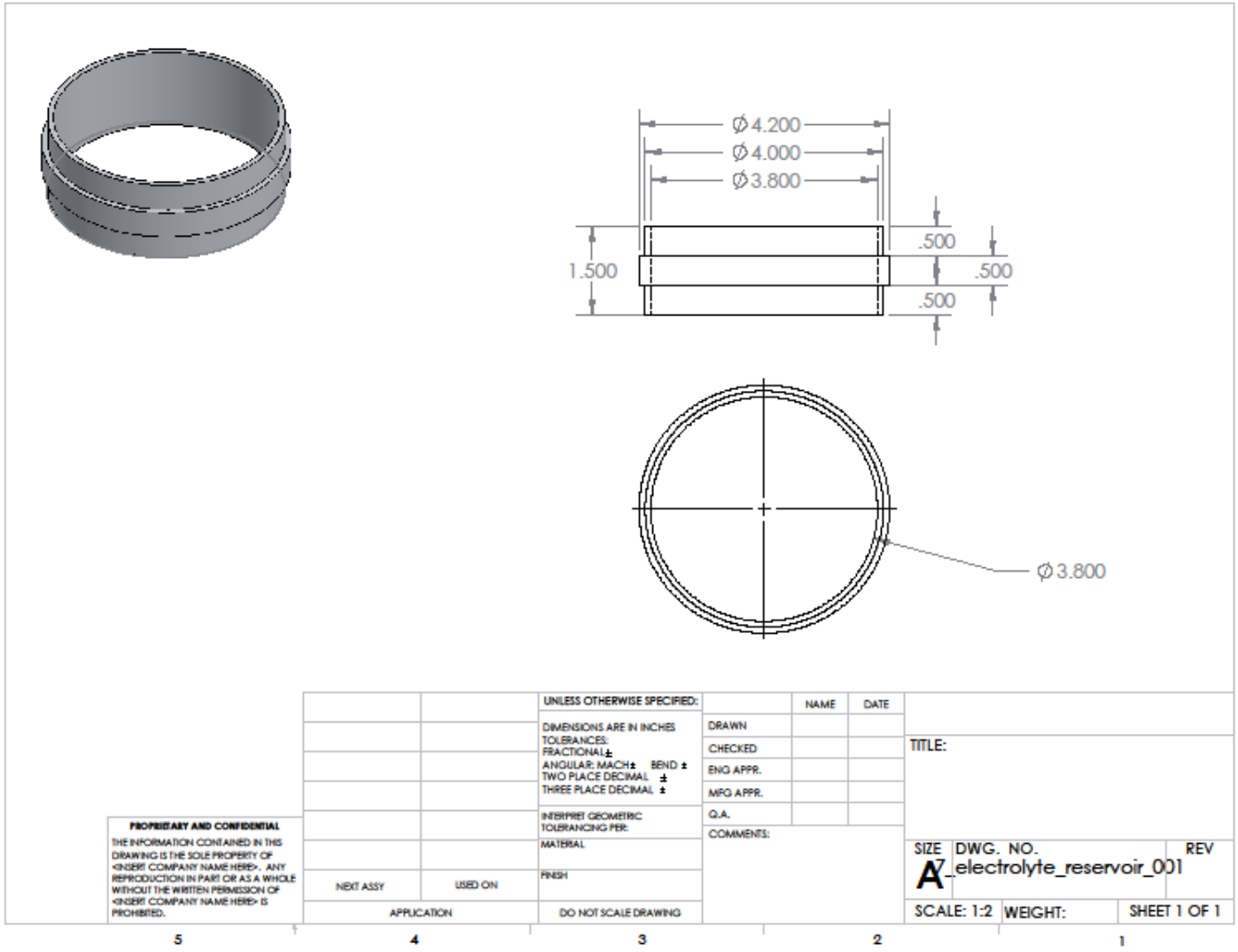

A. 9. Thin film ec-LLS, 4 inch wafer - retainer

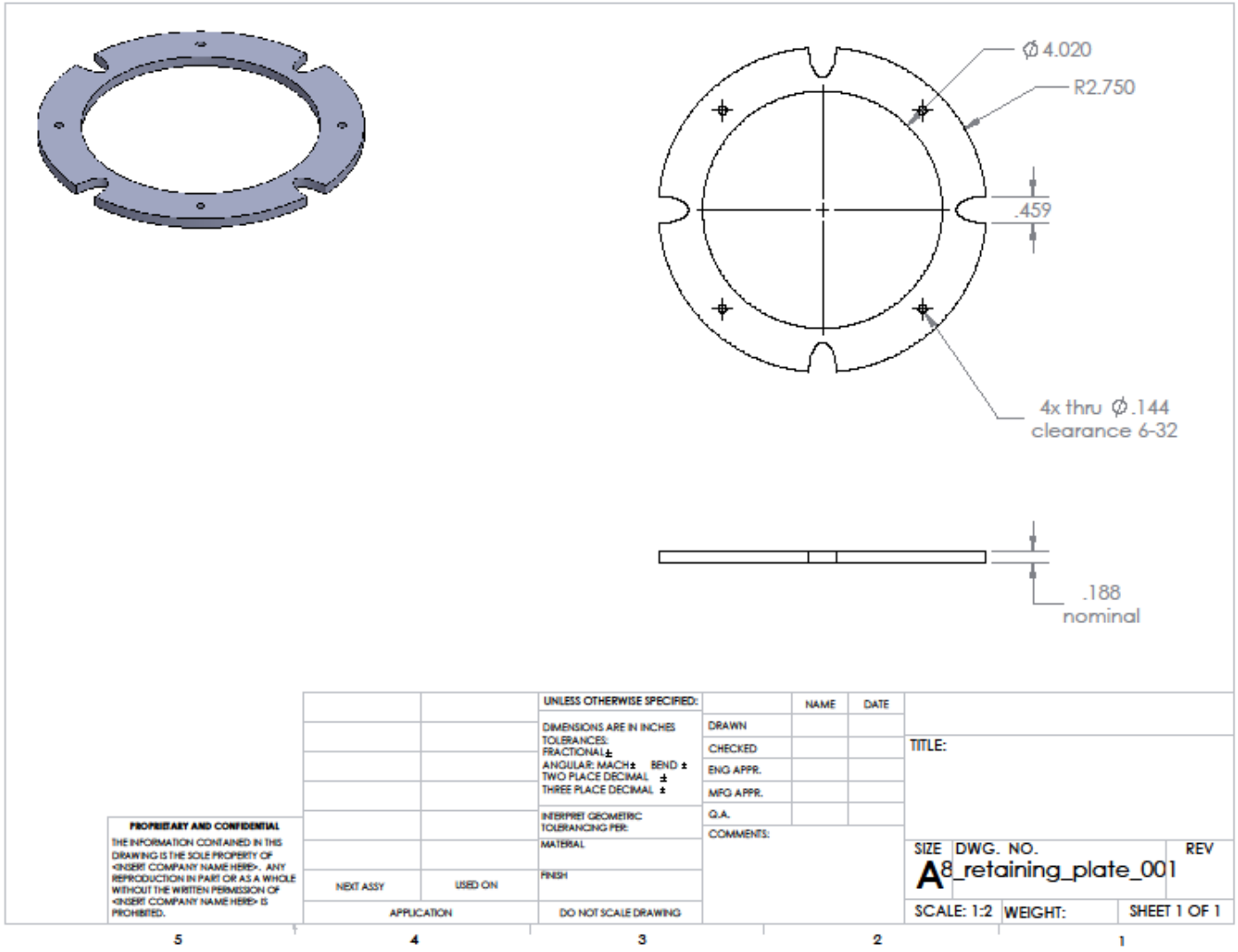

A. 19. Thin film ec-LLS, 4 inch wafer – vacuum infiltration device with flats

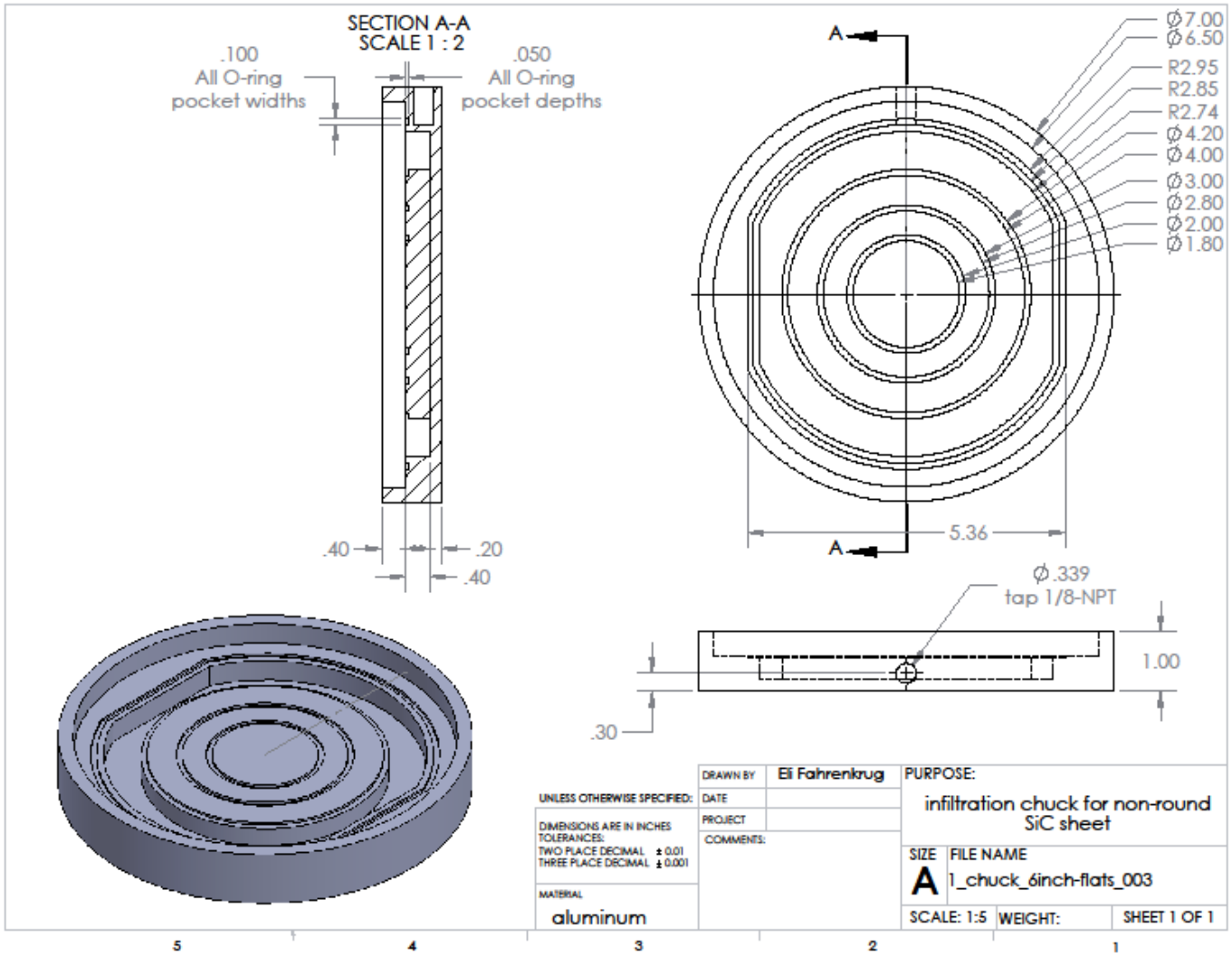

A. 10. Thin film ec-LLS, 4 inch wafer – vacuum infiltration device without flats

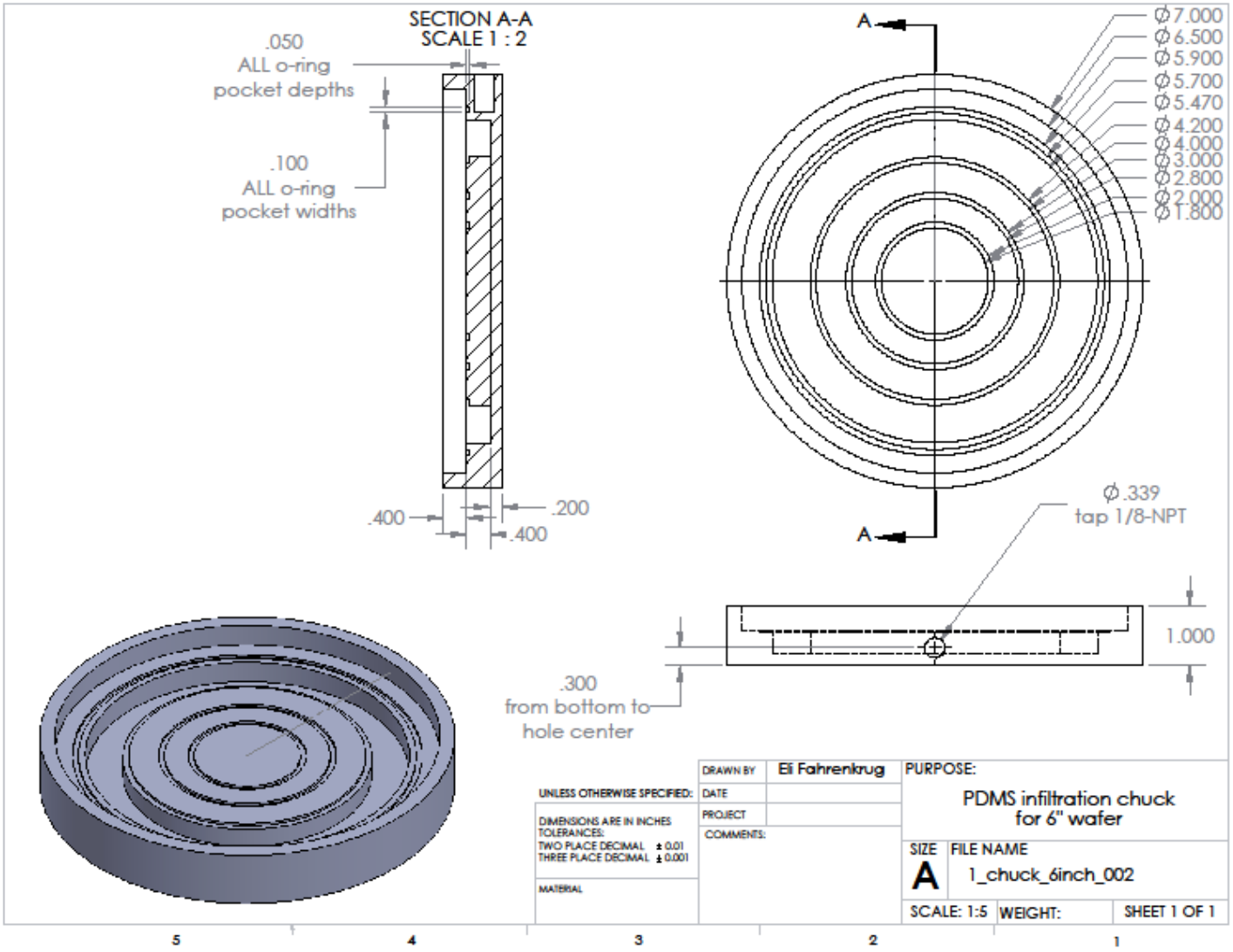
SECTION A-A
SCALE 1 : 2
.050
ALL o-ring
pocket depths
.100
ALL o-ring
pocket widths
.400
.200
.400
A
A
Ø7.000
Ø6.500
Ø5.900
Ø5.700
Ø5.470
Ø4.200
Ø4.000
Ø3.000
Ø2.800
Ø2.000
Ø1.800
Ø.339
tap 1/8-NPT
1.000
.300
from bottom to
hole center
UNLESS OTHERWISE SPECIFIED:
DIMENSIONS ARE IN INCHES
TOLERANCES:
TWO PLACE DECIMAL ± 0.01
THREE PLACE DECIMAL ± 0.001
MATERIAL
DRAWN BY
Eli Fahrenkrug
DATE
PROJECT
COMMENTS:
PURPOSE:
PDMS infiltration chuck
for 6" wafer
SIZE
A
FILE NAME
1_chuck_6inch_002
SCALE: 1:5
WEIGHT:
SHEET 1 OF 1
5
4
3
2
1

A. 11. Lift-out stub - body

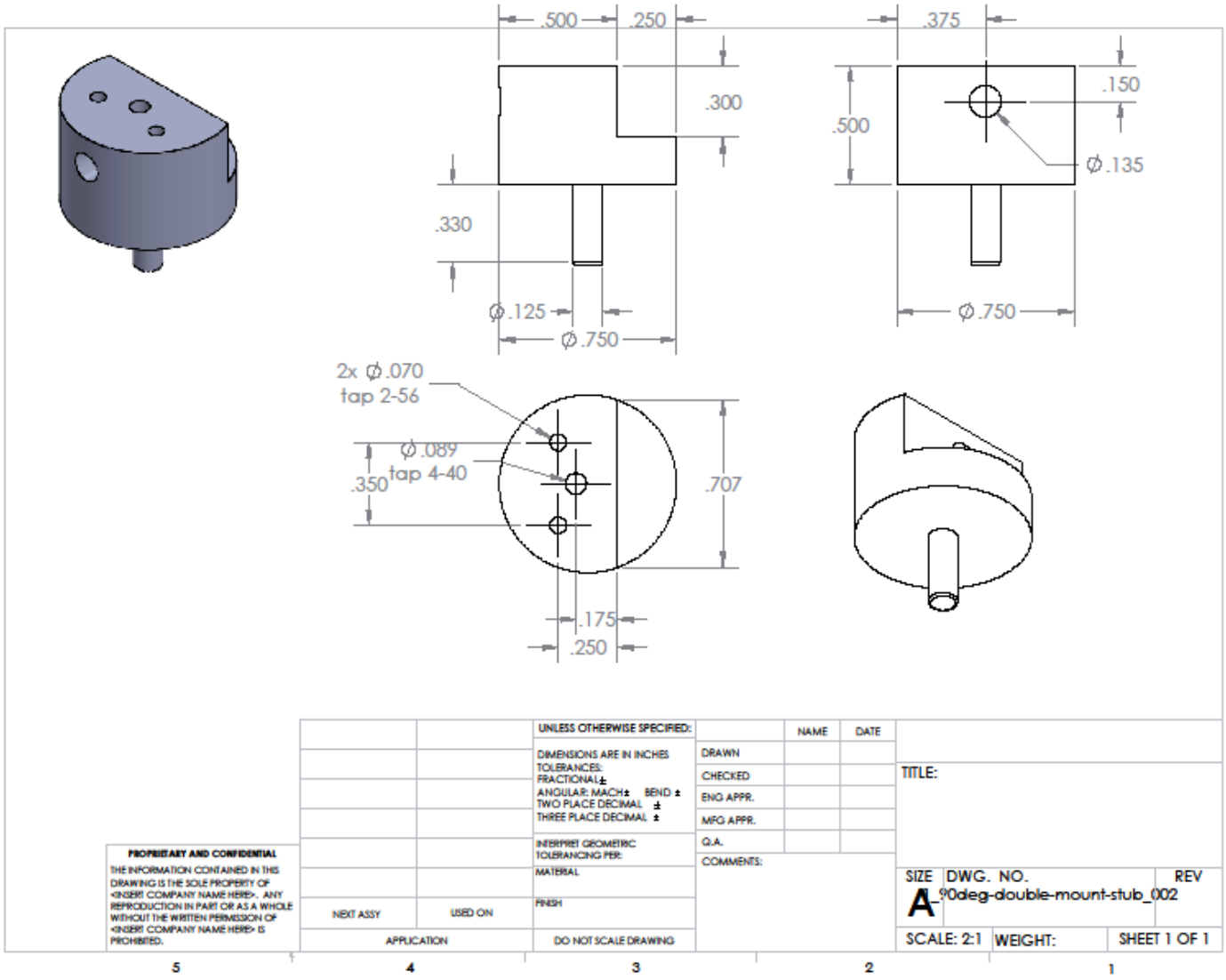

A. 12. Lift-out stub - face

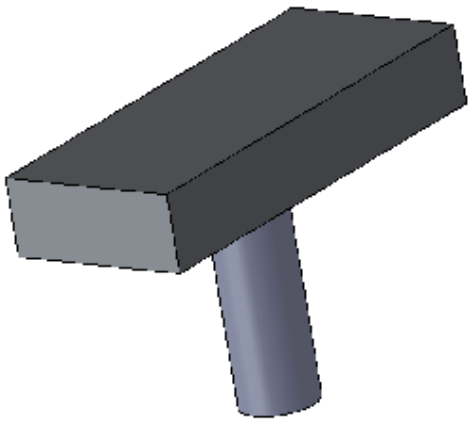

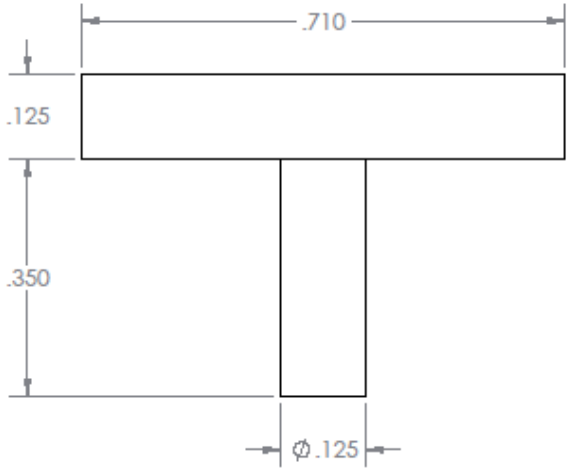

		UNLESS OTHERWISE SPECIFIED:		NAME	DATE
		DIMENSIONS ARE IN INCHES TOLERANCES: FRACTIONAL ± ANGULAR: MACH ± BEND ± TWO PLACE DECIMAL ± THREE PLACE DECIMAL ±	DRAWN		
			CHECKED		
			ENG APPR.		
			MFG APPR.		
		INTERPRET GEOMETRIC TOLERANCING PER:	Q.A.		
		MATERIAL	COMMENTS:		
NEXT ASSY	USED ON	FINISH			
APPLICATION		DO NOT SCALE DRAWING			

PROPRIETARY AND CONFIDENTIAL

THE INFORMATION CONTAINED IN THIS DRAWING IS THE SOLE PROPERTY OF <INSERT COMPANY NAME HERE>. ANY REPRODUCTION IN PART OR AS A WHOLE WITHOUT THE WRITTEN PERMISSION OF <INSERT COMPANY NAME HERE> IS PROHIBITED.

TITLE:

SIZE	DWG. NO.	REV
A	face-mount-stub_rectangle_002	

SCALE: 5:1 | WEIGHT: | SHEET 1 OF 1

5 4 3 2 1

A. 13. Lift-out stub – bus bar